



**HAL**  
open science

# Silver acetylide clusters for the electroreduction of CO<sub>2</sub>: Towards industrial scale electrolysis

Léonard Curet

► **To cite this version:**

Léonard Curet. Silver acetylide clusters for the electroreduction of CO<sub>2</sub>: Towards industrial scale electrolysis. Chemical Sciences. Université de Pau et des Pays de l'Adour, 2024. English. NNT: 2024PAUU3016 . tel-04819092

**HAL Id: tel-04819092**

**<https://theses.hal.science/tel-04819092v1>**

Submitted on 4 Dec 2024

**HAL** is a multi-disciplinary open access archive for the deposit and dissemination of scientific research documents, whether they are published or not. The documents may come from teaching and research institutions in France or abroad, or from public or private research centers.

L'archive ouverte pluridisciplinaire **HAL**, est destinée au dépôt et à la diffusion de documents scientifiques de niveau recherche, publiés ou non, émanant des établissements d'enseignement et de recherche français ou étrangers, des laboratoires publics ou privés.

Présentée et soutenue le 13 Juin 2024

par Léonard CURET

pour obtenir le grade de docteur

de l'Université de Pau et des Pays de l'Adour

Spécialité: Chimie

# Silver acetylide clusters for the electroreduction of CO<sub>2</sub>: Towards industrial scale electrolysis

## MEMBRES DU JURY

### RAPPORTEURS

- Pablo BALLESTER Professor/ ICIQ, Tarragona
- Cyrille COSTENTIN Professor/ Université Grenoble-Alpes

### EXAMINATEURS

- Carolina GIMBERT SURIÑACH Associate Professor/ Autonomous University of Barcelona

### DIRECTEURS

- Emilio PALOMARES Professor/ ICIQ, Tarragona
- Aurélien VITERISI HDR/ Université de Pau et des Pays de l'Adour
- Laurent BILLON Professor/ Université de Pau et des Pays de l'Adour



## Acknowledgements

I'd like first to express my gratitude to Aurelien, my primary supervisor during the last three years, for giving his all to ensure the success of this PhD. I'd want to thank him personally and professionally for what he's done over this time period. We developed a friendship over these years together and I will always cherish our crazy moments imagining new methods or chemicals or our long discussions about life and politics late at night. I hope he learnt as much as I did on our journey together, I wish him all the best in the future.

I'd also like to thank my two other supervisors, Emilio and Laurent, for providing me with this opportunity in the first place, for the time and energy they dedicated to getting this project started and keep it running through the years. Their presence throughout these three years through discussions and means have greatly helped me and opened my perspective on science from careers to politics and financial aspects of scientific projects.

Another PhD had begun inside this project before I arrived, and I would want to express my heartfelt gratitude to Fabio for his warm welcome and his constant assistance throughout our shared time period, as well as for all of the great moments we spent together, whether at work or at our favorite pub, debating on CO<sub>2</sub> reduction till late.

I'd want to thank everyone who has taken part in the project, both at IPREM and ICIQ. Without them this PhD wouldn't have been the same and their help has been crucial to its success. I want to thank especially, William and Didier (the computational team) for the great discussions and shared moments and their dedicated time on the theoretical models presented in this work, Dominique who spent plenty of time trying to figure out the XPS results, the crystallography team in ICIQ who managed to solve the crystalline structures through XRD and ED and Abdel without whom the NMR experiments presented in the second chapter wouldn't have been possible.

I'd also want to thank everyone I met at the polycats unit and at IPREM in general. Most of them weren't directly involved in the scientific aspect of the project but they supported me through the highs and lows of my PhD. I want to personally thank Marie-Hélène who has supported the lab and helped so many of us while keeping a great mood and her interactions with Aurelien are some of the most hilarious moments I have seen in IPREM, Leila who has taught me so much and with whom the late discussions were always great moments, Pierre for the jokes and discussions and his help when I struggled with polymers, Sandra which arrived late on our CO<sub>2</sub> reduction team but has given a lot of energy to it, I will always cherish our long talks and fun moments together, Federico for being so helpful and curious about our project and Antoine for teaching me and many others how to teach chemistry to students.

Having a good group of friends around you for such a challenging journey always helps. What an amazing time I spent working with the PhD students and post-docs around me. I will not go into details but my thanks are going to Alexandre, Alexis, Alina, Arnaud, Axelle, Bastien, Beatrice, Domenico, François, Gregoire, Marine, Marion, Maud, Nabil, Valentina, Anuja and Prithviraj (my office mates) and all the amazing people I met during these years in Pau.

## Table of Content

Abstract .....	4
LIST OF FIGURES AND SCHEMES .....	5
Chapters Figures .....	5
Experimental Part figures .....	9
LIST OF TABLES AND EQUATIONS .....	16
LIST OF ABBREVIATIONS .....	18
<b>Chapter 1 : General Introduction.....</b>	<b>21</b>
1) Global warming and Energy Transition .....	21
2) Carbon Capture, Utilization and Storage (CCUS) .....	23
3) CO <sub>2</sub> Conversion .....	25
4) CO <sub>2</sub> electrocatalysis .....	29
5) CO <sub>2</sub> RR Catalysts.....	34
A) Molecular catalysts.....	34
B) Heterogenous catalysis: metal surface .....	38
C) Heterogeneous Catalysis: Nanoparticles and clusters.....	40
6) Flow cell designs towards industrial application .....	45
A) GDLs and GDEs .....	47
B) Membranes.....	49
References .....	53
<b>Chapter 2 : Measuring the association constant of host-gas complexes in solution <i>via</i> routine NMR titrations using <i>ERETIC</i> quantification: the case of host-CO<sub>2</sub> complexes. ....</b>	<b>68</b>
Introduction .....	68
Results and discussion .....	69
Conclusion.....	75
References .....	76
Experimental section .....	79



## **Chapter 3 : Self-assembled infinite silver cluster with atomic precision as a scalable catalyst for CO<sub>2</sub>-electroreduction under industry-relevant reaction rates**

.....	<b>92</b>
Introduction .....	92
Results and discussion .....	93
Conclusion.....	100
References .....	101
Experimental section .....	104

## **Chapter 4 : Synthesis and characterization of a library of silver acetylides nanoclusters for CO<sub>2</sub> reduction ..... 132**

Introduction .....	132
Results and discussion .....	133
Synthesis and spectral measurements.....	134
Structural characterisations .....	135
CO <sub>2</sub> RR Catalytic properties.....	138
Conclusion.....	141
References .....	142
Experimental Section .....	146

## **Chapter 5 : Porphyrin-silver acetylide cluster catalysts with dual active sites for the electrochemical reduction of CO<sub>2</sub>..... 175**

Introduction .....	175
Results and discussion .....	176
Conclusion.....	180
References .....	181
Experimental section .....	183

## **Conclusion and perspectives ..... 212**

## Abstract

This thesis is devoted, in a broad sense, to the study of the transformation of CO<sub>2</sub> into added-value chemicals and the study of the interaction of CO<sub>2</sub> with organic molecules. Consequently, a large part of the manuscript focuses on the development of novel catalysts for the electrochemical reduction of CO<sub>2</sub> into carbon monoxide. As such, a class of organometallic silver clusters were thoroughly investigated. I first focused on one such cluster, namely silver phenyl acetylide, whose synthesis was optimized, and structural properties were studied in detail. Using an efficient and cost-effective synthesis protocol and unique characterization techniques, we demonstrated that silver acetylide clusters possessed enhanced catalytic properties compared to state-of-the-art catalysts in terms of activation energy, selectivity, and production rate. I further expanded our methodology to the synthesis of a library of silver acetylide-based catalysts, ranging from simple analogues to porphyrin derivatives, which allowed for further understanding of the fundamental aspects of their catalytic properties. A second part of the thesis was dedicated to the development of a complete methodology that enables the quantitative measurement of association constants between a gas and a host in solution using routine NMR spectrometry titrations. It was applied to the measurement of the association constant of two macrocyclic hosts with CO<sub>2</sub>. This methodology constitutes a significant advance since, to the best of my knowledge, no precedent exists in the field.

## LIST OF FIGURES AND SCHEMES

## Chapters Figures

<b>Figure 1.1 a)</b> Global greenhouse emissions by sector <sup>1</sup> ; <b>b)</b> Annual CO <sub>2</sub> emissions trend related to global warming calculated scenarios (red ) trend from implemented policies (blue) limit warming to 2°C with a return at 1.5°C after a high overshoot (green) limit warming to 2°C (cyan) limit warming to 1.5°C with no or limited overshoot. <sup>2</sup> .....	21
<b>Figure 1.2: a)</b> The price of electricity from different power sources <sup>3</sup> <b>b)</b> Energy consumption by sector. Coal (Cyan), Oil (blue), Gas (pale green), Electricity (green) and others (grey). Adapted from <sup>4</sup> .....	22
<b>Figure 1.3 a)</b> Carbonate looping process <sup>7</sup> ; <b>b)</b> Operational and planned capture capacity. (Pale blue) operational, (blue) in construction, (light green) planned construction. Adapted from <sup>11</sup> .....	24
<b>Figure 1.4:</b> Unit cell (left) and P (centre) and H (right) types of cages in the sl structure. Oxygen is shown in red, and hydrogen is in white (calculated from crystalline structure) <sup>14</sup> .....	24
<b>Figure 1.5: a)</b> Schematic representation of the photosynthesis mechanism <sup>17</sup> ; <b>b)</b> Mechanistic diagram depicting photosynthetic CO <sub>2</sub> -to-acetate conversion coupled with water oxidation over S.ovata Cr <sub>2</sub> O <sub>3</sub> /Ru-SrTiO <sub>3</sub> :La, Rh ITO RuO <sub>2</sub> -BiVO <sub>4</sub> :Mo. <sup>18</sup> .....	25
<b>Figure 1.6: a)</b> Chemical structure of ([Ru(bipy) <sub>3</sub> ] <sup>2+</sup> ) sensitiser; <b>b)</b> Molecular structures of the catalyst (Fe-p-TMA) and of its photosensitiser (purpurin, PP). adapted from <sup>31</sup> .....	27
<b>Figure 1.7 a)</b> molecular catalyst in solution <b>b)</b> electropolymerised, <b>c)</b> covalently bound to the semiconductor, <b>d)</b> covalently bound to the semiconductor supramolecular catalyst composed by a photosensitiser (PS)and catalyst (cat). <sup>43</sup> .....	28
<b>Figure 1.8</b> Architecture of the standalone perovskite–BiVO <sub>4</sub> PEC tandem device for bias-free syngas production. Oxygen evolution occurs at the front BiVO <sub>4</sub> photoanode with a Co WOC. An inverse-structure perovskite photocathode reduces CO <sub>2</sub> and protons to CO and H <sub>2</sub> via a CoMTPP molecular catalyst immobilised on a CNT sheet. An embedded copper wire connects the two photoelectrodes in this artificial leaf configuration. <sup>44</sup> .....	28
<b>Figure 1.9 a)</b> Possible renewable energy–powered routes to commodity chemicals driven by electrocatalysis from H <sub>2</sub> O (grey) and CO <sub>2</sub> (purple, red) as feedstocks. <sup>49</sup> ; <b>b)</b> Highest reported Faradaic efficiencies for carbon monoxide (grey squares), formic acid (purple triangles), ethylene (blue diamonds), and ethanol (red circles) and corresponding current densities (green) over the past three decades. <sup>49</sup> .....	30
<b>Figure 1.10.</b> General mechanism of the CO <sub>2</sub> RR catalysed by metals. <sup>61</sup> .....	31
<b>Figure 1.11. a)</b> Typical H-cell configuration used in CO <sub>2</sub> R experiment under a steady stream of CO <sub>2</sub> <b>b)</b> Custom-made three-electrode cell assembly used in the experiments described in this thesis. ....	34
<b>Figure 1.12 a)</b> Chemical structure of Re(bipy)(CO) <sub>3</sub> Cl complex <sup>64</sup> <b>b)</b> Chemical Structure of tetrasulfonated Cobalt phthalocyanine <sup>65</sup> <b>c)</b> chemical structure of Iron tetraphenylporphyrin chloride <sup>66</sup> .....	35

<b>Figure 1.13 a)</b> Chemical structure of Nicyclam <b>b)</b> CO <sub>2</sub> RR catalytic cycle for Nicyclam. Reprinted from JACS. Copyright ACS <sup>67</sup> .....	36
<b>Figure 1.14 a)</b> FeTDHPP structure <sup>70</sup> <b>b)</b> Structure of Fe-o-TMA <sup>71</sup> <b>c)</b> Cobalt phthalocyanine structure <sup>57</sup> .....	36
<b>Figure 1.15 a)</b> Pyrene functionalized iron porphyrin grafted onto carbon nanotubes. <sup>76</sup> <b>b)</b> [Re(bpy)(CO) <sub>3</sub> Cl] catalyst in a porous carbon frame (carbonized MOF) <sup>79</sup> <b>c)</b> Schematic illustration of the chemical structure of Hg MTPP(M=Mn, Fe, Co, Ni, Cu, and Zn) <sup>86</sup> .....	37
<b>Figure 1.16.a)</b> Binding energies of the intermediates ΔECO* and ΔEH* for common transition metals <sup>89</sup> ; <b>b)</b> , Aspects that influence the intrinsic activity of the catalytic site either by an electronic modification of the catalytic site or via non-covalent interactions with modulators or reaction intermediates. <sup>97</sup> .....	39
<b>Figure 1.17 a)</b> The proposed role of hydrophobicity in promoting CO <sub>2</sub> reduction over proton reduction. The illustrations of the operation of the hydrophobic dendrite show the enhanced CO <sub>2</sub> mass transport from the triple-phase boundary between the electrolyte, electrode and gaseous CO <sub>2</sub> . <sup>109</sup> <b>b)</b> CB[6] structure with main building block highlighted in blue. <b>c)</b> Schematic illustration of CO <sub>2</sub> conversion to CO within the cavity of CB[6] adsorbed on an Au surface. <sup>110</sup> .....	40
<b>Figure 1.18 a)</b> Free energy diagrams of CO <sub>2</sub> to CO on Au(111) (yellow), Au(211) (orange and Au <sub>13</sub> cluster (red) <sup>117</sup> <b>b)</b> Ag nanoparticles with size dependency on CO <sub>2</sub> RR activity. <sup>118</sup> <b>c)</b> transmission electron microscopy (TEM) image of Cu nanocubes <sup>120</sup> .....	41
<b>Figure 1.19 a)</b> XRD structure (CCDC: 1020984) of tubular-shaped silver phenylacetylide crystal. <sup>146</sup> <b>b)</b> XRD structure (CCDC: 290250) of a finite Ag tert-butylethynyl acetylide clusters crystal. <sup>151</sup> ....	43
<b>Figure 1.20 a)</b> X-ray diffraction single crystal structure of the Ag <sub>15</sub> cluster showing the two CO <sub>2</sub> molecules as part of the unit cell. <sup>149</sup> <b>b)</b> Zoomed-in representation of the cube-shaped Ag <sub>8</sub> atoms with the two CO <sub>2</sub> molecules. <sup>149</sup> .....	43
<b>Figure 1.21 a)</b> X-ray diffraction single crystal structure of the Ag <sub>32</sub> (C≡CAr) <sub>24</sub> cluster. Ag (blue), C (grey) and F (green). <sup>153</sup> <b>b)</b> CO and H <sub>2</sub> Faradaic efficiency for Ag <sub>32</sub> cluster. <sup>153</sup> <b>c)</b> CO and H <sub>2</sub> Faradaic efficiency for [Ag <sub>32</sub> (DPPE <sub>5</sub> )(SR) <sub>24</sub> ] <sup>2-</sup> . <sup>153</sup> .....	44
<b>Figure 1.22 a)</b> XRD structure of Ag <sub>15</sub> Cu <sub>6</sub> cluster. <sup>150</sup> <b>b)</b> Long-term operation of Ag <sub>15</sub> Cu <sub>6</sub> /C at a -3.25 V cell potential in the MEA-cell <b>c)</b> Long-term stability of Au <sub>7</sub> Ag <sub>8</sub> /GDL at -0.49 V vs RHE. <sup>148</sup> .....	44
<b>Figure 1.23 a)</b> H-Cell design with reduced cathode/anode distance. <sup>92</sup> ; <b>b)</b> cross section schematic view of a CO <sub>2</sub> RR flow cell; <b>c)</b> cross section schematic view of a CO <sub>2</sub> RR MEA cell .....	46
<b>Figure 1.24 a)</b> Representation of a GDE covered with a silver layer as catalyst <sup>167</sup> ; <b>b)</b> SEM images of a carbon gas-diffusion electrode with a deposited copper layer; Contact angle of carbon GDL before electrolysis (145°) <b>b)</b> and after 1h at -0.8 V vs RHE (117°) indicating a loss of hydrophobicity under CO <sub>2</sub> RR conditions XPS spectra at variable show the increase of surface OH and COOH at the surface <sup>161</sup> .....	47
<b>Figure 1.25. a)</b> SEM image of Cu nanoparticles sputtered on the PTFE membrane <b>b)</b> Schematic illustration and Cross-sectional SEM image of the graphite/carbon NPs/Cu/PTFE electrode. <b>c)</b> Long-term performance test of CO <sub>2</sub> reduction to ethylene in 7 M KOH compared with carbon GDE. <sup>161</sup> .....	48

<b>Figure 1.26 a)</b> Performance comparison of CO <sub>2</sub> RR flow cells with AEMs (blue), CEMs (red) and BPMs under reverse bias mode (grey, FB= forward bias) for CO production; <sup>170</sup> <b>b)</b> Comparison of the ion crossing ability for an AEM (Top) and BPM (Bottom) <sup>174</sup> .....	50
<b>Figure 2.1</b> General scheme of host-guest complexes formation, studied herein. ....	69
<b>Figure 2.2.</b> General scheme of the titration methodology showing the equilibrium between dissolved CO <sub>2</sub> (CO <sub>2</sub> (sol)) and gaseous CO <sub>2</sub> (CO <sub>2</sub> (gas)). The total concentration of CO <sub>2</sub> in solution is quantified by <sup>13</sup> C NMR. The chemical shift observed in the <sup>1</sup> H NMR spectra of the corresponding samples serves as the Y axis of the binding isotherm curve.....	70
<b>Figure 2.3.</b> Sections of <sup>1</sup> H NMR spectra (in CDCl <sub>3</sub> ) of macrocycle 1 in the presence of excess CO <sub>2</sub> (120 equivalents), taken from spectra recorded at different time intervals. The blue line corresponds to the reference spectrum acquired under an atmosphere of pure Helium.....	71
<b>Figure 2.4. a)</b> Sections of <sup>1</sup> H NMR spectra (in CDCl <sub>3</sub> ) of macrocycle 1 in the presence of incremental quantities of CO <sub>2</sub> (shown as [CO <sub>2</sub> ]/1 ratio), taken from spectra recorded after a 72h equilibration time; <b>b)</b> Binding isotherm drawn from the corresponding data and curve fit from a 1:1 binding isotherm equation (see SI) .....	72
<b>Figure 2.5.</b> DFT modelled structures of host-guest complexes of macrocycle 1 with <b>a)</b> CO <sub>2</sub> and <b>b)</b> CHCl <sub>3</sub> , with corresponding Gibbs free energy change of formation (from separate components) and hydrogen bonds length between the amide groups and respective guests. ....	73
<b>Figure 2.6. a)</b> Sections of <sup>1</sup> H NMR spectra (in CDCl <sub>3</sub> ) of CB[6] in the presence of incremental quantities of CO <sub>2</sub> (shown as [CO <sub>2</sub> ]/1 ratio), taken from spectra recorded after a 48h equilibration time; <b>b)</b> Binding isotherm drawn from the corresponding data (protons Ha) and curve fit from a 1:1 binding isotherm equation (see SI) .....	74
<b>Figure 3.1.</b> General scheme of silver acetylide's synthesis with a representation of an asymmetric unit of the cluster fragment established by electron diffraction showing two Ag <sub>4</sub> clusters subunits with h and m and h and m ligand bonding types.....	94
<b>Figure 3.2.</b> Electron diffraction structure of silver acetylide AgPh showing <b>a)</b> the infinite arrangement of silver atoms with the two different types of Ag <sub>4</sub> clusters subunits depicted in blue and green, <b>b)</b> the unit cell and crystalline packing of the cylindrical silver clusters with infinite order with radially disposed outward-pointing acetylide groups <b>c)</b> a close view of a cluster fragment in space-filling style, pointing to the somewhat sterically hindered silver cluster.....	95
<b>Figure 3.3.</b> XPS measurements of the starting material <b>a)</b> C1s peak. Phenyl (green) C≡C–Ag(purple) <b>b)</b> Ag3d with the doublet of doublet and of the as-prepared electrodes <b>c)</b> before (down) and after electrolysis (top).....	96
<b>Figure 3.4.</b> Powder diffractograms of the pristine catalyst and of the GDE after catalyst deposition .....	97
<b>Figure 3.5. a)</b> Linear sweep voltammograms of AgPh in N <sub>2</sub> and CO <sub>2</sub> saturated cells <b>b)</b> Linear sweep voltammograms of AgPh and silver foil in CO <sub>2</sub> saturated conditions; <b>c)</b> Histograms showing the faradic efficiency of AgPh resulting from chronoamperograms carried out from -0.63V to -1.13V vs RHE .....	97

<b>Figure 3.6 a)</b> chronopotentiometry experiments between 50 and 300 mA.cm <sup>-2</sup> <b>b)</b> Faradic efficiency of AgPh under CO <sub>2</sub> reduction conditions in a flow cell electrolyser (KHCO <sub>3</sub> (1M) as catholyte and anolyte) and corresponding cathode potential (vs RHE); <b>c)</b> Faradic efficiency evolution over 12h at 100 mA/cm <sup>2</sup> .....	98
<b>Figure 3.7.</b> Schematic of the plausible mechanism of the electrocatalytic CO <sub>2</sub> reaction optimized structures for an Ag <sub>4</sub> possessing <b>a)</b> 4 ligands <b>b)</b> 3 ligands. C, H, O and Ag atoms are represented by grey, white, red and blue spheres, respectively. ....	99
<b>Figure 4.1</b> Schematic representation of the mechanistic details of Scheiber's synthetic route to silver acetylides. The inset shows an X-ray crystal structure of phenyl acetylene-based silver acetylide. ....	133
<b>Figure 4.2.</b> Schematic overview of the library of silver acetylides synthesised using Scheiber's route. The chemical structures are represented in their simplified form as the silver-carbanion species. However, crystal structures of identical and similar derivatives show that the solid-state structure of the compounds depicted form metallic clusters. ....	134
<b>Figure 4.3</b> Powder XRD of the derivatives recorded from 2 to 30° of 2θ values, on a 2D-Phaser benchtop diffractometer (Bragg-Brentano).....	136
<b>Figure 4.4</b> XPS spectra of AgAnisole <b>a)</b> Ag3d <b>b)</b> C1s ; AgOct <b>c)</b> Ag3d <b>d)</b> C1s;AgTfotl <b>e)</b> Ag3d <b>f)</b> C1s;AgThio <b>g)</b> Ag3d <b>h)</b> C1s.....	137
<b>Figure 4.5</b> Cyclic voltammetry of <b>a)</b> Agtol and <b>b)</b> AgAnisole .....	138
<b>Figure 4.6. a)</b> LSV curves of the derivatives recorded from 0 to -2 V vs Ag/AgCl and converted vs RHE; <b>b)</b> Faradic efficiencies of the different derivatives. The data is extracted from 15-minute long chronoamperometry experiments at -0.63 V vs RHE in a CO <sub>2</sub> -saturated 1M KHCO <sub>3</sub> solution. ....	140
<b>Figure 4.7 a)</b> CO <sub>2</sub> to CO current density extracted from the faradic efficiencies measured between -0.63 and -1.13 V vs RHE. <b>b)</b> CO <sub>2</sub> to CO Turnover frequencies (TOFs). The data is extracted from the 15 min long chronoamperometry experiments at -0.63 V vs RHE in a CO <sub>2</sub> -saturated 1M KHCO <sub>3</sub> solution correlated with the calculated catalytically active silver species. ....	141
<b>Figure 5.1.</b> Schematic representation of a metal-porphyrin silver acetylide cluster 2D network synthesised from an alkyne-tetra functionalised porphyrin. This is a hypothetical structure based of reported X-Ray diffraction crystal structures of silver acetylides.....	176
<b>Figure 5.2.</b> Depiction of the synthetic route to mono- and tetrasubstituted silver acetylides clusters. ....	177
<b>Figure 5.3.</b> Powder diffractogram of all four silver acetylides, recorded on a Bruker D2-Phaser X-Ray diffractogram (Bragg-Brentano geometry). ....	178
<b>Figure 5.4.</b> Zoomed in fragments of the XPS spectrum of [FeTaTTPAg] <sub>x</sub> <b>a)</b> C1s electrons emission <b>b)</b> N1s electrons emission <b>c)</b> Ag3d electrons emission <b>d)</b> O1s electrons emission. ....	179
<b>Figure 5.5</b> Faradic efficiency of all four porphyrin-silver acetylide clusters studied herein calculated from chronoamperometry experiments carried out at fixed potential in 3-electrode cell-type. The potentials are reported against RHE. ....	180

**Experimental Part figures**

<b>Figure S2-1.</b> Schematics of the NMR tube, gas filling system (developed in-house). The controller performs the following steps in a completely automated manner: 1) The NMR tube containing a sample of the host in a deuterated solvent is placed under a high vacuum while being held in liquid nitrogen. The precise amount (nmols to mmols) of gas mixture is added via the valves manifold. The sample is subsequently flame-sealed, left to warm up to room temperature and transferred to the NMR spectrometer. ....	86
<b>Figure S2-2.</b> a) The inversion recovery sequence and the expression describing the recovery of magnetisation (Mz) after inversion back toward its equilibrium value (M <sub>0</sub> ) as a function of recovery time (t); a) Experimental result of the inversion-recovery sequence to dissolved CO <sub>2</sub> in CDCl <sub>3</sub> ....	87
<b>Figure S2-3</b> <sup>13</sup> C NMR spectrum in CDCl <sub>3</sub> of ERETIC reference showing the peaks of dissolved <sup>13</sup> CO <sub>2</sub> and with their respective integrals. ....	88
<b>Figure S2-4</b> <sup>13</sup> C NMR spectra in CDCl <sub>3</sub> corresponding to some of the titration samples. The intensity of the CDCl <sub>3</sub> residual peak was kept at an identical intensity, showing the increase in the <sup>13</sup> CO <sub>2</sub> peak with increasing concentration. The <sup>13</sup> CO <sub>2</sub> peak zoomed-out region is shown in the inset. ..	89
<b>Figure S3-1:</b> 3-electrodes Electrochemical Cell.....	105
<b>Figure S3-2: a)</b> 3D printed Flow Cell design <b>b)</b> Prepared GDE in the WE Slot <b>c)</b> Flow Cell setup in the 2-electrode configuration .....	107
<b>Figure S3-3:</b> <sup>1</sup> H NMR spectrum of AgPh in DMSO-d <sub>6</sub> using a 400 MHz spectrometer.....	110
<b>Figure S3-4:</b> IR-ATR spectrum of phenylacetylene (red) and silver phenylacetylide (black). The highlighted peaks are assigned to the C-H stretching (3289 cm <sup>-1</sup> ) of the acetylene, and the peaks at 2109 and 2054 cm <sup>-1</sup> are assigned to the C≡C symmetric stretching for phenylacetylene and AgPh, respectively. ....	111
<b>Figure S3-5:</b> TGA measurement of AgPh <b>a)</b> mass loss (%) vs T (°C) <b>b)</b> 1/T vs T. The first mass loss is assumed to be residual solvents while the second mass loss is attributed to the organic part degradation. ....	111
<b>Figure S3-6</b> Powder XRD of a Freudenberg GDL (Black) A GDL covered with a mixture of Nafion and Carbon Black (Red) A GDL covered with a mixture of Nafion, Carbon Black and AgPh (Blue). The peak observed at 26° is assumed to be a polymer additive on the raw GDL substrate. ....	112
<b>Figure S3-7</b> Powder XRD of an electrode Before (Black) and After (Red) electrolysis. The crystalline structure is maintained during the electrode preparation and lost after electrolysis. ....	113
<b>Figure S3-8</b> Powder XRD between 2° and 60° of an electrode Before (Black) and After (Red) electrolysis. The crystalline structure is maintained during the electrode preparation and lost after electrolysis.....	113
<b>Figure S3-9: a)</b> LSV measurement at 10 mV/s (2nd scan) of the deposited AgPh on the GDE substrate in CO <sub>2</sub> (Black) and N <sub>2</sub> (Red) saturated 1 M KHCO <sub>3</sub> solution <b>b)</b> LSV measurement at 10 mV/s (2nd scan) of the deposited AgPh on the GDE substrate in a CO <sub>2</sub> saturated 1 M KHCO <sub>3</sub> solution. Catalytic threshold is attributed to the intersection point between faradic current tangent and capacitive current tangent. The catalytic threshold is measured to be -0.452 V vs RHE Corresponding to $\eta_{CO_2 \text{ to } CO} = 0.383$ V.....	114

- Figure S3-10:** LSV measurement at 10 mV/s (2nd scan) of the deposited AgPh on the GDE substrate (Black) compared to a silver electrode (mirror polished) (Red) in a CO<sub>2</sub>-saturated 1 M KHCO<sub>3</sub>. The Ag overpotential at 10mA/cm<sup>2</sup> compared with AgPh is measured to be 405 mV. .... 114
- Figure S 3-11: a)** Cyclic voltammograms (CV) of a 25 mM potassium ferrocyanide in a 0.1M KCl solution using an AgPh electrode at various scan rates (5, 10, 15 and 20mV/s). Cathodic and anodic peak currents correspond to the redox activity of ferrocyanide; **b)** Peak current as a function of the square root of scan rate. The ECSA is estimated from the slope of the plot. ECSA= 0.724 cm<sup>2</sup>, R<sup>2</sup>=0.97 ..... 115
- Figure S3-12:** CV measurement at 100 mV/s of the deposited AgPh on the GDE substrate in a N<sub>2</sub> saturated 1 M KHCO<sub>3</sub> solution. The observed reduction peak is attributed to Ag<sup>+</sup> reduction to metallic Ag<sub>24</sub>. The integration of the reduction peak was used to calculate the amount of active silver species on the electrode..... 116
- Figure S3-13: a)** Chronoamperometry (CA)(15min) at various applied potentials (V, E vs RHE) of the deposited AgPh on the GDE substrate in a CO<sub>2</sub>-saturated 1 M KHCO<sub>3</sub>. **b)** Measured faradaic efficiency (FE) from direct GC and NMR quantifications for each CA **c)** CO and H<sub>2</sub> partial Current densities for AgPh at various applied potentials (15min chronoamperometry) in the 1M KHCO<sub>3</sub> aqueous solution **d)** Calculated TOF variation for CO<sub>2</sub>RR ..... 117
- Figure S3-14:** CV measurement at 100 mV/s of the deposited AgPh on the GDE substrate in **a)** N<sub>2</sub> and **b)** CO<sub>2</sub>-saturated 1 M KHCO<sub>3</sub> solution ..... 117
- Figure S3-15:** Electrochemical Impedance Spectroscopy (EIS) **a)** Bode plot **b)** Nyquist plot of a deposited AgPh on a GDE substrate in an N<sub>2</sub> saturated 1 M KHCO<sub>3</sub> solution. The initial Resistance is measured as the point where -Z'' is equal to 0. .... 118
- Figure S3-16:** Cyclic Voltammetry (CV) measurement at 100 mV/s of a silver electrode (mirror polished) in an N<sub>2</sub> saturated 1 M KHCO<sub>3</sub> solution. **a)** CV scans repeated 3 times. No specific feature apart from a reduction peak attributed to surface Ag<sub>2</sub>O. **b)** zoom on the reduction peak..... 118
- Figure S3-17:** Electrochemical Impedance Spectroscopy (EIS) **a)** Bode plot **b)** Nyquist plot of a silver electrode (mirror polished) in an N<sub>2</sub> saturated 1 M KHCO<sub>3</sub> solution. .... 118
- Figure S3-18:** quantitative NMR measurement at variable applied potentials (E vs RHE) (uncorrected). DMSO<sub>2</sub> standard is fixed at 3.1 ppm. **a)** -0.63 V **b)** -0.73V **c)** -0.83V **d)** -0.93V **e)** -1.03V **f)** -1.13V. Observed liquids have been quantified against DMSO<sub>2</sub> and are referenced in 120
- Figure S3-19: a)** Chronopotentiometry (CP)(30min) at various constant currents of the deposited AgPh on the GDE substrate in the Flow Cell device. Both anolyte and catholyte compartments used a 1 M KHCO<sub>3</sub> solution. CO<sub>2</sub> flow rate: 10ml.min<sup>-1</sup>; Electrolyte flow rate: 4ml.min<sup>-1</sup> **b)** Measured faradic efficiency (FE) from direct GC quantification for each preceding CP **c)** CO partial current density depending on iR corrected potential (average value over 30min) **d)** Turnover frequency (TOF) depending on the applied current..... 122
- Figure S3-20:** Faradic yields obtained from in-line GC quantification **a)** 64h long chronopotentiometry at 50 mA.cm<sup>-2</sup> **b)** 12h long chronopotentiometry at 200 mA.cm<sup>-2</sup> of Flow cell experiments (1 M KHCO<sub>3</sub>; counter electrode: Pt on titanium plate (1 cm<sup>2</sup>); working electrode: AgPh/C (geometrical surface: 1 cm<sup>2</sup>)) ..... 122



<b>Figure S3-21:</b> a) Chronopotentiometry at 100 mA/cm <sup>2</sup> (uncorrected cell potential) for a 12h durability test b) Faradic yields from in line GC quantification of 12h long chronopotentiometry Flow cell experiments (1 M KHCO <sub>3</sub> ; counter electrode: Pt on titanium plate (1 cm <sup>2</sup> ); working electrode: AgPh/C (geometrical surface: 1 cm <sup>2</sup> )).....	123
<b>Figure S3-22:</b> XPS Elemental quantification and their related XPS spectra (C1s, F1s and Ag 3d regions) <b>A)</b> carbon black on GDE <b>B)</b> carbon black and Nafion on GDE <b>C)</b> AgPh powder <b>D)</b> AgPh, Carbon black and Nafion on GDE before electrolysis <b>E)</b> AgPh, Carbon black and Nafion on GDE after electrolysis. <b>The observation of O=C-O bond and O content increase after electrolysis are assumed to be carbonate salt accumulation on the GDL surface or the formation of COOH and OH groups onto the GDL.</b> .....	124
<b>Figure S3-23:</b> SEM images of the deposited Ag-Ph mixed with CB and Nafion on a GDE (before electrolysis) <b>a)</b> x100 magnification. <b>b)</b> x2000 magnification <b>c)</b> x 10 000 magnification <b>d)</b> x50 000 magnification <b>e)</b> x100 000 magnification.....	125
<b>Figure S3-24:</b> SEM images of the deposited Ag-Ph mixed with CB 5Vulcan and Nafion on a GDE (after electrolysis) <b>a)</b> x100 magnification <b>b)</b> x2000 magnification <b>c)</b> x 10 000 magnification <b>d)</b> x50 000 magnification <b>e)</b> x100 000 magnification <b>f)</b> x250 000 magnification.....	126
<b>Figure S3-25:</b> EDS elemental mapping of AgPh electrodes <b>a)</b> SEM image at 50 000 magnification <b>b)</b> Silver elemental mapping <b>c)</b> Fluorine elemental mapping EDS indicates a homogeneous deposition of AgPh and Nafion on the electrode surface. <b>The images show a good dispersion of the catalytic Silver material on the surface alongside the Nafion binder.</b> .....	127
<b>Figure S3-26:</b> Microscope images of AgPh <b>a)</b> 10x magnification <b>b)</b> 20x with polarized light <b>c)</b> 50x with polarized light. <b>Formation of anisotropic structures is directly observed upon reaction, leading to needle-shaped crystals. They were confirmed to be of crystalline nature from polarized light.</b> .....	127
<b>Figure S3-27 and Table S3-3:</b> Quantitative elemental analysis by EDS at different regions of an AgPh electrode before electrolysis. (X axis: Energy keV; Y axis: cps).....	128
<b>Figure S3-28:</b> Contact angle of Freudenberg carbon paper <b>a)</b> before and <b>b)</b> after a 15 min electrolysis a 10 mA and of the prepared AgPh electrodes <b>c)</b> before and <b>d)</b> after electrolysis at 200 mA/cm <sup>2</sup> . .....	129
<b>Figure S4-1:</b> 3-electrodes Electrochemical Cell.....	147
<b>Figure S4-2:</b> CO current density evolution with potential of the deposited Ag species on GDE substrates in CO <sub>2</sub> saturated 1 M KHCO <sub>3</sub> solution. <b>Fully carbonated groups are increasing CO current density compared with heteronuclear ligands. Bulky and π-extended structures seem to disfavor reactivity</b> .....	155
<b>Figure S4-3</b> Faradaic efficiency comparison at -0.63V vs RHE from Chronoamperometry (CA)(15min) of the deposited Acetylides on GDE substrates in a CO <sub>2</sub> saturated 1 M KHCO <sub>3</sub> . ....	155
<b>Figure S4-4:</b> IR-ATR of <b>a)</b> AgTol <b>b)</b> AgAnisole <b>c)</b> AgOct <b>d)</b> AgtFTol <b>e)</b> Agt-Bu <b>f)</b> AgThio <b>g)</b> AgPyr <b>h)</b> AgTPA. The disappearance of the strong C≡C-H band is assumed to be due to the formation of the C≡C-Ag bond.....	156

<b>Figure S4-5:</b> Powder X-Ray diffraction (PXRD) of <b>a)</b> AgTol <b>b)</b> AgAnisole <b>c)</b> AgOct <b>d)</b> AgtFTol <b>e)</b> Agt-Bu <b>f)</b> AgThio <b>g)</b> AgPyr <b>h)</b> AgTPA.....	157
<b>Figure S4-6:</b> Sample crystallinity and crystallite size calculated by Scherrer equation.....	158
<b>Figure S4-7:</b> XPS Elemental quantification. <b>AgAnisole C/O ratio is 5.9; AgtFTol C/F is 2.33 and AgThio C/S is 4.37.</b> ....	158
<b>Figure S4-8</b> XPS spectra (Ag 3d and C 1s regions). <b>The species are Ag(I) complexes and the carbon spectra are showing a band corresponding to an Ag-C≡C</b> .....	160
<b>Figure S4-9:</b> CV measurement at 100 mV/s (3 scans) on the GDE substrate in a N <sub>2</sub> saturated 1 M KHCO <sub>3</sub> solution. <b>a)</b> AgTol <b>b)</b> AgAnisole <b>c)</b> AgOct <b>d)</b> AgtFTol <b>e)</b> Agt-Bu <b>f)</b> AgThio <b>g)</b> AgPyr <b>h)</b> AgTPA .....	161
<b>Figure S4-10:</b> MP-AES quantification (10 ppm solution in 3% HNO <sub>3</sub> prepared from a 1000 ppm solution in TFA: H <sub>2</sub> O (1:3)) The results are obtained from a calibration curve of 6 points between 1 and 20 ppm made from a 1000 ppm AgNO <sub>3</sub> solution in 3% HNO <sub>3</sub> (R <sup>2</sup> =0.998). The measured value is in accordance with 1:1 complex being the major product.....	162
<b>Figure S4-11:</b> reduction peak potential integration, electroactive species and active silver loading calculations.....	162
<b>Figure S4-12:</b> LSV measurement at 10 mV/s (2 <sup>nd</sup> scan) of the deposited materials on GDE substrates in CO <sub>2</sub> saturated 1 M KHCO <sub>3</sub> solution <b>a)</b> AgTol <b>b)</b> AgAnisole <b>c)</b> AgOct <b>d)</b> AgtFTol <b>e)</b> Agt-Bu <b>f)</b> AgThio <b>g)</b> AgPyr <b>h)</b> AgTPA .....	163
<b>Figure S4-13:</b> Onset potential and CO <sub>2</sub> RR overpotentials. CO <sub>2</sub> RR overpotentials were calculated from the thermodynamic -0.53 V vs SHE for CO <sub>2</sub> to CO conversion (converted as -0.069 V vs RHE). .....	164
<b>Figure S4-14</b> Electrochemical Impedance Spectroscopy (EIS) AgTol <b>a)</b> Bode plot <b>b)</b> Nyquist plot; AgAnisole <b>c)</b> Bode plot <b>d)</b> Nyquist plot ; AgOct <b>e)</b> Bode plot <b>f)</b> Nyquist plot ; AgtFTol <b>g)</b> Bode plot <b>h)</b> Nyquist plot ; Agt-Bu <b>i)</b> Bode plot <b>j)</b> Nyquist plot ; AgThio <b>k)</b> Bode plot <b>l)</b> Nyquist plot AgPyr ; <b>m)</b> Bode plot <b>n)</b> Nyquist plot ; AgTPA <b>o)</b> Bode plot <b>p)</b> Nyquist plot.....	166
<b>Figure S4-15</b> Cyclic voltammograms (CV) of a 25 mM potassium ferrocyanide in a 0.1M KCl solution using an AgAnisole electrode at various scan rates (5, 10, 15 and 20mV/s) and peak current as a function of the square root of the scan rate variation. AgTol <b>a)</b> CV scans <b>b)</b> fitted curve; AgAnisole <b>c)</b> CV scans <b>d)</b> fitted curve; AgOct <b>e)</b> CV scans <b>f)</b> fitted curve AgtFTol <b>g)</b> CV scans <b>h)</b> fitted curve Agt-Bu <b>i)</b> CV scans <b>j)</b> fitted curve AgThio <b>k)</b> CV scans <b>l)</b> fitted curve AgPyr <b>m)</b> CV scans <b>n)</b> fitted curve AgTPA <b>o)</b> CV scans <b>p)</b> fitted curve.....	168
<b>Figure S4-16</b> The ECSA is calculated from the slope of the plot using the Randles-Sevcik equation. ....	169
<b>Figure S4-17</b> Faradic efficiencies (FE) from direct GC quantification of 15 min long Chronoamperometry (CA) of the deposited materials on the GDE substrate in a CO <sub>2</sub> saturated 1 M KHCO <sub>3</sub> between -0.63 and -1.13 applied potentials (V, E vs RHE) with a step of 0.1 V. <b>a)</b> AgTol <b>b)</b> AgAnisole <b>c)</b> AgOct <b>d)</b> AgtFTol <b>e)</b> Agt-Bu <b>f)</b> AgThio <b>g)</b> AgPyr <b>h)</b> AgTPA .....	170

<b>Figure S4-18</b> CO and H <sub>2</sub> partial Current densities between -0.63 and -1.13 applied potentials (V, E vs RHE) with a step of 0.1 V (15min chronoamperometry) in the 1M KHCO <sub>3</sub> aqueous solution <b>a)</b> AgTol <b>b)</b> AgAnisole <b>c)</b> AgOct <b>d)</b> AgtFTol <b>e)</b> Agt-Bu <b>f)</b> AgThio <b>g)</b> AgPyr <b>h)</b> AgTPA.....	171
<b>Figure S4-19</b> Calculated TOF variation for CO <sub>2</sub> RR <b>a)</b> AgTol <b>b)</b> AgAnisole <b>c)</b> AgOct <b>d)</b> AgtFTol <b>e)</b> Agt-Bu <b>f)</b> AgThio <b>g)</b> AgPyr <b>h)</b> AgTPA.....	172
<b>Figure S5-1:</b> 3 electrodes Electrochemical Cell .....	184
<b>Figure S5-2</b> SEC column at different stages of the separation. Each spot corresponds to a porphyrin derivative.....	186
<b>Figure S5-3 a)</b> UV spectrum of a 10 <sup>-6</sup> M solution of C2 in DCM <b>b)</b> UV spectrum of a 10 <sup>-4</sup> M solution of C2 in DCM. Soret: 417 q bands: 514,549,590,645 .....	187
<b>Figure S5-4 a)</b> C3 solubilised in DCM <b>b)</b> C4 solubilised in DCM. A loss of solubility is observed upon silver addition indicative of the complex formation. ....	188
<b>Figure S5-5 a)</b> UV spectrum of a 10 <sup>-6</sup> M solution of C6 in DCM <b>b)</b> UV spectrum of a 10 <sup>-4</sup> M solution of C6 in DCM. Soret: 419 q bands: 516, 551, 591, 646 .....	190
<b>Figure S5-6 a)</b> UV spectrum of a 10 <sup>-6</sup> M solution of C7 in DCM <b>b)</b> UV spectrum of a 10 <sup>-4</sup> M solution of C7 in DCM. Soret: 416; q bands: 571, 612 .....	191
<b>Figure S5-7 a)</b> UV spectrum of a 10 <sup>-6</sup> M solution of C8 in DCM <b>b)</b> UV spectrum of a 10 <sup>-4</sup> M solution of C8 in DCM. Soret: 413 q bands: 531 .....	192
<b>Figure S5-8 a)</b> C7 solubilised in DCM <b>b)</b> C9 solubilised in DCM. A loss of solubility is observed upon silver addition indicative of the complex formation. ....	193
<b>Figure S5-9 a)</b> C8 solubilised in DCM <b>b)</b> C10 in DCM. A loss of solubility is observed upon silver addition indicative of the complex formation. ....	194
<b>Figure S5-10 a)</b> C6 solubilised in DCM <b>b)</b> C10 in DCM. A loss of solubility is observed upon silver addition indicative of the complex formation. ....	195
<b>Figure S5-11:</b> LSV comparison at 10 mV/s of the deposited materials in a 0.5 M KHCO <sub>3</sub> solution. Potential is uncorrected. ....	196
<b>Figure S5-12:</b> Current density comparison at varying potential of the deposited materials in a 0.5 M KHCO <sub>3</sub> solution. Potential is uncorrected. <b>Ag-TaTTP activity for CO reaches a plateau (corresponding to H<sub>2</sub> evolution increase) while the presence of metalated porphyrins are delaying this effect.</b> ....	196
<b>Figure S5-13:</b> XPS identification and attribution of the carbon chemical environments in the chemical structure.....	197
<b>Figure S5-14:</b> XPS measurements for a reference compound AgPh ( <b>a-b</b> ) and Ag-TaTTP ( <b>c-e</b> ). <b>a)</b> Ag3d spectrum of the reference compound <b>b) c)</b> Ag3d spectrum shows an Ag(I) species (Ag3d 1/2 (375 eV) Ag3d 3/2 (369 eV). <b>d)</b> C1s deconvolution shows a maintained porphyrin structure (Pyrrole band (285.2 and 285.6 eV) and Phenyl band (284.7 eV) with a component at 284 eV attributed to the Ag-C≡C bond. <b>e)</b> N1s shows 2 bands corresponding to the N-H (399.9eV) and N (398 eV) of the free base porphyrin. ....	198

- Figure S5-15** IR spectrum of compound C9 (Black) and its starting material C7 (red). The intensity of the C≡C-H band (3265 cm<sup>-1</sup>) is decreased significantly from C7 to C9 upon addition of silver indicative of the C≡C-Ag bond formation..... 199
- Figure S5-16:** Powder XRD pattern of Ag-FeTaTPP between 2 and 25°. The starting material is not crystalline. The observed peaks are of low intensity hinting for a poorly crystalline final structure with a COF-like arrangement. Crystallinity is measured to be 66% (obtained by comparing the integrated intensity of the background with the peaks). Crystal size is calculated to be 83 Å by Scherrer equation..... 199
- Figure S5-17:** SEM Picture of a prepared Ag-FeTaTPP Electrode. 1 and 2 show quantitative elemental measurements by EDS of Ag-FeTaTPP containing spot and without catalyst respectively. **Material concentration seems to be highly localized (consequently poorly dispersed) and corresponds to the charging parts of the electrode.**..... 200
- Figure S5-18:** SEM-EDS Pictures of Iron and Silver of a prepared Ag-FeTaTPP Electrode at 5000x magnification. Fe and Ag signals intensity correspond to charging amorphous particles which we assume to be the chemical of interest confirming the poor catalyst distribution on the electrode. .... 201
- Figure S5-19:** LSV measurement at 10 mV/s (2<sup>nd</sup> scan) of the deposited Ag-FeTaTPP in a 0.5 M KHCO<sub>3</sub> solution. Potential is uncorrected. The overpotential is measured as -0.478 V vs RHE as the cross point of the coulombic and faradic currents. .... 201
- Figure S5-20: a)** Ag-FeTaTPP measured faradaic efficiency (FE) from direct GC quantification at potential varied between -0.55 and -1.15 V vs RHE in a 0.5 M KHCO<sub>3</sub> solution. Potential is uncorrected **b)** Measured current densities for CO and H<sub>2</sub> with varying potential..... 202
- Figure S5-21:** TGA measurement of (FeTaTPPAg)<sub>n</sub>. The derivative shows two main weight loss steps at 174°C and 376°C..... 202
- Figure S5-22** IR spectrum of compound C10 (Black) and its starting C8 (red). The intensity of the C≡C-H band (3291 cm<sup>-1</sup>) is decreased significantly from C8 to C10 due to the addition of the silver. .... 203
- Figure S5-23:** Powder XRD pattern of Ag-CoTaTPP between 2 and 25°. The starting material is crystalline. The observed peaks are of low intensity hinting for a poorly crystalline final structure with a COF-like arrangement. Crystallinity is measured to be 61% (obtained by comparing the integrated intensity of the background with the peaks). Crystal size is calculated to be 95 Å by Scherrer equation..... 203
- Figure S5-24:** SEM Picture of a prepared Ag-CoTaTPP Electrode. 1 and 2 show quantitative elemental measurements by EDS of Ag-CoTaTPP containing spot and without catalyst respectively. **Material concentration seems to be highly localized (consequently poorly dispersed) and corresponds to the charging parts of the electrode.**..... 204
- Figure S5-25:** SEM-EDS Pictures of Cobalt and Silver of a prepared Ag-CoTaTPP Electrode at 1500x and 50 000x magnification. Co and Ag signals intensity correspond to charging amorphous particles which we assume to be the chemical of interest confirming the poor catalyst distribution on the electrode. .... 205

- Figure S5-26:** LSV measurement at 10 mV/s (2<sup>nd</sup> scan) of the deposited Ag-CoTaTPP in a 0.5 M KHCO<sub>3</sub> solution. Potential is uncorrected. The overpotential is measured as -0.409 V vs RHE as the cross point of the coulombic and faradic currents. .... 205
- Figure S5-27: a)** Ag-CoTaTPP measured faradaic efficiency (FE) from direct GC quantification at potential varied between -0.55 and -1.15 V vs RHE in a 0.5 M KHCO<sub>3</sub> solution. Potential is uncorrected **b)** Measured current densities for CO and H<sub>2</sub> with varying potential..... 206
- Figure S5-28:** TGA measurement of (CoTaTPPAg)<sub>n</sub>. A first step at low temperature is assumed to be a solvent evaporation. The derivative shows two main weight loss steps at 179°C and 475-542°C. .... 206
- Figure S5-29** IR spectrum of compound C11 (Black) and its starting C6 (red). The intensity of the C≡C-H band (3267 cm<sup>-1</sup>) is decreased significantly from C6 to C11 due to the addition of the silver. .... 207
- Figure S5-30:** Powder XRD pattern of Ag-TaTPP between 2 and 25°. The starting material is amorphous. The observed peaks are of low intensity hinting for a poorly crystalline final structure with a COF-like arrangement. Crystallinity is measured to be 68% (obtained by comparing the integrated intensity of the background with the peaks). Crystal size is calculated to be 115 Å by Scherrer equation..... 207
- Figure S5-31:** LSV measurement at 10 mV/s (2<sup>nd</sup> scan) of the deposited Ag-TaTPP in a 0.5 M KHCO<sub>3</sub> solution. Potential is uncorrected. The overpotential is measured as -0.59427 V vs RHE as the cross point of the coulombic and faradic currents ..... 208
- Figure S5-32: a)** Ag-TaTPP measured faradaic efficiency (FE) from direct GC quantification at potential varied between -0.55 and -1.15 V vs RHE in a 0.5 M KHCO<sub>3</sub> solution. Potential is uncorrected **b)** Measured current densities for CO and H<sub>2</sub> with varying potential..... 208
- Figure S5-33:** TGA measurement of (TaTPPAg)<sub>n</sub>. The derivative shows 3 main weight loss steps at 161°C, 198°C and 507°C ..... 209
- Figure S5-34:** TGA measurement comparison for the derivatives. The mass loss is more important for the unmetalled porphyrin but a similar decomposition pattern is observed in every case with a first mass loss between 160 and 200°C followed by a second step. .... 209
- Figure S5-35:** LSV measurement at 10 mV/s (2<sup>nd</sup> scan) of the deposited Ag-CoMaTPP in a 0.5 M KHCO<sub>3</sub> solution. Potential is uncorrected. The overpotential is measured as -0.718 V vs RHE as the cross point of the coulombic and faradic currents. .... 210
- Figure S5-36: a)** Ag-TaTPP measured faradaic efficiency (FE) from direct GC quantification at potential varied between -0.55 and -1.15 V vs RHE in a 0.5 M KHCO<sub>3</sub> solution. Potential is uncorrected **b)** Measured current densities for CO and H<sub>2</sub> with varying potential..... 210
- Figure S 5-37:** X-Ray diffraction single crystal structure of the Oxygen-bridged porphyrin dimer; **a)** unit cell view of the dimers' packing arrangement; **b)** view of the dimer; **c)** side view of the dimer. .... 211

## LIST OF TABLES AND EQUATIONS

### Chapters Tables

<b>Table 1-1</b> Thermodynamic potentials of the main CO <sub>2</sub> RR pathways .....	32
<b>Table 4-1</b> Summary of the most important characteristics of the silver acetylides.....	139

### Experimental Parts Tables

<b>Table S 3-1:</b> Quantification of the liquid products based on Figure S19 measured NMR spectra. ....	121
<b>Table S3-2:</b> XPS Elemental quantification <b>A)</b> carbon black on GDE <b>B)</b> carbon black and Nafion on GDE <b>C)</b> AgPh powder <b>D)</b> AgPh, Carbon black and Nafion on GDE before electrolysis <b>E)</b> AgPh, Carbon black and Nafion on GDE after electrolysis. CB stands for Carbon Black. C Nafion refers to the carbon content related to Nafion polymer and F/Cpolym refers to the ratio of Fluor and carbon signals related to Nafion. ....	123
<b>Figure S3-27</b> and <b>Table S3-3:</b> Quantitative elemental analysis by EDS at different regions of an AgPh electrode before electrolysis. (X axis: Energy keV; Y axis: cps).....	128
<b>Table S 3-4:</b> MP-AES measurement of AgPh (10 ppm solution in 3% HNO <sub>3</sub> prepared from a 1000 ppm solution in TFA: H <sub>2</sub> O (1:3)).....	129
<b>Table S5-1</b> Elemental values obtained from the XPS measurement. The value Ag/acetylene corresponds to the division of total silver integration by the N content (assumed to be only present on the porphyrin core) .....	198

### Chapters Equations

Equation 1-1 .....	23
Equation 1-2 .....	23
Equation 1-3 .....	23
Equation 1-4 .....	26
Equation 1-5 .....	31
Equation 1-6 .....	32
Equation 1-7 .....	32
Equation 1-8 .....	33
Equation 1-9 .....	33
Equation 1-10 .....	33
Equation 1-11 .....	33
Equation 1-12 .....	46
Equation 1-13 .....	46
Equation 1-14 .....	49
Equation 1-15 .....	50

**Experimental Parts Equations**

Equation S2-1 .....	84
Equation S2-2 .....	85
Equation S2-3 .....	85
Equation S2-4 .....	89
Equation S 3-1 .....	105
Equation S3-2 .....	106
Equation S3-3 .....	106
Equation S3-4 .....	106
Equation S3-5 .....	106
Equation S3-6 .....	107
Equation S3-7 .....	115
Equation S3-8 .....	115
Equation S3-9 .....	116
Equation S3-10 .....	116
Equation S4-1 .....	148
Equation S4-2 .....	148
Equation S4-3 .....	148
Equation S4-4 .....	148
Equation S4-5 .....	148
Equation S4-6 .....	149
Equation S4-7 .....	149
Equation S 5-1 .....	184
Equation S5-2 .....	184
Equation S5-3 .....	185

## LIST OF ABBREVIATIONS

ACN Acetonitrile

AEM Anion Exchange Membrane

Ag/AgCl Ag/AgCl/ 3 M KCl

ATR Attenuated total reflectance spectroscopy

ATP Adenosine triphosphate

BID Dielectric-Barrier Discharge Ionization Detector

BPM Bipolar Membrane

CA Chronoamperometry

CB Carbon black

CCUS Carbon capture, utilization, and storage

CE Counter Electrode

CEM Cation Exchange Membranes

CN Coordination number

CNF Carbon nanofiber

CO<sub>2</sub>-EOR CO<sub>2</sub> Enhanced Oil recovery

CO<sub>2</sub>RR Carbon dioxide reduction reaction

COF Covalent-organic framework

COP conference of parties

CoPC Cobalt phthalocyanine

CPE Controlled-potential electrolysis

CV Cyclic voltammetry

D<sub>2</sub>O Deuterated Water

DCM Dichloromethane

DFT Density functional theory

DLS Dynamic light scattering

DMF Dimethylformamide

d<sub>6</sub>-DMSO Deuterated DMSO



ECSA Electrochemical surface area

EDX Energy dispersive X-ray

EIS Electrochemical impedance spectroscopy

EXAFS Extended X-Ray Absorption Fine Structure

FE Faradaic efficiency

FID Flame ionisation detector

FT-IR Fourier-transform infrared spectroscopy

FY Faradaic Yield

GC Gas-chromatography

GDE Gas diffusion electrode

GDL Gas diffusion layer

GHG Greenhouse gases

HER Hydrogen evolution reaction

IC Ionic chromatography

ICP-AES Inductively coupled plasma atomic emission spectroscopy

IEM Ion Exchange membrane

IPCC Intergovernmental Panel on Climate Change

LSV Linear sweep voltammetry

MeOH Methanol

MOF Metal organic framework

NADPH Nicotinamide adenine dinucleotide phosphate

NHE Standard hydrogen electrode

NMR Nuclear magnetic resonance

NPs Nanoparticles

PC Porous carbon

PFSA perfluorosulfonic acid

Py Pyridine

RDS Rate-determining step

RHE Reversible hydrogen electrode

SCE Saturated calomel electrode

SEC Size-exclusion chromatography

ATR-SEIRAS attenuated total reflectance surface-enhanced infrared absorption spectroscopy

SEM Scanning electron microscope

SFEP Surfactant-free emulsion polymerization

SHE Standard hydrogen electrode

TCD Thermal conductivity detector

TEM Transmission electron microscope

TGA Thermogravimetric analysis

TOF Turnover frequency

TON Turnover number

TPP Tetraphenyl porphyrin

UN United Nations

UV Ultra-violet

VdW Van der Waals

XAS X-ray absorption spectroscopy

XANES X-ray absorption near edge structure

XPS X-ray photoelectron spectroscopy

XRD X-ray diffraction

$\eta$  Overpotential

$\nu$  Frequency (Hz)

## Chapter 1: General Introduction

### 1) Global warming and Energy Transition

Arguably, the major challenge of the 21st century is for humankind to shift energy production (**Figure 1.1a**) from fossil fuels (coal, oil, and natural gas) to renewable sources (Solar, wind, hydroelectric, marine, biomass, and geothermal energy). While the widespread use of fossil fuels as an energy source constitutes the underpinnings of our technological evolution and economic growth, it has led to the production and accumulation of greenhouse gases (GHG) in our atmosphere (**Figure 1.1b**).

While the high energy density of fossil fuels makes them an ideal energy source, their combustion generates a substantial amount of impactful waste (mostly gaseous pollutants), among which CO<sub>2</sub> is the most important both in terms of produced volume (37.1 Gt) and negative overall impact. Its accumulation in the atmosphere is the primary cause of global warming as a result of the greenhouse effect. The latter is the consequence of the physical conversion of earth radiation into heat via the absorption of infrared radiation in the atmosphere. The magnitude of heat emitted is directly dependent on the atmospheric GHG concentration, which has increased consistently since the Industrial Revolution and has outmatched all the natural regulation systems. This has led, to date, to a concerning rise in Earth's overall temperature of about 1.2°C with respect to pre-industrial times.

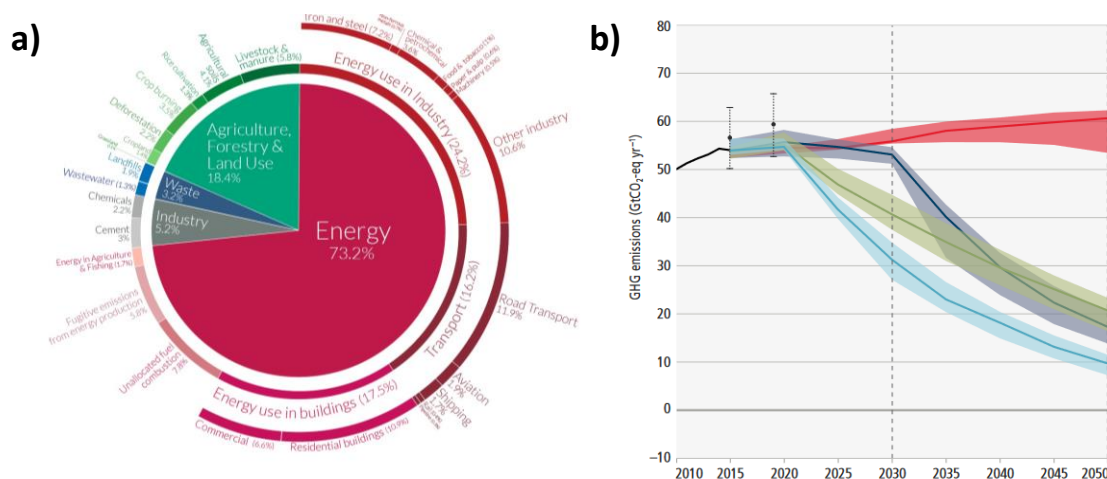


**Figure 1.1 a)** Global greenhouse emissions by sector <sup>1</sup>; **b)** Annual CO<sub>2</sub> emissions trend related to global warming calculated scenarios (red) trend from implemented policies (blue) limit warming to 2°C with a return at 1.5°C after a high overshoot (green) limit warming to 2°C (cyan) limit warming to 1.5°C with no or limited overshoot.<sup>2</sup>

The temperature rise is expected to increase by an average of 3°C globally by 2100 if current economic policies are maintained. Such an increase will likely have damaging consequences on the earth's climate and lead to extreme and unpredictable climatic phenomena. Animal and vegetal species have already started to decrease in number and variety on a worldwide scale, which may have irreversible consequences.

The scale of global warming has raised concerns both in civil society and the political sphere. As such, international regulations are slowly delineated and frequent international meetings, such as the United Nations (UN) Conference of Parties (COP), are organised in an attempt to provide solutions towards control of the global temperature rise through the implementation of economic policies. Among them, the COP21

set fundamental rules to limit the temperature increase below 2°C. Almost 200 countries agreed on the latter terms originating from the Paris Agreement signed in 2015, of which the milestone is to achieve net Zero carbon emissions globally by 2050. Scientific reports from the IPCC<sup>2</sup> have, however, shown that current measures are not sufficient and will likely lead to a temperature overshoot(**Figure 1.1b**). The need for a way to mitigate CO<sub>2</sub> emissions is critical.

Despite the fact that fossil fuels reserves have decreased significantly since the industrial revolution, their global consumption has followed a steady increase to this day. Reserves, especially of coal and oil, are still large enough to provide sufficient energy at a reasonably low market price in the next decades, and therefore their consumption is not expected to drop without political incentive. A transition towards renewable energy sources is therefore required. However, renewable energy sources are still unable to match the efficiency of fossil fuels due to scale limitations and technological constraints on power production and energy storage. Overall, energy production, although still heavily relying on fossil fuels, has seen an important shift to renewable energy sources, which accounted for 11% of total energy consumption by 2022.<sup>1</sup>

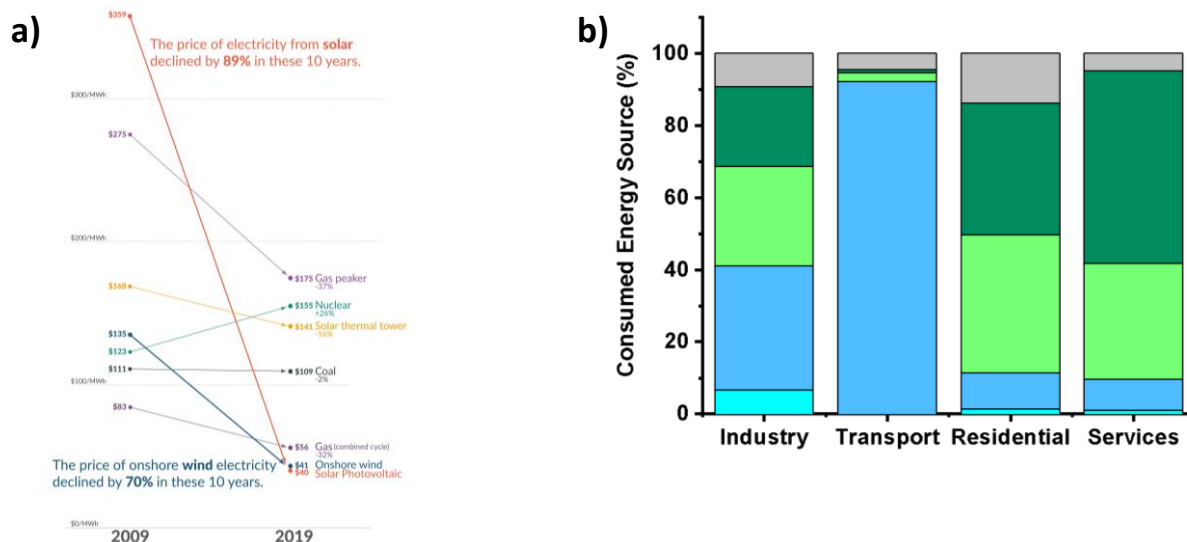


**Figure 1.2:** **a)** The price of electricity from different power sources<sup>3</sup> **b)** Energy consumption by sector. Coal (Cyan), Oil (blue), Gas (pale green), Electricity (green) and others (grey). Adapted from<sup>4</sup>

While the costs of those technologies used to be the principal impediment to their widespread implementation, these have decreased significantly enough for them to compete with fossil fuels-based energy production technologies (**Figure 1.2a**)<sup>3</sup>. One important drawback is that renewable energy sources, mainly solar and wind, generate electricity intermittently, requiring storage capacity in the form of batteries or fuels.

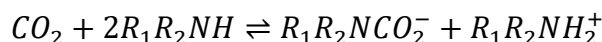
The limited capacity concerning energy storage is particularly slowing down the widespread adoption of renewable electricity as an energy medium in the transportation sector, where indeed, a mere 0.8% of the consumed energy derives from renewable sources while oil represents 92%<sup>4</sup>. The battery field of research has seen very limited improvements in storage capacity in recent years, and the current industry standard, lithium-ion technology, depends on a limited supply of lithium. Although sufficient for small markets such

as consumer goods, it will be unable to meet the global demand for energy storage in the case of transportation (**Figure 1.2b**).

An alternative to the above-mentioned storage limitation has emerged, which advocates for the use of the electricity surplus as a source of energy for the production of fuels. A good example is the recent trend on H<sub>2</sub> production by electrolysis and CO<sub>2</sub> conversion towards fuels which will create a partially circular energy scheme in an ideal technology evolution scenario. The different technologies for CO<sub>2</sub> conversion are still being investigated at the lab scale, but major companies are starting to develop experimental plants. In the case of H<sub>2</sub>, which has been looked upon as particularly promising, important limitations still exist. It possesses a poor energy density compared to oil (1810 compared with 32 000 kJ.L<sup>-1</sup>)<sup>5</sup>, and its implementation in the actual energy market is rather limited.

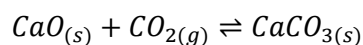
## 2) Carbon Capture, Utilization and Storage (CCUS)

Carbon capture, utilisation, and storage (CCUS) has seen a growth in interest –particularly from the industry– as an alternative to mitigate the adverse effects of global warming. The concept is broadly defined as the capture of gaseous CO<sub>2</sub> from the atmosphere and its storage be it in underground wells or in the form of chemical intermediates. The main advantage of CCUS is that the corresponding technologies, such as post-combustion capture, have already reached industrial maturity. Very common pathways for CO<sub>2</sub> capture involve the use of amines, the most frequently used being monoethanolamine (MEA), 2-amino-2-methyl-1-propanol, diethanolamine, and methyl diethanolamine, which are able to bind CO<sub>2</sub> reversibly (**Equation 1-1**).<sup>6</sup>



**Equation 1-1**

Other pathways involve the formation of carbonates using calcium oxide (CaO) to reversibly form calcium carbonate through a thermal process at 600-700°C (**Equation 1-2**). The carbonate can be used directly in applications such as cement or regenerated to the original CaO via calcination at 900°C to obtain CO<sub>2</sub> as a product to be compressed and stored (**Figure 1.3a**).<sup>7</sup>



**Equation 1-2**

Similarly, in spacecrafts, lithium hydroxide canisters were used as the primary carbon dioxide removal system but have since been replaced by molecular sieves systems comprising zeolites due to the reversibility of the adsorption preventing canister stocks issues. More recently semi-circular systems based on the Sabatier reaction<sup>8</sup> have been integrated in order to directly recycle CO<sub>2</sub> (**Equation 1-3**).<sup>9</sup> The reaction mechanism relies on a reaction between H<sub>2</sub> (produced from water electrolysis) and CO<sub>2</sub> at high temperature and pressure over a nickel catalyst.



**Equation 1-3**

In most cases, the captured CO<sub>2</sub> is directly used in common goods markets such as soft drinks, foodstuffs, fire extinguishers or as a solvent for specific reactions. However, these uses remain marginal. Recently, plants to trap it in underground geological formations such as coal mines or aquifers, both physically and chemically, for later usage have seen rapid development. At present, there are 28 commercially operating CCUS facilities worldwide with a CO<sub>2</sub> removal capacity of around 40 million tons <sup>per</sup> year (Mtpa) (**Figure 1.3b**). Another application for CO<sub>2</sub> is its use by the petrochemical industry in oil extraction through direct injection in the oil pits in a process called CO<sub>2</sub>-EOR (enhanced oil recovery). EOR consumes from 300 to 600 kg of CO<sub>2</sub> per extracted barrel of oil while its subsequent combustion is assumed to release around 500 kg, making its production less damaging in terms of carbon net emissions<sup>10</sup>.

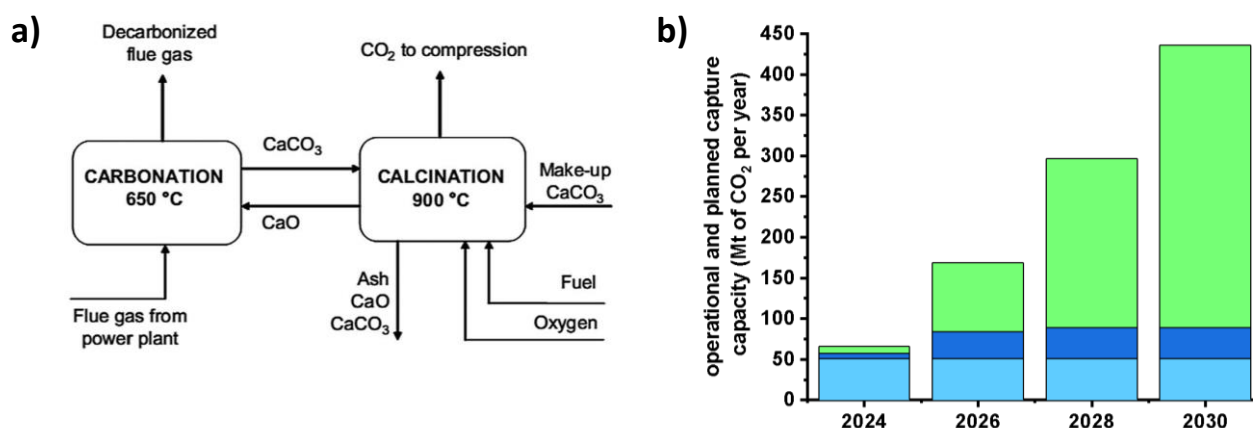


**Figure 1.3 a)** Carbonate looping process <sup>7</sup>; **b)** Operational and planned capture capacity. (Pale blue) operational, (blue) in construction, (light green) planned construction. Adapted from<sup>11</sup>.

Innovative CCUS technologies have been proposed, such as the formation of water clathrates through direct injection of CO<sub>2</sub> in the seabed. Originally a naturally occurring phenomenon, clathrate hydrates have been known to trap effectively permanent gases such as CO<sub>2</sub> and hydrocarbons. These crystalline structures are made of organised water molecules surrounding a guest and organising around it through hydrogen bonding. CO<sub>2</sub> clathrates are organised in a cubic crystal lattice (**Figure 1.4**) and can be found in deep sea floors or in permafrost. Clathrates form readily under proper temperature and pressure conditions and were shown to form in laboratory conditions with a wealth of different guests <sup>12,13</sup>.

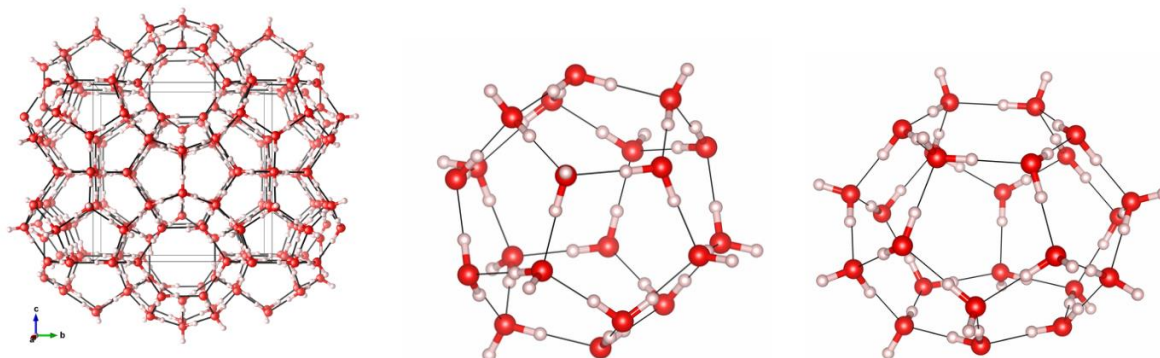


**Figure 1.4:** Unit cell (left) and P (centre) and H (right) types of cages in the sl structure. Oxygen is shown in red, and hydrogen is in white (calculated from crystalline structure) <sup>14</sup>

Although efforts are being made to sequester CO<sub>2</sub> and decrease emissions, the CCUS strategy remains globally limited by the technologies maturity level. However, the direct air CO<sub>2</sub> capture is expected to become cost-competitive (between 94 and 232\$ per tonne of CO<sub>2</sub> sequestered), potentially benefiting the Industry.<sup>15</sup> The development of such infrastructures relies on a niche market to date, but large investments in the field are expected to multiply the total capacity by almost ten times in 2030 (**Figure 1.3b**).<sup>11</sup> As a continuation of the increased CO<sub>2</sub> capture capacities, alternatives to convert CO<sub>2</sub> are needed to prevent storage capping.

### 3) CO<sub>2</sub> Conversion

The conversion of CO<sub>2</sub>, which includes a wide variety of methods, has been attracting considerable attention in academic research. The aim is to transform CO<sub>2</sub> into commercially and energetically useful chemicals to cut off the use of fossil fuels. The reaction involved, formally a reduction reaction, is unfortunately disfavoured under usual atmospheric conditions.<sup>16</sup> Indeed, the CO<sub>2</sub> molecule, similar to most oxides, has a high average C=O bond energy (187 kcal/mole), conferring high stability to the molecule. Consequently, thermodynamic and kinetic energy barriers need to be overcome for the reaction to become favourable. A catalyst is, therefore, needed for any chemical reactivity to occur. These catalysts are grouped into a few distinct categories, and the most relevant to this thesis will be covered in detail below, while a few comments on the other families are hereby presented.

Photosynthetic systems such as plants or bacteria rely on sunlight-driven processes to convert CO<sub>2</sub> to sugars through the Calvin cycle (**Figure 1.5a**).<sup>17</sup> The underlying mechanisms of the chemical transformation of CO<sub>2</sub> by such organisms are nowadays well understood; however, they are impossible to reproduce on an industrial scale due to their overall complexity. They usually rely on organometallic catalysts, such as porphyrins, as light harvesters embedded in complex enzymatic structures (chlorophylls). Upon photon absorption, they generate NADPH and ATP, which react with CO<sub>2</sub> to form a glyceraldehyde-3-phosphate intermediate, which finally yields glucose, sucrose and fructose. These sugars are then used to form polysaccharides such as starch, cellulose, hemicellulose, and pectin, which are part of the cell wall composition. Despite the inspirational relevance of photosynthetic systems, their overall conversion efficiency is usually <1%.

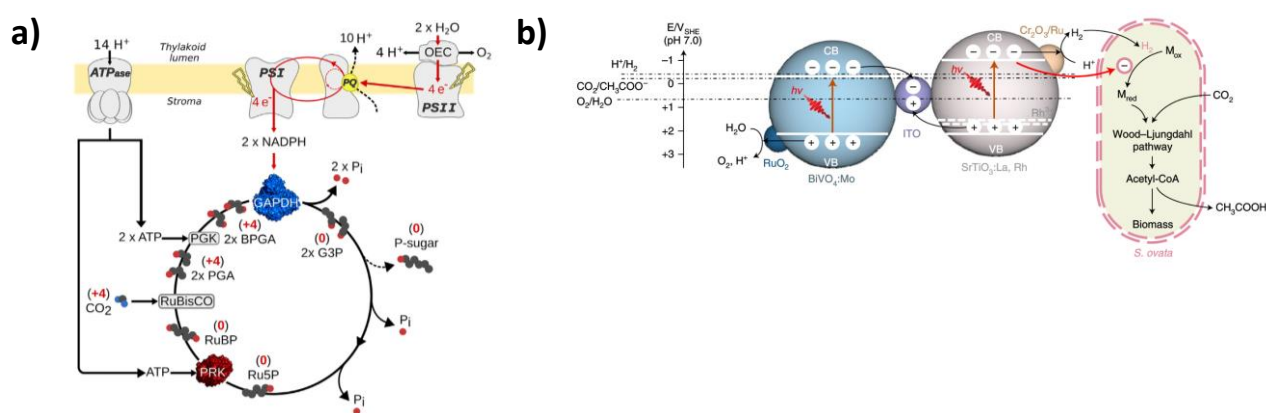
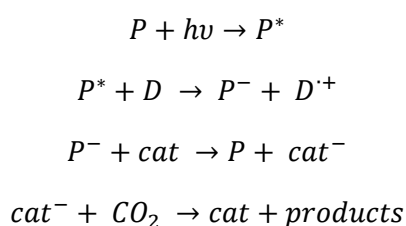


**Figure 1.5:** a) Schematic representation of the photosynthesis mechanism <sup>17</sup>; b) Mechanistic diagram depicting photosynthetic CO<sub>2</sub>-to-acetate conversion coupled with water oxidation over *S.ovata*|Cr<sub>2</sub>O<sub>3</sub>/Ru-SrTiO<sub>3</sub>:La, Rh|ITO|RuO<sub>2</sub>-BiVO<sub>4</sub>:Mo. <sup>18</sup>

Among these systems, microalgae have attracted interest for practical applications due to their important CO<sub>2</sub> fixation efficiency, which is usually 10 to 50 times higher than that of terrestrial plants while requiring no arable land.<sup>19–21</sup> Even though their ability to produce valuable chemicals has attracted growing interest, their use at the industrial scale has still not been realised due to important development costs. The use of semi-synthetic systems involving bacteria has demonstrated higher efficiencies than natural photosynthesis<sup>22</sup>. The use of a semi-artificial system involving semiconductor particles as light harvesters for non-photosynthetic bacteria has led to the formation of acetate with a 0.7% conversion (**Figure 1.5b**).<sup>18</sup> Overall, such systems are promising as they could produce molecules with long carbon skeletons in high selectivity, but their use on the laboratory scale is still exploratory, with bottlenecks regarding their scalability and stability.

Inspired by the photosynthetic processes, the field of synthetic photocatalysis has developed substantially during the last decades as it holds promise for artificial photosynthetic industrial applications. Early systems involved the use of a solubilised photosensitiser/catalytic complex couple (homogeneous catalysis), which were later deposited on p- and n-type semiconductor electrodes (FTO, ITO) (Heterogeneous catalysis), providing for a photoelectrochemical activity.

The fundamental process underlying the photocatalytic reduction of CO<sub>2</sub> involves a photosensitiser (P) with the capability to absorb radiation within the ultraviolet or visible range. This leads to the formation of an excited state (P\*), which subsequently undergoes reductive quenching through a sacrificial donor (D), resulting in the formation of a reduced photosensitiser (P<sup>-</sup>) and an oxidised donor (D<sup>+</sup>). The selection of the photosensitiser is critical, ensuring that P<sup>-</sup> efficiently transfers an electron to the catalyst species (cat), leading to the generation of the reduced catalyst species (cat<sup>-</sup>). In certain scenarios, the photosensitiser and the catalyst consist of a singular entity. The cat<sup>-</sup> then has the capacity to bind CO<sub>2</sub> and initiate the catalytic process, leading to the release of the CO<sub>2</sub> reduction adducts and the regeneration of the catalyst (cat). (**Equation 1-4**)



**Equation 1-4**

Frequently utilized photosensitizers are aromatics such as p-terphenyl and phenazine, as well as polypyridine-coordinated transition metal complexes. Among these, ([Ru(bipy)<sub>3</sub>]<sup>2+</sup>) stands out as the most employed transition metal complex, due its strong visible-light absorption and high photostability (**Figure 1.6a**).

Common active catalyst species include metallic complexes such as Nickel Cyclams, metalloporphyrins, Ru and Re polypyridine complexes, and suspended metal colloids. The catalytic cycle usually involves the reduction of the metal centre to its lowest degree of oxidation, followed by the binding of a CO<sub>2</sub> molecule and a proton-coupled electron transfer from the metal, leading to the formation of the reduced products. In experimental conditions, this ideal mechanism often faces issues such as poor stability of the carbon backbone or deactivation patterns such as the one observed for Nickel cyclam, leading to precipitation of



the metal as colloidal particles. In the specific case of photochemical reactions, complexes tend to degrade under prolonged illumination because of conformation changes in their excited states.

Among the existing pool of catalysts, corrins, corroles, porphyrins and phthalocyanines were shown to be active photo-catalytically without the need for a photosensitiser. They strongly absorb light in the visible spectrum but usually suffer from poor selectivity with significant parasitic H<sub>2</sub> production. In most cases, though, the need for a photosensitiser and sacrificial electron Donor (SED) is still a requirement in order to obtain a relevant CO<sub>2</sub> reduction activity. The main product of CO<sub>2</sub>RR in any of these conditions is usually CO through the 2-electron transfer, but environmental conditions such as the solvent and nature of the sacrificial agent have been shown to favour formate over CO formation.<sup>23</sup>

Their activity is often probed in aprotic polar solvents such as acetonitrile (ACN) or dimethylformamide (DMF), principally due to the solubility of both catalytic species and CO<sub>2</sub> in those media.<sup>24–30</sup> Water-soluble systems have remained rare and challenging due to stability issues and inherently favoured H<sub>2</sub>-production in aqueous medium. An example of such systems is shown in **Figure 1.6b** with trimethylammonium groups in para position of the phenyl rings enabling the solubilisation of an iron porphyrin with a purpurin photosensitiser and triethylamine (TEA) as SED. With a CO selectivity of 95%, this catalyst shows performances similar to most photosynthetic organisms.

One of the main drawbacks of such complexes is the low natural abundance of the active metals. As such, catalysts based on commonly found elements such as iron or nickel have been a main research focus in recent years. However, these examples constitute fundamental systems, and the immobilisation of photocatalysts on solid electrodes is required for practical applications.

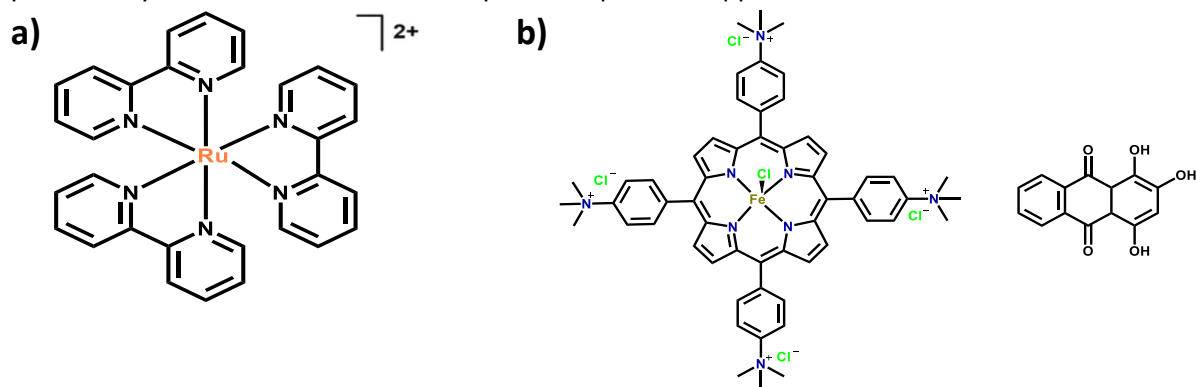


**Figure 1.6:** **a)** Chemical structure of ([Ru(bipy)<sub>3</sub>]<sup>2+</sup>) sensitizer; **b)** Molecular structures of the catalyst (Fe-p-TMA) and of its photosensitiser (purpurin, PP). adapted from <sup>31</sup>

As such, the heterogeneous photoelectrochemical reduction of CO<sub>2</sub> on absorbing semiconductor surfaces or by functionalised semiconductor surfaces has been studied extensively since the 1980s<sup>32,33</sup>. Bockris and co-workers, for instance, obtained a near-quantitative faradaic efficiency (FE) for CO by employing a CdTe absorber with a cobalt phthalocyanine complex. Ni cyclams were a particular focus of their early work because of their ability to produce CO almost exclusively.<sup>34,35</sup> In many cases the active species was solubilised and the reaction occurred at the solid-liquid interface (**Figure 1.7a**) molecular catalyst in solution **b)** electropolymerised, **c)** covalently bound to the semiconductor, **d)** covalently bound to the semiconductor supramolecular catalyst composed by a photosensitiser (PS) and catalyst (cat).<sup>43</sup> However, nowadays, most of the catalysts are adsorbed directly on the electrode's surface. An early method for their

immobilisation involved the direct polymerisation of the active catalyst on the surface of the semiconductor, which favours the separation of the photochemical reaction adducts, decreases the amount of catalyst needed and often increases the interfacial electron transfer from the semiconductor to the catalyst (**Figure 1.7b**).<sup>36,37</sup> Covalent immobilisation usually enables control of the photoelectrode-catalyst interface and the charge transfer by selecting adequate attachment groups. These generally include a wide variety of functionalities borrowed from the field of dye-sensitized solar cells (DSSC). Anchoring groups such as carboxylates and phosphonates have historically dominated the field due to their affinity for oxide semiconductors (**Figure 1.7c**).<sup>38–42</sup> As a follow-up strategy, the use of a photosensitiser in a donor-acceptor configuration has become an active area of research (**Figure 1.7d**).<sup>43</sup>

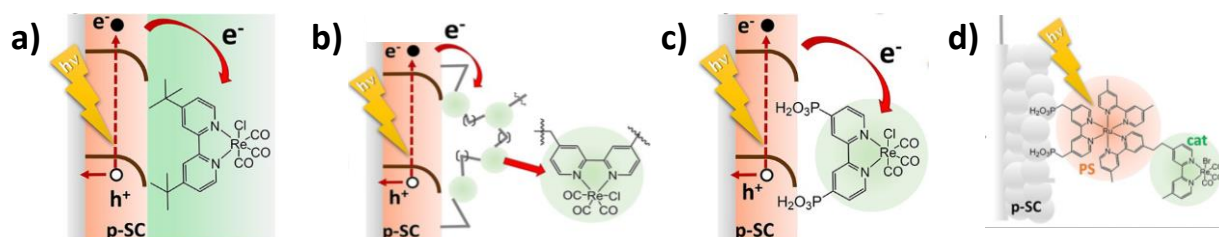


**Figure 1.7** a) molecular catalyst in solution b) electropolymerised, c) covalently bound to the semiconductor, d) covalently bound to the semiconductor supramolecular catalyst composed by a photosensitiser (PS) and catalyst (cat).<sup>43</sup>

Even though, from a thermodynamic perspective, proton-assisted multielectron reduction potentials for CO<sub>2</sub> should fall within the band gap of several semiconductors and derived photocathodes, the chemical transformation involves kinetic activation barriers, resulting in elevated overpotentials for the electrochemical reduction of CO<sub>2</sub>. In order to overcome this issue, novel integrated systems have been fabricated from multiple junction solar cells, able to provide a high enough open circuit voltage to drive both cathode and anode side reactions forward. A practical example from Reisner et al.<sup>44–46</sup> based on the water oxidation and CO<sub>2</sub> reduction anode/cathode couples, exploits a dual-junction perovskite-based semiconductor to provide a high enough potential in the photochemical cell (**Figure 1.8**).



**Figure 1.8** Architecture of the standalone perovskite–BiVO<sub>4</sub> PEC tandem device for bias-free syngas production. Oxygen evolution occurs at the front BiVO<sub>4</sub> photoanode with a Co WOC. An inverse-structure perovskite photocathode reduces CO<sub>2</sub> and protons to CO and H<sub>2</sub> via a CoMTPP molecular catalyst immobilised on a CNT sheet. An embedded copper wire connects the two photoelectrodes in this artificial leaf configuration.<sup>44</sup>

In most cases, however, the stability of photoactive materials under illumination and high carbon footprint are limiting factors. To obtain a suitable catalyst, numerous parameters must be finely tuned, and therefore,

such devices are vowed to remain in the realm of academic research for a prolonged period of time. Although remarkable, a fundamental limitation of such devices lies in the fact that the quantity of electrons photogenerated from direct band gap semiconductors is limited from a thermodynamic point of view. Indeed, similarly to silicon-based solar cells, the theoretical Shockley-Queisser limit implies that only a limited number of electrons can be produced from a photovoltaic photochemical cell under such high voltages required for a CO<sub>2</sub>-reduction/water oxidation couple (10-20mA/cm<sup>2</sup> for a voltage in the order of 2V experimentally). Therefore, these devices will presumably only serve the purpose of production of fuels in household-scale applications in a rather distant future.

### 4) CO<sub>2</sub> electrocatalysis

Among the previously mentioned possibilities, the strategy involving purely electrocatalytic reduction processes has emerged as the most promising. Driven from renewable energy sources, CO<sub>2</sub> electroreduction could mitigate CO<sub>2</sub> emissions. As an example, industrial-scale electrolysis was proven to be feasible for water splitting, which has progressed significantly (8% in 2022)<sup>47</sup> and green hydrogen production is expected to outmatch steam reforming of natural gas and coal gasification by 2050.<sup>48</sup> Importantly, hydrogen is a key precursor of several industrial processes leading to hydrocarbons from CO<sub>2</sub> electroreduction adducts, as depicted in **Figure 1.9a**.<sup>49</sup> For instance, the condensation of green hydrogen and CO derived from the CO<sub>2</sub>RR could lead to the large-scale production of renewable fuels *via* the Fischer-Tropsch and Sabatier processes.<sup>50,51</sup> The electroreduction of CO<sub>2</sub> has substantial advantages over other technologies. That is, an electrolyser can be designed to match a certain selectivity for a desired compound by using the appropriate catalyst and conditions. More importantly, the reaction rate can be adjusted at will by limiting the electrolysis current flowing through the anode and cathode. It is generally accepted that an industrially relevant reaction rate corresponding to an electrolysis current density of 200mA.cm<sup>-2</sup> constitutes a minimum threshold for industrialisation, and the benchmark for catalyst stability is above 1000 hours of continuous use under such current densities.

The most sought-after CO<sub>2</sub> reduction adducts from a market perspective are alcohols, ethylene and methane, as they can be directly used as energy carriers or for industrial processes. However, such products can be particularly challenging to obtain. Important progress has been made on catalysts synthesis, electrolyte and electrolysis cell engineering, and current densities have increased above 100 mA.cm<sup>-2</sup> with high selectivity for C<sub>1</sub> products such as CO or formic acid. The progress is tightly linked with the adoption of gas diffusion electrodes and bulk electrolysis cells, which allow overcoming the CO<sub>2</sub> solubility limit in aqueous electrolytes (in the order of 0.03 M) (ref). Reduction adducts with longer carbon chains, commonly called C<sub>2+</sub> are still challenging to produce with high selectivity due to their dependency on the C-C couplings of two carbonyl reaction intermediates. However, from a broader perspective, rapid technological progress is expected with the encouraging recent results in which ethylene and ethanol were produced with selectivity above 70% and 41%, respectively (**Figure 1.9b**).<sup>49</sup>

The first reported CO<sub>2</sub> electroreduction experiments were performed on a mercury pool and lead electrodes in water-based electrolytes by Bewick et al. in 1969 and 1970, with malate and Glycollate as the main products, respectively.<sup>52,53</sup> The authors observed, at the time, that the reaction had an important overpotential with respect to the thermodynamic values. However, a high faradaic efficiency was reported at low current densities. pH seemed to have a strong influence on the current efficiency, with a lower observed value for CO<sub>2</sub>RR products when the pH was maintained low. This was explained by the fact that

at low pH, the hydrogen evolution reaction (HER), i.e. the reduction of water, was favoured over the CO<sub>2</sub>RR  
52–56.

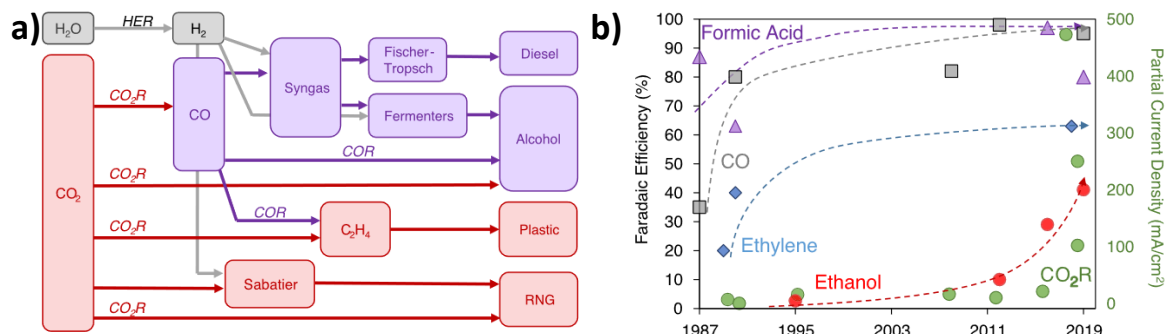


**Figure 1.9 a)** Possible renewable energy–powered routes to commodity chemicals driven by electrocatalysis from H<sub>2</sub>O (grey) and CO<sub>2</sub> (purple, red) as feedstocks.<sup>49</sup>; **b)** Highest reported Faradaic efficiencies for carbon monoxide (grey squares), formic acid (purple triangles), ethylene (blue diamonds), and ethanol (red circles) and corresponding current densities (green) over the past three decades.<sup>49</sup>

Shortly after, in 1974, in the first report of CO<sub>2</sub>RR heterogeneous organometallic catalyst 57, Tamaru et al. Studied phthalocyanines and found that the nature of the metallic centre had a large influence on the activity and showed that Cobalt and Nickel were the most suitable metals for such macrocycles. Since then, a large number of CO<sub>2</sub>RR catalysts have been developed, ranging from molecular catalysts, heterogeneous materials and, more recently, nanoparticles. Moreover, a better understanding of the mechanisms at play has now been reached through *in situ* and *operando* microscopy and spectro-electrochemical measurements (XAS, XPS, UV, IR, Raman etc.)<sup>58–60</sup>.

CO<sub>2</sub>RR catalysts are commonly separated in two major categories, namely the homogeneous and heterogeneous catalysts. These two categories, traditionally distant from a synthetic and analytical approach are nowadays gradually merging. The heterogenization of molecular catalysts has become extremely common and many metallic heterogeneous catalysts are designed to be deposited on electrodes from wet-chemistry methods, with nanoparticles being a main research focus.

The mechanisms of the CO<sub>2</sub>RR catalysed by organometallic catalysts have been well established, pointing to the importance of the secondary sphere interactions for enhanced catalytic properties. Conversely, heterogeneous catalysts mechanisms are still not fully understood with each material favouring rather different pathways depending on their synthesis, structural features and experimental conditions. An accepted general scheme separates the catalytic activity in two main pathways with the formation of the rate determining intermediate being either a non-coordinating or coordinating CO<sub>2</sub> anion. The former intermediate leads to the exclusive production of formic acid, while the latter leads to all other C<sub>1</sub> and C<sub>2+</sub> products (**Figure 1.10**). Most materials can follow either pathway depending on the reaction conditions, however some materials such as Sn, In, Hg and Pb are mainly non-coordinating while Au, Ag, Pd and Cu are coordinating materials. The main research focus is set on coordinating species, with Cu and its various alloys being the at the forefront since it is the only species which has, so far, demonstrated a consistent selectivity towards C<sub>2+</sub> products. The formation of adducts beyond CO requires the formation of a metal-C≡O\* intermediate with a relatively strong binding energy, kinetically disfavoring the direct departure of CO

from the catalytic centre, while keeping it low enough to prevent surface passivation. The formation of C<sub>2</sub> adducts, requires a dimerization step involving two C≡O\* intermediates, which can only occur if held in close physical proximity. This specificity practically rules out any possibility of C<sub>2</sub> adducts formed by molecular monometallic catalysts.

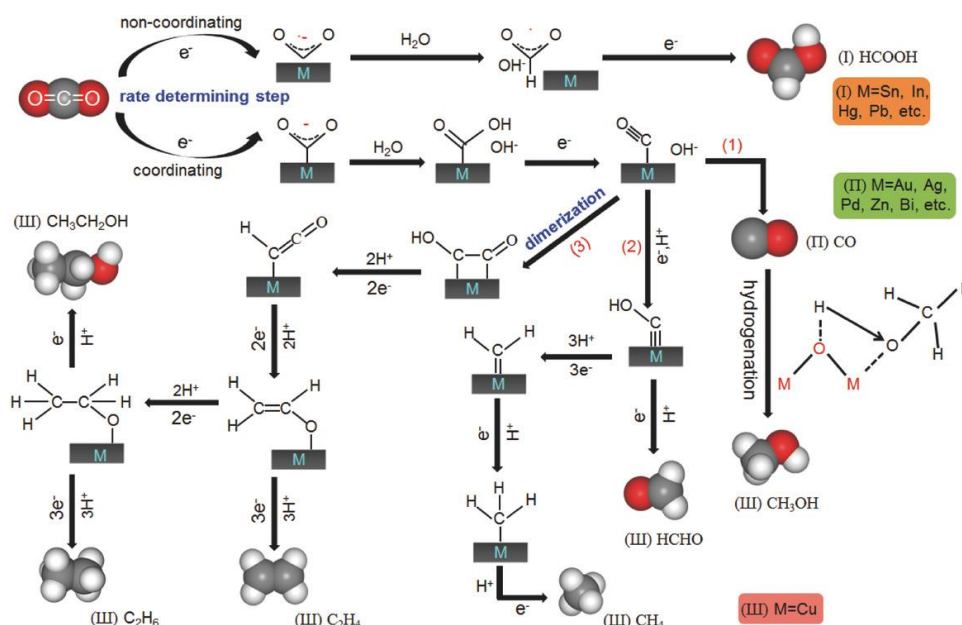


**Figure 1.10.** General mechanism of the CO<sub>2</sub>RR catalysed by metals.<sup>61</sup>

Each intermediate depicted in Figure 1.10 is associated with a kinetic activation barrier, while the overall thermodynamic energetics of the process are expressed in the theoretical Nernst reduction potentials (**Table 1-1**). Additionally, the Nernst equations corresponding to the reduction of CO<sub>2</sub> to molecules such as CO, methane or methanol (**Equation 1-5**) indicate the number of electrons and protons exchanged in the process.

From **Equation 1-5**, the reaction rate is a function of the electrode potential. At equilibrium, the net current is zero, and the electrode potential is defined by the Nernst equation:

$$E = E^{0'} + \frac{RT}{nF} \ln \frac{C_O^*}{C_R^*}$$

**Equation 1-5**

where C<sub>O</sub>\* and C<sub>R</sub>\* is the bulk concentration of Oxidant and reducer, and E<sub>0</sub>' is the thermodynamic Nernst potential.



$\text{CO}_2 + 8\text{H}^+ + 8\text{e}^- \rightarrow \text{CH}_4 + \text{H}_2\text{O}$	$E^\circ = -0.24 \text{ V vs NHE}$
$\text{CO}_2 + \text{e}^- \rightarrow \text{CO}_2^{\bullet-}$	$E^\circ = -1.90 \text{ V vs NHE}$
$2\text{CO}_2 + 12\text{H}^+ + 12\text{e}^- \rightarrow \text{C}_2\text{H}_4 + 4\text{H}_2\text{O}$	$E^\circ = -0.34 \text{ V vs NHE}$
$2\text{CO}_2 + 12\text{H}^+ + 12\text{e}^- \rightarrow \text{C}_2\text{H}_5\text{OH} + 3\text{H}_2\text{O}$	$E^\circ = -0.33 \text{ V vs NHE}$

**Table 1-1** Thermodynamic potentials of the main CO<sub>2</sub>RR pathways

Upon faradaic current flow, the electrode potential deviates from its equilibrium value, and the difference is termed electrode polarization. The extent of polarization is determined by the overpotential  $\eta$ , which, in practical terms, is the difference between the applied electrode potential,  $E_{\text{applied}}$ , and  $E^0$  (products/substrates) at a given current density. The overpotential is proportional to the quantity of energy required to overcome the reaction's kinetic barrier. The overpotential can be separated into three main sub-components: concentration overpotential,  $\eta_{\text{con}}$ ; activation overpotential,  $\eta_{\text{act}}$ ; and ohmic overpotential,  $\eta_{\text{ohmic}}$  (**Equation 1-6**).

$$\eta = \eta_{\text{ohmic}} + \eta_{\text{con}} + \eta_{\text{act}}$$

**Equation 1-6**

The overpotential  $\eta_{\text{cat}}$  is calculated as the difference between  $E$ , the experimental activation potential, and  $E_{\text{NHE}}^0$  the thermodynamic reaction potential (**Equation 1-7**). The activation potential  $E$  is measured experimentally from the iR-corrected Linear Sweep voltammetry (LSV) measurement and corresponds to the crossing point between the capacitive current's tangent and faradaic current's tangent at a low scan rate (usually 10 mV/s). Other methods define this value as the inflexion point of the LSV, leading to variable results in the literature.

$$\eta_{\text{cat}} = E - E_{\text{NHE}}^0$$

**Equation 1-7**

The current density is extracted from the LSV and is directly linked to the reaction rate of the catalytic reaction correlated to the electrode surface. In many studies, the electrode surface is referenced as the geometric surface, but an accurate value can be obtained by measuring the electrochemical surface area (ECSA) using an electrochemical probe or measuring the electrode capacitance.

The faradaic efficiency is a measure of the electron efficiency of the catalytic reaction at the electrode. It consists of a percentage ratio between the number of electrons (electrical charge,  $Q_{\text{exp}}$ ) injected in the system and the corresponding electrons involved in the reaction(s) measured experimentally derived from the quantity of products formed in the gas and liquid phases. The charge is experimentally retrieved from the ChronoAmperogram (CA) and compared with the quantification of the products by GC-MS for permanent gases or by ionic chromatography and NMR for liquid products. In these cases, extremely precise calibrations and reproducible conditions are a priority in order to minimize errors. The final product percentage is obtained from **Equation 1-8**.

$$\text{Faradaic efficiency (\%)} = \frac{Q_{\text{exp}}}{Q_{\text{theo}}} \times 100 = \frac{z \times n \times F}{Q} \times 100$$

## Equation 1-8

Where  $z$  is the number of electrons involved in the reaction,  $n$  is the number of moles of generated product,  $F$  is the Faraday constant and  $Q$  is the charge passed during the catalytic experiment.

The Turnover Number (TON) and Turnover Frequency (TOF) are important values for catalyst comparison. The TON corresponds to the number of catalytic cycles performed before catalyst deactivation. Measuring this value can be time-consuming and difficult to estimate for non-linear degradation rates (e.g. which cannot be described by a single mathematic function), and it is mainly found as the ratio of the number of moles of products produced by the number of active sites (**Equation 1-9**). The TOF is calculated as the TON divided by the reaction time, giving overall information on the catalytic activity for a given compound and is referenced in s<sup>-1</sup> in this work (**Equation 1-10**).

$$TON = \frac{n_{max\ product}}{n_{active\ sites}}$$

## Equation 1-9

$$TOF = \frac{TON}{t_{experiment}}$$

## Equation 1-10

Noteworthy, the TON and TOF numbers are restricted to catalysts consisting of discrete molecules (organic and organometallic structures) and are not suitable for dense metal catalysts. Indeed, the number of catalytic sites per unit area cannot, in principle, be quantified experimentally for metal surfaces

In this thesis the electroactive sites were measured from the integration of the irreversible reduction peak of the catalytic species formation relative to the measured ECSA (**Equation 1-11**). The method is described in detail in the following chapters.

$$\Gamma[Ag] = \frac{q}{nFA}$$

## Equation 1-11

With  $q$ , the charge of reduction peak,  $n$  the number of electrons involved in the reaction,  $F$  the Faraday constant and  $A$  the electrochemical active surface area (ECSA).

The selectivity of catalyst systems for the CO<sub>2</sub> reduction reaction (CO<sub>2</sub>RR) is generally assessed in H-cell electrolyzers at the lab scale, with an ion-exchange membrane separating the anode and cathode compartments (**Figure 1.11a**). This physical separation is necessary to avoid CO<sub>2</sub>RR products, electrolyte ions (Carbonate and bicarbonate) or oxygen crossing from cathode to anode or *vice versa*. This ion crossing leads to a preferential competitive reduction or oxidation of those species against CO<sub>2</sub>RR and OER. This leads to poor cell efficiency and poor faradic efficiency since a fraction of the electrical charge is consumed for an un-desired process. Most often, only cathode potentials are reported in the literature; however, the high ohmic resistance caused by the large gap between anode and cathode (a few centimetres), ion exchange membrane, and dilute electrolytes results in important cell voltages. H-cell cells are also often difficult to operate; for these reasons, modified classical three-electrode cells can be used instead, provided



that the anode is physically separated from the cathode compartment. Bridge tubes of precise porosity were found to provide limited O<sub>2</sub> diffusion from the anode compartment while maintaining a flow of charged species through the pores. A setup depicted in **Figure 1.11b** was used for most of the experiments reported in this thesis.

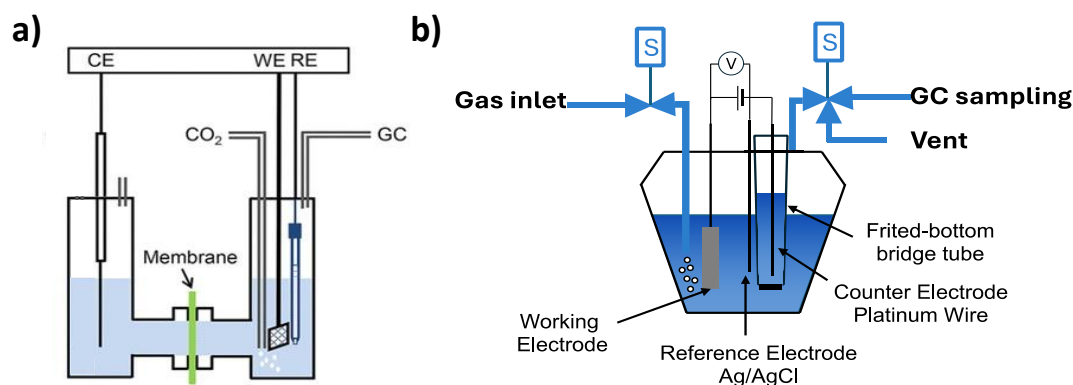


**Figure 1.11.** a) Typical H-cell configuration used in CO<sub>2</sub>R experiment under a steady stream of CO<sub>2</sub> b) Custom-made three-electrode cell assembly used in the experiments described in this thesis.

The lack of reproducibility between laboratories is still a major issue to date. The main source of error revolves around the gas quantification systems and protocols, cell designs and the preparation protocols for both catalysts and electrodes. Gas detection is central for accurate quantification, however, apparatuses details, injection protocols on the GC and calibration curves are either poorly described or missing in many papers. Some published results are often obtained from custom-made cell designs with potential measurements often performed without iR drop compensation making comparisons between catalysts challenging. In some cases, particularly when experiments are carried out on small-scale catalysis, it may be desirable to assess that the detected CO<sub>2</sub>RR adducts are originating from the CO<sub>2</sub> starting material and not arising from catalyst decomposition, electrode surface contamination, contamination in the gas supply or the injection system. This is particularly relevant for liquid products. A methodology involving CO<sub>2</sub>RR experiments carried out with labelled <sup>13</sup>CO<sub>2</sub> using the GC/MS detection and NMR measurements allows discrimination against any potential contamination.

## 5) CO<sub>2</sub>RR Catalysts

### A) Molecular catalysts

Molecular catalysts constitute the foundation of the CO<sub>2</sub> reduction reaction understanding. They usually possess a well-defined catalytic centre comprising a single metal surrounded by ligands where the metal's vacant orbitals and *d* electrons can exhibit multi-valence redox properties. This specificity facilitates the bonding of CO<sub>2</sub> on the electrochemically reduced metal centre. The activity of the metal centre is closely linked to its surrounding environment. The first coordination sphere is actively involved in the electronic transfer, effectively reducing or increasing the reaction potential. Studies have, for example, shown that an increased conjugation in macrocyclic ligands tends to lower the overpotential for CO<sub>2</sub>RR.<sup>62</sup> The second coordination sphere, on the other hand, is tightly linked to the catalytic site activity but can also impact its selectivity. In most cases, molecular catalysts are limited to the promotion of a two-electron CO<sub>2</sub> reduction towards CO and HCOOH with high efficiencies and selectivity. A few examples of molecular catalysts being able to reduce CO<sub>2</sub> further than two electrons have been presented, but such results are still rare.<sup>63</sup> While



state-of-the-art catalysts display particularly high selectivity and activity, one of the main drawbacks of such molecular catalysts remains their time-consuming synthesis and the consequently limited available quantities.

The first reported use of such complexes in homogenous catalysis dates back to 1977 when cobalt and Nickel tetra sulfonated phthalocyanines activities were characterized in water-based electrolytes (**Figure 1.12b**).<sup>65</sup> The Lehn group reported in 1984 the electrocatalytic reduction of CO<sub>2</sub> by a Re(bipy)(CO)<sub>3</sub>Cl complex (**Figure 1.12a**).<sup>64</sup> Nickel Cyclams were reported by Sauvage's group the same year and offered a lower overpotential on a mercury pool electrode, leading to the almost exclusive production of CO (**Figure 1.13a**).<sup>34</sup> Sauvage's group proposed the first mechanism of the CO<sub>2</sub>RR for a molecular catalyst three years later following the observation of a drastic current increase in the Ni<sup>II/I</sup> wave, suggesting the active role of the Ni<sup>I</sup> species (**Figure 1.13b**).<sup>67</sup> The tendency of CO to recombine with [Ni(cyclam)]<sup>+</sup> over prolonged electrolysis leads to the formation of the catalytically inactive Ni(CO)<sub>4</sub> species. Efforts to prevent this phenomenon have been made by synthetic modification of the macrocycle structure, however, leading to minor improvements in the CO<sub>2</sub>RR catalytic performance.

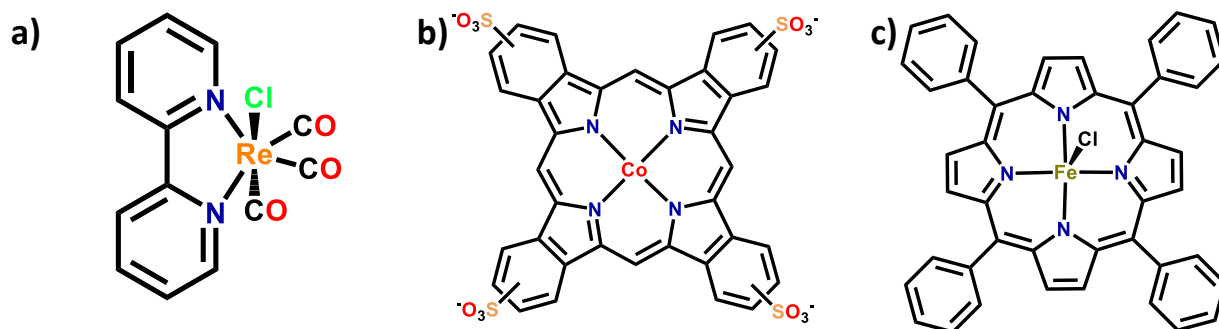


**Figure 1.12** a) Chemical structure of Re(bipy)(CO)<sub>3</sub>Cl complex<sup>64</sup> b) Chemical Structure of tetrasulfonated Cobalt phthalocyanine<sup>65</sup> c) chemical structure of Iron tetraphenylporphyrin chloride<sup>66</sup>

Among the wealth of reported complexes, iron porphyrins are arguably the most widespread catalyst. The mechanism of homogeneously electrogenerated Fe<sup>0</sup> porphyrins has been widely studied in the last decades. Their kinetics have been studied thoroughly by Savéant, Costentin and Robert and set a solid base on theoretical aspects of molecular CO<sub>2</sub>RR catalysis as a whole.<sup>66</sup> Early studies in the 1980s focused on the readily-prepared [Fe(TPP)]Cl (**Figure 1.12c**) in a DMF-based electrolyte, which showed at the time that the catalytic species was the electrogenerated [Fe<sup>0</sup>(TPP)]<sup>2-</sup>. The catalytic activity was relatively low in DMF; however, the addition of Lewis<sup>68</sup> and Bronsted organic acids, such as trifluoroethanol or phenol<sup>69</sup>, tended to increase the activity significantly. Following these results, Costentin and co-workers reported that modifying FeTPP by introducing two phenolic groups in ortho positions of its phenyl groups (FeTDHPP, **Figure 1.14a**) significantly accelerated the rate of CO<sub>2</sub> electroreduction to CO. The catalyst demonstrated 94 % CO faradaic yield over 4 hours of electrolysis and 50 million turnovers at a low overpotential (0.465 V), with no observed degradation<sup>70</sup>. The activity increase was attributed to the local concentration of protons brought in close proximity to the intermediate by the phenolic hydroxyl substituents.

As an alternative strategy to a directional intramolecular H-bonding interaction, the stabilization of negatively charged iron-CO<sub>2</sub> bound intermediates may also be obtained via through-space coulombic interactions with positively charged pendant groups spatially oriented in the proximity of the active site. Following this strategy, the most efficient CO<sub>2</sub>RR homogeneous catalyst was obtained (**Figure 1.14b**). It

displays an impressive TOF of  $10^6 \text{ s}^{-1}$  at 220 mV overpotential with a CO production close to 100% while remaining stable upon long-term electrolysis.<sup>71</sup>

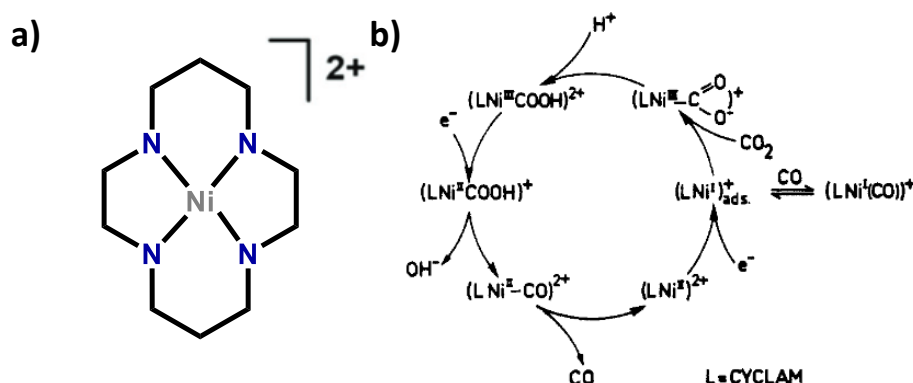


**Figure 1.13** a) Chemical structure of Nicyclam b) CO<sub>2</sub>RR catalytic cycle for Nicyclam. Reprinted from JACS. Copyright ACS<sup>67</sup>

The remarkable activity of porphyrin-based catalysts attracted interest in the immobilization of molecular catalysts on conductive electrodes. Indeed, the heterogenization of molecular catalysts is a prerequisite for practical applications. As such, the deposition of Co and Ni phthalocyanines onto graphite electrodes is the first reported heterogenized organometallic complex (**Figure 1.14c**).<sup>57</sup> In this case, the catalytic species was immobilized simply on the electrode through Van der Waals interactions leading to an improved electrical contact and allowed circumventing the solubility limitations of the organometallic catalysts. Other advantages can be mentioned, for example, the ease of recycling and the improved catalyst weight-to-activity ratio. The deposition usually takes the form of a thin film containing a variable number of active sites (from  $10^{-7}$  down to  $10^{-12} \text{ mol.cm}^{-2}$ ) dependent on the catalyst loading, deposition method, substrate nature and substrate structure. Their mechanism can be pinned down with electrochemical techniques coupled with XAS or STEM.

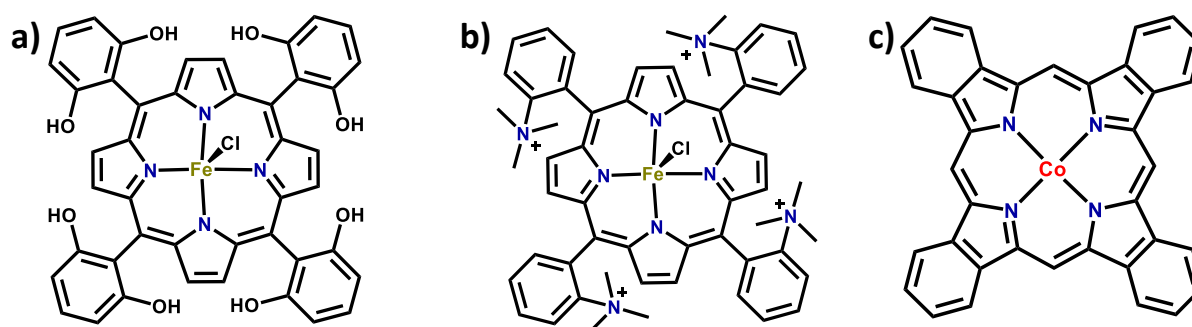


**Figure 1.14** a) FeTDHPP structure<sup>70</sup> b) Structure of Fe-o-TMA<sup>71</sup> c) Cobalt phthalocyanine structure<sup>57</sup>

Concerned by the necessity of creating a strong interaction between the catalyst and surface, the immobilization using functional groups such as carboxylate, phosphate, thiol, amino and diazonium groups has been considered early on, as they form relatively stable films with a low surface coverage<sup>72</sup>. The covalent immobilisation of a modified iron TPP bearing six OH groups in *ortho* and *ortho'* position via peptide coupling on nanotubes pre-functionalised through diazonium coupling, proved equally effective.<sup>73</sup> The catalytic properties (80-90% FE for CO) and stability were maintained for 3h.

The immobilisation using non-covalent  $\pi$ - $\pi$  stacking interactions generally favours high catalyst loading with a lower control on the functionalisation of the electrode surface.<sup>74–76</sup> The first mentioned immobilisation through  $\pi$ - $\pi$  stacking interactions for CO<sub>2</sub>RR was carried with CoPc exploiting the strong interaction between the macrocyclic aromatic core and graphite electrodes.<sup>57</sup> The replacement of the latter with carbon nanotubes<sup>77</sup> resulted in enhanced catalytic properties. The use of a pendant chain is another recurring strategy to form  $\pi$ - $\pi$  stacking interactions **Figure 1.15a** displays a pyrene-modified porphyrin grafted on a carbon nanotube. This strategy resulted in a particularly stable functionalised electrode while the catalytic activity was preserved in a water-based electrolyte.<sup>76</sup>

Although the immobilization of molecular catalysts has been a matter of concern, recent results, particularly on bulk electrolysis<sup>78</sup>, indicate that Van der Waals forces are presumably sufficient so long as the catalyst is immobilized on a porous substrate and that the catalyst is intrinsically insoluble in aqueous medium. An example from our research group is shown in **Figure 1.15b**, in which the [Re(bpy)(CO)<sub>3</sub>Cl] catalyst was found to remain bound into a porous carbon matrix even in the presence of large amounts of ionic liquids.<sup>79</sup> As a consequence, insoluble 3D or 2D materials such as metal-organic framework (MOF) or covalent organic framework (COF) have emerged as an alternative to catalysts immobilization. The inclusion of a catalyst into such a structure can improve their activity and stability (covalent bonding, conductivity) while improving the selectivity of the CO<sub>2</sub>RR by using suitable building blocks.

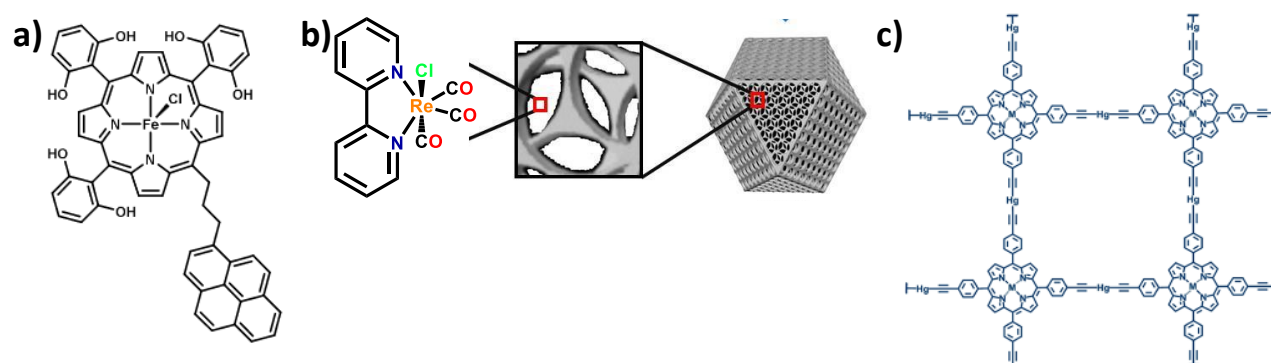


**Figure 1.15 a)** Pyrene functionalized iron porphyrin grafted onto carbon nanotubes.<sup>76</sup> **b)** [Re(bpy)(CO)<sub>3</sub>Cl] catalyst in a porous carbon frame (carbonized MOF)<sup>79</sup> **c)** Schematic illustration of the chemical structure of Hg MTPP (M=Mn, Fe, Co, Ni, Cu, and Zn)<sup>86</sup>

For example, the presence of an amine group in the vicinity of a [Re(2,2-bipyridine-5,5-dicarboxylic acid)(Cl)(CO)<sub>3</sub>] site on a MOF cooperatively enhanced the CO<sub>2</sub>RR's kinetics/selectivity *via* the formation of a presumed carbamate intermediate.<sup>80</sup> Imine-based COFs are particularly interesting as they possess enhanced electronic properties compared to MOF. The synthesis of COFs with an ordered crystalline arrangement relies on reversible reactions between pre-arranged building blocks. The implementation of catalytic sites with aromatic connectivity is considered a way to decrease the overpotential of the active species. (ref or explanation) Additionally, the imine moiety favours the capture of CO<sub>2</sub><sup>81,82</sup> with an increased local CO<sub>2</sub> concentration at the catalytic sites.<sup>83</sup> One of the main drawbacks of these materials is often the lack of control over the thickness of the layer preventing optimum electron and mass transport through the 2D stacks.<sup>84</sup> A new class of materials has emerged in which a pseudo-2D-structure is synthesised under kinetic control, such as the structure presented in **Figure 1.15c**. A network of catalytically active Porphyrin arranged in a square-like fashion was built from the formation of alkyne-Hg bonds. Quite interestingly, the

material has been shown to withstand high current density in a flow cell design with currents reaching up to 1.2 A.cm<sup>-2</sup> with 98.9% selectivity towards CO.<sup>85</sup>

### B) Heterogenous catalysis: metal surface

In 1985, Hori and co-workers published the first of a series of papers in which they demonstrated that elemental gold, silver and copper<sup>87</sup> were particularly active catalysts in the CO<sub>2</sub>RR. Contrary to their molecular counterparts, metal catalysts rely on a large number of poorly characterized active sites with no control over the structure at the molecular and atomic scales. On the other hand, the presence of a higher density of active sites results in higher reaction rates. Some metals were shown to be poor catalysts for the CO<sub>2</sub>RR (Ni, Fe, Ti, Pt) and favour the HER in an aqueous medium. However, a number of them display CO<sub>2</sub>RR activity, such as Ag, Au, and Zn favouring CO formation, or In, Sn, and Cd forming HCOOH in high yield. Theoretically, the nature of the formed products relies on the binding energies of \*CO, \*COOH and \*H intermediates, which are dependent on both the nature and surface structure of the material (**Figure 1.16a**).<sup>88–90</sup> Au and Ag, for example, favour CO formation because of the weak bonding of \*CO regardless of crystalline orientation. Conversely, an overly strong \*CO bonding leads to catalyst poisoning for Pt or Fe. Copper is unique in that it leads to intermediate values of \*CO and \*H binding energies. This property allows the \*CO intermediate to be further reduced towards alcohols or hydrocarbons before gaseous CO is eliminated from the catalytic cycle.<sup>91,92</sup> As a consequence, copper has remained, to date, the most studied metal, being able to produce a wide range of CO<sub>2</sub> reduction products, including CO, methane, ethylene, formate, ethanol and propanol. While the intermediate bonding values for \*CO and \*H enhances the formation of larger carbon chains, the \*H lifetime also favours the formation of H<sub>2</sub> in large quantities, and a polycrystalline Cu foil surface with no specific structuration may produce up to 90% H<sub>2</sub>. Many alloys have been developed to selectively tune the intermediates lifetimes and increase the selectivity, with copper-based bimetallic alloys being the most studied.<sup>93–95</sup> Through theoretical calculations and using active machine learning, it was found that a Cu-Al alloy (10% Al) was a perfectly fit candidate for C<sub>2</sub>H<sub>4</sub> Formation. Subsequent experiments using the latter alloy gave rise to FEs of over 80% at 600 mA.cm<sup>-2</sup> in a flow cell device.<sup>96</sup>

Over the years, the influence of surface faceting, grain boundary density, and morphology on the activity and selectivity of heterogeneous CO<sub>2</sub>RR catalysts have been investigated in depth. Solvent-adsorbate effects, electrolyte-electrode interactions, surface coordination number, and transition state considerations have been revealed to have a great impact on the selectivity and stability of the material. These effects are summarized in **Figure 1.16b** and will be described in detail. The nature of the material greatly influences the interactions between adsorbed species on the catalytic surface. These adsorbate-adsorbates preferentially occur on rough surfaces such as unpolished metals and have been shown to enhance the formation of C<sub>2+</sub> on copper. The adsorbate nature plays an important role in surface reactivity dynamics, and longer-lived intermediates are a primordial step towards carbon-carbon coupling on the surface. In CO<sub>2</sub>RR conditions the HER activity is altered by adsorbate-adsorbate effects. The presence of a \*CO coverage impacts the binding energy of \*H, leading to the suppression or promotion of the reaction. The suppression of HER on Cu and Au, for example, enhances their selectivity towards CO<sub>2</sub>RR. This suppression is not straightforward, and the presence of Cd (a poor HER catalyst) in a CdAu alloy, for example, does not enhance the performance of Au.<sup>98</sup> In the case of Ag, an adsorbate-adsorbate mechanism between a formate (\*OCHO), a proton (H<sup>+</sup>) and a carboxyl intermediate (\*COOH) has been proposed for the favoured formation of the CO pathway.<sup>99</sup>

Weak Interactions between the electrolyte's components and the catalyst's surface were also shown to have a significant impact on the catalyst properties. As such, a difference in activity can be expected upon varying the alkali nature of the most used electrolytes such as bicarbonate, hydroxide or phosphate salts.<sup>100</sup> These variations were explained by the presence of hydrated alkali ions at the edge of the Helmholtz plane, leading to a variation of the local pH. Consequently, a difference in CO<sub>2</sub> concentration near the electrode is occurring according to the nature of the anion. Similarly, ammonium-based cations have been shown to favour the formation of ethylene by displacing the water layer from the catalyst-electrolyte interface and consequently favouring the hydrogen bonding of a CO dimer which is a key intermediate for the formation of ethylene.<sup>101</sup> The Presence of halide salts (KCl, KBr, KI) in solution seems to lead to the presence of adsorbed halide at the surface of a Cu surface with I<sup>-</sup> enhancing the electron transfer to CO<sub>2</sub> and CO, thus leading to an enhanced hydrocarbon formation.<sup>102</sup>

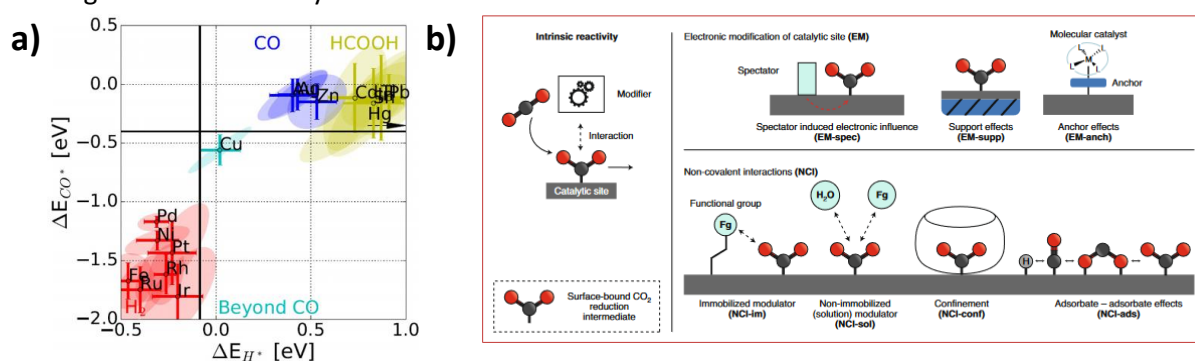


**Figure 1.16.** a) Binding energies of the intermediates  $\Delta E_{CO^*}$  and  $\Delta E_{H^*}$  for common transition metals<sup>89</sup>; b), Aspects that influence the intrinsic activity of the catalytic site either by an electronic modification of the catalytic site or via non-covalent interactions with modulators or reaction intermediates.<sup>97</sup>

In an attempt to control the above interactions, a wealth of methods has been developed. Metal structuration in the form of nanowires<sup>103</sup>, nanowhiskers<sup>104</sup>, nanoparticles<sup>105</sup>, nanoprisms<sup>106</sup>, nanocubes<sup>58</sup> and nanodendrites<sup>107</sup> have been shown to induce a significant shift in selectivity. These rough surfaces were shown to increase the electrode hydrophobicity *via* Cassie-Baxter wetting behaviour, for example.<sup>108</sup> The direct functionalization of the surface by hydrophobic molecules was also shown to form CO<sub>2</sub> and H<sub>2</sub>O concentration gradients near the surface. The latter strategy is often combined with nanostructuring. As such, an example of dendritic copper surface modification through alkane thiol was reported by Wakerley *et. Al.*<sup>109</sup> showing an increase in surface hydrophobicity upon functionalization with octane thiol (**Figure 1.17a**). An important selectivity shift was reported with FEs for ethylene as high as 50% and as high as 22% for ethanol.

The subtle nature of the interactions at play between the substrate and the catalytic surface has appealed to the supramolecular chemistry community. Indeed, examples of host-guest chemistry applied to the field of CO<sub>2</sub>RR have recently been reported. In a particular paper from Reisner and Nau, the use of a cucurbit[6]uril macrocycle adsorbed on an Au surface was shown to modify the activity and selectivity of the catalyst by modifying the nature of surface-bound species (**Figure 1.17b**).<sup>110</sup> The CO<sub>2</sub>RR was shown to occur from macrocycle-bound CO<sub>2</sub>, based on surface-enhanced infrared absorption spectroscopy (SEIRAS) results. The rather high association constant of the CO<sub>2</sub>-macrocycle complex, measured by an indirect fluorescence measurement, confirmed the latter finding. The hydrophobicity of the cavity is a key parameter as it decreases the H<sub>2</sub>O interaction with the intermediates. This phenomenon is observed in the

case of amines, amides<sup>111,112</sup> and imidazolium-based ionic liquids<sup>113,114</sup> where CO<sub>2</sub> reduction intermediates are ascribed as being stabilized by hydrogen bonding and electrostatic interaction on the electrode. Importantly, a subtle balance between CO<sub>2</sub>-host and CO<sub>2</sub>RR product-host interactions must exist. Moreover, competitive association with solubilized salts should be prevented. While such a balance is found in complex enzymatic systems, it remains a challenge for synthetic systems. The use of cationic interactions or competitive non-redox species has been proposed to control the host-guest complex formation.<sup>115</sup> Overall, the concept of reaction confinement can enable chemical control and tunability of the catalytic site on a heterogeneous catalyst (**Figure 1.17c**).

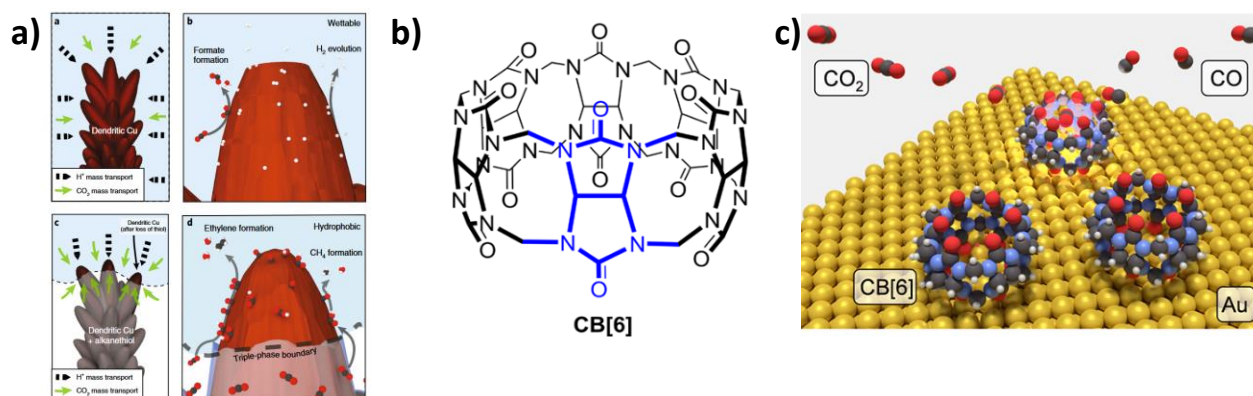


**Figure 1.17** a) The proposed role of hydrophobicity in promoting CO<sub>2</sub> reduction over proton reduction. The illustrations of the operation of the hydrophobic dendrite show the enhanced CO<sub>2</sub> mass transport from the triple-phase boundary between the electrolyte, electrode and gaseous CO<sub>2</sub>.<sup>109</sup> b) CB[6] structure with main building block highlighted in blue. c) Schematic illustration of CO<sub>2</sub> conversion to CO within the cavity of CB[6] adsorbed on an Au surface.<sup>110</sup>

### C) Heterogeneous Catalysis: Nanoparticles and clusters

With the advent of bulk electrolyzers and gas diffusion layers (see part XX), nanoparticles have provided a convenient method to deposit metallic species *via* wet chemistry methods. Although having been a relatively recent research focus, gold-based nanoparticles are the most studied nanoparticles in the CO<sub>2</sub>RR. Their use in medical applications and photonics has set a solid understanding in terms of synthesis and physical properties.<sup>116</sup> The adaptability of Au NPs to the field of CO<sub>2</sub> electroreduction was, therefore, first approached *via* a thorough analysis of the NP size-dependence on the outcome of the CO<sub>2</sub>RR. Monodispersed Au NPs of different sizes (4, 6, 8, and 10 nm, respectively) were used by Sun et al. to investigate their behaviour in the electrocatalytic CO<sub>2</sub>RR (**Figure 1.18a**).<sup>117</sup> Interestingly, their findings indicated that the selectivity of the CO<sub>2</sub>RR towards CO tends to decrease with decreasing NPs size. The explanation for this behaviour lies on the crystalline nature of the active site. Indeed, it was demonstrated that, for gold, a preferential orientation towards the (211) plane favoured the formation of CO, while a preferential (111) orientation favours hydrogen formation. The fact the (111) orientation was preponderant when the crystal size was reduced explained, thus, the decrease in CO selectivity. A similar behaviour is seen when the Ag NPs size is decreased below 5 nm in spherical structures (**Figure 1.18b**).<sup>118</sup> Cu nanoparticles show a dramatic increase of activity when the size is decreased from 15 to 2 nm; however, concomitant with the selectivity shifting towards H<sub>2</sub>.<sup>119</sup>



An elegant strategy to prevent such phenomenon has been to modify the particles' shape and to expose specific crystalline facets. For example, Au nanowires, favouring an orientation towards (211), were found to have very low overpotential while possessing a high FE for CO (94%).<sup>121</sup> Similarly, Ag triangular nanoplates, with preferential (100) facets exposed, are outperforming spherical nanoparticles by producing CO selectively (96.8%) at -0.86V vs RHE.<sup>122</sup> Copper nanocubes have been shown to favour ethylene formation compared with spherical nanoparticles (**Figure 1.18c**),<sup>120</sup> ascribed as a preferential orientation of the crystals when deposited on electrode substrates. Further studies from Buonsanti demonstrated the selectivity-crystal-facet relationship, where Cu-NPs with different geometries exposing different facets lead to markedly different selectivity.<sup>123</sup>

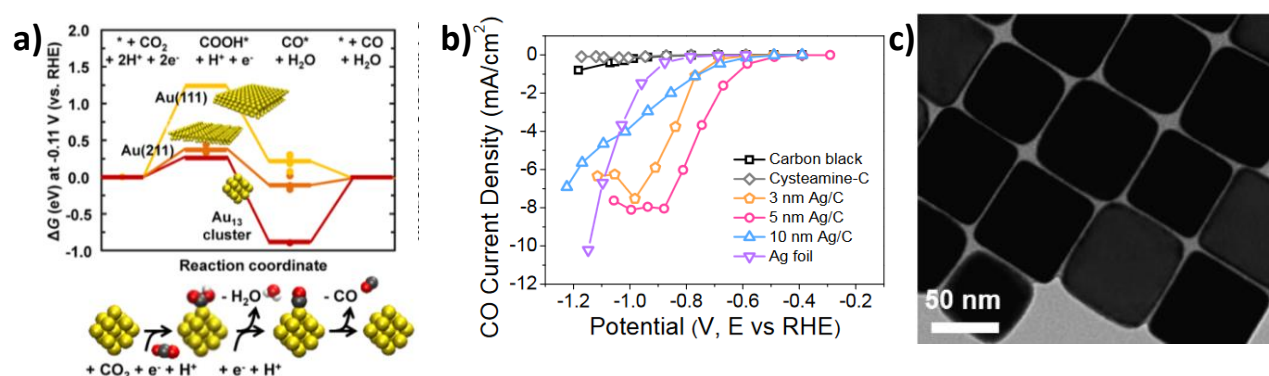


**Figure 1.18** a) Free energy diagrams of CO<sub>2</sub> to CO on Au(111) (yellow), Au(211) (orange and Au<sub>13</sub>cluster (red)<sup>117</sup> b) Ag nanoparticles with size dependency on CO<sub>2</sub>RR activity.<sup>118</sup> c) transmission electron microscopy (TEM) image of Cu nanocubes<sup>120</sup>

Additional to crystal orientation, factors related to the nanoparticles preparation (presence of surface organic ligands, degree of oxidation and defects) have a strong influence on the CO<sub>2</sub>RR activity. The physicochemical and electronic properties of the surface are drastically changed upon surface modification, and strategies involving the use of chelating organic molecules are commonly found in the literature. They can be used to stabilize the NPs and prevent aggregation phenomena or oxidation at the surface but can also be used to modify the electronic properties and the local environment surrounding the active sites by inducing hydrophobic or pH-sensitive functions. A wide variety of chemicals have been used to functionalize NPs, such as surfactants and organics ligands, with thiols, amines and N-heterocyclic carbenes being the main candidates.<sup>124</sup>

While being generally homogeneous in size, morphology and shape, large nanoparticles are still challenging to apply to the CO<sub>2</sub>RR since a performance-structure correlation is somewhat difficult to establish. Moreover, the atomic activity (catalytic activity vs total number of atoms) is extremely low compared to organometallic structures.<sup>125</sup> In the aim of enhancing the atomic activity, and reducing the dependency on crystalline orientation, atomically precise nanoclusters have been developed. They possess unique characteristics with well controlled size (1-3 nm), three-dimensional structure and coordination habits. A wide variety of ligands has been used to prepare such nanoclusters (thiolate and phosphine being the most common ones), and a large library of Au nanoclusters has been tested for CO<sub>2</sub>RR with excellent overall catalytic activity.<sup>126-135</sup> The molecule-like characteristics and precisely defined structures, along with their high activity and selectivity, render nanoclusters ideal catalysts for CO<sub>2</sub>RR.

Alkynyl ligands have recently emerged as a novel form of ligand for stabilizing noble metal nanoclusters,<sup>136</sup> anchoring on a metal atom via both  $\sigma$  and  $\pi$  bondings. They consequently possess unique physicochemical properties, atomic arrangement and catalytic performance deriving from these binding modes. Their ability to comprise large conjugated systems, potentially impacting the electronic structure of the clusters have attracted attention for their luminescent<sup>137,138</sup> and catalytic<sup>139</sup> properties. Alkynyl-gold nanoclusters were isolated for the first time by Tsukoda *et al*,<sup>140-142</sup> and only one example of Alkynyl-gold cluster for CO<sub>2</sub>RR application exists.

Alkynyl silver (or silver acetylides) are among the first organometallic species ever produced, and their structural and coordination chemistries are consequently quite well known. Phenylethynyl silver was, for example, reported as early as 1870.<sup>143</sup> Their preparation was commonly used as a diagnostic test to detect terminal alkynes.<sup>144</sup> Indeed, silver acetylides are known to form readily upon the addition of a terminal alkyne to an ammoniacal silver nitrate solution as an insoluble precipitate. They can be obtained easily on a multigram scale using various synthetic routes and mainly as crystalline solids, which are stable over a prolonged period under ambient conditions as far as light is excluded. They are particularly resistant to hydrolysis due to the strength of the Ag-sp carbon bond and the insoluble nature of their crystals. Extremely acidic conditions (TFSA, TFA, HCl, etc.) are therefore needed to break the cluster structure.

Their solid-state structure was characterised as being part of the clusters class of organometallic structures in the early 1960s through the study of their single crystal X-ray diffraction patterns. The exact structure of the cluster is generally dependent on the alkynyl ligand's structure and the synthesis conditions but the crystal growth mainly displays an infinite arrangement of the metallic core along a direction of space. This metallic core is homogeneously flanked by an outer shell of alkynyl groups linked to silver atoms *via*  $\sigma$  and  $\pi$  bonds in a relative 1:1 silver-to-ligand ratio. The infinite tubular or columnar-shaped nature of the clusters is reminiscent of polymeric structures, explaining their relative insolubility (**Figure 1.19a**).

The silver acetylide formation mechanism relies at first on a  $\pi$ -complex intermediate between Ag<sup>+</sup> and the alkyne. This intermediate complex, characterized by mass spectrometry,<sup>145</sup> is readily deprotonated upon addition of a base such as an amine forming the silver acetylide. The kinetics of the reaction and, consequently, crystal assembling are, therefore, tightly linked with the concentration of both the base and acetylene at the vicinity of a silver ion. Crystals of XRD analysis quality grade can be obtained through slow and controlled diffusion of the reagents (**Figure 1.19a**).<sup>146</sup>

The insoluble nature of silver acetylides may be altered upon addition of triphenylphosphine or other donor ligand.<sup>147</sup> The as-formed soluble species possess remarkable properties when used as nucleophilic reagents as they exhibit extreme mildness and very low basicity, making them complementary to other alkynyl metals reagents. They are generally generated *in situ as reaction intermediates in silver-catalysed* additions of alkynes, for example.<sup>147</sup> The addition of reducing agents enables a relative control of the crystal growth, and nanoclusters can readily form under proper synthetic conditions. Contrary to their polymeric counterparts, they are discrete crystalline nanoparticles with finite sizes, from a few to several tens of atoms, and variable crystalline arrangement related to the synthetic procedures (**Figure 1.19b**). Their synthesis is often performed through the simultaneous addition of a silver salt solution and a reducing agent into an acetylene solution, but a wide spectrum of procedures is available. Contrary to gold nanoclusters, only very few Ag nanoclusters have been tested for CO<sub>2</sub>RR with a recent literature focus on Ag clusters possessing alkynyl ligands<sup>148-150</sup>



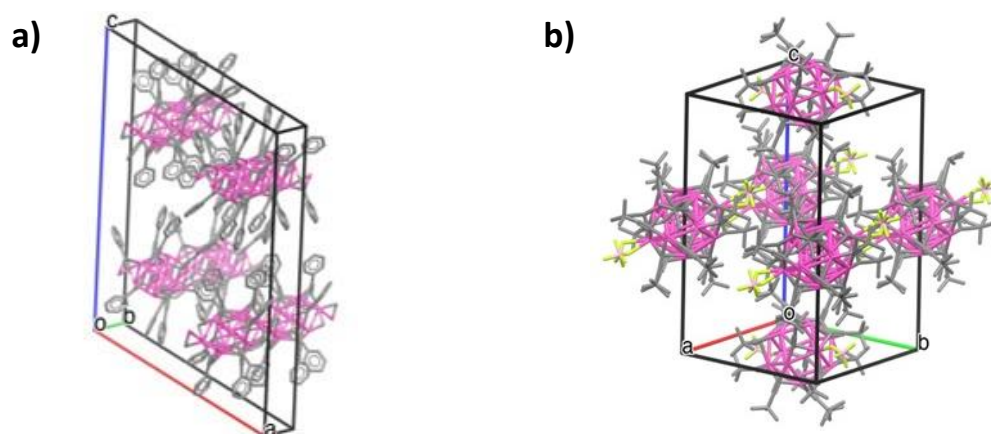


**Figure 1.19** a) XRD structure (CCDC: 1020984) of tubular-shaped silver phenylacetylide crystal.<sup>146</sup> b) XRD structure (CCDC: 290250) of a finite Ag tert-butylethynyl acetylide clusters crystal.<sup>151</sup>

Very recently, Qin et al. described the synthesis of an alkynyl-protected Ag<sub>15</sub>(C≡C-tBu)<sub>12</sub><sup>+</sup> nanocluster (Ag<sub>15</sub>) with a discrete structure. Surprisingly, the authors found that the X-ray diffraction single crystal structure of the cluster contained CO<sub>2</sub> molecules in the unit cell, presumably incorporated into the structure during crystal growth on specific edges of a cubic-shaped part of the structure (**Figure 1.20b**). This unusual behaviour indicated a strong affinity of the silver core towards CO<sub>2</sub> and led the team to test it as a catalyst in the CO<sub>2</sub>RR. A remarkable 95% selectivity towards CO was obtained under optimized CO<sub>2</sub>RR conditions (**Figure 1.20a**).<sup>149</sup> This result surpasses most of the recently reported nanoclusters under similar conditions.<sup>129,131,152</sup> For such materials, TOF can be easily defined, and its maximum value was calculated to be 6.37s<sup>-1</sup> at -1.1 V vs RHE. The selectivity of the cluster was maintained over a 15h period, after which it was seen to decrease significantly together with the TOF. This high selectivity is explained by DFT calculations which demonstrated the *in-situ* formation of a reactive undercoordinated Ag atom from the stripping of a ligand during catalysis.

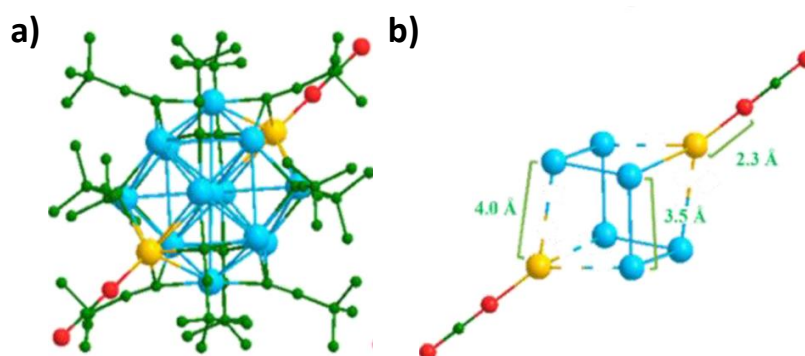


**Figure 1.20** a) X-ray diffraction single crystal structure of the Ag<sub>15</sub> cluster showing the two CO<sub>2</sub> molecules as part of the unit cell.<sup>149</sup> b) Zoomed-in representation of the cube-shaped Ag<sub>8</sub> atoms with the two CO<sub>2</sub> molecules.<sup>149</sup>

A follow-up study from the same team on a different alkynyl-protected Ag nanocluster demonstrated the importance of the alkynyl ligand in the CO<sub>2</sub>RR. They compared the activity (selectivity) of an Ag<sub>32</sub>(C≡CAr)<sub>24</sub> under CO<sub>2</sub>RR conditions with a phosphine and thiolate co-protected Ag<sub>32</sub> cluster (**Figure 1.21a**).<sup>153</sup> The FE towards CO reached an impressive 96% for the alkynyl-protected cluster (Figure 1.21b), while the

phosphine-thiolate-protected cluster reached a 57% FE (**Figure 1.21c**) at a higher potential (-0.8 vs -1 V vs RHE respectively). To understand the difference in catalytic properties for such similar complexes, DFT calculations were performed, and both complexes were shown to possess important energy barriers. The removal of a ligand from the cluster was shown to greatly lower the energy barriers towards COOH\* in both cases (0.4 and 0.5 eV, respectively), while the hydrogen evolution barrier was comparatively higher for the alkynyl (0.51eV) than for the other complex (0.05eV) explaining the large differences in selectivity.

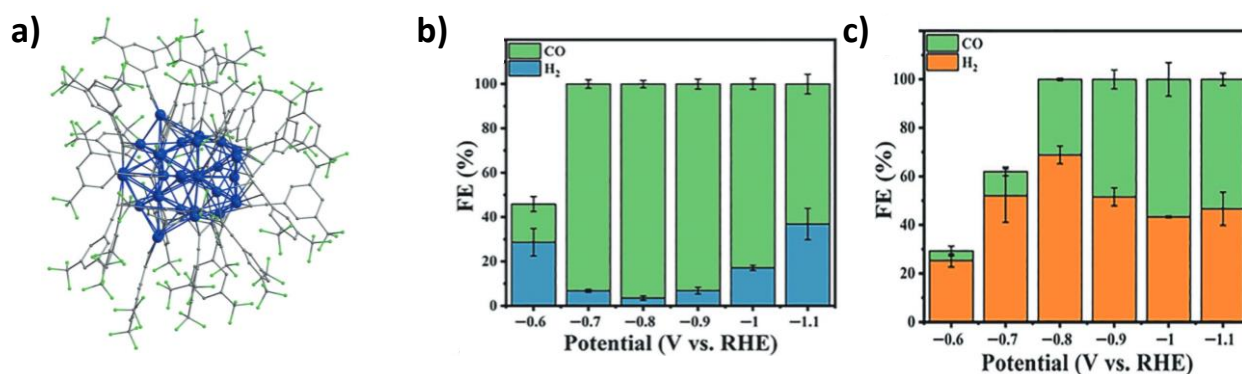


**Figure 1.21 a)** X-ray diffraction single crystal structure of the Ag<sub>32</sub>(C≡CAR)<sub>24</sub> cluster. Ag (blue), C (grey) and F (green).<sup>153</sup> **b)** CO and H<sub>2</sub> Faradaic efficiency for Ag<sub>32</sub> cluster.<sup>153</sup> **c)** CO and H<sub>2</sub> Faradaic efficiency for [Ag<sub>32</sub>(DPPE<sub>5</sub>)(SR)<sub>24</sub>]<sup>2-</sup>.<sup>153</sup>

Following these promising results, several Ag clusters possessing metal inclusions were reported and proposed as potential candidates towards enhanced catalytic properties. A cluster including Cu was recently synthesized in the form of Ag<sub>15</sub>Cu<sub>6</sub> (**Figure 1.22a**).<sup>150</sup> The core of the cluster is arranged in a body-centred cubic structure with four silver atoms at the edges of the cube and central copper atoms in the interior. The cluster is stabilised by both alkynyl and diphosphine ligands. When deposited on carbon GDL, a high catalytic activity towards CO was observed (91.3% at -0.81 V vs RHE). Experiments in an MEA electrolysis cell were performed, and stability over 145 h was observed at -3.25 V cell potential (**Figure 1.22b**). Similarly to the silver-only clusters, the loss of a ligand is critical for the catalytic activity, with the resulting undercoordinated metal atoms being the catalytic centre. \*CO<sub>2</sub> and trans-COOH\* are preferentially bonded to Ag atoms, explaining the catalyst selectivity.

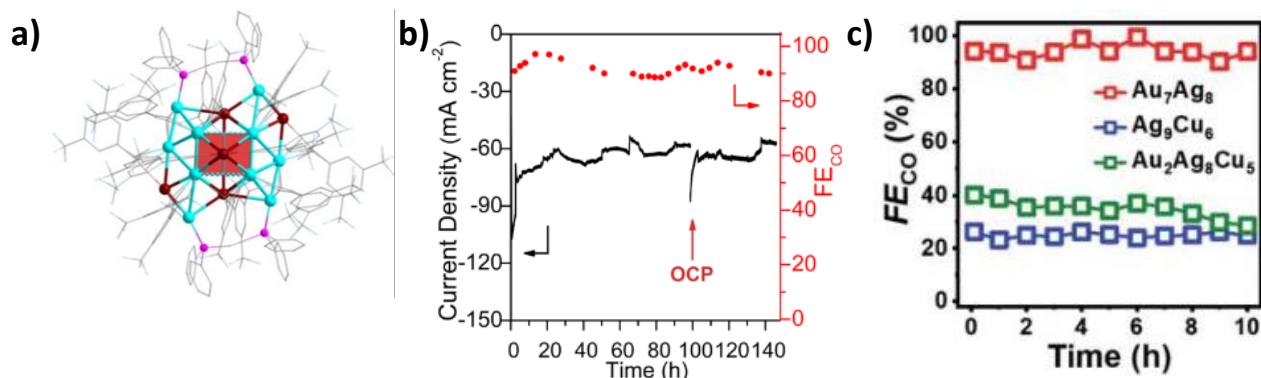


**Figure 1.22 a)** XRD structure of Ag<sub>15</sub>Cu<sub>6</sub> cluster.<sup>150</sup> **b)** Long-term operation of Ag<sub>15</sub>Cu<sub>6</sub>/C at a -3.25 V cell potential in the MEA-cell **c)** Long-term stability of Au<sub>7</sub>Ag<sub>8</sub>/GDL at -0.49 V vs RHE.<sup>148</sup>

In addition to the above examples, mixed bi and tri-metallic clusters containing Au, Ag and Cu have been prepared by Ma et al. The authors synthesised a library of three different clusters with an identical total number of metal atoms, however, with varying relative ratios of metals between the clusters. While the Au<sub>7</sub>Ag<sub>8</sub> clusters were shown to be CO-selective (FE CO 98%), Ag<sub>9</sub>Cu<sub>6</sub> and Au<sub>2</sub>Ag<sub>8</sub>Cu<sub>5</sub> were formate-selective with 47% and 28% FE respectively (**Figure 1.22c**). This atomic exchange was demonstrated to be an effective strategy to selectively tune the electrocatalytic performance of the clusters.<sup>148</sup> Overall, the use of such clusters in CO<sub>2</sub>RR processes has been extremely rare and their application in flow devices at relevant current densities for industry has not been achieved yet. The early results presented herein are very encouraging, and the currently existing expertise on the synthesis of silver acetylides in the laboratory has prompted us to embrace the field. Most of the current thesis will be dedicated to the synthesis and study of silver acetylides in the context of CO<sub>2</sub> electroreduction.

## 6) Flow cell designs towards industrial application

The rate of the CO<sub>2</sub>RR, similarly to other electrocatalytic reactions, is intrinsically limited by the reagent mass transport to the electrode. However, contrary to the former reactions, the limited solubility of CO<sub>2</sub> in aqueous and non-aqueous electrolytes reduces the concentration of CO<sub>2</sub> at the electrode-electrolyte interface, consequently bringing down the reaction rate. Therefore, the rate of the CO<sub>2</sub>RR is generally limited to a few milliamperes of faradic current in a common laboratory 3-electrode cell.<sup>154</sup> H-Cell designs, wherein the compartments are separated by an ion exchange membrane, suffer from a similar limitation, with current densities limited to values lower than 100 mA.cm<sup>-2</sup> (**Figure 1.23a**).<sup>155–157</sup> The CO<sub>2</sub> mass transport limitations render these geometries unsuitable for industrial-scale electrolysis, where high current densities are typically superior to 200mA.cm<sup>-2</sup>, high selectivity, low overpotential and long-term operation (>8000h) are required.<sup>158</sup>

To overcome the above setbacks, flow cell electrolyzers have experienced a surge in popularity in academic research. They comprise similar design features as that of flow reactors, where the anode and cathode are separated into two distinct compartments with a constant reagent flow. Their unique feature is the presence of a gas diffusion layer (GDL), which consists of a porous conductive substrate onto which the CO<sub>2</sub>RR catalysts is deposited, resulting in a so-called gas diffusion electrode (GDE). The latter is then used as the cathode, with gaseous CO<sub>2</sub> being fed from the back of the GDE while the front face is in contact with the electrolyte (catholyte). The diffusion of CO<sub>2</sub> through the porous membrane allows the local concentration of CO<sub>2</sub> to reach concentrations in the vicinity of the catalytic centre several orders of magnitudes higher than in laboratory-scale devices. The electrochemical reaction takes place at a ternary phase, where a gas/catholyte/catalyst interface is formed, allowing the rate to increase significantly. **Figure 1.23b** shows a schematic representation of such a device, where the flow of CO<sub>2</sub> gas is delivered to the cathode and controlled by a mass flow controller.<sup>78,159–165</sup> In most devices, the cathode and anode compartments are circulated with a constant flow of electrolyte (controlled by a peristaltic pump), which is in most cases concentrated KOH (up to 12M) or KHCO<sub>3</sub> for the cathode compartment. A more recent type of cell called membrane electrode assembly (MEA) is electrolyte-free and offers excellent properties when compared with the previous designs (**Figure 1.23c**). To unfold the catalytic events and catalyst evolutions, in situ and operando measurements are a requirement; however, only a few rare experimental techniques are available for flow designs, with the main ones being XAS<sup>59,60</sup> and ATR-SEIRAS<sup>166</sup>.

To evaluate the efficiency of a flow cell or MEA cell, additional parameters are generally considered for comparison. The FE, overpotential, TOF and TON are still relevant for such cells; however, the energy efficiency (EE) is a better description of the system as a whole. While the cell voltage is theoretically given as the sum of the calculated thermodynamic anodic and cathodic couples, the experimental voltage relies on complex phenomena occurring during the catalysis. The dependency on a dynamic flow of liquids and gases often leads to system evolution throughout the experiment timeframe. The EE corresponds to a measure of the FE referenced to the measured cell voltage and the thermodynamic value of the considered reaction (**Equation 1-12**).

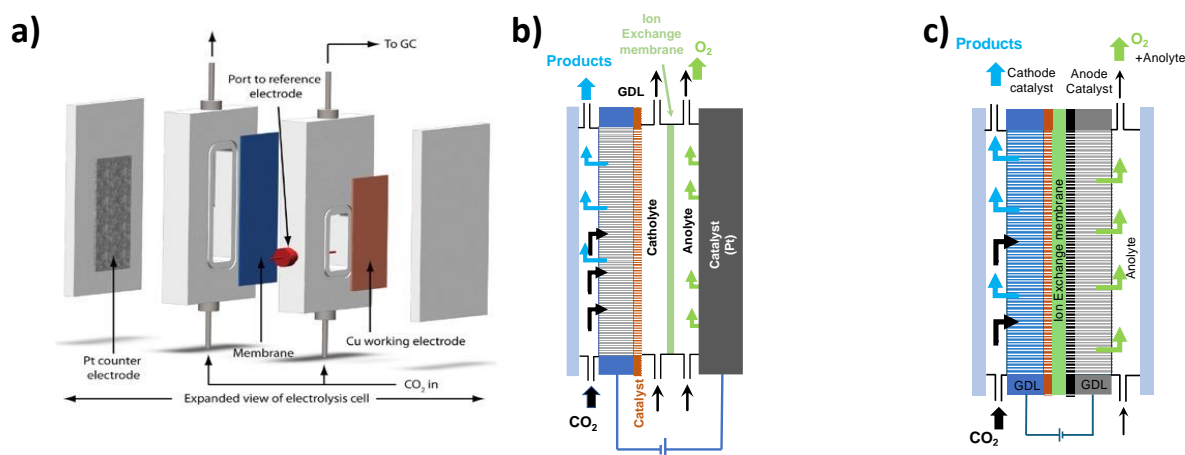


**Figure 1.23** a) H-Cell design with reduced cathode/anode distance.<sup>92</sup>; b) cross section schematic view of a CO<sub>2</sub>RR flow cell; c) cross section schematic view of a CO<sub>2</sub>RR MEA cell

$$EE = \frac{FE_i \times E_i^{0'}}{E_{cell}} \times 100$$

**Equation 1-12**

Where  $FE_i$  is the Faradaic efficiency for product  $i$ ,  $E_i^{0'}$  is the thermodynamic equilibrium potential of the overall reaction that produces  $i$ ,  $E_{cell}$  is the voltage of the cell (potential difference between anode and cathode).

A measure of the amount of reacted CO<sub>2</sub> compared to the total flow is given by the single-pass efficiency (SPE) (**Equation 1-13**). This value measures the process efficiency and accounts for the losses of reagents during the catalysis. These losses are mainly related to CO<sub>2</sub> dissolution (as HCO<sub>3</sub><sup>-</sup> and CO<sub>3</sub><sup>2-</sup>) and CO<sub>2</sub>RR products crossover between compartment.<sup>165</sup>

$$SPE = 100 \times \frac{\text{Consumed } CO_2}{\text{total } CO_2 \text{ injected}} = 100 \times \frac{i \times FE \times t \times V_m}{N \times F \times v_{in}}$$

**Equation 1-13**

Where  $i$  is the current,  $FE$  is the faradaic efficiency for the product,  $V_m$  the molar gas volume (24000 cm<sup>3</sup>.mol<sup>-1</sup>),  $N$  the Avogadro number,  $F$  the faraday constant and  $v_{in}$  the CO<sub>2</sub> gas flow inlet

To circumvent the limitations leading to low EE and SPE a large range of cell designs have been developed, of which the membrane electrode assemblies (MEA) have become the most significant representative. In

this design, the cathode is fed with a flow of humidified CO<sub>2</sub> and it is in direct contact with the ion-exchange membrane, greatly reducing the cathode-anode distance, in turn leading to a reduced cell potential.<sup>78,159,167</sup> When both compartments being fed with a humidified gas flow the overall cell potential is greatly reduced, however at the expense of membrane stability.

### A) GDLs and GDEs

Flow cell systems possess fundamentally different CO<sub>2</sub>RR kinetics than their laboratory scale counterparts due to the high CO<sub>2</sub> concentration at the electrocatalytic interface. The gas diffusion electrodes (GDEs) are fabricated from highly porous hydrophobic Gas Diffusion Layers (GDLs) consisting of either a hydrophobic carbon cloth or a polymeric porous layer of PTFE. Carbon GDLs are often covered with conductive carbon particles on which the active species is deposited, while PTFE GDLs are sputtered with metal layers to enable conductivity while maintaining the intrinsic hydrophobic properties of the polymeric layer. A large variety of carbon-based GDLs are commercially available and are usually formed using carbonized woven carbon fibre, commonly referred to as macroporous surface (MPS). The resulting porous network termed “carbon cloth” offers high conductivity, high gas permeability, and corrosion resistance, however, at the expense of a relatively low mechanical resistance. They are treated with Teflon additives to increase their hydrophobicity and mechanical strength. A top layer consisting of a mixture of carbon black and Teflon forming a microporous layer (MPL) often covers the surface to both increase the electrode hydrophobicity and conductivity. The catalytic material is, in most cases, added to the electrode surface using commonly found techniques such as drop casting<sup>161</sup>, spray-coating<sup>78,163,165</sup>, evaporation<sup>161,163</sup> or sputtering<sup>161,167</sup> (Figure 1.24a).

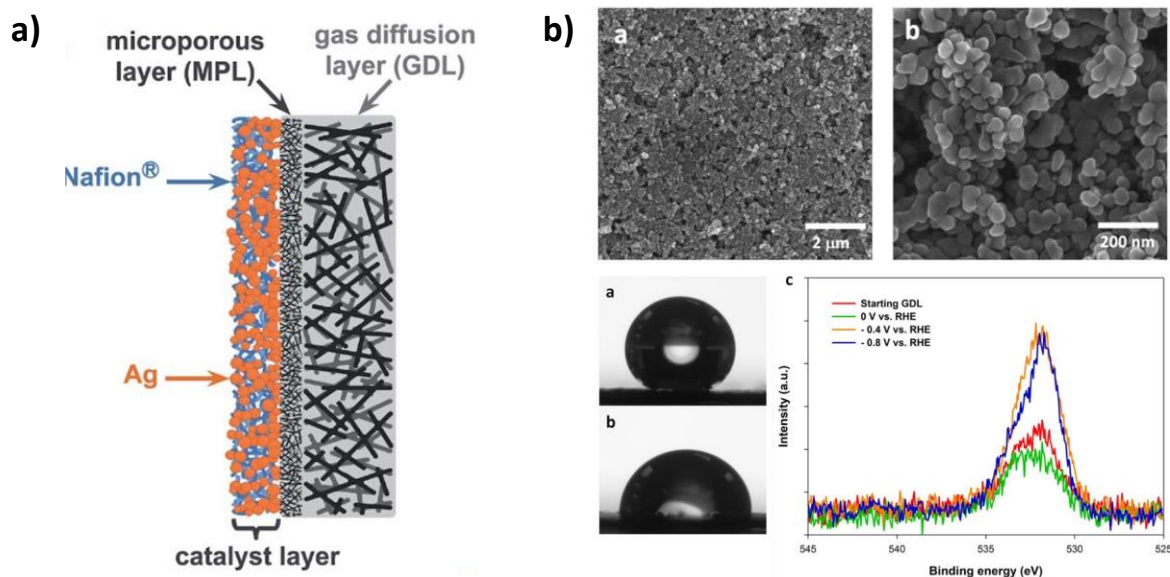


**Figure 1.24** a) Representation of a GDE covered with a silver layer as catalyst<sup>167</sup>; b) SEM images of a carbon gas-diffusion electrode with a deposited copper layer; Contact angle of carbon GDL before electrolysis (145°) b) and after 1h at -0.8 V vs RHE (117°) indicating a loss of hydrophobicity under CO<sub>2</sub>RR conditions XPS spectra at variable show the increase of surface OH and COOH at the surface<sup>161</sup>

The formed gas-diffusion electrodes (GDEs) are usually able to achieve high electrochemical performance compared with bulk materials. However, it is often found that over time, their hydrophobicity decreases significantly. This loss of hydrophobicity leads to the catholyte physically wetting the GDL throughout, with



liquid accumulating inside and up to the back side of the GDE; this effect is commonly referred to as “flooding”. A clear loss of CO<sub>2</sub>RR activity ensues as the path for CO<sub>2</sub> diffusion to the catalytic surface becomes obstructed by the electrolyte. To delay such phenomenon, polymer additives and hydrophobizing agents are used in the ink or suspension of the active species. However, degradation of the activity is still seen over time, and overall cell lifetimes are rarely exceeding 100h in electrolyte-based systems. (**Figure 1.24b**).<sup>161</sup>

Generally, electrode flooding was shown to be independent of CO<sub>2</sub> electrolysis conditions and is actually delayed when CO<sub>2</sub>RR reactions are compared with experiments performed in N<sub>2</sub>.<sup>168</sup> Two mechanisms have been distinguished, both being dependent on the electrolyte salt. In KHCO<sub>3</sub>, the water penetration has been attributed to the electrowetting effects of the exposed carbon nanoparticles from the MPL, reducing the solid-liquid interface surface tension between the electrode and the electrolyte. In KOH, where the applied cell potential is lower, the major flooding source was shown to be the precipitation of KHCO<sub>3</sub> salt, effectively blocking the pores.<sup>169</sup> The electrochemical degradation of carbon-based GDEs sets a fundamental limitation to conductive GDLs. A breakthrough from Sargent and co-workers, published in *Science*, reported the use of a PTFE-based non-conductive GDL. The porous PTFE fibre is electrochemically inert, allowing the CO<sub>2</sub>RR to operate in harsh environments, such as highly alkaline electrolytes. For such GDLs, the catalyst is sputtered on its surface to form a conductive catalyst layer on the PTFE mesh (**Figure 1.25a**). Carbon nanoparticles are then added by spray coating to connect the catalyst and provide uniform current density distribution over the surface. A final layer of graphite is added as the current collector ((**Figure 1.25b**). This strategy was applied for sputtered copper, and an impressive 70% FE towards ethylene was obtained.<sup>161</sup>

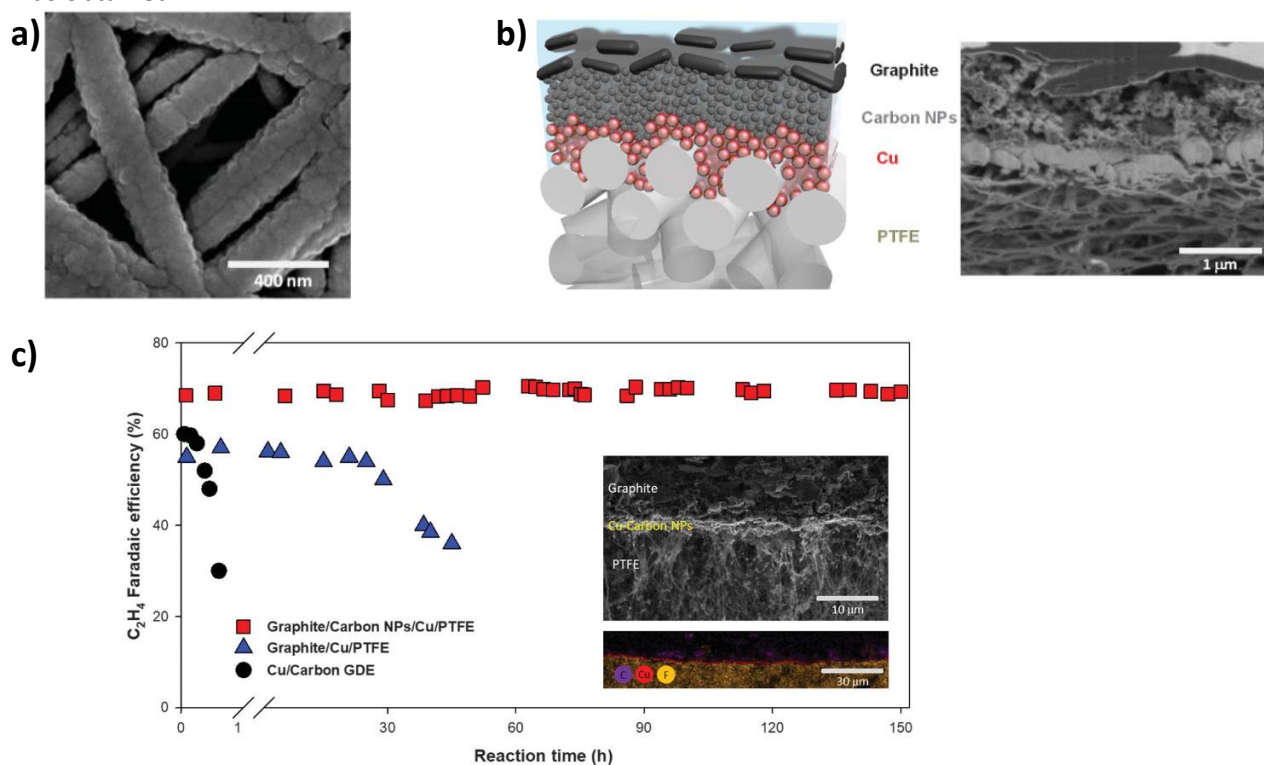


**Figure 1.25.** a) SEM image of Cu nanoparticles sputtered on the PTFE membrane b) Schematic illustration and Cross-sectional SEM image of the graphite/carbon NPs/Cu/PTFE electrode. c) Long-term performance test of CO<sub>2</sub> reduction to ethylene in 7 M KOH compared with carbon GDE.<sup>161</sup>

In this configuration, the hydrophobicity and electrical conductivity specifications of the MPL are decoupled (graphite/carbon nanoparticles/Cu/PTFE electrode). The hydrophobic nature of PTFE protects the GDL from flooding, while the carbon nanoparticles and graphite provide a low resistivity path to the catalyst. This PTFE-based GDE performed for 150 hours in a flow cell configuration without a loss of ethylene selectivity at current densities of 100 mA/cm<sup>2</sup> (**Figure 1.25c**). Conversely, a control experiment carried out on a carbon-based GDL showed a catastrophic drop in selectivity after a few minutes of electrolysis

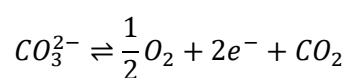
Thus far, the decoupling of gas transport and current transport constitutes the most reliable strategy to prevent flooding. Future work should be oriented towards the development of low overpotential catalysts with high activity since flooding is in direct relation to the applied potential.

## B) Membranes

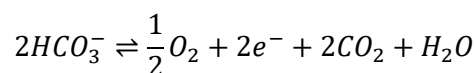
Ion exchange membranes (IEM) are a key constituent of flow cells since they separate the cathode and anode compartments while mediating the necessary ion transfer from one to the other. Historically, flow cell devices were mainly prepared through deposition of the electrocatalyst on IEM electrodes (SPE); however, IEM now exists commercially as three different types: cation exchange (CEM), anion exchange (AEM) and bipolar (BPM).<sup>170</sup> Early work from Hori et al.<sup>171</sup> an electrode consisting of a silver layer deposited on Nafion® (CEM) or Selemion® (AEM).

Cation exchange membranes (CEM) have been used mainly in H-cell setups; they, unfortunately, suffer from a tendency to favour the formation of hydrogen instead of the CO<sub>2</sub> reduction adducts. They generally consist of fluorinated functionalized polymers, including sulfonate, carboxylate and phosphonate groups. The most common CEM is Nafion, a copolymer of poly(tetrafluoroethylene) and polysulfonyl fluoride vinyl ether, which possesses a high proton conductivity (0.2 S/cm) and is stable under reductive and oxidative conditions, making it a perfect candidate for prolonged electrolysis. Nafion® is part of a larger class of ionomer materials including Aquivion® and Fumasep® membranes called PFSA. However, the high associated cost, temperature limitations and the increased concerns regarding their potential toxicity have led to the development of non-fluorinated alternatives.

State-of-the-art flow electrolyzers are fitted with anion exchange membranes (AEM) as they are more suited for the relatively alkaline condition in which CO<sub>2</sub> reduction experiments are generally performed (KOH and KHCO<sub>3</sub>) (**Figure 1.26a**). Ideally, they exchange anions at fast rates from the cathode to the anode. The exchange is performed by hydrophilic cationic groups such as imidazolium and ammonium units, which are incorporated into a polymer backbone. They exhibit better selectivity and efficiency than systems involving cationic membranes with stable CO<sub>2</sub>RR current densities above 0.6 A.cm<sup>-2</sup>. However, due to the AEM permeability for small anionic species, carbonate and bicarbonate ions resulting from the CO<sub>2</sub> dissolution in basic media can be transferred to the anode compartment. CO<sub>2</sub> is then formed at the anode concomitantly with the OER, following **Equation 1-14** and **Equation 1-15**.



**Equation 1-14**



Equation 1-15

This permeability leads to an important loss of reactant from the cathodic compartment and, therefore, significantly reduces EE and SPE due to the parasitic reaction at the anode. It was demonstrated that for a commercial AEM (Fumasep® FAA 30), two out of three CO<sub>2</sub> molecules injected were crossing the membrane towards the anode.<sup>172</sup> To prevent CO<sub>3</sub><sup>2-</sup> crossing, an increase of the current density towards values higher than 1 A.cm<sup>-2</sup> where OH<sup>-</sup> would become the main charge carrier would be needed.<sup>173</sup> A consequence of the highly basic conditions, disfavoring the HER, is the nucleophilic attack potential leading to a degradation of the polymer structure over time.

To circumvent the unwanted crossing of anionic and neutral molecules through AEMs, a new class of IEM has been developed, namely the bipolar membranes (BPM). They are fabricated by laminating a CEM and AEM together and enable the use of different pH at the anode and cathode. They limit anionic (HCO<sub>3</sub><sup>-</sup>/CO<sub>3</sub><sup>2-</sup>, formate, acetate, etc.) and neutral products crossing the membrane through the Donnan exclusion principle (**Figure 1.26b**).<sup>174</sup> They are mainly used in reverse bias mode, i.e., the CEM side being in the cathode compartment. To date, the only commercially available BPM membrane used for CO<sub>2</sub>RR is the Fumasep® FBM, but various BPMs are being used for other electrochemical applications. Their stability is highly dependent on the chemical and physical compatibility of the membranes with the process and several issues have been reported with water accumulation at the membrane interface and decreased mechanical stability over time.<sup>175</sup> Furthermore, the ion transfer rate is dependent on the water dissociation potential at the interface. In this case, the rate of transfer can be increased by a thin interface layer, by increasing the surface area or by using a more suited water dissociation catalyst.

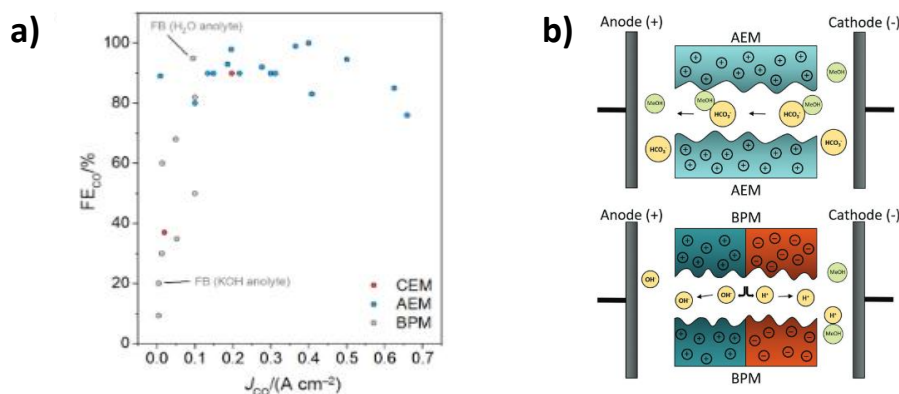


**Figure 1.26 a)** Performance comparison of CO<sub>2</sub>RR flow cells with AEMs (blue), CEMs (red) and BPMs under reverse bias mode (grey, FB= forward bias) for CO production;<sup>170</sup> **b)** Comparison of the ion crossing ability for an AEM (Top) and BPM (Bottom)<sup>174</sup>

A recent study showed that the CO<sub>2</sub>RR could display a high C<sub>2+</sub> yield by adjusting the pH in both compartments using a BPM membrane. The designed setup avoided chemical crossover while maintaining a pH gradient between the two chambers.<sup>165</sup> To prevent losses, a CO<sub>2</sub> recovery system was designed that enabled the recovery and usage of >85% of the injected CO<sub>2</sub> with an almost pure product obtained from the cell outlet. In this case, the use of a bipolar membrane prevents product crossover and the proton stream neutralizes the bicarbonate and carbonate species while keeping a stable pH. The internal



regeneration and recovery of the CO<sub>2</sub> of such a design is a way to avoid expensive and energy-consuming separation procedures.

Overall, the introduction of new commercial membranes is needed in order to prevent issues such as ion crossing and ohmic resistance, which are recurrent causes of flow cell failure. The research focus on BPM for CO<sub>2</sub>RR is very recent, and the technology is the most promising for extended electrolysis time, but issues related to drying membrane interface are still prominent. With research advancement energy efficiencies are expected to be on par with AEM which are the most used systems for high currents CO<sub>2</sub>RR to date.

### THESIS OBJECTIVES

While less than a decade ago, the most prestigious laboratories were reporting mainly CO and formic acid at low current densities (<100 mA.cm<sup>-2</sup>) with non-optimal laboratory-scale cells, the field of CO<sub>2</sub>RR has experienced an impressive leap forward both from a fundamental and technical perspective. As such, high selectivity towards C<sub>2+</sub> at high current density are routinely reported in the literature, with the highest reported selectivity towards ethylene being above 80% at 400 mA.cm<sup>-2</sup>.<sup>96</sup> While cell designs are approaching bulk electrolyser standards, there still remain numerous scientific and engineering challenges before the technology reaches the market. Among others, electrolyte type and concentration, membrane type, MEA or flow cell configuration all have a significant impact on the cell voltage, EE and maximum SPE. From a fundamental perspective, the selectivity of catalysts is rather challenging to rationalise; however, the recent development of *in situ* and *operando* spectroscopies is enabling a finer understanding of the mechanisms occurring during the catalytic events.

Insofar as CO<sub>2</sub> reduction adducts are concerned, ethylene has attracted a lot of attention due to steady market demand. However, the high energetic cost associated with the transformation (12 electrons process) raises concerns on its competitive production *via* the CO<sub>2</sub>RR. Recent progress from academic research have given great hopes for those systems with flourishing partnerships between industry and academic parts. Smaller molecules, such as CO, have a much lower electronic cost (2 electron process) and constitute a very important feedstock for petrochemistry-associated processes. It is, indeed, the starting material for a myriad of essential chemicals such as hydrocarbons, acetic acid, methanol, polycarbonates and isocyanates. The economic value of the production of CO from the CO<sub>2</sub>RR in conjunction with useful anode reactions has been, to my opinion, undervalued in the literature. Therefore, the main objective of this thesis has been the transformation of CO<sub>2</sub> to CO by electrochemical means, both from fundamental and applied perspectives. Due to my background in synthetic chemistry, the focus of my thesis has been centred on the development of novel catalysts to be applied to bulk electrolyser. No particular emphasis was put on the optimization of flow cells or MEA, as it would require dedicated knowledge of applied electrochemistry.

First, inspired by the laboratory expertise in supramolecular chemistry and my early leaning towards the field, I synthesised a macrocyclic host for CO<sub>2</sub>, originally intended for surface functionalisation in the CO<sub>2</sub>RR context. Although the literature has a precedent of hosts designed for the specific encapsulation of gaseous guests, the quantification of the resulting host-guest association constant has been seldom described in the literature, presumably due to technical complexity. In the aim of quantifying the interaction of CO<sub>2</sub> with our macrocyclic hosts in solution an NMR titration method was developed to measure the association constant

of the macrocycle-CO<sub>2</sub> complex in solution (chapter 2). This titration method has no precedent in the literature and constitutes a significant advance in the field. The results were found to be in perfect accordance with a state-of-the-art macrocycle for which an association constant with CO<sub>2</sub> was indirectly measured.<sup>110</sup>

The second and largest part of this thesis is dedicated to the synthesis of silver acetylides clusters and their application to the CO<sub>2</sub>RR under high reaction rates. Building on previous expertise from the laboratory, I revisited the synthesis of silver acetylides using a high-yielding and scalable procedure and applied it to the synthesis of acetylides on a multigram scale. By using an efficient and cost-effective synthesis protocol, we demonstrated that silver acetylides can potentially be applied to the large-scale production of CO<sub>2</sub> electroreduction catalysts. In chapter 3, we, therefore, described the synthesis of a model phenyl acetylide cluster and its full structural characterization. An unprecedented electron diffraction solid-state structure was obtained from a powder sample, confirming the nearly perfect solid-state arrangement throughout the sample. The data, which was complemented by additional characterisation techniques, such as XPS and <sup>1</sup>H-NMR, provided a complete set of structural parameters. Second, a method for depositing a homogeneous layer of silver acetylide catalyst on top of carbon-based GDLs was developed. The resulting GDEs were tested under CO<sub>2</sub>RR conditions in laboratory-scale setups and further optimised in a flow cell electrolyser (designed in our lab) under an electrolysis current higher than 200 mA/cm<sup>2</sup>. A complete mechanistic study was carried out, supported by molecular modelling, demonstrating that the catalytically active species is an Ag(0) atom, formed irreversibly in situ during the catalysis. An FE close to 100% FE for CO could be achieved at industry-relevant rates.

Following these results, a library of different silver acetylides was synthesised from very diverse alkyne precursors (Chapter 4). The reaction was shown to be tolerant to a wide variety of functional groups, and high yields of acetylides were obtained. All the derivatives were comprehensively characterized, and their catalytic properties were assessed in laboratory-scale electrolysis experiments. A broad structure-properties relationship was drawn from the results, pointing to the propensity of certain ligands to suppress the HER efficiently.

Finally, the silver acetylide forming reaction was put to use for the synthesis of hybrid catalysts, in which the cluster serves as a junction between tera-alkyne-functionalized molecular catalysts such as metalated porphyrins. The reaction was shown to be tolerant to such complex molecular structures and provided unique catalysts with complementary features and activity. Their catalytic and structural features were fully characterised (Chapter 5).

## References

- (1) Ritchie, H.; Roser, M. Sector by Sector: Where Do Global Greenhouse Gas Emissions Come From? *Our World Data* **2023**.
- (2) *Climate Change 2022 - Mitigation of Climate Change: Working Group III Contribution to the Sixth Assessment Report of the Intergovernmental Panel on Climate Change*; Intergovernmental Panel on Climate Change (IPCC), Ed.; Cambridge University Press: Cambridge, 2023. <https://doi.org/10.1017/9781009157926>.
- (3) Roser, M. Why Did Renewables Become so Cheap so Fast? *Our World Data* **2023**.
- (4) I.E.A. Final Consumption by Sector and Source. In *OECD, 2018, IEA, Paris* <https://www.iea.org/data-and-statistics/charts/final-consumption-by-sector-and-source-oecd-2018>, IEA; CC BY: Licence; p 4 0.
- (5) Gattrell, M.; Gupta, N.; Co, A. Electrochemical Reduction of CO<sub>2</sub> to Hydrocarbons to Store Renewable Electrical Energy and Upgrade Biogas. *Energy Convers. Manag.* **2007**, *48* (4), 1255–1265. <https://doi.org/10.1016/j.enconman.2006.09.019>.
- (6) Qiao, J.; Liu, Y.; Zhang, J. Electrochemical Reduction of Carbon Dioxide: Fundamentals and Technologies.
- (7) Markewitz, P.; Kuckshinrichs, W.; Leitner, W.; Linssen, J.; Zapp, P.; Bongartz, R.; Schreiber, A.; Müller, T. E. Worldwide Innovations in the Development of Carbon Capture Technologies and the Utilization of CO<sub>2</sub>. *Energy Environ. Sci.* **2012**, *5* (6), 7281. <https://doi.org/10.1039/c2ee03403d>.
- (8) Sabatier, P. *Catalysis in Organic Chemistry*; D. Van Nostrand Company, 1922.
- (9) Vogt, C.; Monai, M.; Kramer, G. J.; Weckhuysen, B. M. The Renaissance of the Sabatier Reaction and Its Applications on Earth and in Space. *Nat. Catal.* **2019**, *2* (3), 188–197. <https://doi.org/10.1038/s41929-019-0244-4>.
- (10) I.E.A. Can CO<sub>2</sub>-EOR really provide carbon-negative oil?, IEA, 2019. <https://www.iea.org/commentaries/can-co2-eor-really-provide-carbon-negative-oil>.
- (11) I.E.A. *CCUS Projects Explorer*, IEA; [//www.iea.org/data-and-statistics/data-tools/ccus-projects-explorer](https://www.iea.org/data-and-statistics/data-tools/ccus-projects-explorer): Paris https, 2023.
- (12) Uchida, T. Physical Property Measurements on CO<sub>2</sub> Clathrate Hydrates. Review of Crystallography, Hydration Number, and Mechanical Properties. *Waste Manag.* **1998**, *17* (5–6), 343–352. [https://doi.org/10.1016/S0956-053X\(97\)10047-2](https://doi.org/10.1016/S0956-053X(97)10047-2).
- (13) Hester, K. C.; Brewer, P. G. Clathrate Hydrates in Nature. *Annu. Rev. Mar. Sci.* **2009**, *1* (1), 303–327. <https://doi.org/10.1146/annurev.marine.010908.163824>.
- (14) Izquierdo-Ruiz, F.; Otero-de-la-Roza, A.; Contreras-García, J.; Prieto-Ballesteros, O.; Recio, J. Effects of the CO<sub>2</sub> Guest Molecule on the SI Clathrate Hydrate Structure. *Materials* **2016**, *9* (9), 777. <https://doi.org/10.3390/ma9090777>.
- (15) Keith, D. W.; Holmes, G.; St. Angelo, D.; Heidel, K. A Process for Capturing CO<sub>2</sub> from the Atmosphere. *Joule* **2018**, *2* (8), 1635. <https://doi.org/10.1016/j.joule.2018.06.010>.

- (16) Fujita, E. Photochemical Carbon Dioxide Reduction with Metal Complexes. *Coord. Chem. Rev.* **1999**, 185–186, 373–384. [https://doi.org/10.1016/S0010-8545\(99\)00023-5](https://doi.org/10.1016/S0010-8545(99)00023-5).
- (17) Gurrieri, L.; Fermani, S.; Zaffagnini, M.; Sparla, F.; Trost, P. Calvin–Benson Cycle Regulation Is Getting Complex. *Trends Plant Sci.* **2021**, 26 (9), 898–912. <https://doi.org/10.1016/j.tplants.2021.03.008>.
- (18) Wang, Q.; Kalathil, S.; Pornrungrroj, C.; Sahm, C. D.; Reisner, E. Bacteria–Photocatalyst Sheet for Sustainable Carbon Dioxide Utilization. *Nat. Catal.* **2022**, 5 (7), 633–641. <https://doi.org/10.1038/s41929-022-00817-z>.
- (19) Razzak, S. A.; Hossain, M. M.; Lucky, R. A.; Bassi, A. S.; de Lasa, H. Integrated CO<sub>2</sub> Capture, Wastewater Treatment and Biofuel Production by Microalgae Culturing—A Review. *Renew. Sustain. Energy Rev.* **2013**, 27, 622–653. <https://doi.org/10.1016/j.rser.2013.05.063>.
- (20) Farrelly, D. J.; Everard, C. D.; Fagan, C. C.; McDonnell, K. P. Carbon Sequestration and the Role of Biological Carbon Mitigation: A Review. *Renew. Sustain. Energy Rev.* **2013**, 21, 712–727. <https://doi.org/10.1016/j.rser.2012.12.038>.
- (21) Singh, J.; Dhar, D. W. Overview of Carbon Capture Technology: Microalgal Biorefinery Concept and State-of-the-Art. *Front. Mar. Sci.* **2019**, 6, 29. <https://doi.org/10.3389/fmars.2019.00029>.
- (22) Liu, C.; Colón, B. C.; Ziesack, M.; Silver, P. A.; Nocera, D. G. Water Splitting–Biosynthetic System with CO<sub>2</sub> Reduction Efficiencies Exceeding Photosynthesis. *Science* **2016**, 352 (6290), 1210–1213. <https://doi.org/10.1126/science.aaf5039>.
- (23) Ishida, H.; Terada, T.; Tanaka, K.; Tanaka, T. Photochemical CO<sub>2</sub> Reduction Catalyzed by [Ru(Bpy)<sub>2</sub>(CO)<sub>2</sub>]<sub>2</sub>+Using Triethanolamine and 1-Benzyl-1,4-Dihydropyridinamide as an Electron Donor.
- (24) Bonin, J.; Robert, M.; Routier, M. Selective and Efficient Photocatalytic CO<sub>2</sub> Reduction to CO Using Visible Light and an Iron-Based Homogeneous Catalyst. *J. Am. Chem. Soc.* **2014**, 136 (48), 16768–16771. <https://doi.org/10.1021/ja510290t>.
- (25) Rosas-Hernández, A.; Alsabeh, P. G.; Barsch, E.; Junge, H.; Ludwig, R.; Beller, M. Highly Active and Selective Photochemical Reduction of CO<sub>2</sub> to CO Using Molecular-Defined Cyclopentadienone Iron Complexes. *Chem. Commun.* **2016**, 52 (54), 8393–8396. <https://doi.org/10.1039/C6CC01671E>.
- (26) Takeda, H.; Ohashi, K.; Sekine, A.; Ishitani, O. Photocatalytic CO<sub>2</sub> Reduction Using Cu(I) Photosensitizers with a Fe(II) Catalyst. *J. Am. Chem. Soc.* **2016**, 138 (13), 4354–4357. <https://doi.org/10.1021/jacs.6b01970>.
- (27) Alsabeh, P. G.; Rosas-Hernández, A.; Barsch, E.; Junge, H.; Ludwig, R.; Beller, M. Iron-Catalyzed Photoreduction of Carbon Dioxide to Synthesis Gas. *Catal. Sci. Technol.* **2016**, 6 (10), 3623–3630. <https://doi.org/10.1039/C5CY01129A>.
- (28) Guo, Z.; Cheng, S.; Cometto, C.; Anxolabéhère-Mallart, E.; Ng, S.-M.; Ko, C.-C.; Liu, G.; Chen, L.; Robert, M.; Lau, T.-C. Highly Efficient and Selective Photocatalytic CO<sub>2</sub> Reduction by Iron and Cobalt Quaterpyridine Complexes. *J. Am. Chem. Soc.* **2016**, 138 (30), 9413–9416. <https://doi.org/10.1021/jacs.6b06002>.

- (29) Ouyang, T.; Hou, C.; Wang, J.-W.; Liu, W.-J.; Zhong, D.-C.; Ke, Z.-F.; Lu, T.-B. A Highly Selective and Robust Co(II)-Based Homogeneous Catalyst for Reduction of CO<sub>2</sub> to CO in CH<sub>3</sub>CN/H<sub>2</sub>O Solution Driven by Visible Light. *Inorg. Chem.* **2017**, *56* (13), 7307–7311. <https://doi.org/10.1021/acs.inorgchem.7b00566>.
- (30) Gracia, L.; Barani, E.; Braun, J.; Carter, A. B.; Fuhr, O.; Powell, A. K.; Fink, K.; Bizzarri, C. Photocatalytic Reduction of CO<sub>2</sub> by Highly Efficient Homogeneous Fe<sup>II</sup> Catalyst Based on 2,6-Bis(1',2',3'-triazolylmethyl)Pyridine. Comparison with Analogues. *ChemCatChem* **2022**, *14* (23), e202201163. <https://doi.org/10.1002/cctc.202201163>.
- (31) Rao, H.; Bonin, J.; Robert, M. Visible-Light Homogeneous Photocatalytic Conversion of CO<sub>2</sub> into CO in Aqueous Solutions with an Iron Catalyst. *ChemSusChem* **2017**, *10* (22), 4447–4450. <https://doi.org/10.1002/cssc.201701467>.
- (32) Bockris, J. O.; Wass, J. C. On the Photoelectrocatalytic Reduction of Carbon Dioxide. *Mater. Chem. Phys.* **1989**, *22* (3–4), 249–280. [https://doi.org/10.1016/0254-0584\(89\)90001-1](https://doi.org/10.1016/0254-0584(89)90001-1).
- (33) Bradley, M. G.; Tysak, T. P-Type Silicon Based Photoelectrochemical Cells for Optical Energy Conversion: Electrochemistry of Tetra-Azomacrocyclic Metal Complexes at Illuminated. *J. Electroanal. Chem. Interfacial Electrochem.* **1982**, *135* (1), 153–157. [https://doi.org/10.1016/0022-0728\(82\)90012-2](https://doi.org/10.1016/0022-0728(82)90012-2).
- (34) Beley, M.; Collin, J.-P.; Ruppert, R.; Sauvage, J.-P. Nickel(II)-Cyclam: An Extremely Selective Electrocatalyst for Reduction of CO<sub>2</sub> in Water. *J. Chem. Soc. Chem. Commun.* **1984**, No. 19, 1315. <https://doi.org/10.1039/c39840001315>.
- (35) Bradley, M. G. Electrocatalytic Reduction of Carbon Dioxide at Illuminated P-Type Silicon Semiconducting Electrodes. *J. Chem. Soc., Chem. Commun* **1983**, 349–350. <https://doi.org/10.1039/C39830000349>.
- (36) Cabrera, C. R.; Abruña, H. D. Electrocatalysis of CO<sub>2</sub> Reduction at Surface Modified Metallic and Semiconducting Electrodes. *J. Electroanal. Chem. Interfacial Electrochem.* **1986**, *209* (1), 101–107. [https://doi.org/10.1016/0022-0728\(86\)80189-9](https://doi.org/10.1016/0022-0728(86)80189-9).
- (37) Leung, J. J.; Vigil, J. A.; Warnan, J.; Edwardes Moore, E.; Reisner, E. Rational Design of Polymers for Selective CO<sub>2</sub> Reduction Catalysis. *Angew. Chem. Int. Ed.* **2019**, *58* (23), 7697–7701. <https://doi.org/10.1002/anie.201902218>.
- (38) Arai, T.; Sato, S.; Uemura, K.; Morikawa, T.; Kajino, T.; Motohiro, T. Photoelectrochemical Reduction of CO<sub>2</sub> in Water under Visible-Light Irradiation by a p-Type InP Photocathode Modified with an Electropolymerized Ruthenium Complex. *Chem Commun* **2010**, *46* (37), 6944–6946. <https://doi.org/10.1039/C0CC02061C>.
- (39) Sato, S.; Morikawa, T.; Saeki, S.; Kajino, T.; Motohiro, T. Visible-Light-Induced Selective CO<sub>2</sub> Reduction Utilizing a Ruthenium Complex Electrocatalyst Linked to a p-Type Nitrogen-Doped Ta<sub>2</sub>O<sub>5</sub> Semiconductor. *Angew. Chem. Int. Ed.* **2010**, *49* (30), 5101–5105. <https://doi.org/10.1002/anie.201000613>.
- (40) Leung, J. J.; Warnan, J.; Ly, K. H.; Heidary, N.; Nam, D. H.; Kuehnel, M. F.; Reisner, E. Solar-Driven Reduction of Aqueous CO<sub>2</sub> with a Cobalt Bis(Terpyridine)-Based Photocathode. *Nat. Catal.* **2019**, *2* (4), 354–365. <https://doi.org/10.1038/s41929-019-0254-2>.

- (41) Neri, G.; Forster, M.; Walsh, J. J.; Robertson, C. M.; Whittles, T. J.; Farràs, P.; Cowan, A. J. Photochemical CO<sub>2</sub> Reduction in Water Using a Co-Immobilised Nickel Catalyst and a Visible Light Sensitiser. *Chem Commun* **2016**, 52 (99), 14200–14203. <https://doi.org/10.1039/C6CC08590C>.
- (42) Zhang, L.; Cole, J. M. Anchoring Groups for Dye-Sensitized Solar Cells. *ACS Appl. Mater. Interfaces* **2015**, 7 (6), 3427–3455. <https://doi.org/10.1021/am507334m>.
- (43) Garcia Osorio, D. A.; Neri, G.; Cowan, A. J. Hybrid Photocathodes for Carbon Dioxide Reduction: Interfaces for Charge Separation and Selective Catalysis. *ChemPhotoChem* **2021**, 5 (7), 595–610. <https://doi.org/10.1002/cptc.202000309>.
- (44) Andrei, V.; Reuillard, B.; Reisner, E. Bias-Free Solar Syngas Production by Integrating a Molecular Cobalt Catalyst with Perovskite–BiVO<sub>4</sub> Tandems. *Nat. Mater.* **2020**, 19 (2), 189–194. <https://doi.org/10.1038/s41563-019-0501-6>.
- (45) Andrei, V.; Ucoski, G. M.; Pornrunroj, C.; Uswachoke, C.; Wang, Q.; Achilleos, D. S.; Kasap, H.; Sokol, K. P.; Jagt, R. A.; Lu, H.; Lawson, T.; Wagner, A.; Pike, S. D.; Wright, D. S.; Hoyer, R. L. Z.; MacManus-Driscoll, J. L.; Joyce, H. J.; Friend, R. H.; Reisner, E. Floating Perovskite–BiVO<sub>4</sub> Devices for Scalable Solar Fuel Production. *Nature* **2022**, 608 (7923), 518–522. <https://doi.org/10.1038/s41586-022-04978-6>.
- (46) Rahaman, M.; Andrei, V.; Wright, D.; Lam, E.; Pornrunroj, C.; Bhattacharjee, S.; Pichler, C. M.; Greer, H. F.; Baumberg, J. J.; Reisner, E. Solar-Driven Liquid Multi-Carbon Fuel Production Using a Standalone Perovskite–BiVO<sub>4</sub> Artificial Leaf. *Nat. Energy* **2023**, 8 (6), 629–638. <https://doi.org/10.1038/s41560-023-01262-3>.
- (47) I.E.A. *Oil 2018, IEA*; CC BY: Paris <https://www.iea.org/reports/oil-2018>, License, 2018.
- (48) I.R.E.N.A.; Bluerisk. *Water for hydrogen production, International Renewable Energy Agency*; Abu Dhabi, United Arab Emirates: Bluerisk, 2023.
- (49) De Luna, P.; Hahn, C.; Higgins, D.; Jaffer, S. A.; Jaramillo, T. F.; Sargent, E. H. What Would It Take for Renewably Powered Electrosynthesis to Displace Petrochemical Processes? *Science* **2019**, 364 (6438), eaav3506. <https://doi.org/10.1126/science.aav3506>.
- (50) Montoya, J. H.; Seitz, L. C.; Chakthranont, P.; Vojvodic, A.; Jaramillo, T. F.; Nørskov, J. K. Materials for Solar Fuels and Chemicals. *Nat. Mater.* **2017**, 16 (1), 70–81. <https://doi.org/10.1038/nmat4778>.
- (51) Seh, Z. W.; Kibsgaard, J.; Dickens, C. F.; Chorkendorff, I.; Nørskov, J. K.; Jaramillo, T. F. Combining Theory and Experiment in Electrocatalysis: Insights into Materials Design. *Science* **2017**, 355 (6321), eaad4998. <https://doi.org/10.1126/science.aad4998>.
- (52) Bewick, A.; Greener, G. P. The Electroreduction of CO<sub>2</sub> to Malate on a Mercury Cathode. *Tetrahedron Lett.* **1969**, 10 (53), 4623–4626. [https://doi.org/10.1016/S0040-4039\(01\)88766-9](https://doi.org/10.1016/S0040-4039(01)88766-9).
- (53) Bewick, A.; Greener, G. P. The Electroreduction of CO<sub>2</sub> to Glycolate on a Lead Cathode. *Tetrahedron Lett.* **1970**, 11 (5), 391–394. [https://doi.org/10.1016/0040-4039\(70\)80093-4](https://doi.org/10.1016/0040-4039(70)80093-4).

- (54) Paik, W.; Andersen, T. N.; Eyring, H. Kinetic Studies of the Electrolytic Reduction of Carbon Dioxide on the Mercury Electrode. *Electrochimica Acta* **1969**, *14* (12), 1217–1232. [https://doi.org/10.1016/0013-4686\(69\)87019-2](https://doi.org/10.1016/0013-4686(69)87019-2).
- (55) Ryu, J.; Andersen, T. N.; Eyring, H. Electrode Reduction Kinetics of Carbon Dioxide in Aqueous Solution. *J. Phys. Chem.* **1972**, *76* (22), 3278–3286. <https://doi.org/10.1021/j100666a029>.
- (56) Hori, Y.; Suzuki, S. Electrolytic Reduction of Carbon Dioxide at Mercury Electrode in Aqueous Solution. *Bull. Chem. Soc. Jpn.* **1982**, *55* (3), 660–665. <https://doi.org/10.1246/bcsj.55.660>.
- (57) Meshitsuka, S.; Ichikawa, M.; Tamaru, K. Electrocatalysis by Metal Phthalocyanines in the Reduction of Carbon Dioxide. *J. Chem. Soc. Chem. Commun.* **1974**, No. 5, 158. <https://doi.org/10.1039/c39740000158>.
- (58) Grosse, P.; Gao, D.; Scholten, F.; Sinev, I.; Mistry, H.; Roldan Cuenya, B. Dynamic Changes in the Structure, Chemical State and Catalytic Selectivity of Cu Nanocubes during CO<sub>2</sub> Electroreduction: Size and Support Effects. *Angew. Chem. Int. Ed.* **2018**, *57* (21), 6192–6197. <https://doi.org/10.1002/anie.201802083>.
- (59) Timoshenko, J.; Roldan Cuenya, B. *In Situ / Operando* Electrocatalyst Characterization by X-Ray Absorption Spectroscopy. *Chem. Rev.* **2021**, *121* (2), 882–961. <https://doi.org/10.1021/acs.chemrev.0c00396>.
- (60) Farmand, M.; Landers, A. T.; Lin, J. C.; Feaster, J. T.; Beeman, J. W.; Ye, Y.; Clark, E. L.; Higgins, D.; Yano, J.; Davis, R. C.; Mehta, A.; Jaramillo, T. F.; Hahn, C.; Drisdell, W. S. Electrochemical Flow Cell Enabling Operando Probing of Electrocatalyst Surfaces by X-Ray Spectroscopy and Diffraction. *Phys Chem Chem Phys* **2019**, *21* (10), 5402–5408. <https://doi.org/10.1039/C8CP07423B>.
- (61) Ma, G.; Qin, L.; Liu, Y.; Fan, H.; Qiao, L.; Yu, C.; Tang, Z. A Review of CO<sub>2</sub> Reduction Reaction Catalyzed by Atomical-Level Ag Nanomaterials: Atom-Precise Nanoclusters and Atomically Dispersed Catalysts. *Surf. Interfaces* **2023**, *36*, 102555. <https://doi.org/10.1016/j.surfin.2022.102555>.
- (62) Wang, M.; Nikolaou, V.; Loiudice, A.; Sharp, I. D.; Llobet, A.; Buonsanti, R. Tandem Electrocatalytic CO<sub>2</sub> Reduction with Fe-Porphyrins and Cu Nanocubes Enhances Ethylene Production. *Chem. Sci.* **2022**, *13* (43), 12673–12680. <https://doi.org/10.1039/D2SC04794B>.
- (63) Boutin, E.; Robert, M. Molecular Electrochemical Reduction of CO<sub>2</sub> beyond Two Electrons. *Trends Chem.* **2021**, *3* (5), 359–372. <https://doi.org/10.1016/j.trechm.2021.02.003>.
- (64) Hawecker, J.; Lehn, J.-M.; Ziessel, R. Electrocatalytic Reduction of Carbon Dioxide Mediated by Re(Bipy)(CO)<sub>3</sub>Cl (Bipy = 2,2'-Bipyridine). *J Chem Soc Chem Commun* **1984**, No. 6, 328–330. <https://doi.org/10.1039/C39840000328>.
- (65) Hiratsuka, K.; Takahashi, K.; Sasaki, H.; Toshima, S. Electrocatalysis by Metal Phthalocyanines in the Reduction of Carbon Dioxide. *Chem. Lett.* **1977**.
- (66) Costentin, C.; Drouet, S.; Passard, G.; Robert, M.; Savéant, J.-M. Proton-Coupled Electron Transfer Cleavage of Heavy-Atom Bonds in Electrocatalytic Processes. Cleavage of a C–O Bond in the Catalyzed Electrochemical Reduction of CO<sub>2</sub>. *J. Am. Chem. Soc.* **2013**, *135* (24), 9023–9031. <https://doi.org/10.1021/ja4030148>.

- (67) Beley, Marc.; Collin, J. Paul.; Ruppert, Romain.; Sauvage, J. Pierre. Electrocatalytic Reduction of Carbon Dioxide by Nickel Cyclam<sup>2+</sup> in Water: Study of the Factors Affecting the Efficiency and the Selectivity of the Process. *J. Am. Chem. Soc.* **1986**, *108* (24), 7461–7467. <https://doi.org/10.1021/ja00284a003>.
- (68) Bhugun, I.; Lexa, D.; Savéant, J.-M. Catalysis of the Electrochemical Reduction of Carbon Dioxide by Iron(0) Porphyrins. Synergistic Effect of Lewis Acid Cations. *J. Phys. Chem.* **1996**, *100* (51), 19981–19985. <https://doi.org/10.1021/jp9618486>.
- (69) Bhugun, I.; Lexa, D.; Saveant, J.-M. Ultraefficient Selective Homogeneous Catalysis of the Electrochemical Reduction of Carbon Dioxide by an Iron(0) Porphyrin Associated with a Weak Bronsted Acid Cocatalyst. *J. Am. Chem. Soc.* **1994**, *116* (11), 5015–5016. <https://doi.org/10.1021/ja00090a068>.
- (70) Costentin, C.; Drouet, S.; Robert, M.; Savéant, J.-M. A Local Proton Source Enhances CO<sub>2</sub> Electroreduction to CO by a Molecular Fe Catalyst. *Science* **2012**, *338* (6103), 90–94. <https://doi.org/10.1126/science.1224581>.
- (71) Azcarate, I.; Costentin, C.; Robert, M.; Savéant, J.-M. Through-Space Charge Interaction Substituent Effects in Molecular Catalysis Leading to the Design of the Most Efficient Catalyst of CO<sub>2</sub>-to-CO Electrochemical Conversion. *J. Am. Chem. Soc.* **2016**, *138* (51), 16639–16644. <https://doi.org/10.1021/jacs.6b07014>.
- (72) Yao, S. A.; Ruther, R. E.; Zhang, L.; Franking, R. A.; Hamers, R. J.; Berry, J. F. Covalent Attachment of Catalyst Molecules to Conductive Diamond: CO<sub>2</sub> Reduction Using “Smart” Electrodes. *J. Am. Chem. Soc.* **2012**, *134* (38), 15632–15635. <https://doi.org/10.1021/ja304783j>.
- (73) Maurin, A.; Robert, M. Catalytic CO<sub>2</sub>-to-CO Conversion in Water by Covalently Functionalized Carbon Nanotubes with a Molecular Iron Catalyst. *Chem. Commun.* **2016**, *52* (81), 12084–12087. <https://doi.org/10.1039/C6CC05430G>.
- (74) Blakemore, J. D.; Gupta, A.; Warren, J. J.; Brunschwig, B. S.; Gray, H. B. Noncovalent Immobilization of Electrocatalysts on Carbon Electrodes for Fuel Production. *J. Am. Chem. Soc.* **2013**, *135* (49), 18288–18291. <https://doi.org/10.1021/ja4099609>.
- (75) Pugliese, S.; Huan, N. T.; Solé-Daura, A.; Li, Y.; Rivera de la Cruz, J.-G.; Forte, J.; Zanna, S.; Krief, A.; Su, B.-L.; Fontecave, M. CO<sub>2</sub> Electroreduction in Water with a Heterogenized C-Substituted Nickel Cyclam Catalyst. *Inorg. Chem.* **2022**, *61* (40), 15841–15852. <https://doi.org/10.1021/acs.inorgchem.2c01645>.
- (76) Maurin, A.; Robert, M. Noncovalent Immobilization of a Molecular Iron-Based Electrocatalyst on Carbon Electrodes for Selective, Efficient CO<sub>2</sub>-to-CO Conversion in Water. *J. Am. Chem. Soc.* **2016**, *138* (8), 2492–2495. <https://doi.org/10.1021/jacs.5b12652>.
- (77) Wang, M.; Torbensen, K.; Salvatore, D.; Ren, S.; Joulié, D.; Dumoulin, F.; Mendoza, D.; Lassalle-Kaiser, B.; Işci, U.; Berlinguette, C. P.; Robert, M. CO<sub>2</sub> Electrochemical Catalytic Reduction with a Highly Active Cobalt Phthalocyanine. *Nat. Commun.* **2019**, *10* (1), 3602. <https://doi.org/10.1038/s41467-019-11542-w>.



- (78) Ren, S.; Joulié, D.; Salvatore, D.; Torbensen, K.; Wang, M.; Robert, M.; Berlinguette, C. P. Molecular Electrocatalysts Can Mediate Fast, Selective CO<sub>2</sub> Reduction in a Flow Cell. *Science* **2019**, *365* (6451), 367–369. <https://doi.org/10.1126/science.aax4608>.
- (79) Grammatico, D.; Tran, H. N.; Li, Y.; Pugliese, S.; Billon, L.; Su, B.; Fontecave, M. Immobilization of a Molecular Re Complex on MOF-derived Hierarchical Porous Carbon for CO<sub>2</sub> Electroreduction in Water/Ionic Liquid Electrolyte. *ChemSusChem* **2020**, *13* (23), 6418–6425. <https://doi.org/10.1002/cssc.202002014>.
- (80) Ryu, U. J.; Kim, S. J.; Lim, H.-K.; Kim, H.; Choi, K. M.; Kang, J. K. Synergistic Interaction of Re Complex and Amine Functionalized Multiple Ligands in Metal-Organic Frameworks for Conversion of Carbon Dioxide. *Sci. Rep.* **2017**, *7* (1), 612. <https://doi.org/10.1038/s41598-017-00574-1>.
- (81) Liu, H.; Chu, J.; Yin, Z.; Cai, X.; Zhuang, L.; Deng, H. Covalent Organic Frameworks Linked by Amine Bonding for Concerted Electrochemical Reduction of CO<sub>2</sub>. *Chem* **2018**, *4* (7), 1696–1709. <https://doi.org/10.1016/j.chempr.2018.05.003>.
- (82) Lin, S.; Diercks, C. S.; Zhang, Y.-B.; Kornienko, N.; Nichols, E. M.; Zhao, Y.; Paris, A. R.; Kim, D.; Yang, P.; Yaghi, O. M.; Chang, C. J. Covalent Organic Frameworks Comprising Cobalt Porphyrins for Catalytic CO<sub>2</sub> Reduction in Water. *Science* **2015**, *349* (6253), 1208–1213. <https://doi.org/10.1126/science.aac8343>.
- (83) Neti, V. S. P. K.; Wu, X.; Deng, S.; Echegoyen, L. Selective CO<sub>2</sub> Capture in an Imine Linked Porphyrin Porous Polymer. *Polym. Chem.* **2013**, *4* (17), 4566. <https://doi.org/10.1039/c3py00798g>.
- (84) Kornienko, N.; Zhao, Y.; Kley, C. S.; Zhu, C.; Kim, D.; Lin, S.; Chang, C. J.; Yaghi, O. M.; Yang, P. Metal-Organic Frameworks for Electrocatalytic Reduction of Carbon Dioxide. *J. Am. Chem. Soc.* **2015**, *137* (44), 14129–14135. <https://doi.org/10.1021/jacs.5b08212>.
- (85) Fang, M.; Xu, L.; Zhang, H.; Zhu, Y.; Wong, W.-Y. Metalloporphyrin-Linked Mercurated Graphynes for Ultrastable CO<sub>2</sub> Electroreduction to CO with Nearly 100% Selectivity at a Current Density of 1.2 A Cm<sup>-2</sup>. *J. Am. Chem. Soc.* **2022**, *144* (33), 15143–15154. <https://doi.org/10.1021/jacs.2c05059>.
- (86) Boutin, E.; Merakeb, L.; Ma, B.; Boudy, B.; Wang, M.; Bonin, J.; Anxolabéhère-Mallart, E.; Robert, M. Molecular Catalysis of CO<sub>2</sub> Reduction: Recent Advances and Perspectives in Electrochemical and Light-Driven Processes with Selected Fe, Ni and Co Aza Macrocyclic and Polypyridine Complexes. *Chem. Soc. Rev.* **2020**, *49* (16), 5772–5809. <https://doi.org/10.1039/D0CS00218F>.
- (87) Hori, Y.; Kikuchi, K.; Suzuki, S. Production of CO and CH<sub>4</sub> in Electrochemical Reduction of CO<sub>2</sub> at Metal Electrodes in Aqueous Hydrogencarbonate Solution. *Chem. Lett.* **1985**, *14*, 1695–1698.
- (88) Zhang, Y.-J.; Sethuraman, V.; Michalsky, R.; Peterson, A. A. Competition between CO<sub>2</sub> Reduction and H<sub>2</sub> Evolution on Transition-Metal Electrocatalysts. *ACS Catal.* **2014**, *4* (10), 3742–3748. <https://doi.org/10.1021/cs5012298>.
- (89) Bagger, A.; Ju, W.; Varela, A. S.; Strasser, P.; Rossmeisl, J. Electrochemical CO<sub>2</sub> Reduction: A Classification Problem. *ChemPhysChem* **2017**, *18* (22), 3266–3273. <https://doi.org/10.1002/cphc.201700736>.

- (90) Liu, X.; Xiao, J.; Peng, H.; Hong, X.; Chan, K.; Nørskov, J. K. Understanding Trends in Electrochemical Carbon Dioxide Reduction Rates. *Nat. Commun.* **2017**, *8* (1), 15438. <https://doi.org/10.1038/ncomms15438>.
- (91) Hori, Y.; Murata, A.; Takahashi, R.; Suzuki, S. Enhanced Formation of Ethylene and Alcohols at Ambient Temperature and Pressure in Electrochemical Reduction of Carbon Dioxide at a Copper Electrode. *J. Chem. Soc. Chem. Commun.* **1988**, No. 1, 17. <https://doi.org/10.1039/c39880000017>.
- (92) Kuhl, K. P.; Cave, E. R.; Abram, D. N.; Jaramillo, T. F. New Insights into the Electrochemical Reduction of Carbon Dioxide on Metallic Copper Surfaces. *Energy Environ. Sci.* **2012**, *5* (5), 7050. <https://doi.org/10.1039/c2ee21234j>.
- (93) Zhao, J.; Xue, S.; Barber, J.; Zhou, Y.; Meng, J.; Ke, X. An Overview of Cu-Based Heterogeneous Electrocatalysts for CO<sub>2</sub> Reduction. *J Mater Chem A* **2020**, *8* (9), 4700–4734. <https://doi.org/10.1039/C9TA11778D>.
- (94) Vasileff, A.; Zhi, X.; Xu, C.; Ge, L.; Jiao, Y.; Zheng, Y.; Qiao, S.-Z. Selectivity Control for Electrochemical CO<sub>2</sub> Reduction by Charge Redistribution on the Surface of Copper Alloys. *ACS Catal.* **2019**, *9* (10), 9411–9417. <https://doi.org/10.1021/acscatal.9b02312>.
- (95) Dickinson, H. L. A.; Symes, M. D. Recent Progress in CO<sub>2</sub> Reduction Using Bimetallic Electrodes Containing Copper. *Electrochem. Commun.* **2022**, *135*, 107212. <https://doi.org/10.1016/j.elecom.2022.107212>.
- (96) Zhong, M.; Tran, K.; Min, Y.; Wang, C.; Wang, Z.; Dinh, C.-T.; De Luna, P.; Yu, Z.; Rasouli, A. S.; Brodersen, P.; Sun, S.; Voznyy, O.; Tan, C.-S.; Askerka, M.; Che, F.; Liu, M.; Seifitokaldani, A.; Pang, Y.; Lo, S.-C.; Ip, A.; Ulissi, Z.; Sargent, E. H. Accelerated Discovery of CO<sub>2</sub> Electrocatalysts Using Active Machine Learning. *Nature* **2020**, *581* (7807), 178–183. <https://doi.org/10.1038/s41586-020-2242-8>.
- (97) Wagner, A.; Sahm, C. D.; Reisner, E. Towards Molecular Understanding of Local Chemical Environment Effects in Electro- and Photocatalytic CO<sub>2</sub> Reduction. *Nat. Catal.* **2020**, *3* (10), 775–786. <https://doi.org/10.1038/s41929-020-00512-x>.
- (98) Jovanov, Z. P.; Hansen, H. A.; Varela, A. S.; Malacrida, P.; Peterson, A. A.; Nørskov, J. K.; Stephens, I. E. L.; Chorkendorff, I. Opportunities and Challenges in the Electrocatalysis of CO<sub>2</sub> and CO Reduction Using Bifunctional Surfaces: A Theoretical and Experimental Study of Au–Cd Alloys. *J. Catal.* **2016**, *343*, 215–231. <https://doi.org/10.1016/j.jcat.2016.04.008>.
- (99) Bohra, D.; Ledezma-Yanez, I.; Li, G.; de Jong, W.; Pidko, E. A.; Smith, W. A. Lateral Adsorbate Interactions Inhibit HCOO<sup>-</sup> While Promoting CO Selectivity for CO<sub>2</sub> Electrocatalysis on Silver. *Angew. Chem. Int. Ed.* **2019**, *58* (5), 1345–1349. <https://doi.org/10.1002/anie.201811667>.
- (100) Resasco, J.; Chen, L. D.; Clark, E.; Tsai, C.; Hahn, C.; Jaramillo, T. F.; Chan, K.; Bell, A. T. Promoter Effects of Alkali Metal Cations on the Electrochemical Reduction of Carbon Dioxide. *J. Am. Chem. Soc.* **2017**, *139* (32), 11277–11287. <https://doi.org/10.1021/jacs.7b06765>.

- (101) Li, J.; Li, X.; Gunathunge, C. M.; Waegele, M. M. Hydrogen Bonding Steers the Product Selectivity of Electrocatalytic CO Reduction. *Proc. Natl. Acad. Sci.* **2019**, *116* (19), 9220–9229. <https://doi.org/10.1073/pnas.1900761116>.
- (102) Varela, A. S.; Ju, W.; Reier, T.; Strasser, P. Tuning the Catalytic Activity and Selectivity of Cu for CO<sub>2</sub> Electroreduction in the Presence of Halides. *ACS Catal.* **2016**, *6* (4), 2136–2144. <https://doi.org/10.1021/acscatal.5b02550>.
- (103) Li, Y.; Cui, F.; Ross, M. B.; Kim, D.; Sun, Y.; Yang, P. Structure-Sensitive CO<sub>2</sub> Electroreduction to Hydrocarbons on Ultrathin 5-Fold Twinned Copper Nanowires. *Nano Lett.* **2017**, *17* (2), 1312–1317. <https://doi.org/10.1021/acs.nanolett.6b05287>.
- (104) De Luna, P.; Quintero-Bermudez, R.; Dinh, C.-T.; Ross, M. B.; Bushuyev, O. S.; Todorović, P.; Regier, T.; Kelley, S. O.; Yang, P.; Sargent, E. H. Catalyst Electro-Redeposition Controls Morphology and Oxidation State for Selective Carbon Dioxide Reduction. *Nat. Catal.* **2018**, *1* (2), 103–110. <https://doi.org/10.1038/s41929-017-0018-9>.
- (105) Tang, W.; Peterson, A. A.; Varela, A. S.; Jovanov, Z. P.; Bech, L.; Durand, W. J.; Dahl, S.; Nørskov, J. K.; Chorkendorff, I. The Importance of Surface Morphology in Controlling the Selectivity of Polycrystalline Copper for CO<sub>2</sub> Electroreduction. *Phys Chem Chem Phys* **2012**, *14* (1), 76–81. <https://doi.org/10.1039/C1CP22700A>.
- (106) Jeon, H. S.; Kunze, S.; Scholten, F.; Roldan Cuenya, B. Prism-Shaped Cu Nanocatalysts for Electrochemical CO<sub>2</sub> Reduction to Ethylene. *ACS Catal.* **2018**, *8* (1), 531–535. <https://doi.org/10.1021/acscatal.7b02959>.
- (107) Reller, C.; Krause, R.; Volkova, E.; Schmid, B.; Neubauer, S.; Rucki, A.; Schuster, M.; Schmid, G. Selective Electroreduction of CO<sub>2</sub> toward Ethylene on Nano Dendritic Copper Catalysts at High Current Density. *Adv. Energy Mater.* **2017**, *7* (12), 1602114. <https://doi.org/10.1002/aenm.201602114>.
- (108) Melnichenko, Y. B.; Lavrik, N. V.; Popov, E.; Bahadur, J.; He, L.; Kravchenko, I. I.; Smith, G.; Pipich, V.; Szekely, N. K. Cavitation on Deterministically Nanostructured Surfaces in Contact with an Aqueous Phase: A Small-Angle Neutron Scattering Study. *Langmuir* **2014**, *30* (33), 9985–9990. <https://doi.org/10.1021/la500963q>.
- (109) Wakerley, D.; Lamaison, S.; Ozanam, F.; Menguy, N.; Mercier, D.; Marcus, P.; Fontecave, M.; Mougél, V. Bio-Inspired Hydrophobicity Promotes CO<sub>2</sub> Reduction on a Cu Surface. *Nat. Mater.* **2019**, *18* (11), 1222–1227. <https://doi.org/10.1038/s41563-019-0445-x>.
- (110) Wagner, A.; Ly, K. H.; Heidary, N.; Szabó, I.; Földes, T.; Assaf, K. I.; Barrow, S. J.; Sokołowski, K.; Al-Hada, M.; Kornienko, N.; Kuehnel, M. F.; Rosta, E.; Zebger, I.; Nau, W. M.; Scherman, O. A.; Reisner, E. Host–Guest Chemistry Meets Electrocatalysis: Cucurbit[6]Urill on a Au Surface as a Hybrid System in CO<sub>2</sub> Reduction. *ACS Catal.* **2020**, *10* (1), 751–761. <https://doi.org/10.1021/acscatal.9b04221>.
- (111) Nichols, E. M.; Derrick, J. S.; Nistanaki, S. K.; Smith, P. T.; Chang, C. J. Positional Effects of Second-Sphere Amide Pendants on Electrochemical CO<sub>2</sub> Reduction Catalyzed by Iron Porphyrins. *Chem. Sci.* **2018**, *9* (11), 2952–2960. <https://doi.org/10.1039/C7SC04682K>.

- (112) Cao, Z.; Zacate, S. B.; Sun, X.; Liu, J.; Hale, E. M.; Carson, W. P.; Tyndall, S. B.; Xu, J.; Liu, X.; Liu, X.; Song, C.; Luo, J.; Cheng, M.; Wen, X.; Liu, W. Tuning Gold Nanoparticles with Chelating Ligands for Highly Efficient Electrocatalytic CO<sub>2</sub> Reduction. *Angew. Chem. Int. Ed.* **2018**, *57* (39), 12675–12679. <https://doi.org/10.1002/anie.201805696>.
- (113) Lau, G. P. S.; Schreier, M.; Vasilyev, D.; Scopelliti, R.; Grätzel, M.; Dyson, P. J. New Insights Into the Role of Imidazolium-Based Promoters for the Electroreduction of CO<sub>2</sub> on a Silver Electrode. *J. Am. Chem. Soc.* **2016**, *138* (25), 7820–7823. <https://doi.org/10.1021/jacs.6b03366>.
- (114) Rosen, B. A.; Salehi-Khojin, A.; Thorson, M. R.; Zhu, W.; Whipple, D. T.; Kenis, P. J. A.; Masel, R. I. Ionic Liquid-Mediated Selective Conversion of CO<sub>2</sub> to CO at Low Overpotentials. *Science* **2011**, *334* (6056), 643–644. <https://doi.org/10.1126/science.1209786>.
- (115) Jeon, Y.-M.; Kim, J.; Whang, D.; Kim, K. Molecular Container Assembly Capable of Controlling Binding and Release of Its Guest Molecules: Reversible Encapsulation of Organic Molecules in Sodium Ion Complexed Cucurbituril. *J. Am. Chem. Soc.* **1996**, *118* (40), 9790–9791. <https://doi.org/10.1021/ja962071x>.
- (116) Giljohann, D. A.; Seferos, D. S.; Daniel, W. L.; Massich, M. D.; Patel, P. C.; Mirkin, C. A. Gold Nanoparticles for Biology and Medicine. *Angew. Chem. Int. Ed.* **2010**, *49* (19), 3280–3294. <https://doi.org/10.1002/anie.200904359>.
- (117) Zhu, W.; Michalsky, R.; Metin, Ö.; Lv, H.; Guo, S.; Wright, C. J.; Sun, X.; Peterson, A. A.; Sun, S. Monodisperse Au Nanoparticles for Selective Electrocatalytic Reduction of CO<sub>2</sub> to CO. *J. Am. Chem. Soc.* **2013**, *135* (45), 16833–16836. <https://doi.org/10.1021/ja409445p>.
- (118) Kim, C.; Jeon, H. S.; Eom, T.; Jee, M. S.; Kim, H.; Friend, C. M.; Min, B. K.; Hwang, Y. J. Achieving Selective and Efficient Electrocatalytic Activity for CO<sub>2</sub> Reduction Using Immobilized Silver Nanoparticles. *J. Am. Chem. Soc.* **2015**, *137* (43), 13844–13850. <https://doi.org/10.1021/jacs.5b06568>.
- (119) Reske, R.; Mistry, H.; Behafarid, F.; Roldan Cuenya, B.; Strasser, P. Particle Size Effects in the Catalytic Electroreduction of CO<sub>2</sub> on Cu Nanoparticles. *J. Am. Chem. Soc.* **2014**, *136* (19), 6978–6986. <https://doi.org/10.1021/ja500328k>.
- (120) Wang, Y.; Shen, H.; Livi, K. J. T.; Raciti, D.; Zong, H.; Gregg, J.; Onadoko, M.; Wan, Y.; Watson, A.; Wang, C. Copper Nanocubes for CO<sub>2</sub> Reduction in Gas Diffusion Electrodes. *Nano Lett.* **2019**, *19* (12), 8461–8468. <https://doi.org/10.1021/acs.nanolett.9b02748>.
- (121) Zhu, W.; Zhang, Y.-J.; Zhang, H.; Lv, H.; Li, Q.; Michalsky, R.; Peterson, A. A.; Sun, S. Active and Selective Conversion of CO<sub>2</sub> to CO on Ultrathin Au Nanowires. *J. Am. Chem. Soc.* **2014**, *136* (46), 16132–16135. <https://doi.org/10.1021/ja5095099>.
- (122) Liu, S.; Tao, H.; Zeng, L.; Liu, Q.; Xu, Z.; Liu, Q.; Luo, J.-L. Shape-Dependent Electrocatalytic Reduction of CO<sub>2</sub> to CO on Triangular Silver Nanoplates. *J. Am. Chem. Soc.* **2017**, *139* (6), 2160–2163. <https://doi.org/10.1021/jacs.6b12103>.
- (123) De Gregorio, G. L.; Burdyny, T.; Loiudice, A.; Iyengar, P.; Smith, W. A.; Buonsanti, R. Facet-Dependent Selectivity of Cu Catalysts in Electrochemical CO<sub>2</sub> Reduction at Commercially Viable Current Densities. *ACS Catal.* **2020**, *10* (9), 4854–4862. <https://doi.org/10.1021/acscatal.0c00297>.

- (124) Ortuño, M. A.; López, N. Reaction Mechanisms at the Homogeneous–Heterogeneous Frontier: Insights from First-Principles Studies on Ligand-Decorated Metal Nanoparticles. *Catal Sci Technol* **2019**, *9* (19), 5173–5185. <https://doi.org/10.1039/C9CY01351B>.
- (125) Franco, F.; Rettenmaier, C.; Jeon, H. S.; Roldan Cuenya, B. Transition Metal-Based Catalysts for the Electrochemical CO<sub>2</sub> Reduction: From Atoms and Molecules to Nanostructured Materials. *Chem. Soc. Rev.* **2020**, *49* (19), 6884–6946. <https://doi.org/10.1039/D0CS00835D>.
- (126) Yuan, S.-F.; He, R.-L.; Han, X.-S.; Wang, J.-Q.; Guan, Z.-J.; Wang, Q.-M. Robust Gold Nanocluster Protected with Amidinates for Electrocatalytic CO<sub>2</sub> Reduction. *Angew. Chem. Int. Ed.* **2021**, *60* (26), 14345–14349. <https://doi.org/10.1002/anie.202103060>.
- (127) Gao, Z.-H.; Wei, K.; Wu, T.; Dong, J.; Jiang, D.; Sun, S.; Wang, L.-S. A Heteroleptic Gold Hydride Nanocluster for Efficient and Selective Electrocatalytic Reduction of CO<sub>2</sub> to CO. *J. Am. Chem. Soc.* **2022**, *144* (12), 5258–5262. <https://doi.org/10.1021/jacs.2c00725>.
- (128) Kulkarni, V. K.; Khiarak, B. N.; Takano, S.; Malola, S.; Albright, E. L.; Levchenko, T. I.; Aloisio, M. D.; Dinh, C.-T.; Tsukuda, T.; Häkkinen, H.; Crudden, C. M. N-Heterocyclic Carbene-Stabilized Hydrido Au<sub>24</sub> Nanoclusters: Synthesis, Structure, and Electrocatalytic Reduction of CO<sub>2</sub>. *J. Am. Chem. Soc.* **2022**, *144* (20), 9000–9006. <https://doi.org/10.1021/jacs.2c00789>.
- (129) Zhuang, S.; Chen, D.; Liao, L.; Zhao, Y.; Xia, N.; Zhang, W.; Wang, C.; Yang, J.; Wu, Z. Hard-Sphere Random Close-Packed Au<sub>47</sub>Cd<sub>2</sub>(TBBT)<sub>31</sub> Nanoclusters with a Faradaic Efficiency of Up to 96 % for Electrocatalytic CO<sub>2</sub> Reduction to CO. *Angew. Chem. Int. Ed.* **2020**, *59* (8), 3073–3077. <https://doi.org/10.1002/anie.201912845>.
- (130) Narouz, M. R.; Osten, K. M.; Unsworth, P. J.; Man, R. W. Y.; Salorinne, K.; Takano, S.; Tomihara, R.; Kaappa, S.; Malola, S.; Dinh, C.-T.; Padmos, J. D.; Ayoo, K.; Garrett, P. J.; Nambo, M.; Horton, J. H.; Sargent, E. H.; Häkkinen, H.; Tsukuda, T.; Crudden, C. M. N-Heterocyclic Carbene-Functionalized Magic-Number Gold Nanoclusters. *Nat. Chem.* **2019**, *11* (5), 419–425. <https://doi.org/10.1038/s41557-019-0246-5>.
- (131) Li, S.; Nagarajan, A. V.; Alfonso, D. R.; Sun, M.; Kauffman, D. R.; Mpourmpakis, G.; Jin, R. Boosting CO<sub>2</sub> Electrochemical Reduction with Atomically Precise Surface Modification on Gold Nanoclusters. *Angew. Chem. Int. Ed.* **2021**, *60* (12), 6351–6356. <https://doi.org/10.1002/anie.202016129>.
- (132) Liu, X.; Wang, E.; Zhou, M.; Wan, Y.; Zhang, Y.; Liu, H.; Zhao, Y.; Li, J.; Gao, Y.; Zhu, Y. Asymmetrically Doping a Platinum Atom into a Au<sub>38</sub> Nanocluster for Changing the Electron Configuration and Reactivity in Electrocatalysis. *Angew. Chem. Int. Ed.* **2022**, *61* (31), e202207685. <https://doi.org/10.1002/anie.202207685>.
- (133) Xu, J.; Xiong, L.; Cai, X.; Tang, S.; Tang, A.; Liu, X.; Pei, Y.; Zhu, Y. Evolution from Superatomic Au<sub>24</sub>Ag<sub>20</sub> Monomers into Molecular-like Au<sub>43</sub>Ag<sub>38</sub> Dimeric Nanoclusters. *Chem Sci* **2022**, *13* (9), 2778–2782. <https://doi.org/10.1039/D1SC07178E>.
- (134) Wan, X.-K.; Wang, J.-Q.; Wang, Q.-M. Ligand-Protected Au<sub>55</sub> with a Novel Structure and Remarkable CO<sub>2</sub> Electroreduction Performance. *Angew. Chem. Int. Ed.* **2021**, *60* (38), 20748–20753. <https://doi.org/10.1002/anie.202108207>.

- (135) Sun, Y.; Liu, X.; Xiao, K.; Zhu, Y.; Chen, M. Active-Site Tailoring of Gold Cluster Catalysts for Electrochemical CO<sub>2</sub> Reduction. *ACS Catal.* **2021**, *11* (18), 11551–11560. <https://doi.org/10.1021/acscatal.1c02193>.
- (136) Lei, Z.; Wan, X.-K.; Yuan, S.-F.; Guan, Z.-J.; Wang, Q.-M. Alkynyl Approach toward the Protection of Metal Nanoclusters. *Acc. Chem. Res.* **2018**, *51* (10), 2465–2474. <https://doi.org/10.1021/acs.accounts.8b00359>.
- (137) Kobayashi, N.; Kamei, Y.; Shichibu, Y.; Konishi, K. Protonation-Induced Chromism of Pyridylethynyl-Appended [Core+ Exo]-Type Au<sub>8</sub> Clusters. Resonance-Coupled Electronic Perturbation through  $\pi$ -Conjugated Group. *J. Am. Chem. Soc.* **2013**, *135* (43), 16078–16081. <https://doi.org/10.1021/ja4099092>.
- (138) Sugiuchi, M.; Shichibu, Y.; Nakanishi, T.; Hasegawa, Y.; Konishi, K. Cluster– $\pi$  Electronic Interaction in a Superatomic Au<sub>13</sub> Cluster Bearing  $\sigma$ -Bonded Acetylide Ligands. *Chem. Commun.* **2015**, *51* (70), 13519–13522. <https://doi.org/10.1039/C5CC04312C>.
- (139) Wan, X.-K.; Wang, J.-Q.; Nan, Z.-A.; Wang, Q.-M. Ligand Effects in Catalysis by Atomically Precise Gold Nanoclusters. *Sci. Adv.* **2017**, *3* (10), e1701823. <https://doi.org/10.1126/sciadv.1701823>.
- (140) Maity, P.; Tsunoyama, H.; Yamauchi, M.; Xie, S.; Tsukuda, T. Organogold Clusters Protected by Phenylacetylene. *J. Am. Chem. Soc.* **2011**, *133* (50), 20123–20125. <https://doi.org/10.1021/ja209236n>.
- (141) Maity, P.; Wakabayashi, T.; Ichikuni, N.; Tsunoyama, H.; Xie, S.; Yamauchi, M.; Tsukuda, T. Selective Synthesis of Organogold Magic Clusters Au<sub>54</sub>(C≡CPh)<sub>26</sub>. *Chem. Commun.* **2012**, *48* (49), 6085. <https://doi.org/10.1039/c2cc18153c>.
- (142) Maity, P.; Takano, S.; Yamazoe, S.; Wakabayashi, T.; Tsukuda, T. Binding Motif of Terminal Alkynes on Gold Clusters. *J. Am. Chem. Soc.* **2013**, *135* (25), 9450–9457. <https://doi.org/10.1021/ja401798z>.
- (143) Glaser, C. Untersuchungen Über Einige Derivate Der Zimmtsäure. *Justus Liebigs Ann. Chem.* **1870**, *154* (2), 137–171. <https://doi.org/10.1002/jlac.18701540202>.
- (144) Vogel, A. I. *A Text-Book of Practical Organic Chemistry: Incl. Qualitative Organic Analysis*, 3. ed.; new impr.; Longmans: London, 1977.
- (145) Létinois-Halbes, U.; Pale, P.; Berger, S. Ag NMR as a Tool for Mechanistic Studies of Ag-Catalyzed Reactions: Evidence for in Situ Formation of Alkyn-1-Yl Silver from Alkynes and Silver Salts. *J. Org. Chem.* **2005**, *70* (23), 9185–9190. <https://doi.org/10.1021/jo0511546>.
- (146) Liu, X.; Yi, Q.; Han, Y.; Liang, Z.; Shen, C.; Zhou, Z.; Sun, J.; Li, Y.; Du, W.; Cao, R. A Robust Microfluidic Device for the Synthesis and Crystal Growth of Organometallic Polymers with Highly Organized Structures. *Angew. Chem. Int. Ed.* **2015**, *54* (6), 1846–1850. <https://doi.org/10.1002/anie.201411008>.
- (147) Létinois-Halbes, U.; Pale, P.; Berger, S. Triphenylphosphane Complex Formation with Hexyn-1-yl Silver. *Magn. Reson. Chem.* **2004**, *42* (9), 831–834. <https://doi.org/10.1002/mrc.1403>.
- (148) Ma, X.; Sun, F.; Qin, L.; Liu, Y.; Kang, X.; Wang, L.; Jiang, D.; Tang, Q.; Tang, Z. Electrochemical CO<sub>2</sub> Reduction Catalyzed by Atomically Precise Alkynyl-Protected Au<sub>7</sub>Ag<sub>8</sub>, Ag<sub>9</sub>Cu<sub>6</sub>, and Au<sub>2</sub>Ag<sub>8</sub>Cu<sub>5</sub>

Nanoclusters: Probing the Effect of Multi-Metal Core on Selectivity. *Chem Sci* **2022**, *13* (34), 10149–10158. <https://doi.org/10.1039/D2SC02886G>.

(149) Qin, L.; Sun, F.; Ma, X.; Ma, G.; Tang, Y.; Wang, L.; Tang, Q.; Jin, R.; Tang, Z. Homoleptic Alkynyl-Protected Ag<sub>15</sub> Nanocluster with Atomic Precision: Structural Analysis and Electrocatalytic Performance toward CO<sub>2</sub> Reduction. *Angew. Chem. Int. Ed.* **2021**, *60* (50), 26136–26141. <https://doi.org/10.1002/anie.202110330>.

(150) Deng, G.; Kim, J.; Bootharaju, M. S.; Sun, F.; Tang, Q.; Hwang, Y. J.; Hyeon, T. Body-Centered-Cubic-Kernelled Ag<sub>15</sub>Cu<sub>6</sub> Nanocluster with Alkynyl Protection: Synthesis, Total Structure, and CO<sub>2</sub> Electroreduction.

(151) Abu-Salah, O. M.; Ja'far, M. H.; Al-Ohaly, A. R.; Al-Farhan, K. A.; Al-Enzi, H. S.; Dolomanov, O. V.; Howard, J. A. K. Synthesis and Structural Characterization of a Halide-Free Rhombohedral Silver-Alkynyl Cage Complex [Ag<sub>14</sub>(C<sub>2</sub>tBu)<sub>12</sub>][BF<sub>4</sub>]<sub>2</sub>. *Eur. J. Inorg. Chem.* **2006**, *2006* (12), 2353–2356. <https://doi.org/10.1002/ejic.200600128>.

(152) Lin, X.; Ma, W.; Sun, K.; Sun, B.; Fu, X.; Ren, X.; Liu, C.; Huang, J. [AuAg<sub>26</sub>(SR)<sub>18</sub>S]– Nanocluster: Open Shell Structure and High Faradaic Efficiency in Electrochemical Reduction of CO<sub>2</sub> to CO. *J. Phys. Chem. Lett.* **2021**, *12* (1), 552–557. <https://doi.org/10.1021/acs.jpcllett.0c03416>.

(153) Chen, L.; Sun, F.; Shen, Q.; Qin, L.; Liu, Y.; Qiao, L.; Tang, Q.; Wang, L.; Tang, Z. Homoleptic Alkynyl-Protected Ag<sub>32</sub> Nanocluster with Atomic Precision: Probing the Ligand Effect toward CO<sub>2</sub> Electroreduction and 4-Nitrophenol Reduction. *Nano Res.* **2022**, *15* (10), 8908–8913. <https://doi.org/10.1007/s12274-022-4812-6>.

(154) Singh, M. R.; Clark, E. L.; Bell, A. T. Effects of Electrolyte, Catalyst, and Membrane Composition and Operating Conditions on the Performance of Solar-Driven Electrochemical Reduction of Carbon Dioxide. *Phys. Chem. Chem. Phys.* **2015**, *17* (29), 18924–18936. <https://doi.org/10.1039/C5CP03283K>.

(155) Qiao, J.; Liu, Y.; Hong, F.; Zhang, J. A Review of Catalysts for the Electroreduction of Carbon Dioxide to Produce Low-Carbon Fuels. *Chem Soc Rev* **2014**, *43* (2), 631–675. <https://doi.org/10.1039/C3CS60323G>.

(156) Li, T.; Cao, Y.; He, J.; Berlinguette, C. P. Electrolytic CO<sub>2</sub> Reduction in Tandem with Oxidative Organic Chemistry. *ACS Cent. Sci.* **2017**, *3* (7), 778–783. <https://doi.org/10.1021/acscentsci.7b00207>.

(157) He, J.; Dettelbach, K. E.; Salvatore, D. A.; Li, T.; Berlinguette, C. P. High-Throughput Synthesis of Mixed-Metal Electrocatalysts for CO<sub>2</sub> Reduction. *Angew. Chem. Int. Ed.* **2017**, *56* (22), 6068–6072. <https://doi.org/10.1002/anie.201612038>.

(158) Verma, S.; Kim, B.; Jhong, H. “Molly”; Ma, S.; Kenis, P. J. A. A Gross-Margin Model for Defining Technoeconomic Benchmarks in the Electroreduction of CO<sub>2</sub>. *ChemSusChem* **2016**, *9* (15), 1972–1979. <https://doi.org/10.1002/cssc.201600394>.

(159) Li, Y. C.; Zhou, D.; Yan, Z.; Gonçalves, R. H.; Salvatore, D. A.; Berlinguette, C. P.; Mallouk, T. E. Electrolysis of CO<sub>2</sub> to Syngas in Bipolar Membrane-Based Electrochemical Cells. *ACS Energy Lett.* **2016**, *1* (6), 1149–1153. <https://doi.org/10.1021/acsenergylett.6b00475>.

- (160) Wang, G.; Pan, J.; Jiang, S. P.; Yang, H. Gas Phase Electrochemical Conversion of Humidified CO<sub>2</sub> to CO and H<sub>2</sub> on Proton-Exchange and Alkaline Anion-Exchange Membrane Fuel Cell Reactors. *J. CO<sub>2</sub> Util.* **2018**, *23*, 152–158. <https://doi.org/10.1016/j.jcou.2017.11.010>.
- (161) Dinh, C.-T.; Burdyny, T.; Kibria, M. G.; Seifitokaldani, A.; Gabardo, C. M.; García De Arquer, F. P.; Kiani, A.; Edwards, J. P.; De Luna, P.; Bushuyev, O. S.; Zou, C.; Quintero-Bermudez, R.; Pang, Y.; Sinton, D.; Sargent, E. H. CO<sub>2</sub> Electroreduction to Ethylene via Hydroxide-Mediated Copper Catalysis at an Abrupt Interface. *Science* **2018**, *360* (6390), 783–787. <https://doi.org/10.1126/science.aas9100>.
- (162) Karapinar, D.; Creissen, C. E.; Rivera De La Cruz, J. G.; Schreiber, M. W.; Fontecave, M. Electrochemical CO<sub>2</sub> Reduction to Ethanol with Copper-Based Catalysts. *ACS Energy Lett.* **2021**, *6* (2), 694–706. <https://doi.org/10.1021/acsenergylett.0c02610>.
- (163) Niu, Z.-Z.; Chi, L.-P.; Liu, R.; Chen, Z.; Gao, M.-R. Rigorous Assessment of CO<sub>2</sub> Electroreduction Products in a Flow Cell. *Energy Environ. Sci.* **2021**, *14* (8), 4169–4176. <https://doi.org/10.1039/D1EE01664D>.
- (164) Liu, W.; Zhai, P.; Li, A.; Wei, B.; Si, K.; Wei, Y.; Wang, X.; Zhu, G.; Chen, Q.; Gu, X.; Zhang, R.; Zhou, W.; Gong, Y. Electrochemical CO<sub>2</sub> Reduction to Ethylene by Ultrathin CuO Nanoplate Arrays. *Nat. Commun.* **2022**, *13* (1), 1877. <https://doi.org/10.1038/s41467-022-29428-9>.
- (165) Perazio, A.; Creissen, C. E.; Rivera De La Cruz, J. G.; Schreiber, M. W.; Fontecave, M. Acidic Electroreduction of CO<sub>2</sub> to Multi-Carbon Products with CO<sub>2</sub> Recovery and Recycling from Carbonate. *ACS Energy Lett.* **2023**, *8* (7), 2979–2985. <https://doi.org/10.1021/acsenergylett.3c00901>.
- (166) Avilés Acosta, J. E.; Lin, J. C.; Un Lee, D.; Jaramillo, T. F.; Hahn, C. Electrochemical Flow Reactor Design Allows Tunable Mass Transport Conditions for Operando Surface Enhanced Infrared Absorption Spectroscopy. *ChemCatChem* **2023**, *15* (15), e202300520. <https://doi.org/10.1002/cctc.202300520>.
- (167) Lees, E. W.; Mowbray, B. A. W.; Salvatore, D. A.; Simpson, G. L.; Dvorak, D. J.; Ren, S.; Chau, J.; Milton, K. L.; Berlinguette, C. P. Linking Gas Diffusion Electrode Composition to CO<sub>2</sub> Reduction in a Flow Cell. *J. Mater. Chem. A* **2020**, *8* (37), 19493–19501. <https://doi.org/10.1039/D0TA03570J>.
- (168) Yang, K.; Kas, R.; Smith, W. A.; Burdyny, T. Role of the Carbon-Based Gas Diffusion Layer on Flooding in a Gas Diffusion Electrode Cell for Electrochemical CO<sub>2</sub> Reduction. *ACS Energy Lett.* **2021**, *6* (1), 33–40. <https://doi.org/10.1021/acsenergylett.0c02184>.
- (169) Leonard, M. E.; Clarke, L. E.; Forner-Cuenca, A.; Brown, S. M.; Brushett, F. R. Investigating Electrode Flooding in a Flowing Electrolyte, Gas-Fed Carbon Dioxide Electrolyzer. *ChemSusChem* **2020**, *13* (2), 400–411. <https://doi.org/10.1002/cssc.201902547>.
- (170) Habibzadeh, F.; Mardle, P.; Zhao, N.; Riley, H. D.; Salvatore, D. A.; Berlinguette, C. P.; Holdcroft, S.; Shi, Z. Ion Exchange Membranes in Electrochemical CO<sub>2</sub> Reduction Processes. *Electrochem. Energy Rev.* **2023**, *6* (1), 26. <https://doi.org/10.1007/s41918-023-00183-9>.
- (171) Hori, Y.; Ito, H.; Okano, K.; Nagasu, K.; Sato, S. Silver-Coated Ion Exchange Membrane Electrode Applied to Electrochemical Reduction of Carbon Dioxide. *Electrochimica Acta* **2003**, *48* (18), 2651–2657. [https://doi.org/10.1016/S0013-4686\(03\)00311-6](https://doi.org/10.1016/S0013-4686(03)00311-6).



(172) Pătru, A.; Binninger, T.; Pribyl, B.; Schmidt, T. J. Design Principles of Bipolar Electrochemical Co-Electrolysis Cells for Efficient Reduction of Carbon Dioxide from Gas Phase at Low Temperature. *J. Electrochem. Soc.* **2019**, *166* (2), F34–F43. <https://doi.org/10.1149/2.1221816jes>.

(173) Weng, L.-C.; Bell, A. T.; Weber, A. Z. Towards Membrane-Electrode Assembly Systems for CO<sub>2</sub> Reduction: A Modeling Study. *Energy Env. Sci* **2019**, *12* (6), 1950–1968. <https://doi.org/10.1039/C9EE00909D>.

(174) Li, Y. C.; Yan, Z.; Hitt, J.; Wycisk, R.; Pintauro, P. N.; Mallouk, T. E. Bipolar Membranes Inhibit Product Crossover in CO<sub>2</sub> Electrolysis Cells. *Adv. Sustain. Syst.* **2018**, *2* (4), 1700187. <https://doi.org/10.1002/adsu.201700187>.

(175) Peng, S.; Xu, X.; Lu, S.; Sui, P.-C.; Djilali, N.; Xiang, Y. A Self-Humidifying Acidic–Alkaline Bipolar Membrane Fuel Cell. *J. Power Sources* **2015**, *299*, 273–279. <https://doi.org/10.1016/j.jpowsour.2015.08.104>.

## Chapter 2: Measuring the association constant of host-gas complexes in solution *via* routine NMR titrations using *ERETIC* quantification: the case of host-CO<sub>2</sub> complexes.

### Introduction

Supramolecular chemistry has had a tremendous impact on the field of organic chemistry since the early discovery of host-guest complexes by Lehn, Cram and Pedersen.<sup>1</sup> Such systems have found applications in biology,<sup>2,3</sup> materials chemistry,<sup>4,5</sup> interlocked molecules,<sup>6-8</sup> and molecular machines,<sup>9,10</sup> to name a few. However, the supramolecular chemistry of gases, *i.e.* the study of host-gas complexes, has been largely overlooked.<sup>11-13</sup> This is rather surprising since some of the essential biological processes sustaining life rely on the interaction of gases with large biomolecules such as haemoglobin.<sup>14</sup> Indeed, the process of aerobic respiration, shared by the plant and animal realms, relies on the transport and reaction of O<sub>2</sub> within complex enzymatic catalytic centres, giving off CO<sub>2</sub> that is selectively transported out of the living organisms. The recent interest in CO<sub>2</sub> capture and CO<sub>2</sub> reduction has sparked interest in the supramolecular chemistry of gases. However, initiatives have remained scarce.<sup>15-18</sup> The likely reason lies in the fact that studying the interaction of gases with organic molecules has a high degree of technical complexity. Indeed, studying the interaction of a host with gaseous guests implies that a sample of gas is dissolved together with its host in a solvent where the study is to be performed. Then, the Host-Guest (HG) interaction, usually weak from a thermodynamic standpoint, is to be assessed by an accessible spectroscopy method (ideally NMR or UV-visible absorption).<sup>19</sup> The kinetics of the HG exchange are generally fast, therefore, a precise quantification of the HG interaction strength, in the form of an association constant, requires performing a titration. The guest, a gas in this case, is added in incremental amounts to a host solution, therefore requiring a precise quantification of the gas concentration in solution.<sup>19</sup> Although some early papers on host-gas complexes report binding constants measured *via* NMR with a fixed amount of gas guest, this was rendered possible only by the fact that the host-gas exchange was particularly slow on the NMR time scale, therefore giving access to a direct [HG]/[H] ratio.<sup>20-29</sup> Such systems are generally limited to gases whose diffusion in and out of the host is slow on the NMR time scale, such as Xenon or SbF<sub>6</sub>. Bartik and co-workers reported an early titration method for <sup>129</sup>Xe and a cucurbituril guest, however, its technical aspects were not reported.<sup>30</sup> More recent examples make use of indirect measurements, where the host is first bound by a chromophore and then displaced by the gas to be studied.<sup>28</sup> Although very elegant, the above methods bear intrinsic limitations, the most important of which is that the fraction of gas present in solution is approximated empirically, generally from Henry's law. The latter, formally an approximation of Raoult's law, is antagonistic to the study of host-guest interactions since it assumes that intermolecular interactions (between gas and solute) are negligible. An error on the experimental binding constant likely ensues. As such, To the best of our knowledge, there is, to date, no universal method for measuring the binding constant of an organic host and common permanent gases.

Therefore, herein, we describe a general method that allows measuring the binding constant of an organic host with any common permanent gas. It relies on a standard HG titration, in which a solution of a fixed host concentration in a deuterated solvent is titrated with incremental amounts of gaseous sample. The accuracy and versatility of the methods rely on the two following principles. First, a proprietary system

allows for the injection of precise amounts of gas (from nmol up to mmol) into the headspace of gas-tight NMR tubes. Second, the fraction of gas dissolved in the liquid sample is accurately quantified via heteroatomic, <sup>1</sup>H or <sup>13</sup>C NMR (depending on the gas to be quantified) using well-established quantification methods. By subsequently recording <sup>1</sup>H NMR spectra of the corresponding samples, a precise link between HG-complexation-induced <sup>1</sup>H chemical shift and a precise guest concentration can be established. Repeating the process in incremental concentrations of gas allows drawing an entire titration curve, which, upon fitting to a binding isotherm equation, provides access to a binding constant in a very similar way to that used for classical HG complexes. The method was proven suitable for measuring binding constants as low as sub-unity and over 1000 so long as the host has sufficient solubility in the solvent to be used for the titration. Furthermore, complementary DFT calculations allowed for establishing the nature of the supramolecular interaction between both macrocyclic hosts and the gas molecule.

## Results and discussion

Our involvement in the design of hosts for CO<sub>2</sub> in the context of CO<sub>2</sub> capture prompted us to develop a method to accurately quantify the interaction of CO<sub>2</sub> with organic hosts. Following from original work of Leigh and co-workers on benzylic amide macrocycles,<sup>31</sup> we set out to quantify the association constant of such type of macrocycle with CO<sub>2</sub> in solution. The host, originally designed to form a set of four hydrogen bonds with the CO<sub>2</sub> carbonyl lone pairs, had not been previously assessed as a host for CO<sub>2</sub> in solution. For comparison purposes, the study was extended to include a cucurbituril host (CB[6]) whose binding constant with CO<sub>2</sub> has been reported to be in the order of 250M<sup>-1</sup> using an indirect measurement method.<sup>16</sup> To perform the study, a soluble tetra-amide macrocycle (**1**) was first synthesized using a recently described route, while CB[6] was purchased from commercial sources (**Figure 2.1**).

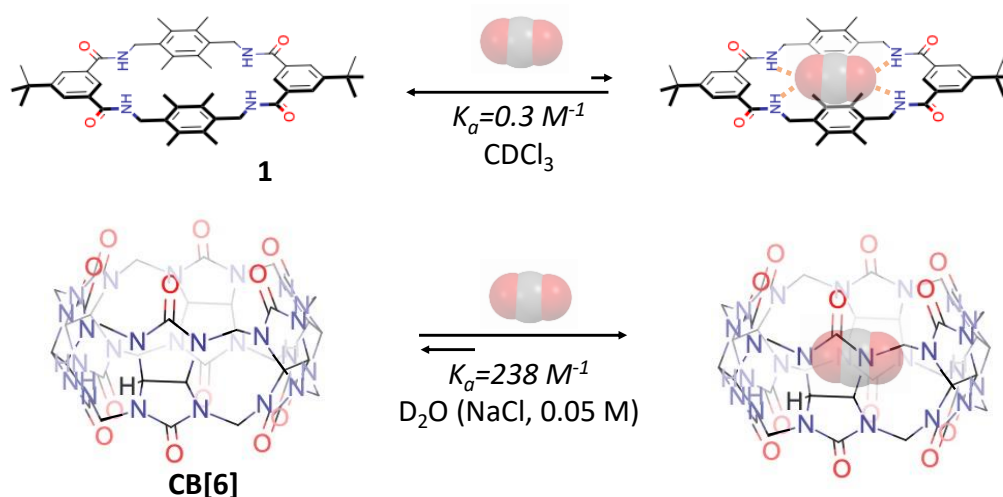


**Figure 2.1** General scheme of host-guest complexes formation, studied herein.

First and foremost, it is essential to note that adding gaseous samples to the headspace of an NMR tube implies that only a fraction, generally small, of the gas dissolves in the liquid phase under equilibrium. Although Henry's constant has been used in previous HG studies to quantify the amount of gas dissolved in solution, this would require a precise measurement of the NMR tube headspace pressure as well as

temperature, a feature generally not implemented. More importantly, the latter constant, essentially the fractional ratio between partial pressure and molar fraction dissolved in the liquid phase, is merely an approximation of Raoult's law in the specific case of highly dilute solutions of volatile compounds in liquids. Indeed, Raoult's Law states that the vapour pressure of a compound above a solution is directly proportional to its mole fraction in that solution (see equation in SI). However, the equation assumes an ideal behaviour of the components in the mixture, that is, all crossed-intermolecular interactions between the gas and liquid are negligible. This rarely occurs in practice since molecules of either solvent or gas likely interact with one another, having a consequential effect on the vapour pressure. This is particularly the case for host-gas complexes in solution since, indeed, a significant interaction between the host and the gas is to be expected. Therefore, a direct NMR quantification of the gas dissolved in the liquid phase, simultaneous to the HG titration, is of capital importance. For that matter, the method developed herein relies on quantifying the mole fraction of CO<sub>2</sub> dissolved in the titration solution *via* <sup>13</sup>C NMR. **Figure 2.2** shows a general scheme of the titration methodology.

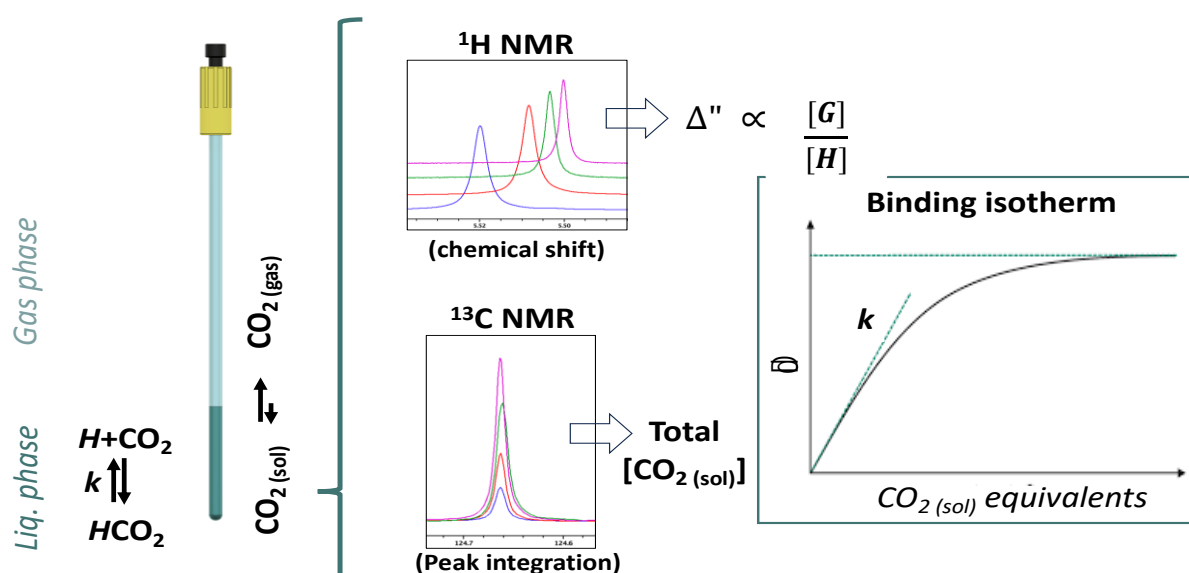


**Figure 2.2.** General scheme of the titration methodology showing the equilibrium between dissolved CO<sub>2</sub> (CO<sub>2</sub> (sol)) and gaseous CO<sub>2</sub> (CO<sub>2</sub> (gas)). The total concentration of CO<sub>2</sub> in solution is quantified by <sup>13</sup>C NMR. The chemical shift observed in the <sup>1</sup>H NMR spectra of the corresponding samples serves as the Y axis of the binding isotherm curve.

Although rarely used for quantification, <sup>13</sup>C NMR can yield reliable results so long as the spin is left to fully relax before a new pulse is sent to the sample. In other words, the recycle delay (d1) is to be set 5 times longer than the longitudinal relaxation time  $T_1$  of the carbon atom to be quantified. A qualitative <sup>13</sup>C-NMR spectrum of a sample of dissolved CO<sub>2</sub> in D<sub>2</sub>O is shown in **Figure S2-3**, where the typical peak of dissolved CO<sub>2</sub> is detected at 124 ppm. A precise  $T_1$  value (30 sec.) for the carbon atom of CO<sub>2</sub> was established experimentally using an inversion-recovery routine from the NMR spectrometer (See SI for details). Consequently, a value of 150 sec. was used for subsequent quantifications of CO<sub>2</sub> from <sup>13</sup>C NMR spectra. Finally, and quite importantly, for the HG ratio to be established during the titration experiment, a specific type of external standard calibration is necessary to relate the area of the peak given by the CO<sub>2</sub> to its concentration. For that matter, the *ERETIC* (*Electronic REference To access In vivo Concentrations*) quantification method is pivotal to the study.<sup>32</sup> Indeed, the function allows for the area of the CO<sub>2</sub> peak to

be related to an external standard of CO<sub>2</sub> whose spectrum was recorded in identical conditions to that of the quantification method (see SI for details). The concentration of CO<sub>2</sub> in the *ERETIC* external standard was established from a precisely weighed amount of solid DMSO<sub>2</sub> (routinely used standard) dissolved in the sample. Noteworthy, although the titration could theoretically be carried out with regular CO<sub>2</sub>, the rather low amounts of CO<sub>2</sub> required for high binding constant hosts fall below the quantification limit of non-cryogenic NMR probes. Therefore, <sup>13</sup>C-labelled CO<sub>2</sub> (99%, <sup>13</sup>C) was used throughout this study to obtain the lowest possible signal/noise ratios within a practical accumulation time. The titration sequence is depicted in **Figure 2.2**, while the gas filling procedure is achieved by a proprietary system consisting of two mass flow controllers and a microcontroller-based user interface, allowing adding any He/CO<sub>2</sub> mixtures to the headspace of the NMR tube. The user interface controls the flow of gas and the precise switching of microvalves from a manifold connected to the NMR tube's inlet, timed in such a way as to consecutively place the tube under a high vacuum and fill it with a precise mole quantity of gas (**Figure S2-1**). The fraction amount of dissolved CO<sub>2</sub> is quantified upon equilibration using the above method.

The establishment of the above methodology prompted us to apply it to the titration of macrocycle **1** with <sup>13</sup>CO<sub>2</sub>. A preliminary qualitative analysis of a sample of **1** in CDCl<sub>3</sub>, with an excess of CO<sub>2</sub>, shows an apparent change in multiplicity of the peaks B and C with respect to the spectrum of a reference macrocycle in pure Helium. The multiplicity of B and C slowly evolves back to the doublet and triplet multiplicity, respectively, however, with a significant change in chemical shift. This is evidence of a temporary change in the chemical environment of the corresponding protons, consistent with a change in conformation or the displacement of solvent molecules from the cavity of the macrocycle. The fact that no significant chemical shift is observed for the NH protons advocates for the former hypothesis. The process is slow on the NMR timescale, however, once equilibrium is reached, the exchange process is fast, leading to peaks with the original multiplicity (**Figure 2.3**).

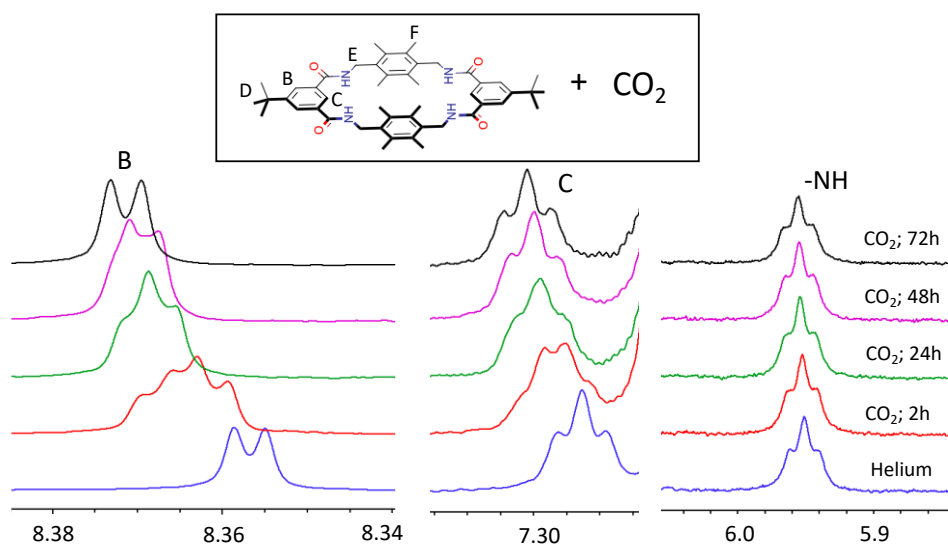


**Figure 2.3.** Sections of <sup>1</sup>H NMR spectra (in CDCl<sub>3</sub>) of macrocycle **1** in the presence of excess CO<sub>2</sub> (120 equivalents), taken from spectra recorded at different time intervals. The blue line corresponds to the reference spectrum acquired under an atmosphere of pure Helium.

Further to this qualitative analysis, the *bindsim* ([supramolecular.org](http://supramolecular.org)) online software was used to estimate the optimum concentration conditions of the host and guest to carry out a complete titration experiment.<sup>19</sup>

Considering an initial hypothetical binding constant of 10, the excess H/G ratio required to reach the plateau of the isotherm was expected to be over 100. Since only a fraction of the CO<sub>2</sub> dissolves in the liquid phase (CDCl<sub>3</sub>), under such high H/G ratios, the corresponding quantity of CO<sub>2</sub> present in the headspace is high enough to induce a pressure over 10 bars. To accommodate such high pressures, pressure-proof NMR tubes were fabricated, allowing for filling the tubes to a pressure above that limit and sealing them to remain leak-free over long periods of time (the details of the filling and sealing processes are described in the SI). A first exploratory titration trial indicated that the binding constant was likely below the initially expected value, however, the study confirmed the validity of the CO<sub>2</sub> quantification method (see SI for further details). As a result of this first optimization experiment, an optimum ratio was found between the concentration of host in CDCl<sub>3</sub> and the required H/G ratio for a complete titration. **Figure 2.4** shows a graph of a full titration of macrocycle **1** with <sup>13</sup>CO<sub>2</sub> fitted to a 1:1 binding isotherm equation, giving a sub-unity binding constant. Although quite surprising at first glance, this result is consistent with DFT models (see below) and, more importantly, validates our titration methodology. Although the typical plateau of a binding isotherm was not reached, the quality of the curve fitting is a strong indication that the method can serve the purpose of measuring very low host-gas binding constants. The low value of *K<sub>a</sub>* would require an over-1000-fold excess of CO<sub>2(sol)</sub>, which would induce pressures approaching 100 bars, a pressure for which no commercial NMR tubes are rated. Compensating with a higher host concentration was not possible since the solubility of the macrocycle was limited.

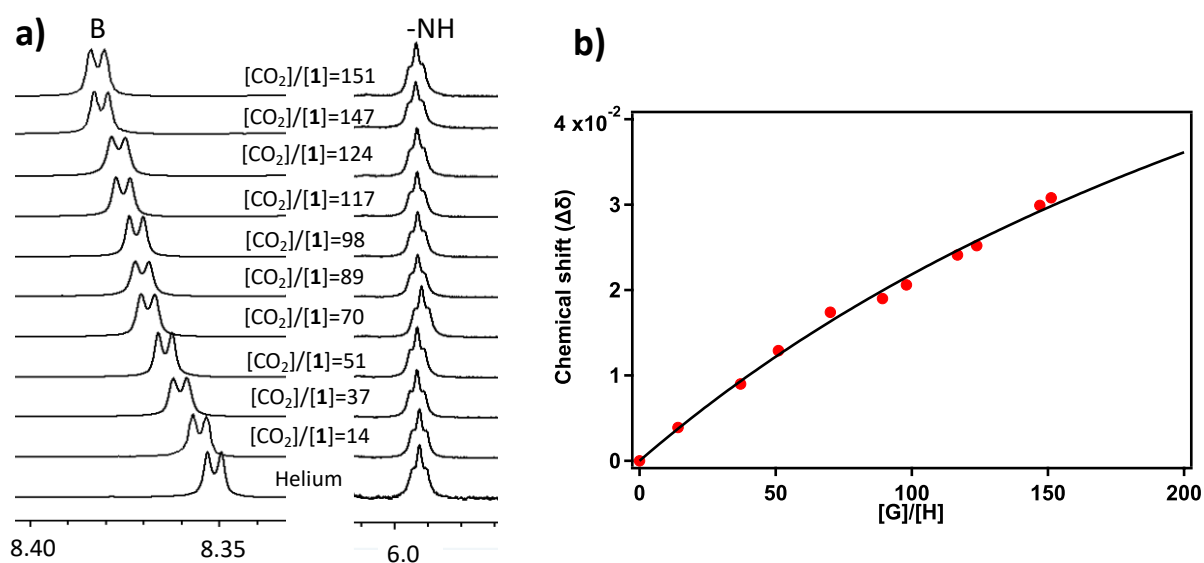


**Figure 2.4.** a) Sections of <sup>1</sup>H NMR spectra (in CDCl<sub>3</sub>) of macrocycle **1** in the presence of incremental quantities of CO<sub>2</sub> (shown as [CO<sub>2</sub>]/1 ratio), taken from spectra recorded after a 72h equilibration time; b) Binding isotherm drawn from the corresponding data and curve fit from a 1:1 binding isotherm equation (see SI)

The latter constant, together with the fact that no chemical shift is observed on the NH protons upon CO<sub>2</sub> addition, is indicative of the macrocycle cavity being bound by a solvent molecule with which the CO<sub>2</sub> molecule competes. Indeed, the macrocycle cavity is likely partially occupied by a solvent molecule even in the presence of a significant excess of CO<sub>2</sub>, as indicated by the low binding constant. Binding events may occur with hydrogen bonds within the cavity's proximity, with the CO<sub>2</sub> molecule pointing outward, thus explaining the shifts observed for protons *B* and *C* in the <sup>1</sup>H spectra. Attempts were made to carry out the

titration in solvents having a weaker expected interaction with the macrocycle's cavity, such as aliphatic or aromatic solvents. However, the solubility of macrocycle **1** in either type of solvent or a mixture thereof was too low to be meaningful.

To substantiate the latter hypothesis, theoretical DFT calculations were carried out to quantify the macrocycle's interaction with either CO<sub>2</sub> or CHCl<sub>3</sub> from a thermodynamic point of view. Consequently, energy minimization routines were carried out on free-macrocycle **1** using a first-principles calculations within the density functional theory (DFT) theoretical model, confirming the existence of two thermodynamically favourable conformations, chair and boat, as demonstrated experimentally in numerous past reports (see SI for details). Energy minimization routines were subsequently performed, including the two guests (CO<sub>2</sub> and CHCl<sub>3</sub>) in the cavity of the macrocycle in the chair conformation, known to be the most common of both conformations. Results show that host-guest complexes of macrocycle **1** with any of the guests assessed (in the gas phase) are thermodynamically favourable, as seen by the negative  $\Delta G$  (**Figure 2.5**). However, comparing the energy difference between the two theoretical HG complexes reveals how the energy of the **1**: CO<sub>2</sub> complex is no more favoured than the **1**: CHCl<sub>3</sub> complex on purely thermodynamic grounds. In fact, according to the energy values, the formation of the host-solvent complex is slightly more favourable. Although these values can be mitigated by the solvent-solvent and complementary cross-component affinities in solution (see Hunter and co-workers),<sup>33,34</sup> the trend is in agreement with our experimental results. That is, despite the CO<sub>2</sub> molecule fitting rather well in the macrocycle cavity interior (**Figure 2.5a**), the hydrogen bonds formed between the CO<sub>2</sub> oxygen atoms and the macrocycle's amide hydrogens are, on average, of a similar length to those of the modelled **1**-CHCl<sub>3</sub> complex (**Figure 2.5b**). Despite the favourable preorganization of the NH groups around the CO<sub>2</sub> linear structure, the chlorine-carbon bond from the solvent molecule is significantly more polarized than the carbonyl groups of CO<sub>2</sub>, thus resulting in a stronger interaction with the macrocycle's amide hydrogen atoms.

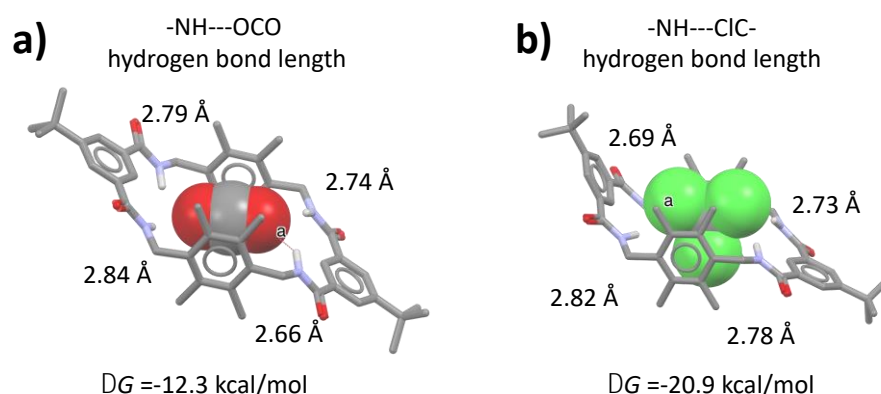


**Figure 2.5.** DFT modelled structures of host-guest complexes of macrocycle **1** with **a)** CO<sub>2</sub> and **b)** CHCl<sub>3</sub>, with corresponding Gibbs free energy change of formation (from separate components) and hydrogen bonds length between the amide groups and respective guests.

To further demonstrate that our methodology is applicable to a wide range of host-gas systems, we studied the interaction of CO<sub>2</sub> with a cucurbit[6]uril (CB[6]). The choice of CB[6] was motivated by the recent

interest as a host for gases, particularly CO<sub>2</sub>. Reports showed that CBs have a high affinity for gases such as hydrocarbons and CO<sub>2</sub>, reporting binding constants of several hundred in aqueous media, assessed using an indirect titration method. An HG complex formed from CB[6] and a fluorescent diammonium guest serve as a titration probe. The change in fluorescence upon displacement of the guest allowed for measuring the binding constant with CO<sub>2</sub>, using an approximated concentration of CO<sub>2</sub> estimated from Henry's law.

Knowing the expected approximate binding constant range, the optimum host concentration range was established to allow for an accurate titration in our conditions. A preliminary study revealed that the limitations of the CB[6]-CO<sub>2</sub> system are opposite to the case of macrocycle **1** in that the limited solubility of CB[6] in D<sub>2</sub>O, together with the somewhat higher expected binding constant, required small quantities of CO<sub>2</sub> to be quantified from the liquid phase. Nevertheless, a 1.25mM concentration of CB[6] was achieved in a 0.05M solution of NaCl in D<sub>2</sub>O. The titration was carried out aiming at an approximate 0.5 to 30 G/H ratio, using precise mixtures of <sup>13</sup>CO<sub>2</sub> in Helium. The <sup>13</sup>CO<sub>2</sub>/Helium ratio was adjusted so that the total volume of gas added to the headspace of the NMR tubes was identical in all samples to induce a pressure equal to atmospheric pressure. The very low solubility of Helium in D<sub>2</sub>O ensures that any interference with the H/G complex is minimized since the quantity of CO<sub>2</sub> in solution is, in all cases, significantly higher than that of Helium since its solubility is the poorest of all permanent gases. A complete titration curve for the CB[6]-CO<sub>2</sub> system is shown in **Figure 2.6b**, fitted with a binding isotherm curve.

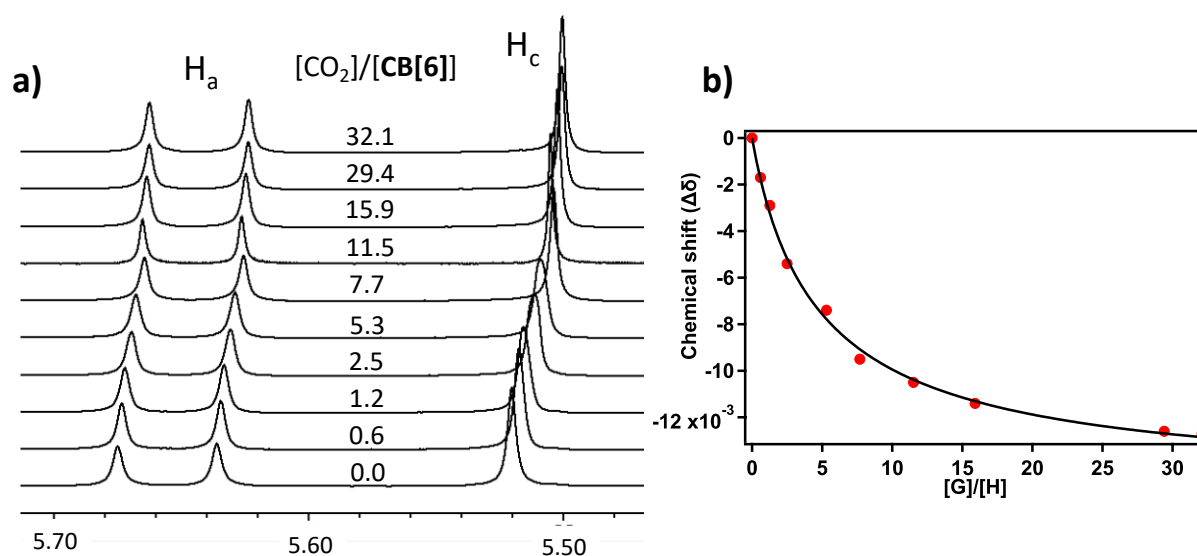


**Figure 2.6.** **a)** Sections of <sup>1</sup>H NMR spectra (in CDCl<sub>3</sub>) of CB[6] in the presence of incremental quantities of CO<sub>2</sub> (shown as [CO<sub>2</sub>]/1 ratio), taken from spectra recorded after a 48h equilibration time; **b)** Binding isotherm drawn from the corresponding data (protons H<sub>a</sub>) and curve fit from a 1:1 binding isotherm equation (see SI)

Some points along the titration curve show some slight discrepancy with the fitting curve (e.g. point at G/H=5.4). Such a gap most likely originates from the intrinsic error upon integrating the CO<sub>2</sub> peak of the corresponding <sup>13</sup>C-NMR spectra. However, the data is well within expected accuracy since as many scans as possible were recorded to minimize the spectra's signal-to-noise ratio. A value of 256 scans was deemed within practical range, with an approximate scan accumulation time of about 10 hours, for the first five samples of the titration curve, while a value of 64 was deemed sufficient for the second half of the H/G ratios of the curve. All in all, the data proves the validity and versatility of the method, which yielded a



binding constant of 238 M<sup>-1</sup> with good enough accuracy and in complete agreement with previous reports. Noteworthy, these results were obtained from a standard 400Mhz NMR spectrometer, however, a sensitivity over a magnitude higher can be expected from modern spectrometers equipped with a cryogenic probe, therefore cutting the accumulation times to less than an hour. The significantly larger binding constant between CO<sub>2</sub> and CB[6] may appear counterintuitive since no particular interactions are involved in the association. However, this system exemplifies the widely accepted “high-energy water” theory of Cucurbiturils host-guests association.<sup>30,35</sup> As such, water bound in the hydrophobic cavity of the cucurbituril (CB) leads to high-energy CB-water adducts that will readily minimize their energy by replacing the water with any less hydrophobic guest present in solution.

### Conclusion

In the present study, we have described a universal method that allows the binding constant of virtually any host-gas complex to be measured with great accuracy using routine NMR titration techniques. The method relies on using orthogonal NMR methods to, on the one hand, probe the change in the chemical environment of the host (<sup>1</sup>H NMR) and, on the other hand, to quantify the amount of gas dissolved in the sample (<sup>13</sup>C NMR or Heteronuclear NMR). The method is adaptable to a wide variety of gases such as carbon dioxide, carbon monoxide, oxygen, nitrogen, ammonia, methane, or high hydrocarbons, which all exist commercially labelled with an NMR-compatible isotope. Finally, although the method was carried out on a standard 400Mhz NMR spectrometer, the widespread use of cryogenic NMR probes would allow for a complete H-G titration to be carried out within a workday time range.

Additionally, our study confirms that hydrogen bonding between a symmetrical, low-overall dipolar moment molecule, such as CO<sub>2</sub> and a host, remains weak. Despite the fact that the hydrogen atoms of the host are pre-arranged to fit the gas guest tightly enough, the likelihood of a similar or higher magnitude interaction between the host and the solvent is usually stronger. Indeed, a solvent providing sufficient solubility for the host will likely have a significant dipole moment, leading to a very small  $\Delta\Delta G$  difference between the Host-solvent and Host-gas complexes. It is not excluded that the interaction between CO<sub>2</sub> and a rigid host with a thigh fit within the cavity may be stronger than that with a solvent molecule. However, the discrimination between the two potential guests, gas and solvent, would be accomplished on steric grounds. The results obtained with the CB[6] host demonstrate that the rather hydrophobic nature of CO<sub>2</sub> and the high ‘energy-water’ mode of guest inclusion of CB can lead to a high binding constant. The lower than-optimum packing ratio, in the range of 22%,<sup>[36]</sup> allows us to rule out Van der Waals forces as a significant factor in producing strong interactions between CB and non-polar gases such as CO<sub>2</sub>. Our result demonstrates that a high binding constant is dictated by the energy difference between host-solvent and host-gas for the formation of a thermodynamically favoured Host-gas complex.

## References

- (1) Front Matter. In *Supramolecular Chemistry*; John Wiley & Sons, Ltd, 1995; p I–X. <https://doi.org/10.1002/3527607439.fmatter>.
- (2) Ma, X.; Zhao, Y. Biomedical Applications of Supramolecular Systems Based on Host–Guest Interactions. *Chem. Rev.* **2015**, *115* (15), 7794–7839. <https://doi.org/10.1021/cr500392w>.
- (3) Uhlenheuer, D. A.; Petkau, K.; Brunsveld, L. Combining Supramolecular Chemistry with Biology. *Chem. Soc. Rev.* **2010**, *39* (8), 2817. <https://doi.org/10.1039/b820283b>.
- (4) Aida, T.; Meijer, E. W.; Stupp, S. I. Functional Supramolecular Polymers. *Science* **2012**, *335* (6070), 813–817. <https://doi.org/10.1126/science.1205962>.
- (5) Harada, A.; Takashima, Y.; Nakahata, M. Supramolecular Polymeric Materials via Cyclodextrin–Guest Interactions. *Acc. Chem. Res.* **2014**, *47* (7), 2128–2140. <https://doi.org/10.1021/ar500109h>.
- (6) Stoddart, J. F. The Chemistry of the Mechanical Bond. *Chem. Soc. Rev.* **2009**, *38* (6), 1802. <https://doi.org/10.1039/b819333a>.
- (7) Gil-Ramírez, G.; Leigh, D. A.; Stephens, A. J. Catenanes: Fifty Years of Molecular Links. *Angew Chem Int Ed* **2015**, *54* (21), 6110–6150. <https://doi.org/10.1002/anie.201411619>.
- (8) Fielden, S. D. P.; Leigh, D. A.; Woltering, S. L. Molecular Knots. *Angew Chem Int Ed* **2017**, *56* (37), 11166–11194. <https://doi.org/10.1002/anie.201702531>.
- (9) Balzani, V.; Credi, A.; Raymo, F. M.; Stoddart, J. F. Artificial Molecular Machines. *Angew. Chem. Int. Ed.* **2000**, *39* (19), 3348–3391. [https://doi.org/10.1002/1521-3773\(20001002\)39:19<3348::AID-ANIE3348>3.0.CO;2-X](https://doi.org/10.1002/1521-3773(20001002)39:19<3348::AID-ANIE3348>3.0.CO;2-X).
- (10) Kay, E. R.; Leigh, D. A.; Zerbetto, F. Synthetic Molecular Motors and Mechanical Machines. *Angew Chem Int Ed* **2007**, *46* (1–2), 72–191. <https://doi.org/10.1002/anie.200504313>.
- (11) Rudkevich, D. M. Supramolecular Chemistry of Gases. In *Progress in Inorganic Chemistry*; Karlin, K. D., Ed.; John Wiley & Sons, Inc.: Hoboken, NJ, USA, 2008; pp 205–246. <https://doi.org/10.1002/9780470144428.ch4>.
- (12) Rudkevich, D. M. Emerging Supramolecular Chemistry of Gases. *Angew. Chem. Int. Ed.* **2004**, *43* (5), 558–571. <https://doi.org/10.1002/anie.200300606>.
- (13) Rudkevich, D. M. Progress in Supramolecular Chemistry of Gases. *European Journal of Organic Chemistry* **2007**, *2007* (20), 3255–3270. <https://doi.org/10.1002/ejoc.200700165>.
- (14) Krzywda, S.; Murshudov, G. N.; Brzozowski, A. M.; Jaskolski, M.; Scott, E. E.; Klizas, S. A.; Gibson, Q. H.; Olson, J. S.; Wilkinson, A. J. Stabilizing Bound O<sub>2</sub> in Myoglobin by Valine<sup>68</sup> (E11) to Asparagine Substitution. *Biochemistry* **1998**, *37* (45), 15896–15907. <https://doi.org/10.1021/bi9812470>.
- (15) Wagner, A.; Sahm, C. D.; Reisner, E. Towards Molecular Understanding of Local Chemical Environment Effects in Electro- and Photocatalytic CO<sub>2</sub> Reduction. *Nat Catal* **2020**, *3* (10), 775–786. <https://doi.org/10.1038/s41929-020-00512-x>.
- (16) Wagner, A.; Ly, K. H.; Heidary, N.; Szabó, I.; Földes, T.; Assaf, K. I.; Barrow, S. J.; Sokołowski, K.; Al-Hada, M.; Kornienko, N.; Kuehnle, M. F.; Rosta, E.; Zebger, I.; Nau, W. M.; Scherman, O. A.; Reisner, E. Host–Guest Chemistry Meets Electrocatalysis: Cucurbit[6]Urils on a Au Surface as a Hybrid System in CO<sub>2</sub> Reduction. *ACS Catal.* **2020**, *10* (1), 751–761. <https://doi.org/10.1021/acscatal.9b04221>.

- (17) Kane, C. M.; Banisafar, A.; Dougherty, T. P.; Barbour, L. J.; Holman, K. T. Enclathration and Confinement of Small Gases by the Intrinsically OD Porous Molecular Solid, Me<sub>4</sub>H<sub>2</sub>SiMe<sub>2</sub>. *J. Am. Chem. Soc.* **2016**, *138* (13), 4377–4392. <https://doi.org/10.1021/jacs.5b11395>.
- (18) Kim, H.; Kim, Y.; Yoon, M.; Lim, S.; Park, S. M.; Seo, G.; Kim, K. Highly Selective Carbon Dioxide Sorption in an Organic Molecular Porous Material. *J. Am. Chem. Soc.* **2010**, *132* (35), 12200–12202. <https://doi.org/10.1021/ja105211w>.
- (19) Thordarson, P. Determining Association Constants from Titration Experiments in Supramolecular Chemistry. *Chem. Soc. Rev.* **2011**, *40* (3), 1305–1323. <https://doi.org/10.1039/C0CS00062K>.
- (20) Huber, G.; Legrand, F.-X.; Lewin, V.; Baumann, D.; Heck, M.-P.; Berthault, P. Interaction of Xenon with Cucurbit[5]Uril in Water. *ChemPhysChem* **2011**, *12* (6), 1053–1055. <https://doi.org/10.1002/cphc.201100068>.
- (21) Cram, D. J.; Tanner, M. E.; Knobler, C. B. Host-Guest Complexation. 58. Guest Release and Capture by Hemispherands Introduces the Phenomenon of Constrictive Binding. *J. Am. Chem. Soc.* **1991**, *113* (20), 7717–7727. <https://doi.org/10.1021/ja00020a039>.
- (22) Branda, N.; Wyler, R.; Rebek, J. Encapsulation of Methane and Other Small Molecules in a Self-Assembling Superstructure. *Science* **1994**, *263* (5151), 1267–1268. <https://doi.org/10.1126/science.8122107>.
- (23) Branda, N.; Grotzfeld, R. M.; Valdes, C.; Rebek, J. Jr. Control of Self-Assembly and Reversible Encapsulation of Xenon in a Self-Assembling Dimer by Acid-Base Chemistry. *J. Am. Chem. Soc.* **1995**, *117* (1), 85–88. <https://doi.org/10.1021/ja00106a010>.
- (24) Riddell, I. A.; Smulders, M. M. J.; Clegg, J. K.; Nitschke, J. R. Encapsulation, Storage and Controlled Release of Sulfur Hexafluoride from a Metal–Organic Capsule. *Chem. Commun.* **2011**, *47* (1), 457–459. <https://doi.org/10.1039/C0CC02573A>.
- (25) Hines, J. H.; Wanigasekara, E.; Rudkevich, D. M.; Rogers, R. D. Calix[4]Arenes Immobilized in a Cellulose-Based Platform for Entrapment and Detection of NO<sub>x</sub> Gases. *J. Mater. Chem.* **2008**, *18* (34), 4050–4055. <https://doi.org/10.1039/B803289K>.
- (26) Huber, G.; Berthault, P.; Nguyen, A. L.; Pruvost, A.; Barriet, E.; Rivollier, J.; Heck, M.-P.; Prieur, B. Cucurbit[5]Uril Derivatives as Oxygen Carriers. *Supramolecular Chemistry* **2019**, *31* (10), 668–675. <https://doi.org/10.1080/10610278.2019.1655565>.
- (27) Fusaro, L.; Locci, E.; Lai, A.; Luhmer, M. NMR Study of the Reversible Trapping of SF<sub>6</sub> by Cucurbit[6]Uril in Aqueous Solution. *J. Phys. Chem. B* **2008**, *112* (47), 15014–15020. <https://doi.org/10.1021/jp806685z>.
- (28) Florea, M.; Nau, W. M. Strong Binding of Hydrocarbons to Cucurbituril Probed by Fluorescent Dye Displacement: A Supramolecular Gas-Sensing Ensemble. *Angew. Chem. Int. Ed.* **2011**, *50* (40), 9338–9342. <https://doi.org/10.1002/anie.201104119>.
- (29) Kim, B. S.; Ko, Y. H.; Kim, Y.; Lee, H. J.; Selvapalam, N.; Lee, H. C.; Kim, K. Water Soluble Cucurbit[6]Uril Derivative as a Potential Xe Carrier for <sup>129</sup>Xe NMR-Based Biosensors. *Chem. Commun.* **2008**, No. 24, 2756. <https://doi.org/10.1039/b805724a>.
- (30) Haouaj, M. E.; Ho Ko, Y.; Luhmer, M.; Kim, K.; Bartik, K. NMR Investigation of the Complexation of Neutral Guests by Cucurbituril. *J. Chem. Soc., Perkin Trans. 2* **2001**, No. 11, 2104–2107. <https://doi.org/10.1039/b105535f>.
- (31) Johnston, A. G.; Leigh, D. A.; Murphy, A.; Smart, J. P.; Deegan, M. D. The Synthesis and Solubilization of Amide Macrocycles via Rotaxane Formation. *J. Am. Chem. Soc.* **1996**, *118* (43), 10662–10663. <https://doi.org/10.1021/ja962046r>.

- (32) Akoka, S.; Barantin, L.; Trierweiler, M. Concentration Measurement by Proton NMR Using the ERETIC Method. *Anal. Chem.* **1999**, *71* (13), 2554–2557. <https://doi.org/10.1021/ac981422i>.
- (33) Hunter, C. A. Quantifying Intermolecular Interactions: Guidelines for the Molecular Recognition Toolbox. *Angew. Chem. Int. Ed.* **2004**, *43* (40), 5310–5324. <https://doi.org/10.1002/anie.200301739>.
- (34) Driver, M. D.; Williamson, M. J.; Cook, J. L.; Hunter, C. A. Functional Group Interaction Profiles: A General Treatment of Solvent Effects on Non-Covalent Interactions. *Chem. Sci.* **2020**, *11* (17), 4456–4466. <https://doi.org/10.1039/D0SC01288B>.
- (35) Biedermann, F.; Uzunova, V. D.; Scherman, O. A.; Nau, W. M.; De Simone, A. Release of High-Energy Water as an Essential Driving Force for the High-Affinity Binding of Cucurbit[*n*]Urils. *J. Am. Chem. Soc.* **2012**, *134* (37), 15318–15323. <https://doi.org/10.1021/ja303309e>.
- (36) Nau, W. M.; Florea, M.; Assaf, K. I. Deep Inside Cucurbiturils: Physical Properties and Volumes of Their Inner Cavity Determine the Hydrophobic Driving Force for Host–Guest Complexation. *Israel Journal of Chemistry* **2011**, *51* (5–6), 559–577. <https://doi.org/10.1002/ijch.201100044>.

## Experimental section

### Materials

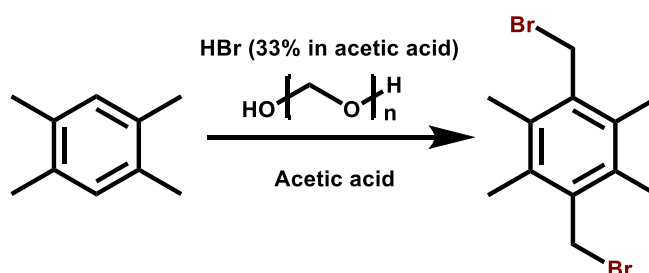
Unless stated otherwise, all reagents were purchased from Sigma-Aldrich and used without further purification. Dry CH<sub>2</sub>Cl<sub>2</sub> and THF were obtained from a PureSolv™ solvent purification system (Innovative Technologies, Inc., MA). Dry DMF was purchased from Sigma-Aldrich and used without purification. Thin layer chromatography was performed on Silica gel 60 F<sub>254</sub> plates (Merck). Silica gel (60-200μm) was purchased from VWR, and the columns were prepared by mixing elution solvents with the appropriate amount of silica prior to its addition to the column. Preparative size exclusion chromatography was carried out in THF (BHT stabilised) using biobeads S-X3 Support (Bio-Rad) as the stationary phase with an approximate 3mL/min flow. CDCl<sub>3</sub> and D<sub>2</sub>O were purchased from Innovachem and used without further purification unless stated otherwise. <sup>13</sup>CO<sub>2</sub> (98% <sup>13</sup>C) was purchased from Cambridge isotope laboratories (CIL, US).

### NMR

<sup>1</sup>H and <sup>13</sup>C NMR spectra were recorded on a Brüker AVANCE 400 MHz or an ASCEND 400 MHz at a constant temperature of 300 K unless stated otherwise. Coupling constants J are reported in hertz (Hz). Standard abbreviations indicating multiplicity were used as follows: m = multiplet, quint. = quintet, q = quartet, t = triplet, d = doublet, s = singlet, br = broad.

### Synthesis

**C1** : 1,4-bis(bromomethyl)-2,3,5,6-tetramethylbenzene



The procedure was based on a modified procedure by Smith and al.<sup>1</sup>. Durene (9.932 g ; 73.2 mmol) and paraformaldehyde (4.443g; 0.148 mol) were dissolved in acetic acid (60 mL). HBr in acetic acid (30mL (33 %wt)) was added dropwise at room temperature. The reaction mixture was heated at 80°C overnight and the precipitate was collected by filtration and washed with cold acetic acid. The final product was obtained after recrystallization in EtOAc (30mL) as white needles (11.876g, 37.1 mmol, 51 % yield).

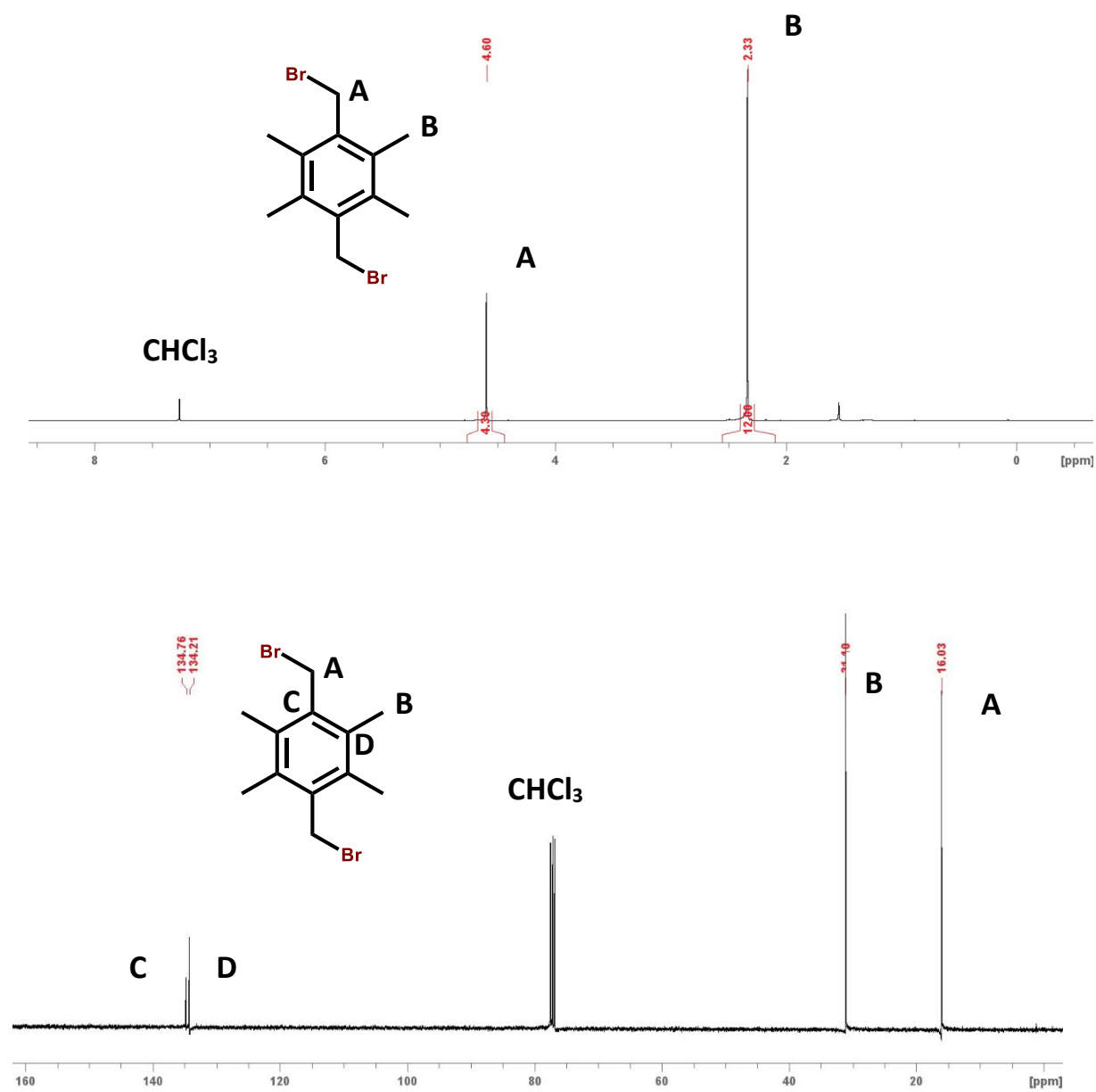
<sup>1</sup>H NMR (400 MHz) CDCl<sub>3</sub>: 4.62 (s, 4H) ; 2.36 (s, 12H)

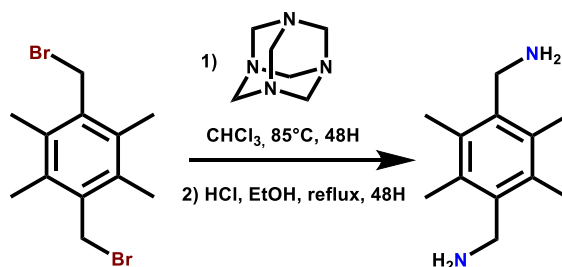
# Silver acetylide cluster catalysts for the electroreduction of CO<sub>2</sub>: Towards industrial scale electrolysis

Léonard CURET

<sup>13</sup>CNMR (100 MHz, CDCl<sub>3</sub>)δ: 134.7, 134.2, 31.2, 16.2

Solubility: CHCl<sub>3</sub>, CH<sub>2</sub>Cl<sub>2</sub>



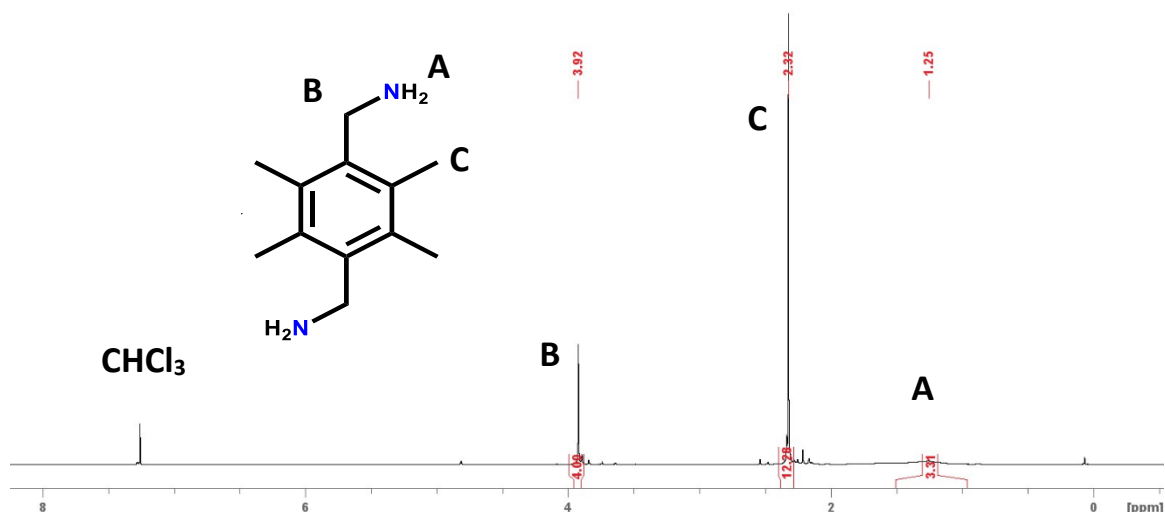
**C2** :2,3,5,6-tetramethyl-1,4-Benzenedimethanamine

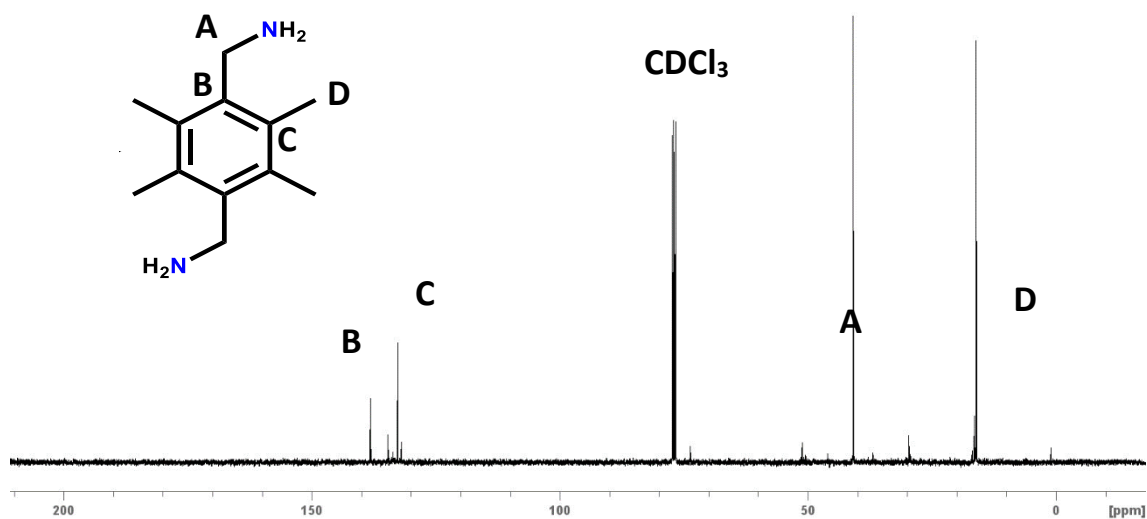
1,4-bis(bromomethyl)-2,3,5,6-tetramethylbenzene (4.972g; 0.155 mol) and hexamethylenetetramine (6.60g; 0.47 mmol) were added together in chloroform (300 mL) and, the reaction was refluxed for 48h. The mixture was cooled to room temperature, collected by filtration and washed with ice-cold chloroform. The solid was suspended in ethanol (300 mL). Concentrated HCl<sub>aq</sub> (50 mL) was added and the mixture was refluxed for 48h. The mixture was cooled to 0°C, and the resulting precipitate was collected by filtration and washed with ice-cold ethanol. The solid was suspended in a Na<sub>2</sub>CO<sub>3</sub> saturated solution (50 mL) with stirring, then chloroform (150mLx3) was added to extract the free amine. The organic phases were combined and dried over MgSO<sub>4</sub>. The solvent was removed to give 2,3,5,6-tetramethyl-1,4-Benzenedimethanamine (2.279g; 75% yield; 11.79 mmol)

<sup>1</sup>H NMR (400 MHz) CDCl<sub>3</sub>: 4.62 (s, 4H); 2.36 (s, 12H); 1.25(m, 4H)

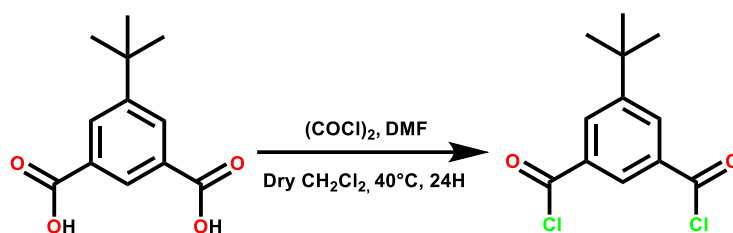
<sup>13</sup>CNMR (100 MHz, CDCl<sub>3</sub>)δ: 138.2; 132.6; 40.9; 16.15

Solubility: CHCl<sub>3</sub>, THF<sub>(poor)</sub>





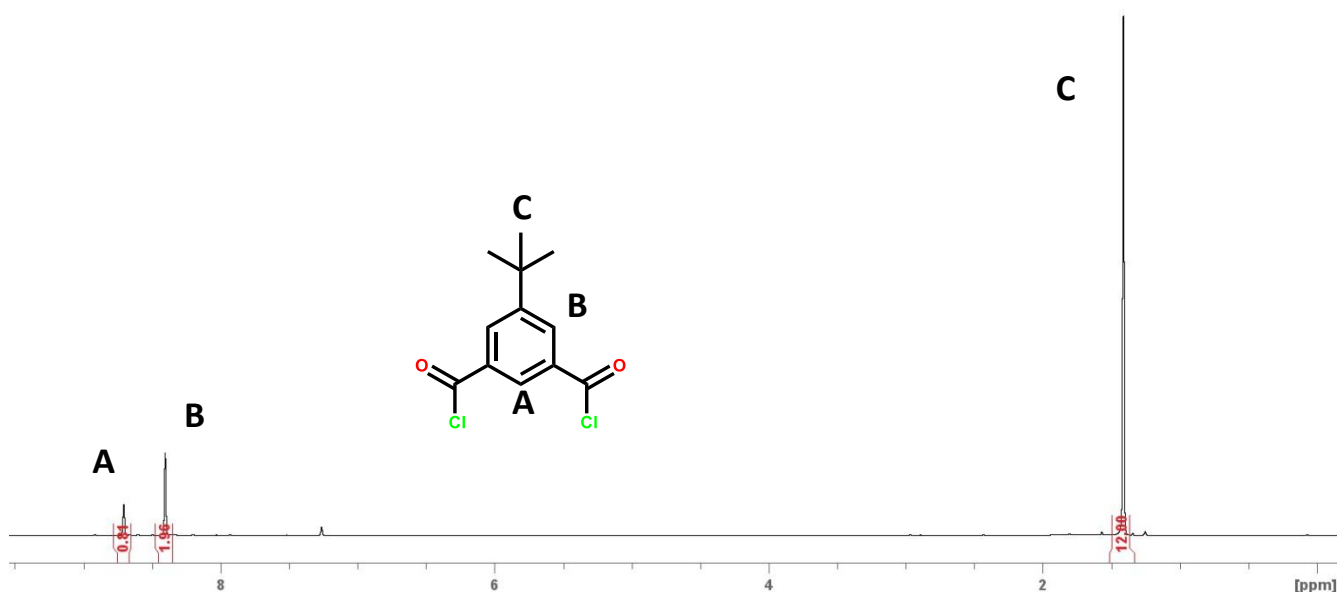
C3: 5-(tert-butyl)isophthaloyl dichloride



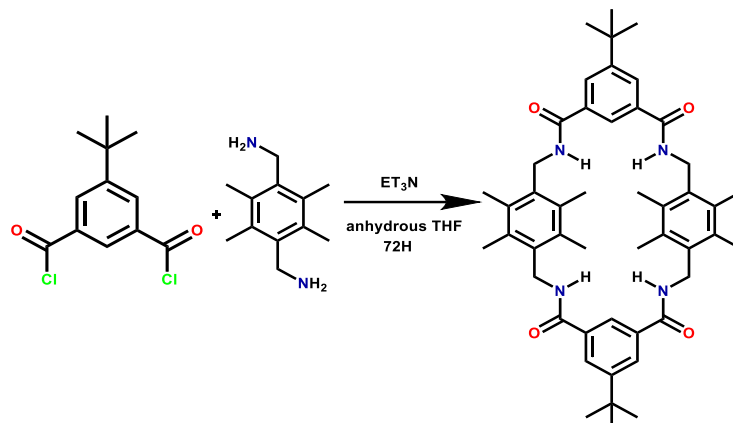
5-tertbutylisophthalic acid (520 mg, 2.3 mmol) was solubilized in dry DCM (40 mL) under an N<sub>2</sub> atmosphere. Oxalyl chloride (0.73 mL, 9.4 mmol, 4eq) was added to the solution, then dry DMF (50µL) was added, and the solution was stirred at 50°C for 5h. The reaction was carefully distilled under vacuum, and the resulting yellow solid (606 mg, 2.3 mmol) was used without further purification.

Solubility: CHCl<sub>3</sub>, CH<sub>2</sub>Cl<sub>2</sub>, THF

<sup>1</sup>H NMR (400 MHz) CDCl<sub>3</sub>: 8.70 (1H,s) ; 8.40 (2H,s) ; 1.41 (12H,s)





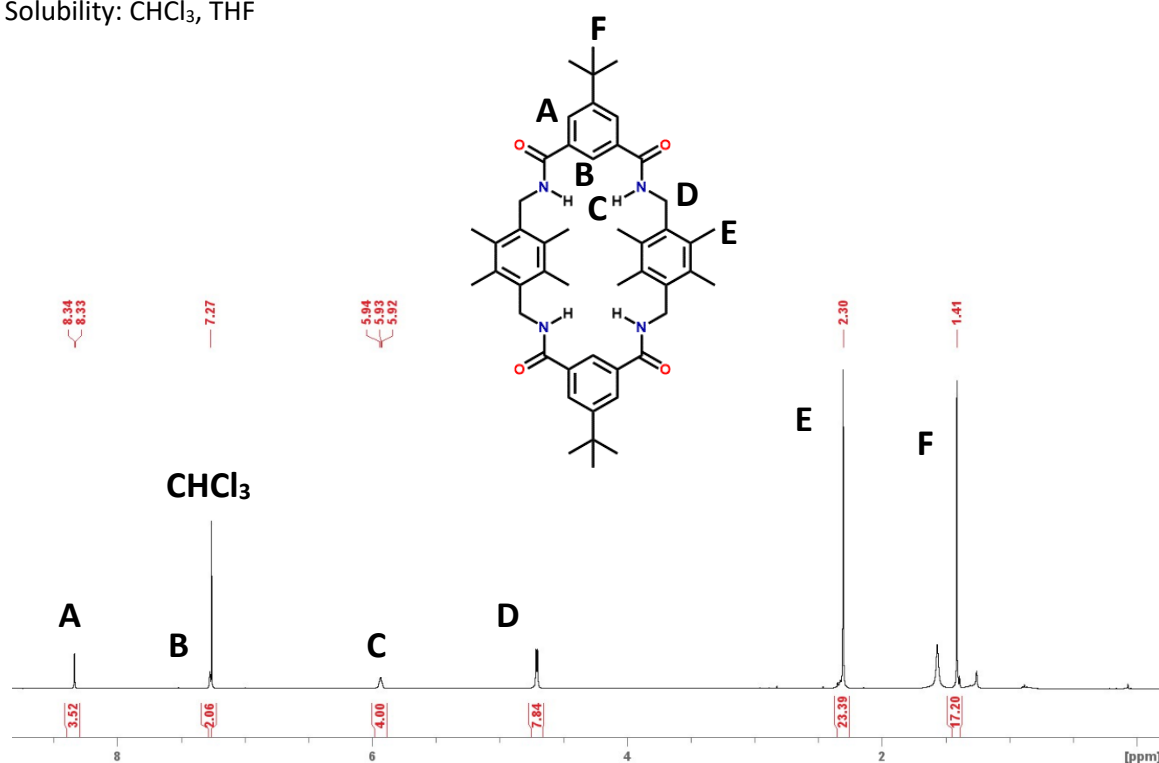
**C4: Tetraamide macrocycle**

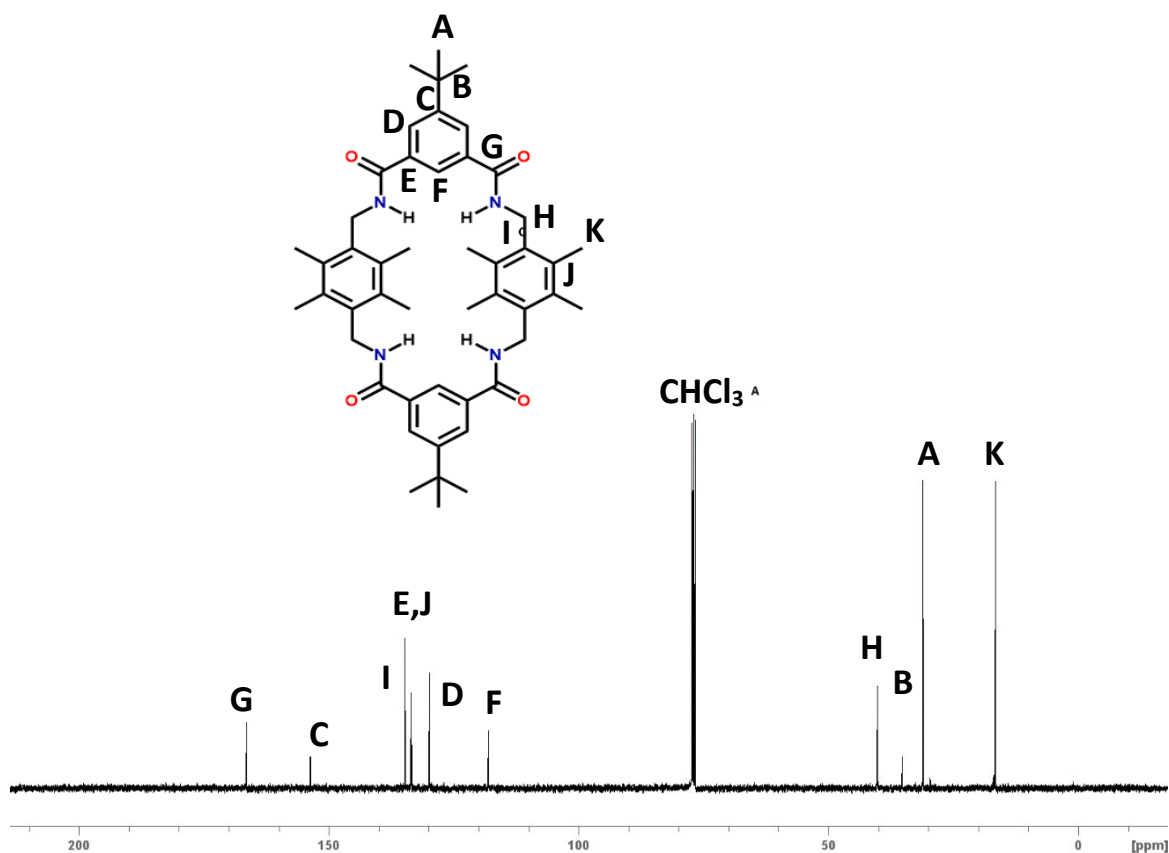
A solution of **C2** (450 mg; 2.34 mmol) in 700 mL of anhydrous THF was prepared under N<sub>2</sub>. Distilled Triethylamine (2.5 mL) was added. A solution of **C3** (606 mg, 2.3mmol) in anhydrous DCM (50mL) was added dropwise over 24H with a syringe pump. After 48h, the solvent was evaporated under reduced pressure, and the resulting solid was dissolved in chloroform (250 mL) and filtered. The filtrate was dried and the resulting solid was purified *via* flash chromatography on silica gel (80 chloroform: 20 acetone). The product was dried under reduced pressure to obtain a white powder. and was further purified on a preparative SEC column (biobeads sx-3, THF). It was finally precipitated in hexane to remove residual BHT and obtained a white powder (50 mg; 5.6%; 66μmol)

<sup>1</sup>H NMR (400 MHz) CDCl<sub>3</sub>: 8.33 (4H,d) ; 7.27 (2H,t) ; 7.93 (4H,t) ; 4.70 (8H,d) ; 2.3 (24H,s) ; 2.30 (24H,s) ; 1.41 (18H,s)

<sup>13</sup>CNMR (100 MHz, CDCl<sub>3</sub>)δ: 166.6 ; 153.8 ; 134.9 ; 133.7 ; 133.6 ; 130.0 ; 118.2 ; 40.4 ; 35.4 ; 31.3 ; 16.7

Solubility: CHCl<sub>3</sub>, THF





## Gas/liquid phases equilibrium

### Raoult's Law

Raoult's Law states that the vapor pressure of a compound above a solution is directly proportional to its mole fraction in that solution (Equation S2-1).

$$p_i = p_i^0 x_{S(i)}$$

Equation S2-1

Where:  $p_i^0$  is the vapour pressure of the pure compound I in the headspace vapour;  $x_{S(i)}$  is the mole fraction of compound I in the liquid phase.

Consequently, the concentration of a compound in the vapour phase is proportional to its concentration in the liquid phase. The equation, however, assumes that the components in the mixture behave in an ideal manner. In practice, this rarely occurs because molecules likely interact with one another and have an impact on the vapour pressure. To compensate for the latter interaction, Raoult's Law is modified with activity coefficients (Equation S2-2).

$$p_i = p_i^0 \cdot \gamma_i \cdot x_{S(i)}$$

**Equation S2-2**

Where  $\gamma_i$  is the activity coefficient of compound  $i$  in the sample mixture.

## Henry's Law

The value of  $\gamma_i$  depicted above may change with concentration. In a dilute solution, e.g. concentrations less than approximately 0.1%, the molecular interactions for a compound will be almost exclusively with other molecules in the sample matrix (solvent) and not with those of itself. This allows approximating  $\gamma_i$  to a constant over a range of applied conditions. Under these conditions, Henry's Law may apply. This states that, at a constant temperature, the amount of a gas dissolved in a liquid is directly proportional to the partial pressure of that gas at equilibrium with that liquid (Equation S3).

$$p_i = H_i \cdot x_{S(i)}$$

**Equation S2-3**

$p_i$  is the gas partial pressure,  $H_i$  is the Henry's Law constant for compound  $i$  in the sample matrix and  $x_{S(i)}$  is the molar fraction of the solute S in the liquid phase.

It is important to note, therefore, that Henry's law is an approximation of Raoult's law and that it is only valid in specific conditions of concentrations. Importantly, the adoption of the approximation is antagonistic to the concept being studied. That is, the quantification of the interactions between a gaseous substance and a solute would be attempted using an approximation (Henry's law) that assumes their non-existence. The method reported herein allows overcoming this assumption by performing a direct quantification of the total amount of gas dissolved in the NMR sample (bound + unbound).

## Gas filling system

The NMR tubes were filled with precise amounts of CO<sub>2</sub> gas or mixtures of CO<sub>2</sub>/helium in precise proportions using a homemade gas filling system described in Figure S2-1. Note that thick pressure-proof NMR tubes (1.4 mm wall thickness, purchased from Norell, USA) were fitted with a plastic top into which an HPLC-type PEEK connector can be screwed in using a viton o'ring to provide a tight seal between the connector and the tube upper edge. The gas injection system consists of a microcontroller-based user interface, which allows for the automated injection of pre-programmed amounts of gases (pure or mixture)

in the NMR tube. The addition is performed while the NMR tube (containing the deuterated solvent and host) is maintained at cryogenic temperature (liquid N<sub>2</sub>). This allows for sequentially placing the tube under high vacuum (3.5 10<sup>-1</sup> mbars) and injecting an accurately measured amount of gas *via* two mass flow controllers at a specified flow rate (typically 5 ml/min). The quantity of gas added is controlled by the opening and closing of microvalves from a manifold at a precise timing interval to allow a desired volume into the tube (converted into a mole amount by the interface). The fact that the NMR tube is maintained at a low temperature throughout the addition allows for injecting a large excess of gas without generating a significant pressure increase during the injection (since the vapour pressure of most permanent gases at -196 °C is below atmospheric pressure). Subsequent to the injection, the inlet valve is maintained closed, allowing for the inlet tubing (1/8" PEEK tubing) to be flame-sealed between the connector and the valve (Figure S2-1). The gas pressure rises (up to 14 bars depending on the volume of gas added) when the tube is allowed to warm up to room temperature.

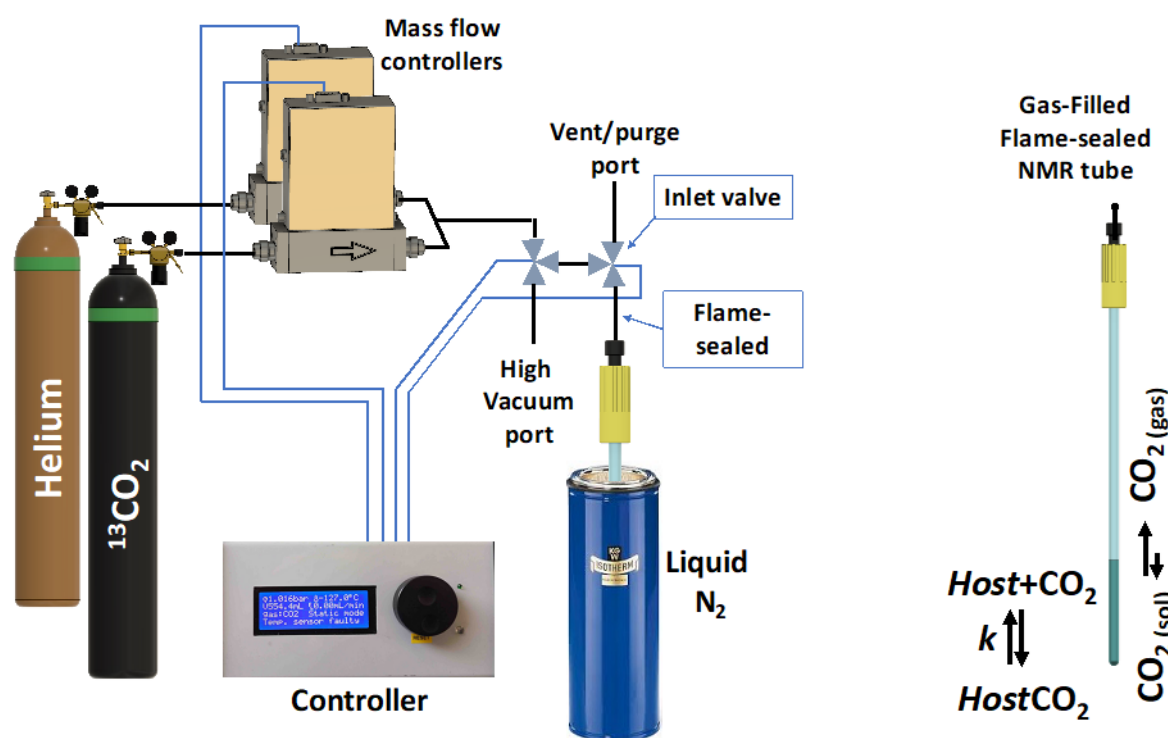


**Figure S2-1.** Schematics of the NMR tube, gas filling system (developed in-house). The controller performs the following steps in a completely automated manner: 1) The NMR tube containing a sample of the host in a deuterated solvent is placed under a high vacuum while being held in liquid nitrogen. The precise amount (nmols to mmols) of gas mixture is added via the valves manifold. The sample is subsequently flame-sealed, left to warm up to room temperature and transferred to the NMR spectrometer.

<sup>13</sup>C NMR data

## Inverse recovery sequence

In the inversion-recovery experiment, the nuclei are first allowed to relax fully to their equilibrium states along the z-axis. A 180-degree pulse is then applied, therefore inverting the signal, which is then allowed to relax for a time  $\tau$  that is varied between experiments. After each variable time, a 90-degree pulse is applied, and an NMR spectrum is recorded in which the peak intensities are a function of the variable delay  $\tau$  and the individual T<sub>1</sub> relaxation rates (**Error! Reference source not found.**). Fitting these data to a function will then yield the T<sub>1</sub> values. The longitudinal relaxation is an exponential recovery process, and these values are relaxation time constants. Hence, the recovery rate  $R_1 = 1/T_1$ . The graph in Figure 1 shows the inversion-recovery plot for CO<sub>2</sub> in CDCl<sub>3</sub>, showing that the magnetisation has recovered after 5xT<sub>1</sub> by ~99% and is complete.

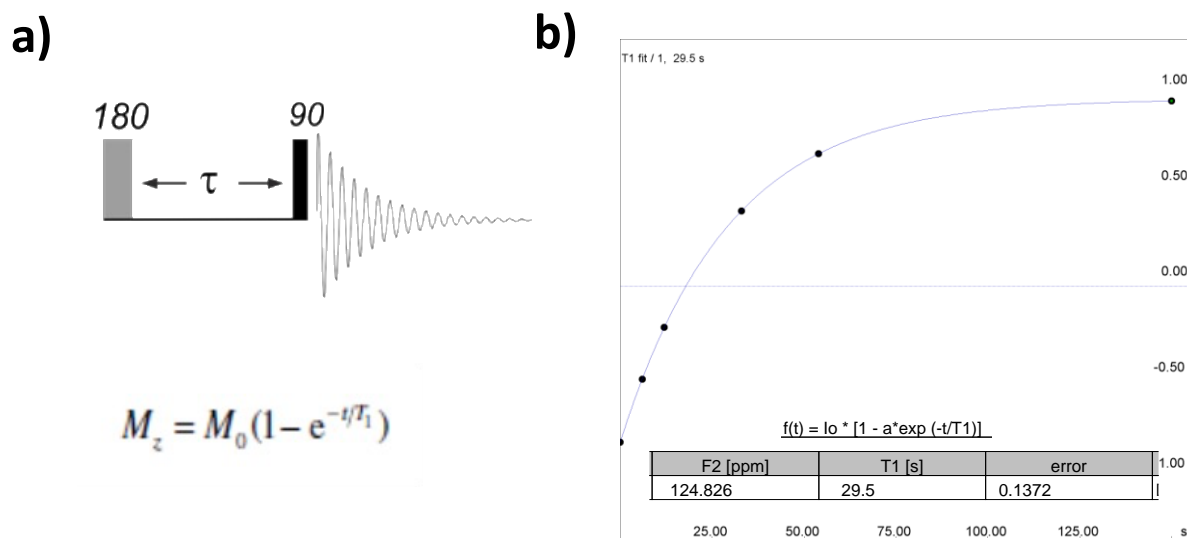


**Figure S2-2.** a) The inversion recovery sequence and the expression describing the recovery of magnetisation ( $M_z$ ) after inversion back toward its equilibrium value ( $M_0$ ) as a function of recovery time ( $t$ ); a) Experimental result of the inversion-recovery sequence to dissolved CO<sub>2</sub> in CDCl<sub>3</sub>

## ERETIC

For a supramolecular host-guest interaction to be measured accurately, the sample must be free of any additional species other than the host and the guest. Therefore, using an internal standard to quantify the amount of dissolved CO<sub>2</sub> is not recommended since a potential unwanted interaction between the two species could exist. An alternative technique to the use of internal standards was published in 1999 by the group of Serge Akoka called ERETIC (Electronic Reference to access In vivo Concentrations). Instead of

adding an internal standard as a form of a chemical species, in ERETIC, the spectrum is “spiked” with a new resonance using a signal generated on a free channel of the NMR spectrometer. Since all modern spectrometers can generate shaped rf pulses, ERETIC uses an exponential decay shape to spike the spectrum. This signal can be recorded from the receiver along with the FID (inverse ERETIC) or sent to an unused coil in the probe to radiate (normal eretic). Regardless, the NMR signal entering the receiver now has a new frequency component added and a subsequent Fourier transform will yield a spectrum with a “synthetic” peak added in. An initial calibration of the area of this eretic signal against a standard of known concentration then allows using this signal to quantify components of unknown concentration. The Bruker topspin software offers a direct ERETIC measurement in which, using a modified procedure from the original ERETIC, no apparent ERETIC peak is present in the spectra. The software automatically relates the area of a selected peak to the concentration according to the external reference previously measured.

**Error! Reference source not found.** shows a spectrum of a typical ERETIC reference used in the titration experiment. A pressure-tight NMR tube containing a known amount of DMSO<sub>2</sub> (60mg) is filled with a gaseous amount of CO<sub>2</sub> (100 μmols). The characteristic peak of <sup>13</sup>CO<sub>2</sub> (at 124 ppm) is integrated and the concentration of dissolved CO<sub>2</sub> is given by relating the integral of the CO<sub>2</sub> peak with that of DMSO<sub>2</sub> (corrected for the natural abundance of carbon). A superimposition of <sup>13</sup>C-NMR spectra corresponding to the titration of macrocycle 1 is shown in **Error! Reference source not found.**. The increase in <sup>13</sup>C peak area is correlated with the amount of CO<sub>2</sub> solubilised.

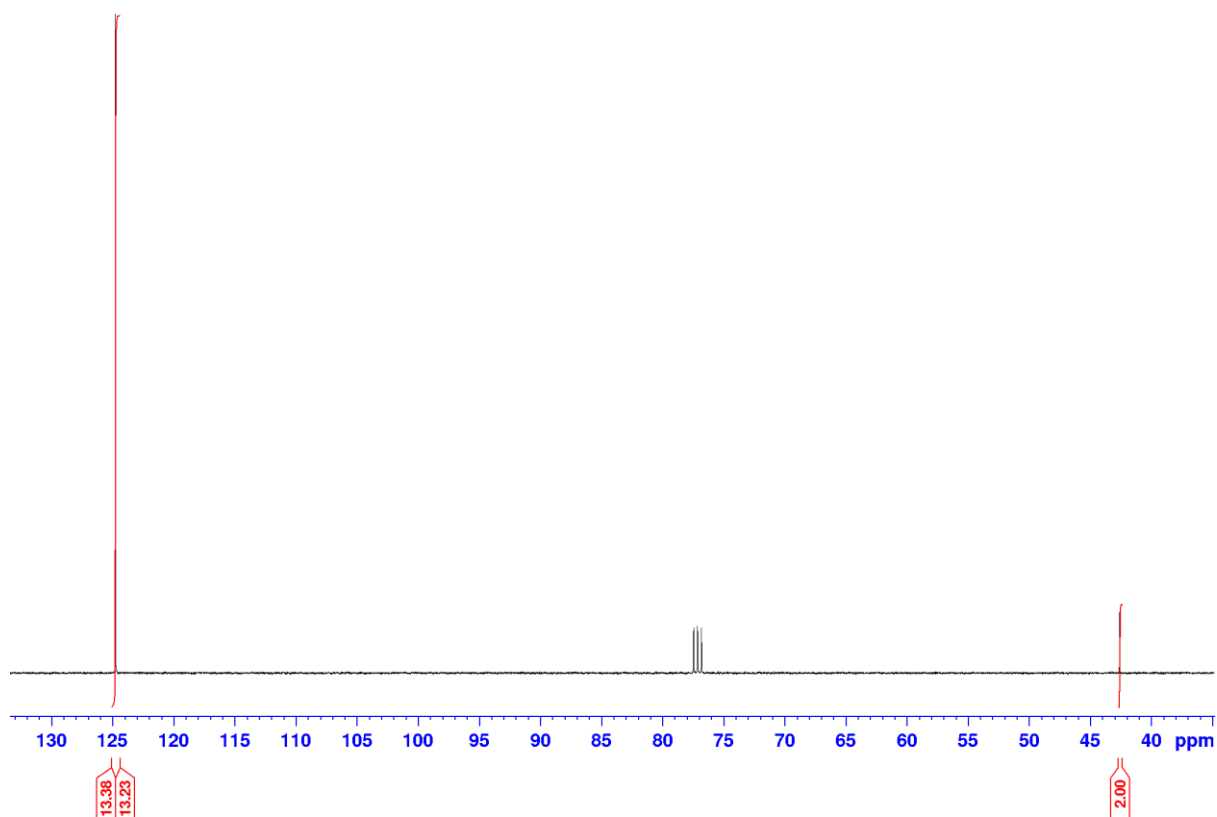


**Figure S2-3** <sup>13</sup>C NMR spectrum in CDCl<sub>3</sub> of ERETIC reference showing the peaks of dissolved <sup>13</sup>CO<sub>2</sub> and with their respective integrals.

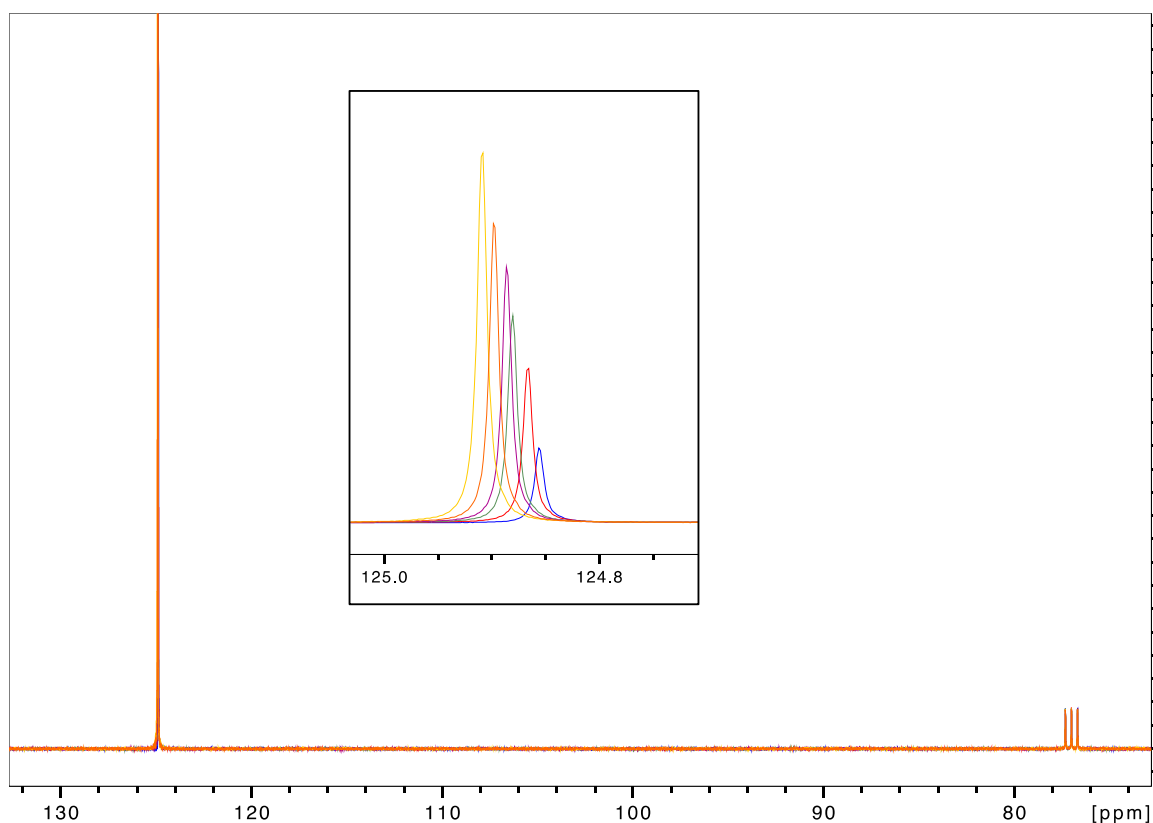


**Figure S2-4** <sup>13</sup>C NMR spectra in CDCl<sub>3</sub> corresponding to some of the titration samples. The intensity of the CDCl<sub>3</sub> residual peak was kept at an identical intensity, showing the increase in the <sup>13</sup>CO<sub>2</sub> peak with increasing concentration. The <sup>13</sup>CO<sub>2</sub> peak zoomed-out region is shown in the inset.

NMR Titration experiments were conducted in CDCl<sub>3</sub> or D<sub>2</sub>O at 25 °C. Increasing amounts of gaseous <sup>13</sup>CO<sub>2</sub> were added to the macrocyclic host, and <sup>1</sup>H NMR and <sup>13</sup>C NMR spectra were acquired after each addition. The titration isotherms were fitted to a 1:1 binding model using Thordarson's equation shown below (Equation S4).2 A standard non-linear squares method within the Igor Pro software was used for determining the binding constant (K<sub>a</sub>). Δδ, plotted in the y-axis, represents the changes in the chemical shift of host protons, ΔΔHG represents the chemical shift difference between host and host-guest complex and [G]0/[H]0 is plotted in the x-axis. K<sub>a</sub> and ΔΔHG were treated as unknown for the fitting process. All of the titrations were independently duplicated.

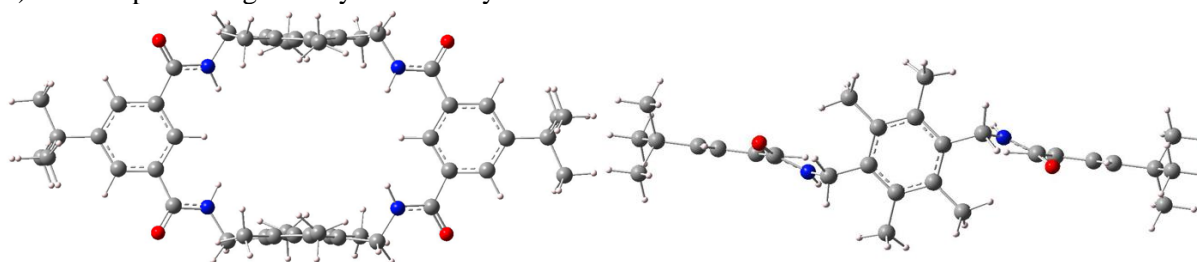
$$\Delta\delta = \frac{\delta_{\Delta HG}}{[H_0]} \left\{ \frac{1}{2} \left[ \left( x[H_0] + [H_0] + \frac{1}{K_a} \right) - \sqrt{\left( x[H_0] + [H_0] + \frac{1}{K_a} \right)^2 + 4x[H_0]^2} \right] \right\}$$

**Equation S2-4**

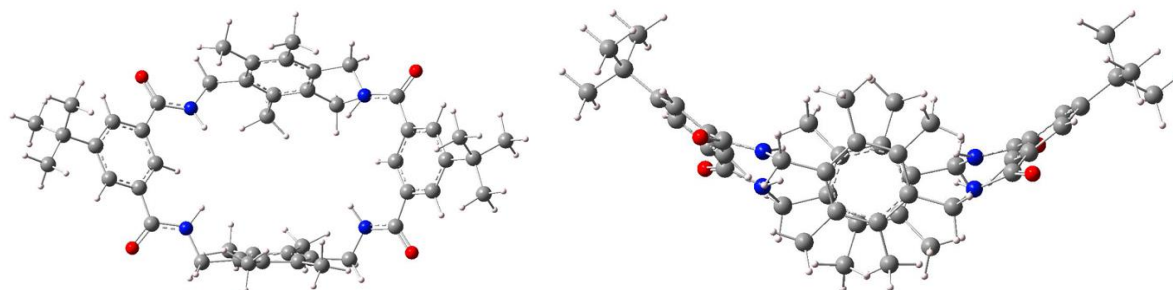
### Computational details

All density functional theory (DFT) calculations were performed using the Gaussian 16 software [3] under the B3LYP functional [3,4] Van der Waals interactions were considered by introducing D3(BJ) empirical dispersion correction proposed by Grimme [5]. The 6-31+G(d) basis set was chosen for describing C, H and O atoms [6]. All simulations were performed within the gas phase. Geometry optimizations were carried out with the *opt=tight* Gaussian's option. Vibrational frequency calculations were done to verify the stability of all obtained stationary point and estimate Gibb's free energies. Interaction energies were computed with the 6-311++G(d,p) basis set on top of relaxed structures and by removing the BSSE contribution estimated with the Counterpoise correction [7].

a) DFT-optimized geometry of Macrocycle **1** chair.



b) DFT-optimized geometry of Macrocycle **1** boat.



### References

- (1) Liu, W.; Oliver, A. G.; Smith, B. D. Macrocyclic Receptor for Precious Gold, Platinum, or Palladium Coordination Complexes. *J. Am. Chem. Soc.* 2018, *140* (22), 6810–6813. <https://doi.org/10.1021/jacs.8b04155>.
  - (2) Thordarson, P. Determining Association Constants from Titration Experiments in Supramolecular Chemistry. *Chem. Soc. Rev.* 2011, *40* (3), 1305–1323. <https://doi.org/10.1039/C0CS00062K>.
- [3] Gaussian 16, Revision C.01, Frisch, M. J.; Trucks, G. W.; Schlegel, H. B.; Scuseria, G. E.; Robb, M. A.; Cheeseman, J. R.; Scalmani, G.; Barone, V.; Petersson, G. A.; Nakatsuji, H.; Li, X.; Caricato, M.; Marenich, A. V.; Bloino, J.; Janesko, B. G.; Gomperts, R.; Mennucci, B.; Hratchian, H. P.; Ortiz, J. V.; Izmaylov, A.



F.; Sonnenberg, J. L.; Williams-Young, D.; Ding, F.; Lipparini, F.; Egidi, F.; Goings, J.; Peng, B.; Petrone, A.; Henderson, T.; Ranasinghe, D.; Zakrzewski, V. G.; Gao, J.; Rega, N.; Zheng, G.; Liang, W.; Hada, M.; Ehara, M.; Toyota, K.; Fukuda, R.; Hasegawa, J.; Ishida, M.; Nakajima, T.; Honda, Y.; Kitao, O.; Nakai, H.; Vreven, T.; Throssell, K.; Montgomery, J. A., Jr.; Peralta, J. E.; Ogliaro, F.; Bearpark, M. J.; Heyd, J. J.; Brothers, E. N.; Kudin, K. N.; Staroverov, V. N.; Keith, T. A.; Kobayashi, R.; Normand, J.; Raghavachari, K.; Rendell, A. P.; Burant, J. C.; Iyengar, S. S.; Tomasi, J.; Cossi, M.; Millam, J. M.; Klene, M.; Adamo, C.; Cammi, R.; Ochterski, J. W.; Martin, R. L.; Morokuma, K.; Farkas, O.; Foresman, J. B.; Fox, D. J. Gaussian, Inc., Wallingford CT, 2016.

[4] a) Vosko, S.H.; Wilk, L.; Nusair, M. “Accurate spin-dependent electron liquid correlation energies for local spin density calculations: a critical analysis”, *Can. Journal of Phys.* **1980**, *58*, 1200–1211, DOI: [10.1139/p80-159](https://doi.org/10.1139/p80-159) b) Lee, C.; Yang, W.; Parr, R. G. “Development of the Colle-Salvetti correlation-energy formula into a functional of the electron density”, *Phys. Rev. B* **1988**, *37*, 785–789, DOI: [10.1103/PhysRevB.37.785](https://doi.org/10.1103/PhysRevB.37.785) c) Becke, A. D. “Density-functional thermochemistry. III. The role of exact exchange”, *J. Chem. Phys.* **1993**, *98*, 5648–5652, DOI: [10.1063/1.464913](https://doi.org/10.1063/1.464913) d) Stephens, P. J.; Devlin, F. J.; Chabalowski, C. F.; Frisch, M. J. “Ab Initio Calculation of Vibrational Absorption and Circular Dichroism Spectra Using Density Functional Force Fields”, *J. Phys. Chem.* **1994**, *98*, 11623–11627, DOI: [10.1021/j100096a001](https://doi.org/10.1021/j100096a001)

[5] Grimme, S.; Ehrlich S.; Goerigk, L. “Effect of the damping function in dispersion corrected density functional theory”, *J. Comp. Chem.* **2011**, *32*, 1456–65. DOI: [10.1002/jcc.21759](https://doi.org/10.1002/jcc.21759)

[6] a) Feller, D. “The role of databases in support of computational chemistry calculations”, *J. Comput. Chem.* **1996**, *17*, 1571–1586, DOI: [10.1002/\(SICI\)1096-987X\(199610\)17:13<1571::AID-JCC9>3.0.CO;2-P](https://doi.org/10.1002/(SICI)1096-987X(199610)17:13<1571::AID-JCC9>3.0.CO;2-P) b) Schuchardt, K.L.; Didier, B. T. ; Elsethagen, T.; Sun, L.; Gurumoorthi, V.; Chase, J.; Li, J.; Windus, T.L. “Basis Set Exchange: A Community Database for Computational Sciences”, *J. Chem. Inf. Model.* **2007**, *47*, 1045–1052, DOI: [10.1021/ci600510j](https://doi.org/10.1021/ci600510j) c) Pritchard, B. P.; Altarawy, D.; Didier, B.; Gibson, T. D.; Windus, T. L. “A New Basis Set Exchange: An Open, Up-to-date Resource for the Molecular Sciences Community.” *J. Chem. Inf. Model.* **2019**, *59*, 4814–4820, DOI: [10.1021/acs.jcim.9b00725](https://doi.org/10.1021/acs.jcim.9b00725)

[7] a) Boys, S. F.; Bernardi, F. “Calculation of Small Molecular Interactions by Differences of Separate Total Energies – Some Procedures with Reduced Errors,” *Mol. Phys.*, **1970**, *19*, 553. DOI: [10.1080/00268977000101561](https://doi.org/10.1080/00268977000101561) b) Simon, S.; Duran, M.; Dannenberg, J.J. “How does basis set superposition error change the potential surfaces for hydrogen bonded dimers?,” *J. Chem. Phys.*, **1996**, *105*, 11024–31. DOI: [10.1063/1.472902](https://doi.org/10.1063/1.472902)

## Chapter 3: Self-assembled infinite silver cluster with atomic precision as a scalable catalyst for CO<sub>2</sub>-electroreduction under industry-relevant reaction rates

### Introduction

The electrochemical reduction of CO<sub>2</sub> into feedstocks, such as carbon monoxide (CO), methane, or higher molecular weight hydrocarbons, is a promising alternative for offsetting greenhouse gas emissions.<sup>1-4</sup> The transformation, generally mediated by a catalyst of metallic nature under electrochemical conditions, has attracted considerable interest from the scientific community.<sup>5,6</sup> Since the pioneering work of Hori, the properties of copper, gold or silver have been well studied.<sup>7-9</sup> While silver and gold have an intrinsic propensity for efficiently reducing CO<sub>2</sub> into CO with high selectivity, copper has shown a very variable selectivity, producing a mixture of gaseous hydrocarbons and alcohols. Aside from these considerations, there is now a general consensus that catalysts should be assessed under industrially relevant reaction rates.<sup>10-12</sup> As such, flow cells and membrane electrode assemblies are commonly accepted designs that allow overcoming the mass transport limitations resulting from the poor solubility (**Error! Reference source not found.**) of CO<sub>2</sub> in aqueous media.<sup>13-17</sup> They involve the use of gas diffusion layers (GDLs), allowing the formation of a gas/electrolyte/catalyst interface where the local concentration of CO<sub>2</sub> rises far above its solubility limit, thus allowing the CO<sub>2</sub>RR to perform at high reaction rates.<sup>18,19</sup> The GDLs require that the catalyst is immobilised on the surface, imposing a significant limitation on the types of catalysts that can be adapted to bulk electrolysis. Indeed, the microporous nature of carbon-based or PTFE-based GDLs commonly used in CO<sub>2</sub> electroreduction renders this process challenging, particularly for metal catalysts.<sup>20</sup> Several types of molecular or hybrid catalysts have been considered as possible alternatives, such as metal-organic frameworks,<sup>21</sup> transition-metal complexes,<sup>22-24</sup> polyoxometalates,<sup>25</sup> carbon-based metal-free materials<sup>26</sup> or two-dimensional materials.<sup>27</sup> Metal clusters have been recently described in this context since they combine attributes of both metallic and molecular catalysts, presenting themselves as discrete crystalline materials that can readily be immobilised on GDLs with controlled surface coverage.<sup>28-30</sup> Their chemical structure consists of a main core composed of several metal atoms linked through metal-metal bonds and organic 'ligands' that are orderly distributed on the outer shell.<sup>31</sup> Discrete clusters of gold,<sup>32</sup> copper<sup>33</sup> and silver<sup>34-36</sup> with different types of capping ligands have been recently shown to display remarkable catalytic properties. Clusters comprising alkynyl ligands have proved particularly well suited for the CO<sub>2</sub>RR, as they involve stable alkyne-silver bonds, allowing for the direct modulation of the silver cluster's geometry and electronic properties by tailoring the chemical structure of the organic moiety. However, their synthesis, similarly to most catalysts, is generally incompatible with industrial-scale production and their performance is often limited to laboratory-scale electrolyzers.

To tackle the above setbacks, herein, we describe a unique silver acetylide cluster displaying an infinite tubular structure and demonstrate its ability to efficiently catalyse the CO<sub>2</sub>RR under very high reaction rates in a flow cell electrolyser. Electrolysis currents higher than 300 mA/cm<sup>2</sup> were achieved with very high selectivity towards CO (>95%). The versatility of our catalysts is further enhanced by the fact that its synthesis involves only one extremely reproducible synthetic step carried out in aqueous media from an inexpensive commercially available alkyne precursor and silver nitrate. The reaction was scaled up to

multigram quantities (over 20g), and the catalyst was obtained in quantitative yields with no required purification, producing only ammonium nitrate as a by-product. The catalyst was isolated as a nanocrystalline powder from which an electron diffraction structure was fully resolved from the as-synthesised material using cutting-edge nanocrystal electron diffraction technology. The structure consists of infinite silver tubular clusters with perfect crystalline arrangement packed in orthorhombic Pna21 unit cell. The insoluble nature of the catalyst allowed for facile immobilisation of the as-synthesised nanocrystalline powder onto carbon paper GDLs, providing a direct structure-characteristics relationship. The resulting elevated surface area led to a turnover frequency (TOF) as high as 11s<sup>-1</sup>. Finally, a thorough chemical and physical characterisation supported by DFT modelling provided solid evidence on the mechanistic fundamentals governing the selectivity of the catalyst towards CO. Accordingly, it appears that the unique infinite tubular structure with atomically precise order is, to our understanding, an essential parameter for the stability of the catalyst over repetitive catalytic cycles, while the ligands impede catalyst poisoning by maintaining the oxidation state of the non-catalytic silver atoms.

### Results and discussion

The catalytic properties of discrete silver acetylides towards the CO<sub>2</sub>RR have been reported very recently in the literature, with only three papers published to date.<sup>32,34–36</sup> Their organic-inorganic hybrid nature infers a high degree of structural versatility due to the ease of synthesis of large libraries of silver acetylide from commercially available alkynes. However, the existing reports rely on complex synthetic procedures, generally carried out on a scale limited to a few tens of milligrams of starting reagents, with reported yields typically below 10%. The formed compounds generally have defined crystalline packing and unit cells with crystallite sizes in the range of a few tens of nanometres, providing a very high surface area required for higher catalytic activity while preserving a precise arrangement of the clusters in the solid state, hence, the recent coining of “atomically precise” catalysts. While the above catalysts display remarkable selectivity, their performance under high electrolysis rates is yet to be demonstrated.

Scheiber and co-workers showed that silver acetylides form readily as highly insoluble species from mixing a methanolic solution of an alkyne precursor with an aqueous silver ammoniacal solution. The above procedure was employed herein and optimised to synthesise silver phenylacetylide from commercially available phenylacetylene. Upon addition of the alkyne dissolved in methanol to a solution of ammoniacal silver nitrate, the formation of a white frothy precipitate ensues almost instantly, indicative of the formation of the silver acetylide species, which was isolated as a poorly soluble solid by simple filtration, in quantitative yields (>99%) from a 20g scale reaction (**Figure 3.1**).

The solubility in DMSO was, however, sufficient to characterise the cluster *via* <sup>1</sup>H NMR, which shows one unusually broad phenyl proton peak reminiscent of polymeric species. The <sup>1</sup>H NMR spectrum is consistent with the quantitative formation of silver acetylide, evidenced by the absence of the acetylene peak from the starting material (see SI). Similarly, the absence of the C≡C-H stretching band (3289 cm<sup>-1</sup>) in the solid-state infrared spectrum with respect to the starting alkyne, is further evidence of the formation of the Ag-C≡C bond (**Figure S3-4**). Additionally, a shift of the C≡C stretching band from 2109 cm<sup>-1</sup> to 2054 cm<sup>-1</sup> further confirms the latter observation.

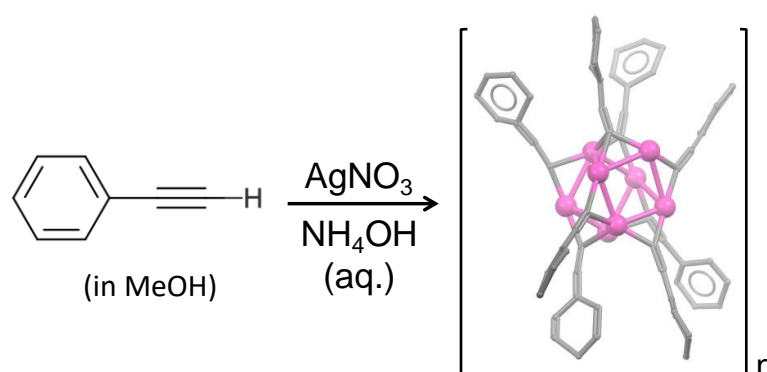


**Figure 3.1.** General scheme of silver acetylide's synthesis with a representation of an asymmetric unit of the cluster fragment established by electron diffraction showing two Ag<sub>4</sub> clusters subunits with h and m and h and m ligand bonding types.

To gain additional information on the solid-state structure of the silver acetylide, a first qualitative observation using a polarized light microscope gave insight of the crystalline nature of the formed species (**Figure S3-26**). Powder XRD characterisation was therefore carried out. To our surprise, despite the acetylides' fast formation kinetics, powder diffractograms show well-resolved peaks archetypical of polycrystalline materials (**Figure 3.4**). The peak width is consistent with crystallite sizes in the range of a few hundred nanometres as calculated from the Scherer equation. To obtain precise structural information on the organometallic cluster, the growth of X-ray diffraction-quality single crystals was attempted by slow diffusion of a solution of the alkynes in methanol to a solution of ammoniacal silver in similar conditions as those used for bulk synthesis. However, needle-shaped crystals unsuitable for X-ray diffraction would form regardless of the conditions employed during the crystallisation experiments. These size limitations led us to explore electron diffraction as an alternative method for acquiring structural data.

Contrary to single-crystal X-ray diffraction, electron diffraction was recently demonstrated to provide diffraction data of sufficiently high quality from crystals whose size is in the range of those found in powder samples. Advanced instruments combining both electron microscopy and diffraction techniques now allow for selecting and recording diffraction data from powders' crystallites in all directions of space and resolving their structure with similar accuracy to single crystal X-ray diffraction. Consequently, electron diffraction data were collected directly from the as-synthesised catalyst allowing for structure. The silver acetylide was found to pack in the Pna21 space group, displaying a unique infinite tubular silver core structure composed of covalently linked silver atoms repeating along the b parameter of the unit cell, with the organic ligands radially disposed on the cluster circumference. The asymmetric unit comprises an Ag<sub>8</sub> cluster subunit assembled with eight [Ph-C≡C]<sup>-</sup> ligands. The latter consists of two parallel Ag<sub>4</sub> squares oriented at a 90° angle with respect to one another and stacked along the b-axis (**Figure 3.2**). One of the Ag<sub>4</sub> squares contains two μ<sup>2</sup>-η<sup>1</sup>,η<sup>2</sup> and two μ<sup>3</sup>-η<sup>1</sup>,η<sup>1</sup>,η<sup>1</sup> [Ph-C≡C]<sup>-</sup> units, while the other contains four μ<sup>3</sup>-η<sup>1</sup>,η<sup>1</sup>,η<sup>1</sup> [Ph-C≡C]<sup>-</sup> units. The two Ag<sub>4</sub> squares are linked by the bridging [Ph-C≡C]<sup>-</sup> ligands and Ag-Ag bonds. The extension of Ag<sub>8</sub> along the b-axis gives a highly organised tubular silver cluster. Importantly, in addition to providing precise structural determination revealing the polymeric nature of the crystalline arrangement, the exact correspondence of the molecular packing with the nanocrystalline powder later used as the catalyst allows for the establishment of a direct structure-properties relationship. This unique feature provided by electron diffraction structure determination has no precedent in the field.

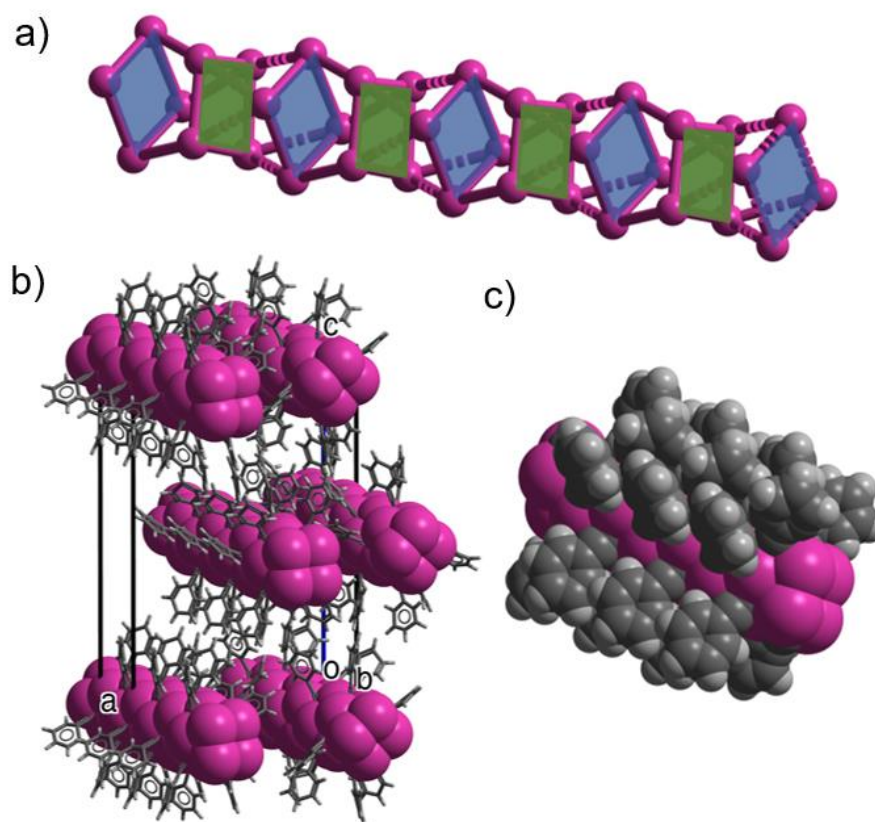


**Figure 3.2.** Electron diffraction structure of silver acetylide AgPh showing **a)** the infinite arrangement of silver atoms with the two different types of Ag<sub>4</sub> clusters subunits depicted in blue and green, **b)** the unit cell and crystalline packing of the cylindrical silver clusters with infinite order with radially disposed outward-pointing acetylide groups **c)** a close view of a cluster fragment in space-filling style, pointing to the somewhat sterically hindered silver cluster.

X-ray diffraction data provided important information on the solid-state structure of the cluster; however, the inherent properties of the crystallites' surface dictate the catalytic properties to an equally important extent. For that matter, XPS analysis was employed to characterise pristine powders, assembled GDEs and post-catalysis GDEs. **Figure 3.3** shows the XPS spectra of pristine AgPh nanopowder. A distinct binding energy peak centred at 284.3 eV is observed in the C1s emission region, and was attributed to the carbon bonds within the phenyl ring. A peak is observed at 283.5 eV, which was attributed to the silver-carbon bond (C≡C–Ag) of the acetylide (**Figure 3.3a**). The Ag 3d emission region contains a well-resolved spin-orbit doublet at 374.2 eV and 368.3 eV ascribed to Ag(I) species from the full-width-at-half-maximum (FWHM) (**Figure 3.3b**).

Interestingly, the deconvolution into two sets of slightly shifted peaks of seemingly identical structure corroborates the presence of the two types of Ag<sub>4</sub> clusters with ligands displaying different hapticity and bridging characteristics. Importantly, quantitative analysis shows a nearly identical ratio of C≡C–Ag and Ag (3d) peak area, unequivocally confirming that the 1:1 Ag/ligand ratio determined from the electron diffraction structure is maintained on the catalyst's surface (**Table S3-2**). Further metal quantification from

dilute solutions of AgPh using microwave plasma atomic emission spectroscopy (MP-AES) provided additional evidence that the latter ratio is maintained throughout the bulk of the material (**Table S 3-4**).

To assess the catalytic activity of AgPh, the silver cluster was subsequently deposited on carbon-based gas diffusion layers typically used for CO<sub>2</sub> reduction. Using a standard procedure, the GDL was coated with a nanoparticles-Nafion-AgPh ink by successive deposition-evaporation sequences at 80°C until the appropriate weight-amount of catalyst was deposited. The catalyst loading was optimised by varying the weight-amount of the catalyst with respect to the carbon nanoparticles and Nafion to maximise the catalytic characteristics, particularly the faradic efficiency towards the major adduct. Results show that the catalyst loading could be decreased to a great extent without a significant impact on the selectivity. A catalyst loading of 0.4 mg/cm<sup>2</sup> was eventually found to be optimum with regard to selectivity towards the main adduct. EDS-SEM images of an electrode confirmed a homogenous dispersion of both the Nafion binder and catalyst on the surface (**Figure S3-25**).

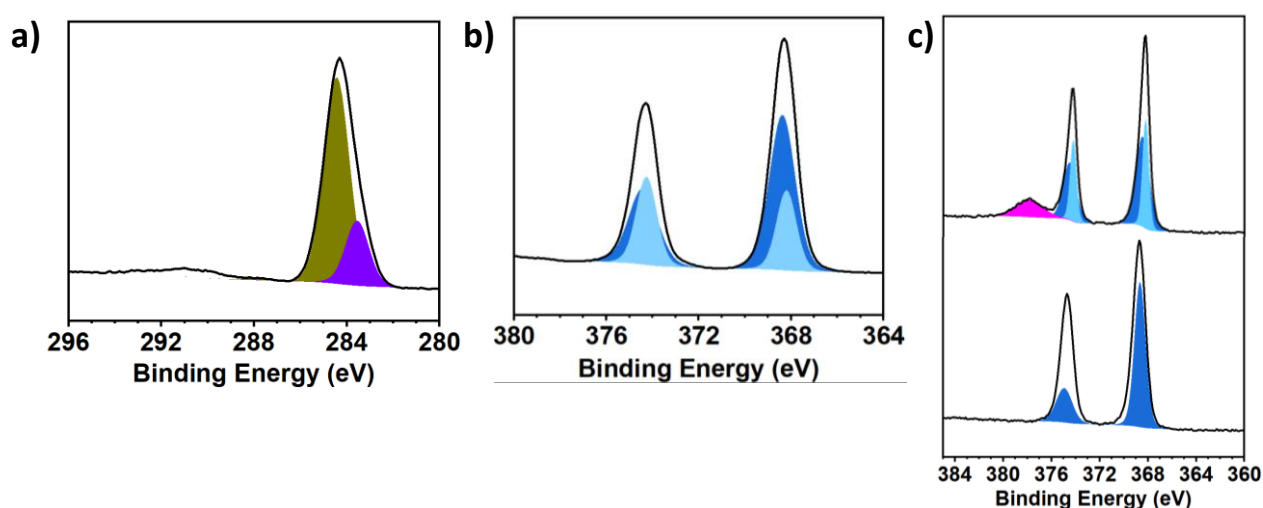


**Figure 3.3.** XPS measurements of the starting material **a)** C1s peak. Phenyl (green) C≡C-Ag(purple) **b)** Ag3d with the doublet of doublet and of the as-prepared electrodes **c)** before (down) and after electrolysis (top)

Further XRD characterisation of the pristine GDEs revealed that the catalyst retains its original nanocrystalline form throughout the deposition process (**Figure S3-6**). The presence of the most intense peaks of the diffraction pattern arising from the (002) and (201) diffraction planes confirms the structure's integrity. In contrast, the slight discrepancy in peak intensity with respect to the calculated diffractogram is strong evidence of the crystals orienting towards a preferred face upon deposition. This is to be expected, owing to the needle-shaped crystals (**Figure 3.4**). The virtually identical peaks' FWHM with respect to the powder diffractogram is evidence that the crystallites have not undergone any significant change in size during the deposition process. This further confirms that the sonicating step prior to deposition on the GDLs and the deposition temperature are not detrimental to the catalyst from a morphological standpoint. The stability upon deposition is further confirmed by XPS, which shows unaltered FWHM of the Ag3d peaks of the GDL compared with the pristine material (**Figure 3.3c**).

The catalytic activity of the above GDEs was first tested with a homemade (**Figure S3-1**) 3-electrode cell in a 1 M potassium bicarbonate electrolyte. The linear sweep voltammetry (LSV) at 10mV/s was measured in both N<sub>2</sub> and CO<sub>2</sub> saturated conditions and showed a clear catalytic wave with a measured catalytic threshold

at -0.45 V vs RHE corresponding to a 0.38 V overpotential vs CO<sub>2</sub>RR potential (**Figure 3.5a**). The shown potentials were all iR corrected using electrochemical impedance spectroscopy (EIS) (**Figure S3-15**).

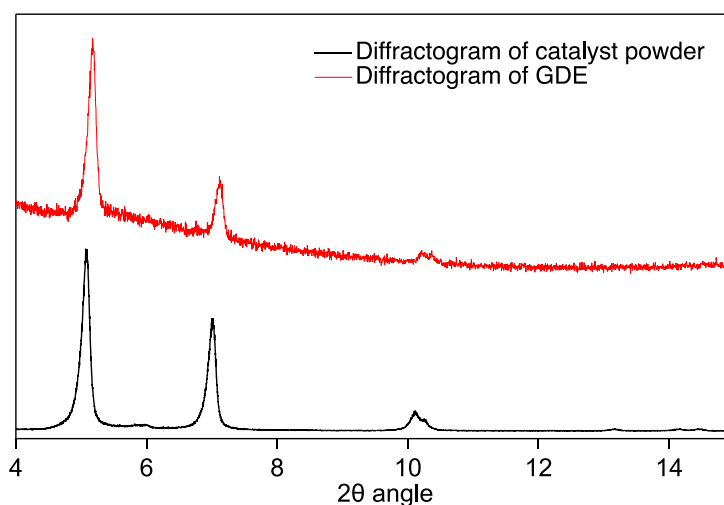


**Figure 3.4.** Powder diffractograms of the pristine catalyst and of the GDE after catalyst deposition

Noteworthy, a 400 mV overpotential difference was observed from an LSV experiment carried out in identical conditions with a mirror-polished silver foil electrode, indicative of enhanced electrochemical activity (**Figure S3-10**). Finally, to assess the selectivity of our catalyst, a series of chronoamperometry experiments were carried out with 0.1V increments from -0.63V to -1.13V vs RHE applied potentials (measured vs. Ag/AgCl and subsequently converted to RHE) (**Figure S3-13**). The produced gaseous and liquid products were sampled and quantified from the cell's headspace and liquid electrolyte after 15 min (**Figure 3.5b**).

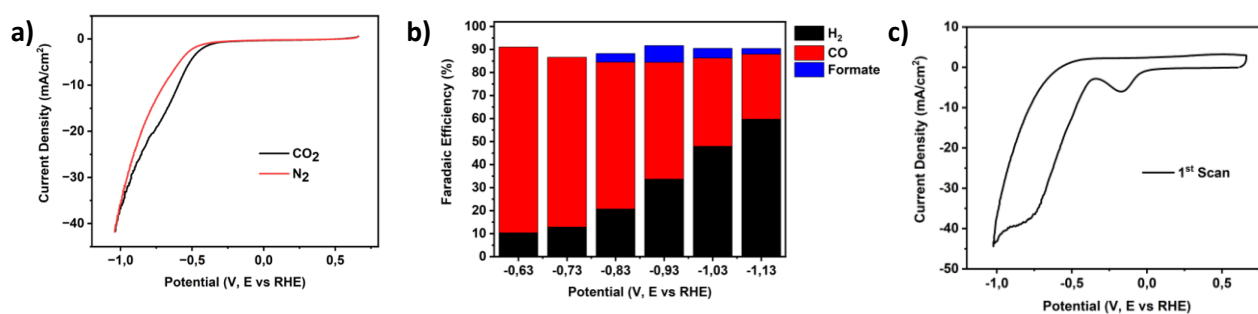


**Figure 3.5.** a) Linear sweep voltammograms of AgPh in N<sub>2</sub> and CO<sub>2</sub> saturated cells b) Linear sweep voltammograms of AgPh and silver foil in CO<sub>2</sub> saturated conditions; c) Histograms showing the faradic efficiency of AgPh resulting from chronoamperograms carried out from -0.63V to -1.13V vs RHE

Interestingly, AgPh showed a high faradic efficiency towards CO at low overpotentials, with FE reaching 80 % at electrolysis potentials as low as -0.63 Volts (vs RHE). Importantly, AgPh showed an elevated propensity to suppress the competing hydrogen evolution reaction (HER). As such, the selectivity of the CO<sub>2</sub>RR remains reasonably high over a wide range of voltages, reaching high electrolysis currents (5-10 mA/cm<sup>2</sup> for CO<sub>2</sub>RR) for laboratory-scale electrolysis cells (**Figure S3-13**). The quantification of the liquid products in the electrolyte by <sup>1</sup>H NMR (**Figure S3-18**) showed the presence of small amounts of non-volatile formate at higher overpotentials with a maximum FE of 7% at -0.93V (**Table S 3-1**).



These preliminary results prompted us to apply our silver acetylide-containing GDEs to a bulk electrolyser flow cell system. The latter consisted of a home-designed and 3D-printed flow cell (**Figure S3-2**), and Freudenberg H24C5 was selected as the GDL support due to its demonstrated suitability for bulk electrolysers. Constant current chronopotentiometry experiments were carried out in KHCO<sub>3</sub> (1M) under currents varying from 25 mA/cm<sup>2</sup> up to 300 mA/cm<sup>2</sup> (**Figure 3.6a**). An outstanding selectivity towards CO was observed over the whole range of electrolysis current density tested, whereas HER was kept to a minimum even under currents as high as 300 mA/cm<sup>2</sup> (**Figure 3.6b**). The potentials (measured against Ag/AgCl microelectrode) remained exceptionally low (-1.8 V vs RHE at 300 mA/cm<sup>2</sup>). Based on the previous quantification of the catalytically active silver, the turnover frequency (TOF) accounted for a value as high as 11 s<sup>-1</sup> at the highest applied current density.

Quite importantly, the catalyst showed exceptional stability over an extended electrolysis time, as shown in **Figure 3.6c**. Indeed, continuous electrolysis under current density as high as 100 mA/cm<sup>2</sup> led to the production of a majority of CO over the whole experiment time frame, with hydrogen composition increasing only slightly (**Figure S3-21**). The overall FE of CO drops from 99% to 91% after 12h of sustained electrocatalytic conditions. We attribute this slow FE decrease to the gradual electrowetting of the GDL.<sup>37,38</sup> Consequently we observe a slight increase in H<sub>2</sub> evolution over time. We confirmed herein this wetting effect using contact angle measurements on a bare GDL compared with a prepared electrode (**Figure S3-28**).

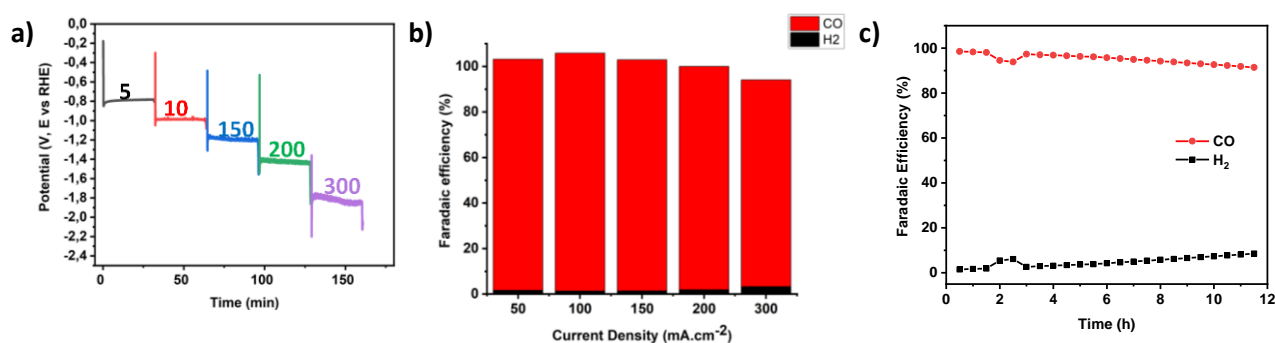


**Figure 3.6 a)** chronopotentiometry experiments between 50 and 300 mA.cm<sup>-2</sup> **b)** Faradic efficiency of AgPh under CO<sub>2</sub> reduction conditions in a flow cell electrolyser (KHCO<sub>3</sub> (1M) as catholyte and anolyte) and corresponding cathode potential (vs RHE); **c)** Faradic efficiency evolution over 12h at 100 mA/cm<sup>2</sup>

Finally, although AgPh showed an overwhelming CO selectivity, reminiscent of pure silver (0), the presence of liquid products in detectable amounts and the polymetallic structure of the cluster's core indicate that the organic moiety plays a mediating effect in the selectivity of the whole catalyst. The electrochemical characterisation of AgPh by cyclic voltammetry in the absence of CO<sub>2</sub> shows a clear irreversible reduction wave under negative potentials (-0.208V vs RHE) attributed to the reduction of Ag(I) centres from the cluster to Ag (0). The fact that this reduction wave is only present during the first cycle of the CV experiment is indicative of a stable Ag (0) intermediate (**Figure 3.5c**). Upon further cycling, no further reduction waves are observed other than the faradic reduction of the surrounding water, strongly suggesting that the previously formed Ag(0) centre constitutes the active catalytic species (**Figure S3-14**). Importantly, the coulombic charge associated with the reduction wave can be directly linked to the number of catalytic centres formed during the first reduction event (see SI for details and how it relates to the turnover frequency (TOF)). Consequently, about 7-mole % of the silver present on the GDE is electrochemically



reduced to Ag (0) prior to the catalysis. The later reduction to Ag (0) is further confirmed by post-electrolysis XPS analysis a cycled GDE at -0.83V vs RHE. As seen in **Figure 3.3c**, the Ag (3d) emission peaks observed in used GDEs fit with convoluted peaks of a blend of Ag(I) and Ag (0). The binding energies are consistent with pure Ag (I) in the pristine GDEs, while it is seen to partially turn to Ag (0) upon cycling. The polymetallic nature of the catalyst and the organic ligand structuration likely provides the necessary stability to accommodate the structural defects and maintain the cluster's structural integrity throughout the catalytic process.

These experimental findings further prompted us to perform DFT modelling to confirm that the catalytic activity and selectivity involve an Ag (0) active species. Taking the above observations into account and for simplification purposes, a silver tetramer possessing alkynyl ligands bound with  $\eta^2$  hapticity in a  $\mu^2$  bridging fashion was used as an AgPh theoretical model. Thereafter, two reaction paths were modelled in which either the above cluster was considered the catalytic species or when an analogue in which an alkynyl ligand was purposely removed to create the active Ag (0) species. (See Supporting Information for details). Plausible electrocatalytic mechanisms and their corresponding Gibbs free energy pathways are depicted in **Figure 3.7**.

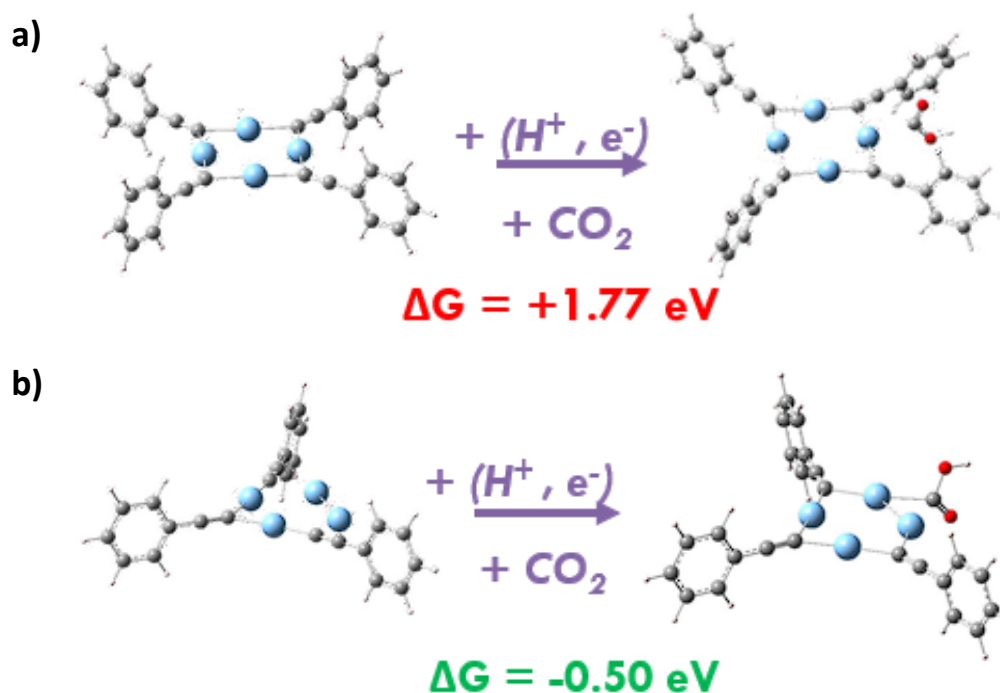


**Figure 3.7.** Schematic of the plausible mechanism of the electrocatalytic CO<sub>2</sub> reaction optimized structures for an Ag<sub>4</sub> possessing **a)** 4 ligands **b)** 3 ligands. C, H, O and Ag atoms are represented by grey, white, red and blue spheres, respectively.

Interestingly, the formation of \*COOH species from the original Ag(I) species has a high associated  $\Delta G$  (+1.77 eV) (**Figure 3.7a**). The formation of the same intermediate from a cluster to which an alkynyl ligand has been previously removed is, on the other hand, very favourable from a thermodynamic perspective with a  $\Delta G$  of -0.50eV (**Figure 3.7b**). A similar trend is observed for the competing reduction of protons, with associated  $\Delta G$  in the same range. The selectivity towards CO is, therefore, attributed to kinetic factors, such as the wider availability of CO<sub>2</sub> in the vicinity of the catalytic interface.

## Conclusion

In conclusion, we have described a multigram scale synthesis of a novel silver alkynyl cluster which self-assembles into infinite tubular silver clusters in a perfectly crystalline manner. The solid-state structure of the cluster was determined by electron diffraction from the catalyst powder, confirming the molecular arrangement throughout the entire sample. The insoluble nature of the material allowed for deposition from a pre-formed colloidal ink *via* a simple drop-casting procedure, with no significant structural change upon GDE fabrication. The catalyst's catalytic properties were assessed under laboratory-scale and flow cell electrolyser conditions, showing an overwhelming selectivity for CO at low reaction overpotentials. Most importantly, GDEs fabricated from AgPh were shown to perform with selectivity towards CO well above 95% in bulk electrolysis under electrolysis currents as high as 300mA/cm and TOF values above 11s<sup>-1</sup>.

In addition to the outstanding catalytic performance, specific electrochemistry experiments and characterisation techniques supported by molecular modelling allowed the establishment of mechanistic aspects of the CO<sub>2</sub> electroreduction catalysed by silver clusters. CV experiments correlated with XPS measurements provided experimental evidence of the *in-situ* formation of an Ag (0) catalytic species under reducing conditions. DFT modelling further confirmed these experimental findings, showing that the \*COOH intermediate formation is only favoured if a silver atom had previously been stripped of an alkynyl ligand, essentially turning the former atom to an Ag (0) oxidation state. The CO<sub>2</sub> molecule, therefore, is reduced from a catalytically active Ag (0) atom, part of the tubular cluster structure. We believe that the infinite nature of the cluster plays a significant role in maintaining the catalytic activity stable throughout successive cycles. Indeed, the excess charge resulting from the ligand's loss is likely accommodated by the perfectly ordered network of Ag-Ag bonded atoms likely delocalising the charge over the whole length of the tubular structure. In addition to supporting the Ag cluster's structure, the ligands presumably shield the Ag atoms and prevent unwanted side reactions that would otherwise lead to the passivation of the catalyst surface. Therefore, the infinite nature of the Ag cluster is possibly the reason for their superior properties compared to the discrete silver acetylide clusters described thus far in this application.

All in all, the method described herein allows for the effortless synthesis of alkynyl clusters whose structure is polymeric in the crystalline sense. The latter types of clusters were shown to be better adapted to CO<sub>2</sub> electroreduction under high reaction rates than their discrete counterparts. Importantly, the scale to which they can be synthesised with no loss of crystalline features, together with cost-effectiveness aspects, provide strong arguments in favour of potential industrial applications. A rough extrapolation of the catalysis features presented herein indicates that the CO's weight production by unit time would likely reach over 1T/hour per kilogram of catalyst. The approximate price of the latter weight of the catalyst is estimated to be less than 1000 dollars, considering the price of the precursors, rendering it an insignificant parameter in the electrolysis process.

## References

- (1) Service, R. Can the World Make the Chemicals It Needs without Oil? *Science* **2019**. <https://doi.org/10.1126/science.aaz5517>.
- (2) Smith, W. A.; Burdyny, T.; Vermaas, D. A.; Geerlings, H. Pathways to Industrial-Scale Fuel Out of Thin Air from CO<sub>2</sub> Electrolysis. *Joule* **2019**, *3* (8), 1822–1834. <https://doi.org/10.1016/j.joule.2019.07.009>.
- (3) Hepburn, C.; Adlen, E.; Beddington, J.; Carter, E. A.; Fuss, S.; Mac Dowell, N.; Minx, J. C.; Smith, P.; Williams, C. K. The Technological and Economic Prospects for CO<sub>2</sub> Utilization and Removal. *Nature* **2019**, *575* (7781), 87–97. <https://doi.org/10.1038/s41586-019-1681-6>.
- (4) Bushuyev, O. S.; De Luna, P.; Dinh, C. T.; Tao, L.; Saur, G.; van de Lagemaat, J.; Kelley, S. O.; Sargent, E. H. What Should We Make with CO<sub>2</sub> and How Can We Make It? *Joule* **2018**, *2* (5), 825–832. <https://doi.org/10.1016/j.joule.2017.09.003>.
- (5) Qiao, J.; Liu, Y.; Zhang, J. Electrochemical Reduction of Carbon Dioxide: Fundamentals and Technologies.
- (6) Huang, C.-H.; Tan, C.-S. A Review: CO<sub>2</sub> Utilization. *Aerosol Air Qual. Res.* **2014**, *14* (2), 480–499. <https://doi.org/10.4209/aaqr.2013.10.0326>.
- (7) Hori, Y.; Murata, A.; Takahashi, R.; Suzuki, S. Enhanced Formation of Ethylene and Alcohols at Ambient Temperature and Pressure in Electrochemical Reduction of Carbon Dioxide at a Copper Electrode. *J. Chem. Soc., Chem. Commun.* **1988**, No. 1, 17. <https://doi.org/10.1039/c39880000017>.
- (8) Hori, Y.; Murata, A.; Takahashi, R. Formation of Hydrocarbons in the Electrochemical Reduction of Carbon Dioxide at a Copper Electrode in Aqueous Solution. *J. Chem. Soc., Faraday Trans. 1* **1989**, *85* (8), 2309. <https://doi.org/10.1039/f19898502309>.
- (9) Hori, Y.; Murata, A.; Kikuchi, K.; Suzuki, S. Electrochemical Reduction of Carbon Dioxide to Carbon Monoxide at a Gold Electrode in Aqueous Potassium Hydrogen Carbonate.
- (10) Burdyny, T.; Smith, W. A. CO<sub>2</sub> Reduction on Gas-Diffusion Electrodes and Why Catalytic Performance Must Be Assessed at Commercially-Relevant Conditions. *Energy Environ. Sci.* **2019**, *12* (5), 1442–1453. <https://doi.org/10.1039/C8EE03134G>.
- (11) De Luna, P.; Hahn, C.; Higgins, D.; Jaffer, S. A.; Jaramillo, T. F.; Sargent, E. H. What Would It Take for Renewably Powered Electrosynthesis to Displace Petrochemical Processes? *Science* **2019**, *364* (6438), eaav3506. <https://doi.org/10.1126/science.aav3506>.
- (12) Stephens, I. E. L.; Chan, K.; Bagger, A.; Boettcher, S. W.; Bonin, J.; Boutin, E.; Buckley, A. K.; Buonsanti, R.; Cave, E. R.; Chang, X.; Chee, S. W.; Da Silva, A. H. M.; De Luna, P.; Einsle, O.; Endrődi, B.; Escudero-Escribano, M.; Ferreira De Araujo, J. V.; Figueiredo, M. C.; Hahn, C.; Hansen, K. U.; Haussener, S.; Hunegnaw, S.; Huo, Z.; Hwang, Y. J.; Janáky, C.; Jayathilake, B. S.; Jiao, F.; Jovanov, Z. P.; Karimi, P.; Koper, M. T. M.; Kuhl, K. P.; Lee, W. H.; Liang, Z.; Liu, X.; Ma, S.; Ma, M.; Oh, H.-S.; Robert, M.; Cuenya, B. R.; Rossmeisl, J.; Roy, C.; Ryan, M. P.; Sargent, E. H.; Sebastián-Pascual, P.; Seger, B.; Steier, L.; Strasser, P.; Varela, A. S.; Vos, R. E.; Wang, X.; Xu, B.; Yadegari, H.; Zhou, Y. 2022 Roadmap on Low Temperature Electrochemical CO<sub>2</sub> Reduction. *J. Phys. Energy* **2022**, *4* (4), 042003. <https://doi.org/10.1088/2515-7655/ac7823>.
- (13) Gao, D.; Wei, P.; Li, H.; Lin, L.; Wang, G.; Bao, X. Designing Electrolyzers for Electrocatalytic CO<sub>2</sub> Reduction. *Acta Physico Chimica Sinica* **2020**, *0* (0), 2009021–0. <https://doi.org/10.3866/PKU.WHXB202009021>.
- (14) Chen, C.; Khosrowabadi Kotyk, J. F.; Sheehan, S. W. Progress toward Commercial Application of Electrochemical Carbon Dioxide Reduction. *Chem* **2018**, *4* (11), 2571–2586. <https://doi.org/10.1016/j.chempr.2018.08.019>.
- (15) Nguyen, T. N.; Dinh, C.-T. Gas Diffusion Electrode Design for Electrochemical Carbon Dioxide Reduction. *Chem. Soc. Rev.* **2020**, *49* (21), 7488–7504. <https://doi.org/10.1039/D0CS00230E>.

- (16) Salvatore, D. A.; Gabardo, C. M.; Reyes, A.; O'Brien, C. P.; Holdcroft, S.; Pintauro, P.; Bahar, B.; Hickner, M.; Bae, C.; Sinton, D.; Sargent, E. H.; Berlinguette, C. P. Designing Anion Exchange Membranes for CO<sub>2</sub> Electrolysers. *Nat Energy* **2021**, *6* (4), 339–348. <https://doi.org/10.1038/s41560-020-00761-x>.
- (17) Lin, J.; Yan, S.; Zhang, C.; Hu, Q.; Cheng, Z. Electroreduction of CO<sub>2</sub> toward High Current Density. *Processes* **2022**, *10* (5), 826. <https://doi.org/10.3390/pr10050826>.
- (18) Weekes, D. M.; Salvatore, D. A.; Reyes, A.; Huang, A.; Berlinguette, C. P. Electrolytic CO<sub>2</sub> Reduction in a Flow Cell. *Acc. Chem. Res.* **2018**, *51* (4), 910–918. <https://doi.org/10.1021/acs.accounts.8b00010>.
- (19) Lees, E. W.; Mowbray, B. A. W.; Salvatore, D. A.; Simpson, G. L.; Dvorak, D. J.; Ren, S.; Chau, J.; Milton, K. L.; Berlinguette, C. P. Linking Gas Diffusion Electrode Composition to CO<sub>2</sub> Reduction in a Flow Cell. *J. Mater. Chem. A* **2020**, *8* (37), 19493–19501. <https://doi.org/10.1039/D0TA03570J>.
- (20) Dinh, C.-T.; Burdyny, T.; Kibria, M. G.; Seifitokaldani, A.; Gabardo, C. M.; García De Arquer, F. P.; Kiani, A.; Edwards, J. P.; De Luna, P.; Bushuyev, O. S.; Zou, C.; Quintero-Bermudez, R.; Pang, Y.; Sinton, D.; Sargent, E. H. CO<sub>2</sub> Electroreduction to Ethylene via Hydroxide-Mediated Copper Catalysis at an Abrupt Interface. *Science* **2018**, *360* (6390), 783–787. <https://doi.org/10.1126/science.aas9100>.
- (21) Lei, Z.; Xue, Y.; Chen, W.; Qiu, W.; Zhang, Y.; Horike, S.; Tang, L. MOFs-Based Heterogeneous Catalysts: New Opportunities for Energy-Related CO<sub>2</sub> Conversion. *Adv. Energy Mater.* **2018**, *8* (32), 1801587. <https://doi.org/10.1002/aenm.201801587>.
- (22) Ren, S.; Joulié, D.; Salvatore, D.; Torbensen, K.; Wang, M.; Robert, M.; Berlinguette, C. P. Molecular Electrocatalysts Can Mediate Fast, Selective CO<sub>2</sub> Reduction in a Flow Cell. *Science* **2019**, *365* (6451), 367–369. <https://doi.org/10.1126/science.aax4608>.
- (23) Wang, M.; Torbensen, K.; Salvatore, D.; Ren, S.; Joulié, D.; Dumoulin, F.; Mendoza, D.; Lassalle-Kaiser, B.; Işci, U.; Berlinguette, C. P.; Robert, M. CO<sub>2</sub> Electrochemical Catalytic Reduction with a Highly Active Cobalt Phthalocyanine. *Nat Commun* **2019**, *10* (1), 3602. <https://doi.org/10.1038/s41467-019-11542-w>.
- (24) Franco, F.; Rettenmaier, C.; Jeon, H. S.; Roldan Cuenya, B. Transition Metal-Based Catalysts for the Electrochemical CO<sub>2</sub> Reduction: From Atoms and Molecules to Nanostructured Materials. *Chem. Soc. Rev.* **2020**, *49* (19), 6884–6946. <https://doi.org/10.1039/D0CS00835D>.
- (25) Cao, Y.; Chen, Q.; Shen, C.; He, L. Polyoxometalate-Based Catalysts for CO<sub>2</sub> Conversion. *Molecules* **2019**, *24* (11), 2069. <https://doi.org/10.3390/molecules24112069>.
- (26) Liu, S.; Yang, H.; Su, X.; Ding, J.; Mao, Q.; Huang, Y.; Zhang, T.; Liu, B. Rational Design of Carbon-Based Metal-Free Catalysts for Electrochemical Carbon Dioxide Reduction: A Review. *Journal of Energy Chemistry* **2019**, *36*, 95–105. <https://doi.org/10.1016/j.jechem.2019.06.013>.
- (27) Huang, X.; Zhang, Y.-B. Reticular Materials for Electrochemical Reduction of CO<sub>2</sub>. *Coordination Chemistry Reviews* **2021**, *427*, 213564. <https://doi.org/10.1016/j.ccr.2020.213564>.
- (28) Ma, G.; Qin, L.; Liu, Y.; Fan, H.; Qiao, L.; Yu, C.; Tang, Z. A Review of CO<sub>2</sub> Reduction Reaction Catalyzed by Atomical-Level Ag Nanomaterials: Atom-Precise Nanoclusters and Atomically Dispersed Catalysts. *Surfaces and Interfaces* **2023**, *36*, 102555. <https://doi.org/10.1016/j.surfin.2022.102555>.
- (29) Zhao, S.; Jin, R.; Jin, R. Opportunities and Challenges in CO<sub>2</sub> Reduction by Gold- and Silver-Based Electrocatalysts: From Bulk Metals to Nanoparticles and Atomically Precise Nanoclusters. *ACS Energy Lett.* **2018**, *3* (2), 452–462. <https://doi.org/10.1021/acsenergylett.7b01104>.
- (30) Chen, L.; Wang, L.; Shen, Q.; Liu, Y.; Tang, Z. All-Alkynyl-Protected Coinage Metal Nanoclusters: From Synthesis to Electrocatalytic CO<sub>2</sub> Reduction Applications. *Mater. Chem. Front.* **2023**. <https://doi.org/10.1039/D2QM01282K>.
- (31) Park, H.; Shin, D. J.; Yu, J. Categorization of Quantum Dots, Clusters, Nanoclusters, and Nanodots. *J. Chem. Educ.* **2021**, *98* (3), 703–709. <https://doi.org/10.1021/acs.jchemed.0c01403>.
- (32) Wang, J.; Xu, F.; Wang, Z.; Zang, S.; Mak, T. C. W. Ligand-Shell Engineering of a Au<sub>28</sub> Nanocluster Boosts Electrocatalytic CO<sub>2</sub> Reduction. *Angew Chem Int Ed* **2022**, *61* (32). <https://doi.org/10.1002/anie.202207492>.

- (33) Liu, L.; Wang, Z.; Wang, Z.; Wang, R.; Zang, S.; Mak, T. C. W. Mediating CO<sub>2</sub> Electroreduction Activity and Selectivity over Atomically Precise Copper Clusters. *Angew Chem Int Ed* **2022**, *61* (35), e202205626. <https://doi.org/10.1002/anie.202205626>.
- (34) Qin, L.; Sun, F.; Ma, X.; Ma, G.; Tang, Y.; Wang, L.; Tang, Q.; Jin, R.; Tang, Z. Homoleptic Alkynyl-Protected Ag<sub>15</sub> Nanocluster with Atomic Precision: Structural Analysis and Electrocatalytic Performance toward CO<sub>2</sub> Reduction. *Angewandte Chemie International Edition* **2021**, *60* (50), 26136–26141. <https://doi.org/10.1002/anie.202110330>.
- (35) Chen, L.; Sun, F.; Shen, Q.; Qin, L.; Liu, Y.; Qiao, L.; Tang, Q.; Wang, L.; Tang, Z. Homoleptic Alkynyl-Protected Ag<sub>32</sub> Nanocluster with Atomic Precision: Probing the Ligand Effect toward CO<sub>2</sub> Electroreduction and 4-Nitrophenol Reduction. *Nano Res.* **2022**, *15* (10), 8908–8913. <https://doi.org/10.1007/s12274-022-4812-6>.
- (36) Deng, G.; Kim, J.; Bootharaju, M. S.; Sun, F.; Lee, K.; Tang, Q.; Hwang, Y. J.; Hyeon, T. Body-Centered-Cubic-Kernelled Ag<sub>15</sub> Cu<sub>6</sub> Nanocluster with Alkynyl Protection: Synthesis, Total Structure, and CO<sub>2</sub> Electroreduction. *J. Am. Chem. Soc.* **2023**, *145* (6), 3401–3407. <https://doi.org/10.1021/jacs.2c10338>.
- (37) Baumgartner, L. M.; Goryachev, A.; Koopman, C. I.; Franzen, D.; Ellendorff, B.; Turek, T.; Vermaas, D. A. Electrowetting Limits Electrochemical CO<sub>2</sub> Reduction in Carbon-Free Gas Diffusion Electrodes. *Energy Adv.* **2023**, *2* (11), 1893–1904. <https://doi.org/10.1039/D3YA00285C>.
- (38) Baumgartner, L. M.; Koopman, C. I.; Forner-Cuenca, A.; Vermaas, D. A. When Flooding Is Not Catastrophic—Woven Gas Diffusion Electrodes Enable Stable CO<sub>2</sub> Electrolysis. *ACS Appl. Energy Mater.* **2022**, *5* (12), 15125–15135. <https://doi.org/10.1021/acsaem.2c02783>.

## Experimental section

### Materials

Phenylacetylene (98%) was purchased from Aldrich and distilled under reduced pressure. 25% ammonia solution (for analysis EMSURE® ISO, Reag. Ph Eur), silver nitrate (ReagentPlus®, ≥99.0% for titration), absolute ethanol, Nafion® perfluorinated resin (5 wt% solution in a mixture of lower aliphatic alcohols containing 5% water), dimethyl sulfone (standard for quantitative NMR, TraceCERT®), and potassium bicarbonate (ACS reagent, 99.7%, powder, crystals, or granules) were purchased from Sigma-Aldrich. K<sub>4</sub>(Fe(CN)<sub>6</sub>·3H<sub>2</sub>O (>99%) was purchased from ChemLab. Vulcan (XC-72) carbon black, FBM PK bipolar membrane (Fumasep) and Freudenberg GDL (H24C5) were purchased from Fuel Cell Store. Methanol (>99.5%, Pharmapur®, Ph Eur, BP, NF) was obtained from Scharlab. CDCl<sub>3</sub> (99.8%) and D<sub>2</sub>O were purchased from Innovachem. Silver Foil (99.97%) was purchased from Advent Research Materials. Polycrystalline diamond suspension (MetaDi™ Supreme) was purchased from Buelher. Aluminium oxide powder (REF: 6.2802.000; 0.3µm) was obtained from Metrohm. All electrolytes were prepared using Milli-Q water.

### Materials characterization

#### NMR

The <sup>1</sup>H-NMR analyses were conducted using a Bruker Ultrashield spectrometer with a <sup>1</sup>H frequency of 400 MHz.

#### MP-AES

MP-AES measurements were performed on an Agilent 4210 model using a 1000 ppm Ag standard (prepared from AgNO<sub>3</sub>) and diluted accordingly in a 3% HNO<sub>3</sub> solution to obtain a calibration curve ranging from 1 to 20 ppm (6 points). Quantification was done by preparing precisely a 1000 ppm solution of AgPh in a mixture of trifluoroacetic acid and Milli-Q water. The prepared solution was then diluted in HNO<sub>3</sub> (3%) to obtain a 10 ppm concentration of the compound.

#### XPS

X-ray Photoelectron Spectroscopy (XPS) measurements were carried out with a THERMO Escalab 250Xi spectrometer, using focused monochromatic Al Kα radiation (hν = 1486.6 eV) with an Xray spot size of 650µm for longer axis ellipse. The high-energy resolution spectra were recorded with constant pass energy of 20 eV. The charge neutralization was used for all the acquisitions. The pressure in the analysis chamber was around 2×10<sup>-7</sup>mbar during analyses. Short acquisition time spectra were recorded before each experiment to check that the samples were not subject to degradation during the X-ray irradiation. The binding energy scale was calibrated using the C 1s peak at 285.0 eV from the hydrocarbon contamination always present at the samples surface. For data analysis, the spectra were mathematically fitted using Casa XPS software, employing a least-squares algorithm and a non-linear baseline. The fitting of peaks in the experimental curves was achieved through a combination of Gaussian (70%) and Lorentzian (30%) distributions.

## Powder XRD

Powder X-ray Diffraction (PXRD) characterization was performed using a Bruker D2 Phaser powder diffractometer equipped with a Cu K $\alpha$  radiation source with a wavelength of 1.5406 Å. XRD patterns were recorded in the 2 $\theta$  range of 10° to 80° with a step size of 0.021° and a counting time of 0.05 seconds per step. The crystallite sizes were determined using DIFFRAC.EVA software.

## SEM-EDS

Scanning electron microscopy (SEM) was performed on an APREO 2 SEM (Thermo-Fisher Scientific) with an EDX XFlash 6-100 (Bruker) for qualitative and quantitative elemental measurements. Measurements were done using a 2.00 kV accelerating Voltage and 25pA for the beam current.

## ATR-IR

ATR-IR characterization was performed on a Nicolet iS50 (Thermo Scientific) with 64 scans.

## 3-Electrodes Cell Electrochemical Characterization

Electrochemical tests were conducted using a custom-made three-electrode, leak-tight cell. The anode, consisting of a platinum wire, was enclosed in a bridge tube. The cell was filled with 40 mL of a 1 M KHCO<sub>3</sub> solution as the electrolyte. The reference electrode employed was an Ag/AgCl electrode immersed in a 3M KCl solution ( $E^0=0.210$  V vs NHE). The working electrode was a Gas Diffusion Electrode (GDE) with a surface area of 2 cm<sup>2</sup>, integrated into a support structure, exposing 1 cm<sup>2</sup> of its surface directly to the electrolyte.



**Figure S3-1:** 3-electrodes Electrochemical Cell

The pH value of the CO<sub>2</sub>-saturated electrolyte was measured to be 6.8 before electrolysis. The potentials were measured against Ag/AgCl (3M). iR

compensation losses between the working and reference electrodes were measured using electrochemical impedance spectroscopy (EIS) measurements from 100kHz to 0.1Hz. Electrode potential after iR correction was converted to the RHE (Reversible Hydrogen Electrode) scale using

$E (RHE) = E (Ag/AgCl) + 0.059 * pH + E_0(Ag/AgCl)$ . pH value is measured to be 7.8 for the CO<sub>2</sub>-saturated electrolyte and 8.4 when N<sub>2</sub> is saturated. The overpotential ( $\eta$ ) was calculated according to Equation S3-2<sup>1</sup>. Faradaic efficiency was calculated from (Equation S3-3). The intrinsic activity of the catalyst was calculated from 4 and Equation S3-5 For Turnover Number (TON) and Turnover Frequency (TOF), respectively.

Before chronoamperometry experiments, the electrolyte underwent a 15-minute purge with either N<sub>2</sub> or CO<sub>2</sub> (at a flow rate of 35 mL/min), depending on the experiment. The purge was done using a Mass Flow Controller (MFC) (Bronkhorst EL-FLOW prestige FG-201CV) and constant stirring to eliminate air from both the solution and the cell headspace. Electrochemical tests were carried out using a potentiostat PGSTAT 204 (Metrohm) and analyzed on the NOVA software.

$$E (RHE) = E (Ag/AgCl) + 0.059 * pH + E^0(Ag/AgCl)$$

**Equation S 3-1**

With  $E(Ag/AgCl)$  the measured corrected potential,  $E^0(Ag/AgCl)=0.210$  V the standard potential at 3M KCl, pH=7.8 in CO<sub>2</sub> saturated 1M KHCO<sub>3</sub> solution

$$\eta = E(RHE) - E_{RHE}^0$$

**Equation S3-2**

With  $E_{RHE}^0 = -0.069$  V for the CO<sub>2</sub> to CO reduction at pH = 7.8

Faradaic efficiency was obtained by direct quantification of the gas products:

$$\text{Faradaic efficiency (\%)} = \frac{Q_{exp}}{Q_{theo}} \times 100 = \frac{z \times n \times F}{Q} \times 100$$

**Equation S3-3**

Where z is the number of electrons involved in the reaction, n the number of moles of generated product, F the faraday constant and Q the charge passed during the catalytic experiment.

$$TON = \frac{n_{max\ product}}{n_{active\ sites}}$$

**Equation S3-4**

With  $n_{max\ product}$  the number of moles of products obtained during electrolysis,  $n_{active\ sites}$  the number of moles of active species on the electrode

$$TOF = \frac{TON}{t_{experiment}}$$

**Equation S3-5**

With  $t_{experiment}$  the experiment time in seconds

### 3-Electrodes Cell Liquid products

Electrochemical tests were conducted using a custom-made three-electrode, leak-tight cell. The anode, consisting of a platinum wire, was enclosed in a bridge tube. The cell was filled with 20 mL of a 1 M KHCO<sub>3</sub> solution as the electrolyte. The reference electrode was an Ag/AgCl electrode 3M KCl solution. Working electrode was a Gas Diffusion Electrode (GDE) with a surface area of 2 cm<sup>2</sup> with 1 cm<sup>2</sup> of its surface directly exposed to the electrolyte.

Chronoamperometry experiments were performed to assess the liquid products (15 minutes). The electrolyte underwent a 15-minute purge with CO<sub>2</sub> (at a flow rate of 35 mL/min) before each measurement. This purge was done using a Mass Flow Controller (MFC) (Bronkhorst EL-FLOW prestige FG-201CV) and



constant stirring to eliminate air from both the solution and the cell headspace. After each experiment the electrolyte from the cell was replaced and analysed by quantitative NMR. Quantitative spectra were recorded following a procedure based on an article from T.Chatterjee et al.<sup>2</sup>, employing a water suppression method. The measured spectra consisted of 128 scans with a delay time of 25 seconds (T<sub>1</sub>= 5s), and DMSO<sub>2</sub> was used as the standard for the quantitative measurement. The NMR tubes were prepared by mixing 392 μL of the electrolyte, 40 mL of a 4mM DMSO<sub>2</sub> solution and 48 μL of D<sub>2</sub>O. The chemical shifts were calibrated based on the peak of the standard at 3.1 ppm. The following equation was used to quantify the liquid products

$$C_{\text{product of interest, tube}} = C_{\text{internal standard, tube}} \frac{\frac{I_{\text{product of interest}}}{H_{\text{product of interest}}}}{\frac{I_{\text{internal standard}}}{H_{\text{internal standard}}}}$$

Equation S3-6

### Flow Cell electrochemical characterisation

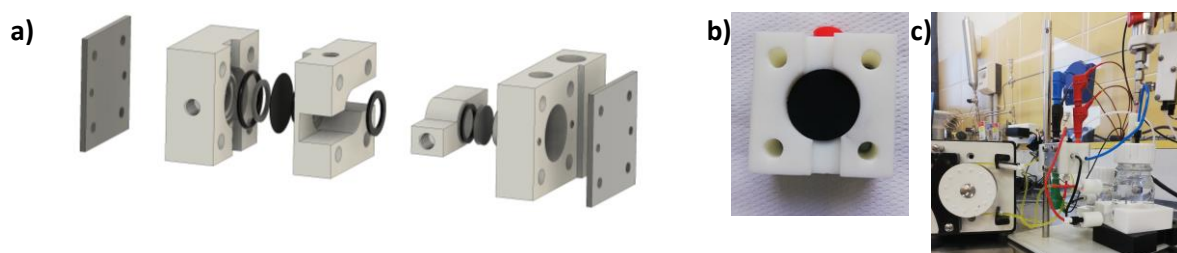


**Figure S3-2:** a) 3D printed Flow Cell design b) Prepared GDE in the WE Slot c) Flow Cell setup in the 2-electrode configuration

Flow experiments were performed on a custom-made Flow cell (). The design was made in order to fit a 3cm<sup>2</sup> GDE with a window of 1cm<sup>2</sup> to the catholyte compartment. The anode is a platinum coated titanium electrode and the potential is controlled using a micro-Ag/AgCl electrode (3M KCl). The 2 electrolyte compartments were separated by a Fumasep FAB-PK membrane (AEM). The catholyte and anolyte flow were adjusted at 2mL/min using a peristaltic pump. The CO<sub>2</sub> flow was fixed at 25mL/min using a Mass Flow Controller (Bronkhorst EL-FLOW prestige FG-201CV).

### Gas quantification

Permanent gases were identified and quantified using gas chromatography (GCMS-QP2010-plus, Shimadzu, Japan) equipped with a packed column (ShinCarbon ST, 2m; 0.53 mm, mesh80/100, Restek, USA) for permanent gases separation. Helium (6.0, Alphagaz 2, AirLiquide) was used as carrier gas. A Dielectric-Barrier Discharge Ionisation Detector (BID, Shimadzu, DL < 0.1ppm) was used to quantify all permanent gases (H<sub>2</sub>, CO, Methane, Ethane, ethylene) with a range of calibration curves made from 0.1, 1 and 10% standard mixtures in CO<sub>2</sub> with at least 4 points for each calibration curve (R<sup>2</sup>>0.98). A relative linearity is observed between calibration curves indicating a trustworthy method for results comparison between each calibration curve. Sampling from the electrolysis cell's head space was carried *via* proprietary automated-sampling system operating solenoid valves at timed intervals transferring a sample of the cell's head space to a GC-sample loop (500 μL) followed by the subsequent injection to the GC column.

## Computational details

All density functional theory (DFT) calculations were performed using the Gaussian 16 software<sup>3</sup> under the B3LYP functional<sup>3-7</sup> Van der Waals interactions were considered by introducing D3(BJ) empirical dispersion correction proposed by Grimme<sup>8</sup> The 6-31+G(d) basis set was chosen for describing C, H and O atoms, while the LANL2TZ(f) one was used for Ag atoms<sup>9-13</sup>. All simulations were performed within the gas phase. Geometry optimizations were carried out with the opt=*tight* Gaussian's option. Vibrational frequency calculations were done to verify the stability of all obtained stationary points and estimate Gibb's free energies. Interaction energies were computed with the 6-311++G(d,p) basis set on top of relaxed structures and by removing the BSSE contribution estimated with the Counterpoise correction<sup>14,15</sup>.

## Electrodes preparation

### CV and LSV electrodes

The AgPh Electrodes were prepared following a modified procedure from M. Robert et al<sup>16</sup>. Vulcan XC-72 Carbon Black (3 mg) was sonicated in Absolute ethanol (2mL) for 30min. To the slurry was added Nafion® perfluorinated resin (10 µL of a 5 wt% solution in a mixture of lower aliphatic alcohols containing 5% water) and the mixture was sonicated for 30min. To this mixture was added a suspension of the acetylide (0.8 mg) in absolute ethanol (1mL) and the mixture was sonicated for 30min. The suspension was then deposited by dropcasting on a gas diffusion layer (Freudenberg H24C5; 2 cm<sup>2</sup>) at 80°C. The electrodes were then dried under reduced pressure at 40°C overnight.

The Silver foil electrode was prepared by polishing a disk (1.6 cm diameter) on a P1000 then P2000 Silicon Carbide paper followed by ultrasound cleaning for 10 min in Milli-Q water. The disks were further polished using a polycrystalline diamond suspension (3µm) and alumina powder (0.3µm) to obtain mirror-polished electrodes, which were cleaned by ultrasound bath in Milli-Q water for 10 min.

### Flow cell electrodes preparation

The AgPh Electrodes were prepared following a common procedure<sup>16</sup>. Vulcan XC-72 Carbon Black (4.5 mg) was sonicated in Absolute ethanol (2mL) for 30min. To the slurry was added Nafion® perfluorinated resin (15 µL of a 5 wt% solution in a mixture of lower aliphatic alcohols containing 5% water) and the mixture was sonicated for 30min. To this mixture was added a suspension of the acetylide (0.4 mg.cm<sup>-2</sup>) in absolute ethanol (1mL) and the mixture was sonicated for 30min. The suspension was then deposited by dropcasting on a gas diffusion layer (Freudenberg H24C5; 3 cm<sup>2</sup>) at 80°C. The electrodes were then dried under reduced pressure at 40°C overnight.

### Stability assessment of GDEs

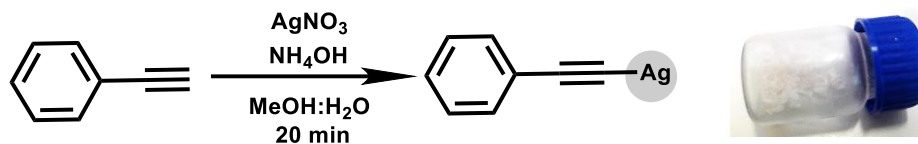
To ascertain the stability of these materials during electrode deposition and subsequent electrolysis, a comprehensive series of tests was conducted. In the initial step, we prepared a reference electrode (Freudenberg H24C5) coated with a layer of Carbon Black (Vulcan XC-72) to establish a baseline binding energy of 284.3 eV (**Table S3-2**). Subsequently, a second electrode comprising Nafion and CB was prepared, featuring a distinctive C 1s binding energy peak at 291.4 eV attributed to the C-F bonds of Nafion and used as a reference point for polymer stability (F/C ratio =2.8) (**Table S3-2**).

In the next phase, a third electrode was prepared, incorporating AgPh (0.4 mg/cm<sup>2</sup>) into the previous mixture. Unsurprisingly, the C-C binding energy corresponding to AgPh remains obscured by the prominent peak at 283.4 eV from the carbon CB matrix. Nevertheless, the silver binding energy (368.8 eV), while slightly shifted ( $\Delta$ energy = 0.5 eV), likely due to the proximity of substantial fluorine content, exhibits an unaltered width at half-maximum, indicative of material integrity (**Table S3-2**).

Finally, a fourth electrode, prepared identically to the third, underwent electrolysis within a CO<sub>2</sub>-saturated 0.5M KHCO<sub>3</sub> solution (20 min purge at 50 mL/min) containing a -1.5V (Reference Electrode: Ag/AgCl (3M); Counter Electrode: Pt wire) for a duration of 15 minutes. Analysis of the C 1s spectrum reveals the presence of K 2p peaks (296 eV and 293.2 eV) and O=CO peaks at 288.6 eV, attributed to residual carbonate originating from the electrolyte. Slight shifts in the peaks corresponding to Nafion in the C 1s and F 1s spectra ( $\Delta$ energy = 0.3 eV) are attributed to the presence of KHCO<sub>3</sub> at the surface or to a marginal degradation. The observed variation of the F/C ratio ( $\Delta$ =0.3) can be attributed to the presence of carbonate species.

Examination of the Ag 3d spectrum reveals the presence of two distinct Ag species, as evidenced by asymmetrical peaks with the emergence of a satellite peak (377.8 eV). The first species aligns with the starting material (368.8 eV), with an identical width at half-maximum. The second species, more prominent, exhibits a narrower profile (368.2 eV), typically associated with metallic silver<sup>17,18</sup>, and is attributed as the source of the satellite peak.

## Synthesis of Silver phenylacetylide



$\text{AgNO}_3$  (15.4684g mmol) was solubilized in a mixture of MeOH (40 mL) and water (10 mL). To this solution was added dropwise a concentrated solution of  $\text{NH}_4\text{OH}$  (25%) (5mL). The solution turned brown and became clear again at the end of the addition. A solution of phenylacetylene (10mL) in MeOH (10mL) was then added slowly to the mixture, and a white precipitate started forming directly, and the solution was stirred at RT for 3H. The solution was filtered on a nylon membrane filter (0.4 $\mu\text{m}$ ), and the resulting white solid was washed with water, then MeOH and dried under a reduced atmosphere with phosphorus pentoxide for 48H. The obtained product was a white solid (18.83 g; 99% yield to phenylacetylene).

$^1\text{H}$  NMR (400 MHz) DMSO-d<sub>6</sub>: 6.97 (6H,s)

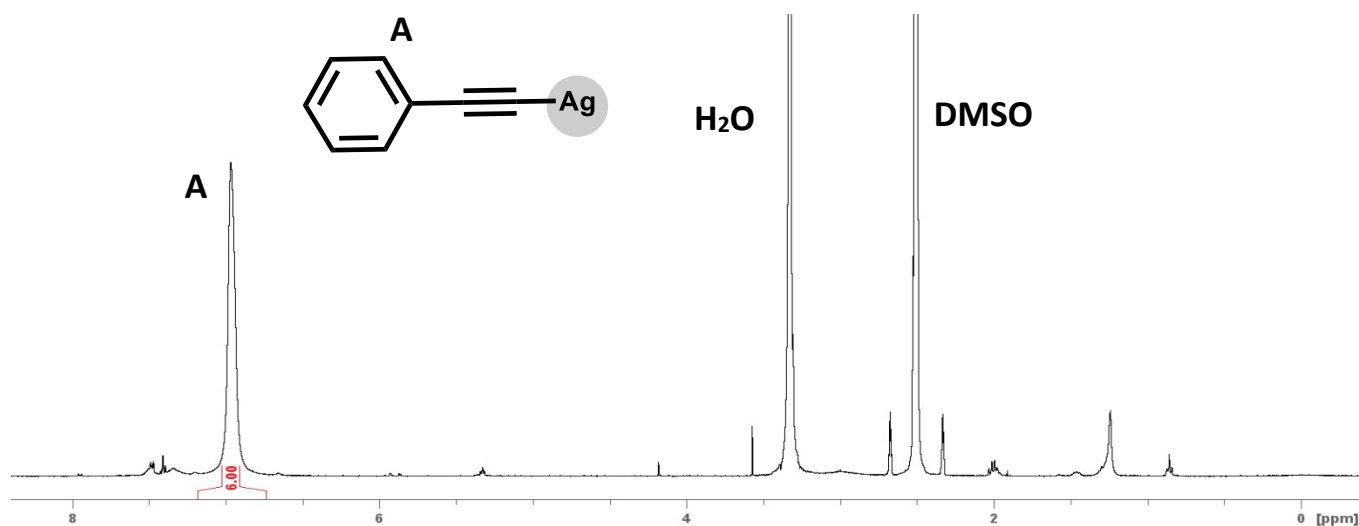
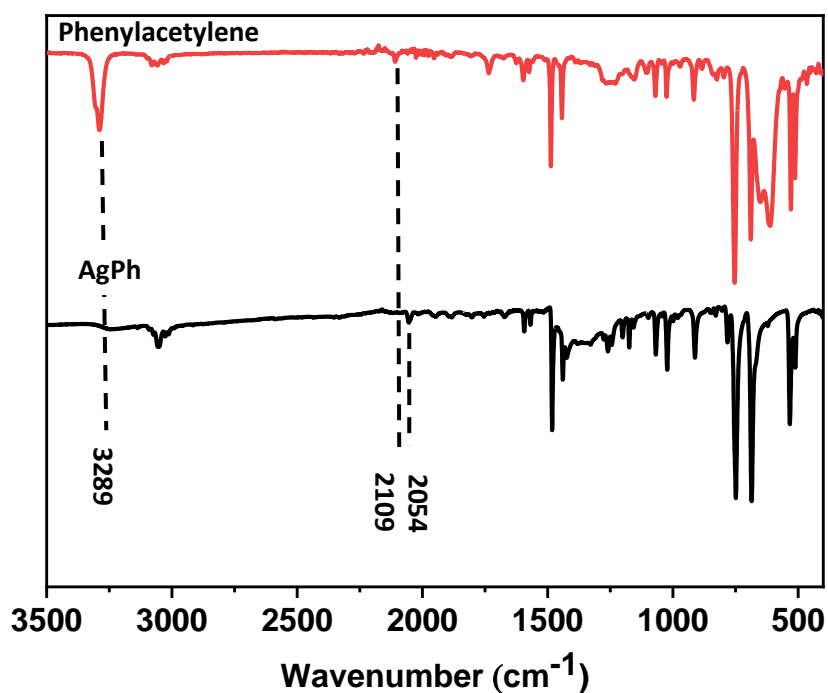
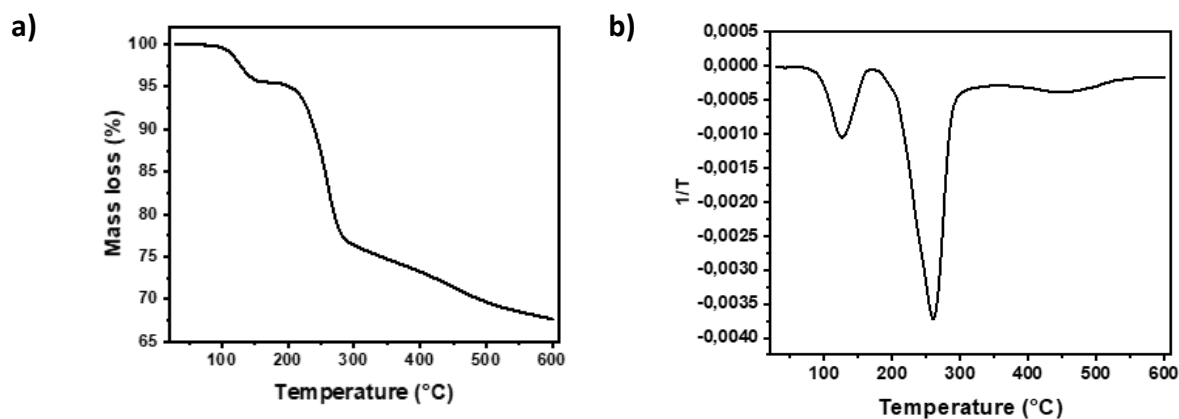


Figure S3-3:  $^1\text{H}$  NMR spectrum of  $\text{AgPh}$  in DMSO-d<sub>6</sub> using a 400 MHz spectrometer



**Figure S3-4:** IR-ATR spectrum of phenylacetylene (red) and silver phenylacetylide (black). The highlighted peaks are assigned to the C-H stretching (3289 cm<sup>-1</sup>) of the acetylene, and the peaks at 2109 and 2054 cm<sup>-1</sup> are assigned to the C≡C symmetric stretching for phenylacetylene and AgPh, respectively.



**Figure S3-5:** TGA measurement of AgPh **a)** mass loss (%) vs T (°C) **b)** 1/T vs T. The first mass loss is assumed to be residual solvents while the second mass loss is attributed to the organic part degradation.

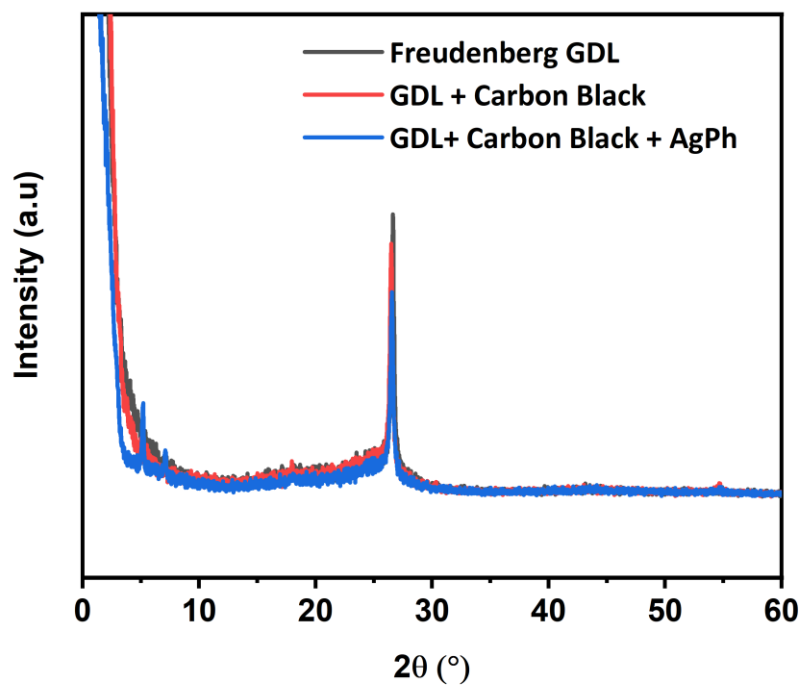


**Figure S3-6** Powder XRD of a Freudenberg GDL (Black) A GDL covered with a mixture of Nafion and Carbon Black (Red) A GDL covered with a mixture of Nafion, Carbon Black and AgPh (Blue). The peak observed at 26° is assumed to be a polymer additive on the raw GDL substrate.

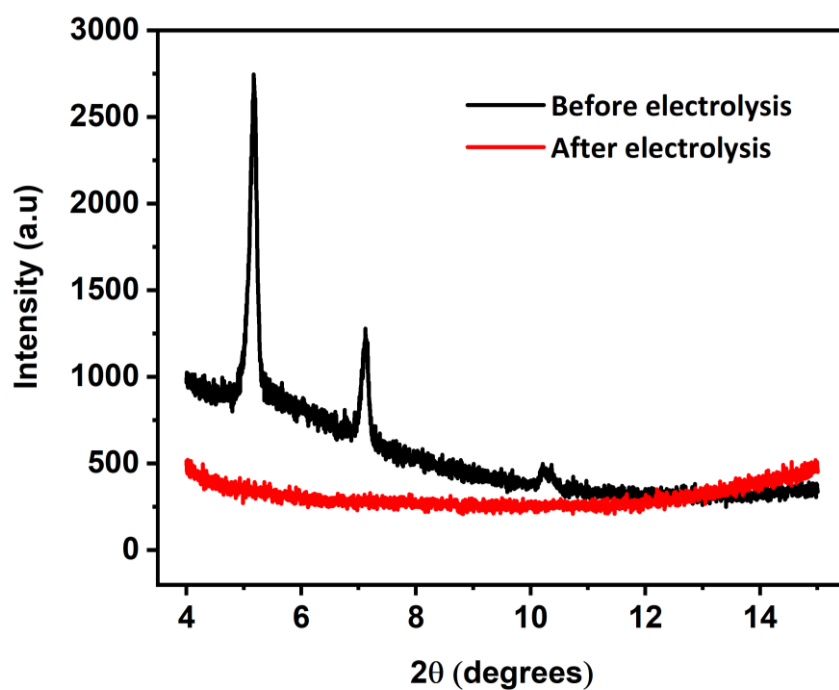


**Figure S3-7** Powder XRD of an electrode Before (Black) and After (Red) electrolysis. The crystalline structure is maintained during the electrode preparation and lost after electrolysis.

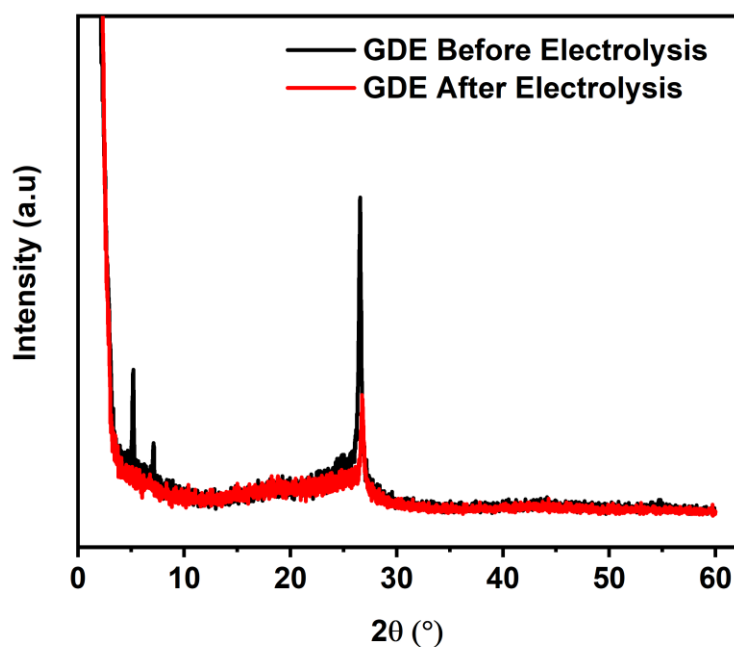


**Figure S3-8** Powder XRD between 2° and 60° of an electrode Before (Black) and After (Red) electrolysis. The crystalline structure is maintained during the electrode preparation and lost after electrolysis

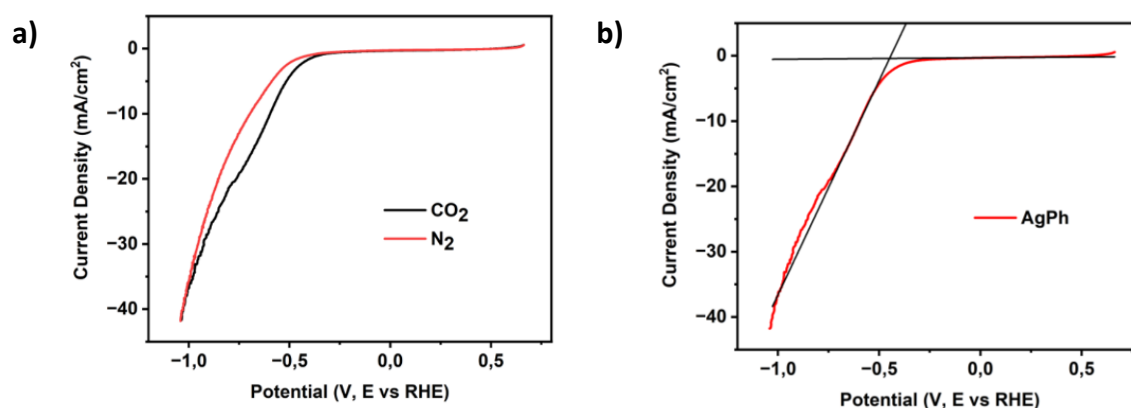


**Figure S3-9:** a) LSV measurement at 10 mV/s (2nd scan) of the deposited AgPh on the GDE substrate in CO<sub>2</sub> (Black) and N<sub>2</sub> (Red) saturated 1 M KHCO<sub>3</sub> solution b) LSV measurement at 10 mV/s (2nd scan) of the deposited AgPh on the GDE substrate in a CO<sub>2</sub> saturated 1 M KHCO<sub>3</sub> solution. Catalytic threshold is attributed to the intersection point between faradic current tangent and capacitive current tangent. The catalytic threshold is measured to be -0.452 V vs RHE Corresponding to  $\eta_{CO_2 \text{ to } CO} = 0.383$  V.

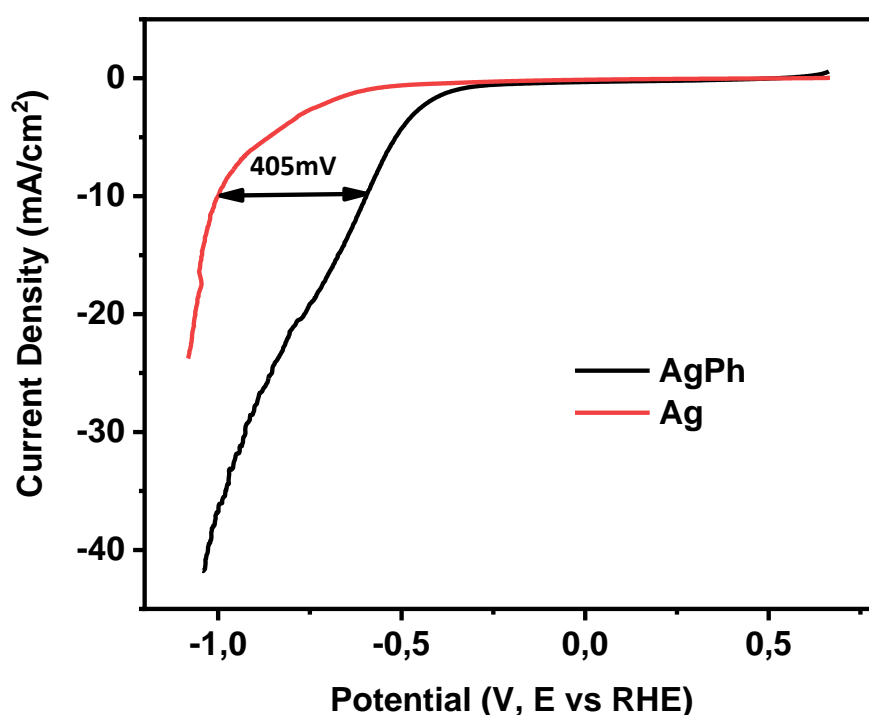


**Figure S3-10:** LSV measurement at 10 mV/s (2nd scan) of the deposited AgPh on the GDE substrate (Black) compared to a silver electrode (mirror polished) (Red) in a CO<sub>2</sub>-saturated 1 M KHCO<sub>3</sub>. The Ag overpotential at 10mA/cm<sup>2</sup> compared with AgPh is measured to be 405 mV.



### Calculation of TON and TOF

The Turnover Number (TON) and Turnover frequency (TOF) of AgPh for CO production were calculated from the following equations:

$$TON = \frac{n_{max\ CO}}{n_{active\ sites}}$$

Equation S3-7

$$TOF = \frac{TON}{t_{experiment}}$$

Equation S3-8

With  $n_{max\ CO}$  corresponding to the CO production at a given potential or current and  $n_{active\ sites}$  corresponding to the number of active catalytic species on the electrode and  $t_{experiment}$  the experiment time in s.

Following a common methodology<sup>20-23</sup>, the Electrochemically active surface area (ECSA) of the electrode was estimated by probing the redox reaction of the ferricyanide/ferrocyanide couple. Cyclic voltammetry (CV) were recorded at various scan rates (5, 10, 15 and 20 mV/s) with a 25 mM concentration of K<sub>3</sub>[Fe(CN)<sub>6</sub>] in a 0.1 M KCl supporting electrolyte solution. The solution was initially degassed with N<sub>2</sub>. Then the potential of the working electrode was swept between 700 mV and -200 mV vs. Ag/AgCl (3 M KCl) at variable scan rates (mV s<sup>-1</sup>). Between each CV, the solution was bubbled with N<sub>2</sub> and stirred to quickly reach back to the initial conditions.

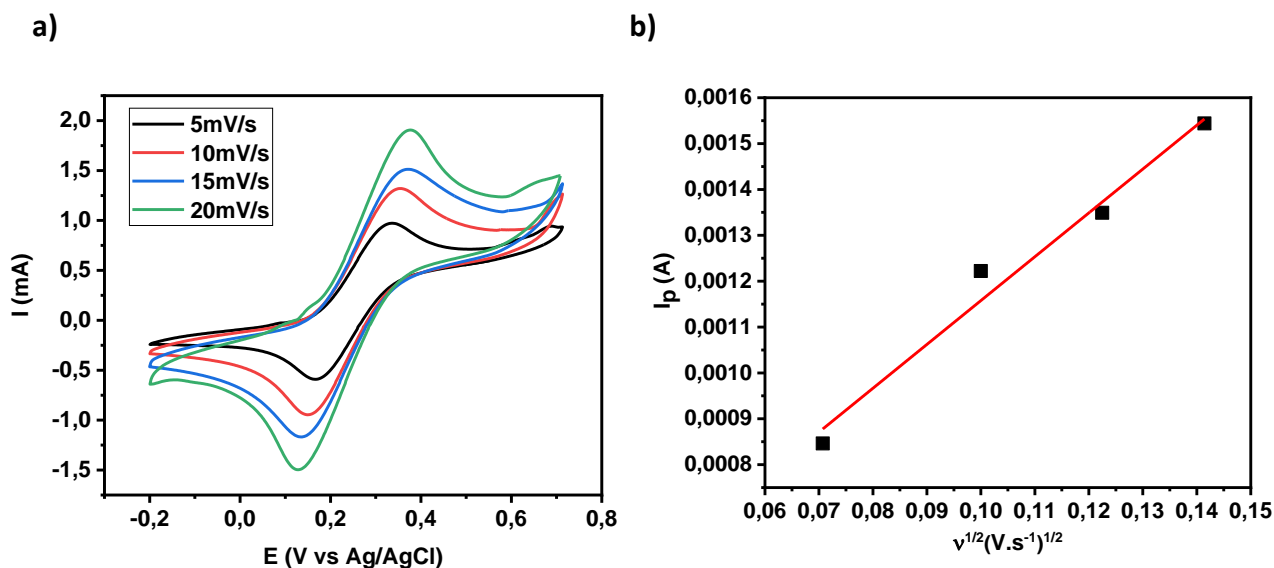


**Figure S 3-11:** a) Cyclic voltammograms (CV) of a 25 mM potassium ferrocyanide in a 0.1M KCl solution using an AgPh electrode at various scan rates (5, 10, 15 and 20mV/s). Cathodic and anodic peak currents correspond to the redox activity of ferrocyanide; b) Peak current as a function of the square root of scan rate. The ECSA is estimated from the slope of the plot. ECSA= 0.724 cm<sup>2</sup>, R<sup>2</sup>=0.97

Electrochemically active surface areas (ECSA) were estimated from the Randles-Sevcik equation, as follows:

$$I_p = (2.69 \times 10^5) n^{3/2} A D^{1/2} \nu^{1/2} C$$

**Equation S3-9**

with  $I_p$ : reduction peak current,  $n$ : number of moles of electrons per mole of electroactive species,  $A$ : area of electrode (cm<sup>2</sup>),  $D$ : diffusion coefficient (cm<sup>2</sup>.s<sup>-1</sup>),  $\nu$ : scan rate (V.s<sup>-1</sup>),  $C$ : concentration (mol.cm<sup>-3</sup>). The diffusion coefficient of ferricyanide is  $3.85 \times 10^{-6}$  cm<sup>2</sup> s<sup>-1</sup> at its concentration  $25 \times 10^{-6}$  mol.cm<sup>-3</sup>. The ECSA ( $A$ ) is estimated from the slope of the plot of  $I_p$  versus  $\nu^{1/2}$ .

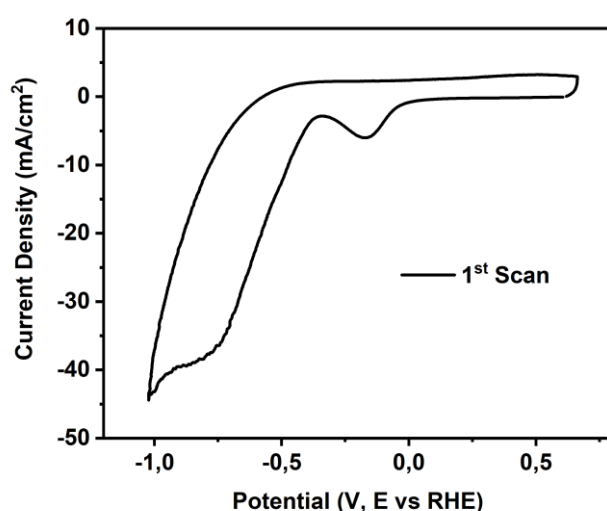
The surface loading ( $\Gamma[\text{Ag}]$  as mol cm<sup>-2</sup>) of the catalyst was calculated through the integration of the reduction wave at -0.218V vs RHE attributed to  $\text{Ag}^+ \rightarrow \text{Ag}$  on the CV scan (**Figure S3-12**) using the equation:

$$\Gamma[\text{Ag}] = q/nFA$$

**Equation S3-10**

where  $q$  is the charge (C) obtained from the integration of the reduction peak divided by the scan rate,  $n$  is the number of electrons involved in the redox process per Ag centre ( $n = 1$ ),  $F$  is the Faraday constant (96485 C mol<sup>-1</sup>), and  $A$  is the electrode surface area (0.724 cm<sup>2</sup>).

The obtained value was then correlated with the amount of Ag deposited on the electrode (1.85  $\mu\text{mol}$ ) which corresponds to 6.96% of active silver catalyst on the electrode. Calculated TOFs are represented in **Figure S3-13** and **Figure S3-19**.  $\text{TOF}_{\text{max}}$  was measured at 300mA/cm<sup>2</sup> and was calculated to be 10.95 s<sup>-1</sup> in our flow cell device.

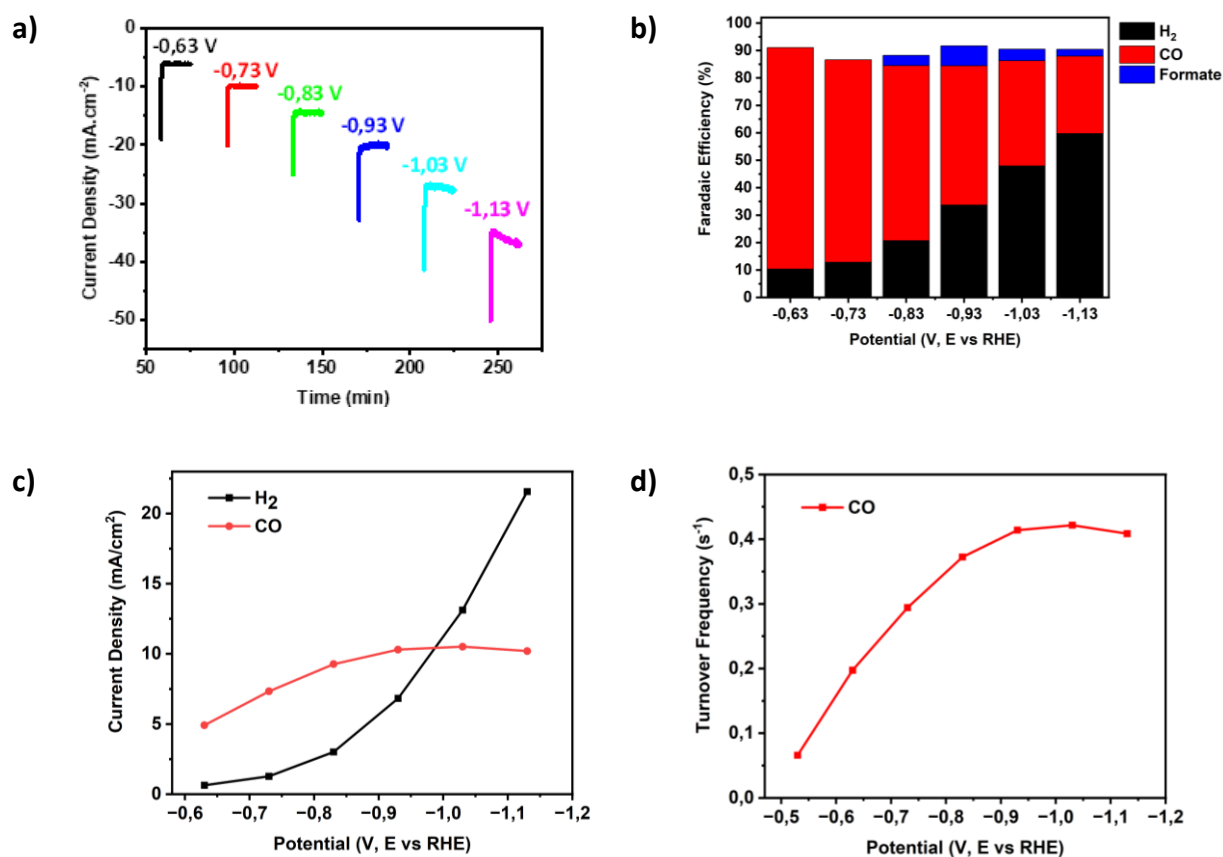


$$\Gamma[\text{Ag}] = q/nFA$$

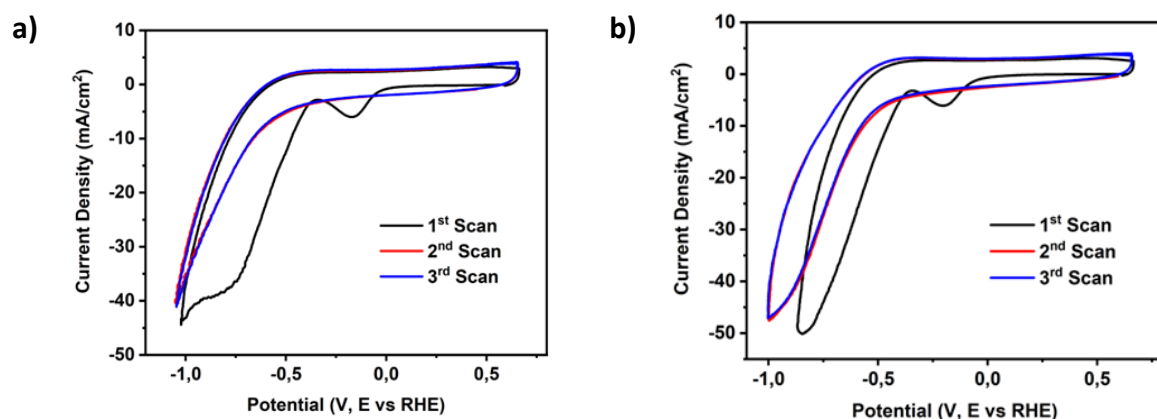
$$q = 9.0172 \text{ mC}$$

$$\Gamma[\text{Ag}] = 129 \text{ nmol}$$

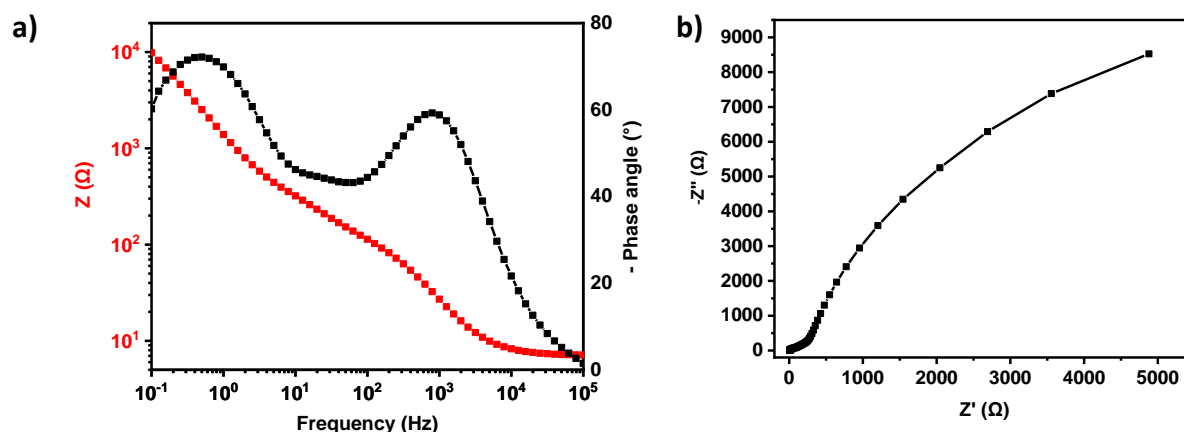
**Figure S3-12:** CV measurement at 100 mV/s of the deposited AgPh on the GDE substrate in a N<sub>2</sub> saturated 1 M KHCO<sub>3</sub> solution. The observed reduction peak is attributed to Ag<sup>+</sup> reduction to metallic Ag<sub>24</sub>. The integration of the reduction peak was used to calculate the amount of active silver species on the electrode.



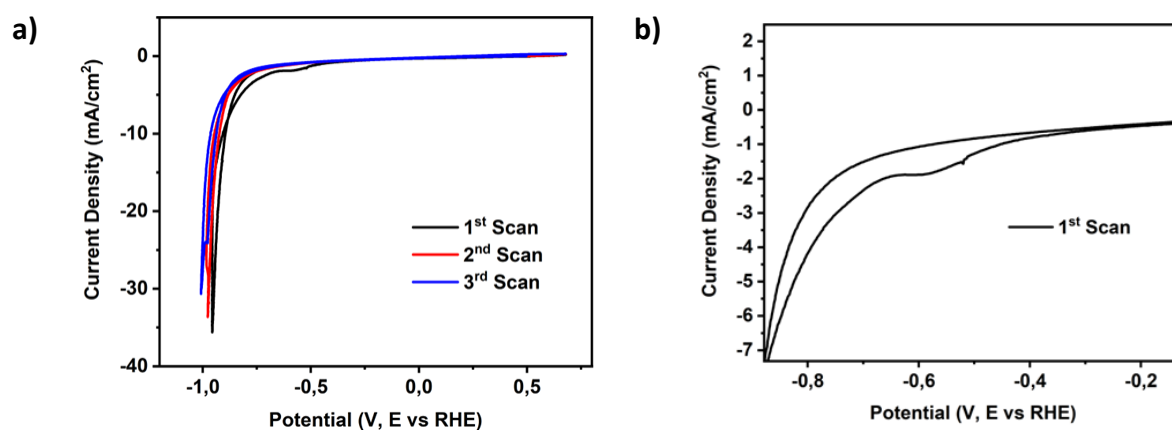
**Figure S3-13:** **a)** Chronoamperometry (CA)(15min) at various applied potentials (V, E vs RHE) of the deposited AgPh on the GDE substrate in a CO<sub>2</sub>-saturated 1 M KHCO<sub>3</sub>. **b)** Measured faradaic efficiency (FE) from direct GC and NMR quantifications for each CA **c)** CO and H<sub>2</sub> partial Current densities for AgPh at various applied potentials (15min chronoamperometry) in the 1M KHCO<sub>3</sub> aqueous solution **d)** Calculated TOF variation for CO<sub>2</sub>RR



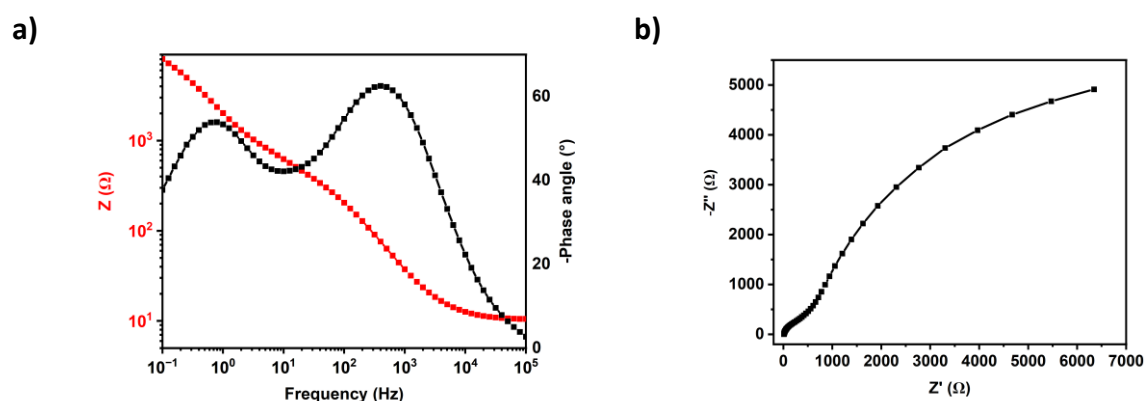
**Figure S3-14:** CV measurement at 100 mV/s of the deposited AgPh on the GDE substrate in **a)** N<sub>2</sub> and **b)** CO<sub>2</sub>-saturated 1 M KHCO<sub>3</sub> solution



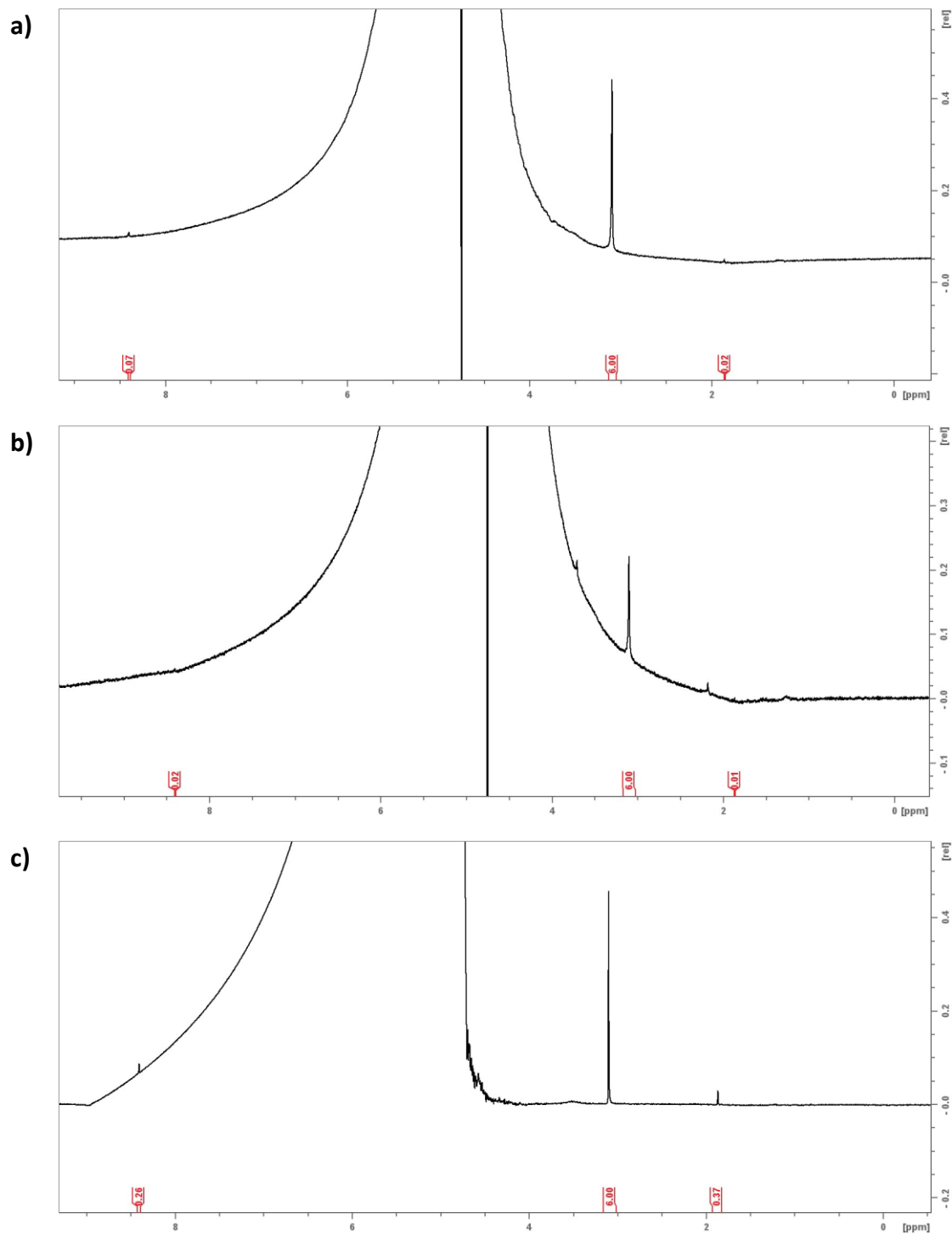
**Figure S3-15:** Electrochemical Impedance Spectroscopy (EIS) **a)** Bode plot **b)** Nyquist plot of a deposited AgPh on a GDE substrate in an N<sub>2</sub> saturated 1 M KHCO<sub>3</sub> solution. The initial Resistance is measured as the point where  $-Z''$  is equal to 0.



**Figure S3-16:** Cyclic Voltammetry (CV) measurement at 100 mV/s of a silver electrode (mirror polished) in an N<sub>2</sub> saturated 1 M KHCO<sub>3</sub> solution. **a)** CV scans repeated 3 times. No specific feature apart from a reduction peak attributed to surface Ag<sub>2</sub>O. **b)** zoom on the reduction peak



**Figure S3-17:** Electrochemical Impedance Spectroscopy (EIS) **a)** Bode plot **b)** Nyquist plot of a silver electrode (mirror polished) in an N<sub>2</sub> saturated 1 M KHCO<sub>3</sub> solution.



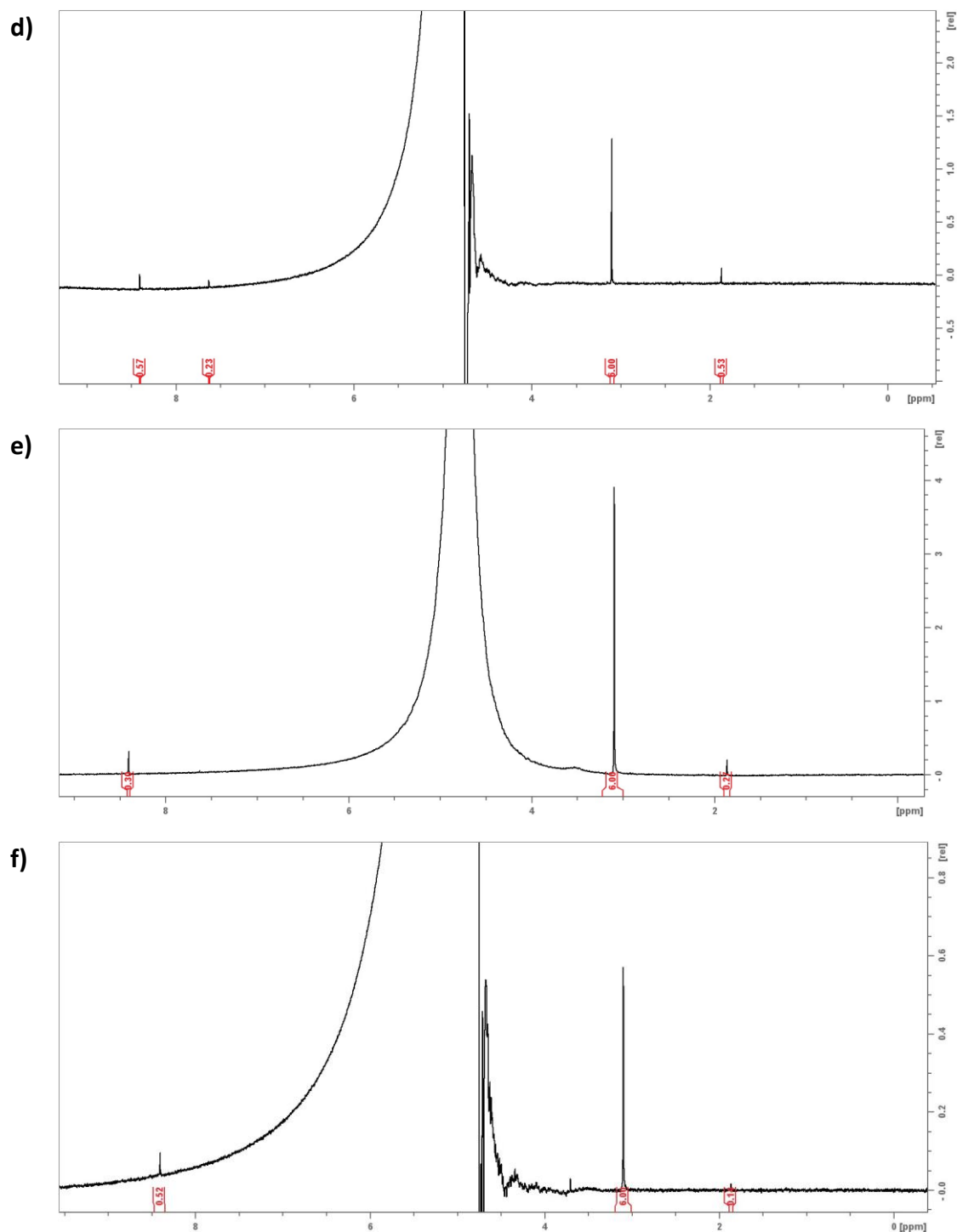


**Figure S3-18:** quantitative NMR measurement at variable applied potentials (E vs RHE) (uncorrected). DMSO<sub>2</sub> standard is fixed at 3.1 ppm. **a)** -0.63 V **b)** -0.73V **c)** -0.83V **d)** -0.93V **e)** -1.03V **f)** -1.13V. Observed liquids have been quantified against DMSO<sub>2</sub> and are referenced in

Applied potential (V, E vs RHE)	iR Corrected potential (V, E vs RHE)	Formate (%FE)
-0.63	-0.60	3.32
-0.73	-0.68	0.62
-0.83	-0.77	3,75
-0.93	-0.84	7,31
-1.03	-0.89	4,2
-1.13	-0.93	2,5

**Table S 3-1:** Quantification of the liquid products based on Figure S19 measured NMR spectra.

**Electrolyte before -1.5V contains liquid but their observed signal is barely distinguishable from the baseline and therefore these electrolytes were not quantified due to errors being larger than the potentially extracted value.**

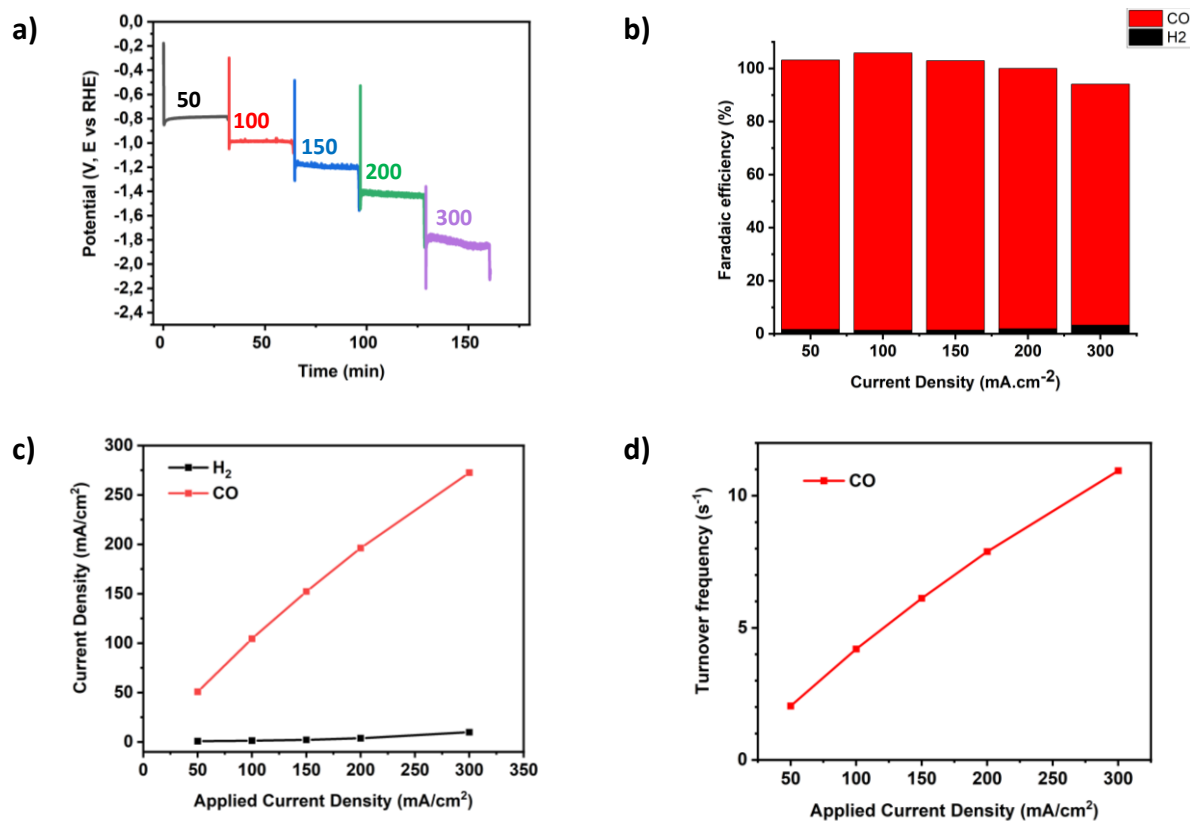


**Figure S3-19:** a) Chronopotentiometry (CP)(30min) at various constant currents of the deposited AgPh on the GDE substrate in the Flow Cell device. Both anolyte and catholyte compartments used a 1 M KHCO<sub>3</sub> solution. CO<sub>2</sub> flow rate: 10ml.min<sup>-1</sup>; Electrolyte flow rate: 4ml.min<sup>-1</sup> b) Measured faradaic efficiency (FE) from direct GC quantification for each preceding CP c) CO partial current density depending on iR corrected potential (average value over 30min) d) Turnover frequency (TOF) depending on the applied current.

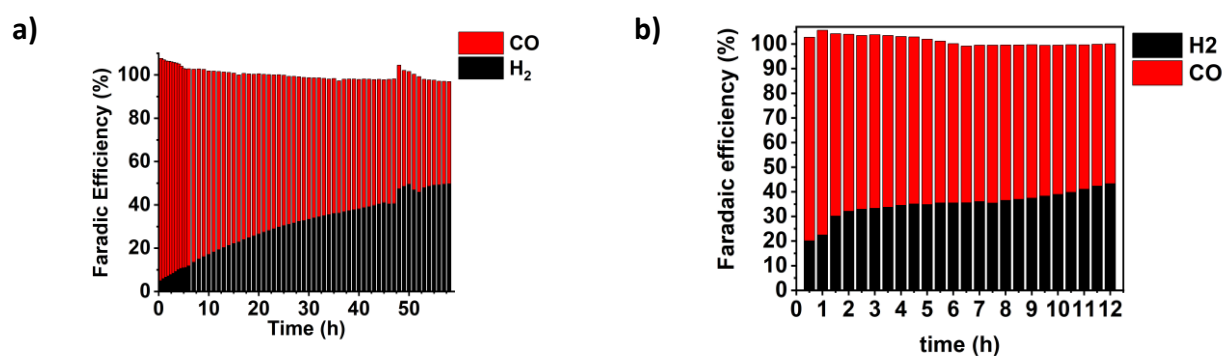


**Figure S3-20:** Faradaic yields obtained from in-line GC quantification a) 64h long chronopotentiometry at 50 mA.cm<sup>-2</sup> b) 12h long chronopotentiometry at 200 mA.cm<sup>-2</sup> of Flow cell experiments (1 M KHCO<sub>3</sub>; counter electrode: Pt on titanium plate (1 cm<sup>2</sup>); working electrode: AgPh/C (geometrical surface: 1 cm<sup>2</sup>))



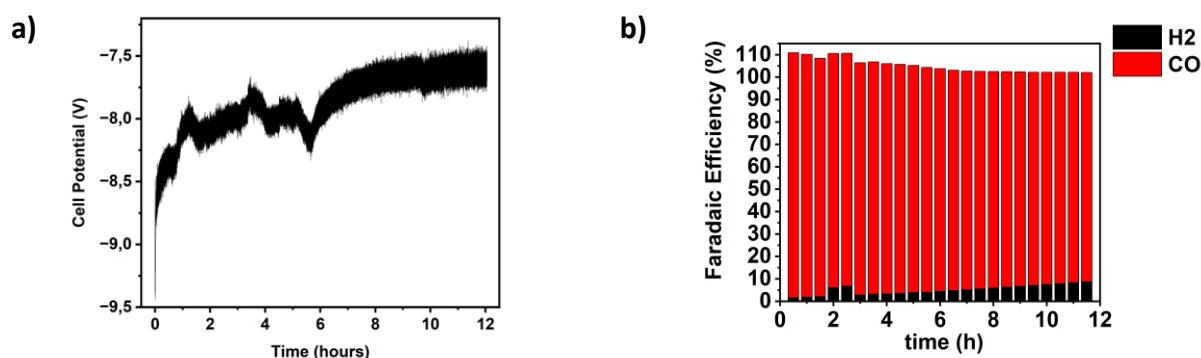


**Figure S3-21:** a) Chronopotentiometry at 100 mA/cm<sup>2</sup> (uncorrected cell potential) for a 12h durability test b) Faradaic yields from in line GC quantification of 12h long chronopotentiometry Flow cell experiments (1 M KHCO<sub>3</sub>; counter electrode: Pt on titanium plate (1 cm<sup>2</sup>); working electrode: AgPh/C (geometrical surface: 1 cm<sup>2</sup>))

	CB	C Nafion	C autre	O	Ag	S	F	K	F/C polymer
A)	99,3			0,5		0,2			
B)	56,7	10,4		3,1		0,7	29,2		2,8
C)			81,2	3	15,8				
D)	52,1	9,7	6,1	3,1	1,8	0,7	26,5		2,7
E)	40	8,1	15,2	9	1,3	0,9	20,6	1,9	2,5

**Table S3-2:** XPS Elemental quantification **A)** carbon black on GDE **B)** carbon black and Nafion on GDE **C)** AgPh powder **D)** AgPh, Carbon black and Nafion on GDE before electrolysis **E)** AgPh, Carbon black and Nafion on GDE after electrolysis. CB stands for Carbon Black. C Nafion refers to the carbon content related to Nafion polymer and F/Cpolym refers to the ratio of Fluor and carbon signals related to Nafion.

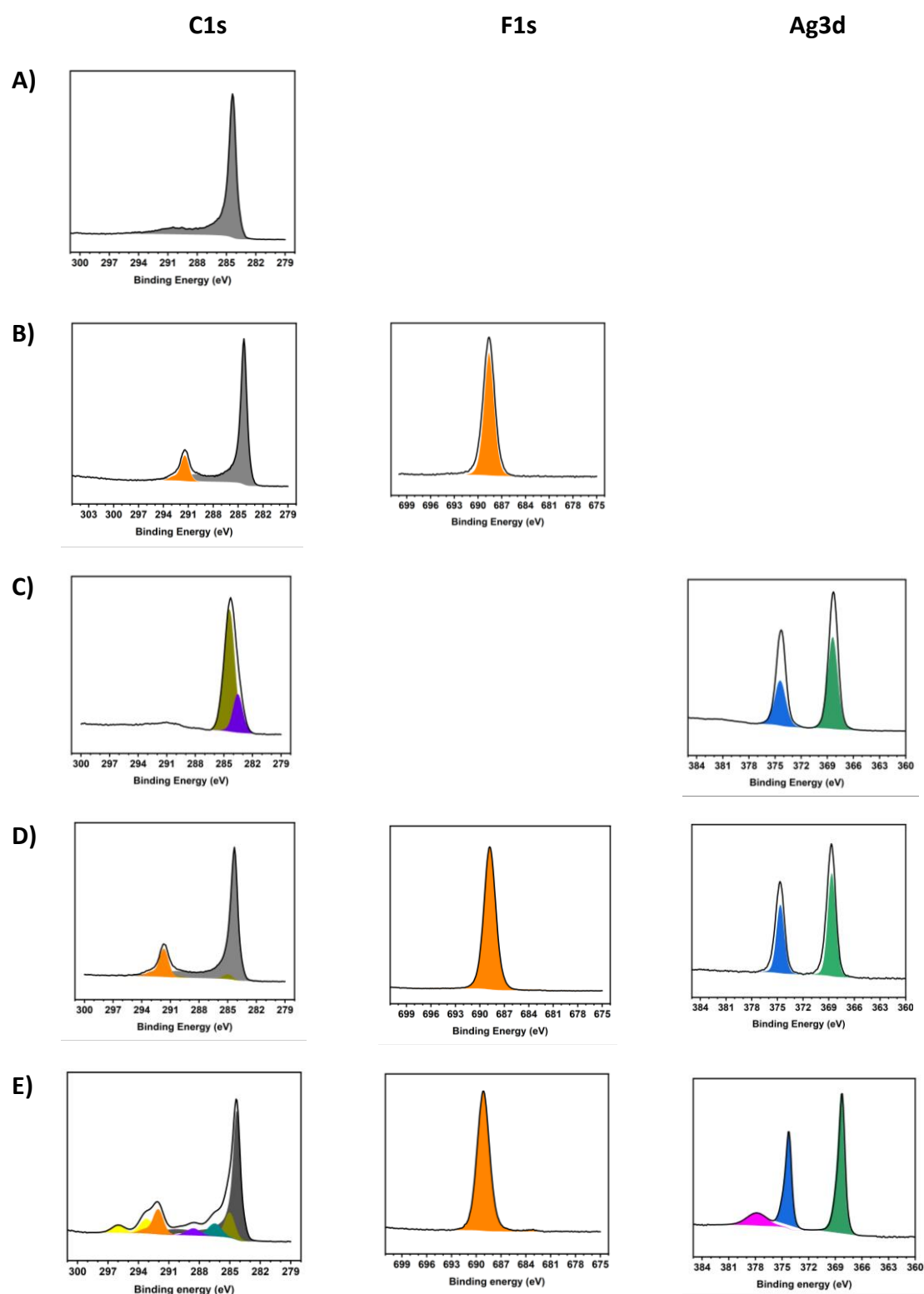


**Figure S3-22:** XPS Elemental quantification and their related XPS spectra (C1s, F1s and Ag 3d regions) **A)** carbon black on GDE **B)** carbon black and Nafion on GDE **C)** AgPh powder **D)** AgPh, Carbon black and Nafion on GDE before electrolysis **E)** AgPh, Carbon black and Nafion on GDE after electrolysis. **The observation of O=CO bond and O content increase after electrolysis are assumed to be carbonate salt accumulation on the GDL surface or the formation of COOH and OH groups onto the GDL.**

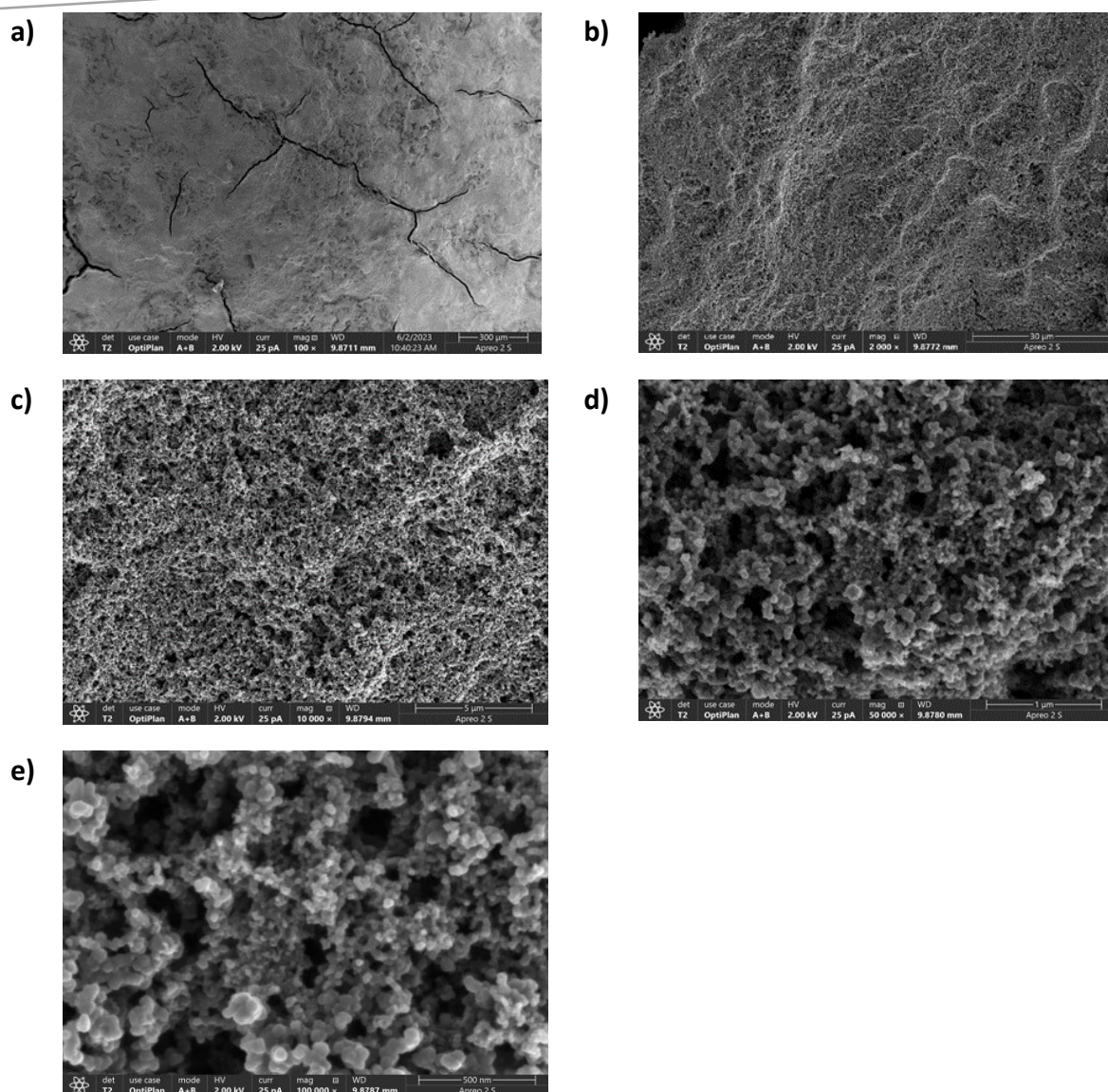


**Figure S3-23:** SEM images of the deposited Ag-Ph mixed with CB and Nafion on a GDE (before electrolysis) **a)** x100 magnification. **b)** x2000 magnification **c)** x 10 000 magnification **d)** x50 000 magnification **e)** x100 000 magnification.

The obtained surface is rough with apparent cracks in the smaller magnifications attributed to the drying of the material slurry during the material deposition. When the magnification is enhanced the carbon particles are becoming apparent and a large surface roughness is observed confirming a high surface area of the electrode. Unusual Structures or aggregates corresponding to silver acetylide are not observed.

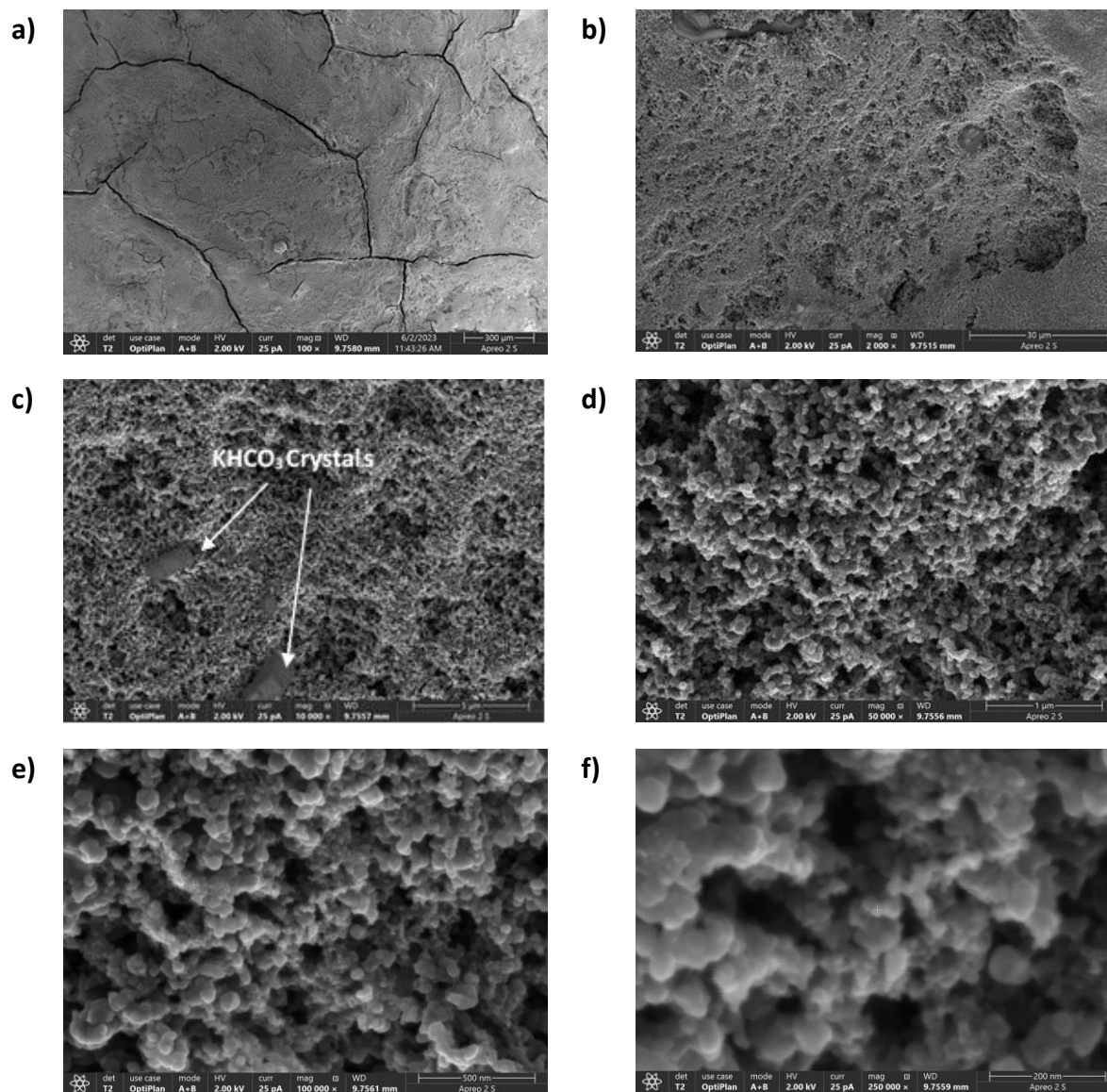


**Figure S3-24:** SEM images of the deposited Ag-Ph mixed with CB 5Vulcan and Nafion on a GDE (after electrolysis) **a)** x100 magnification **b)** x2000 magnification **c)** x 10 000 magnification **d)** x50 000 magnification **e)** x100 000 magnification **f)** x250 000 magnification.

**The observed cracks are due to the deposition technique and do not enlarge upon electrolysis. Important roughness and porosity are seen. Apart from the deposition of bicarbonate crystals, there is no visual degradation of the electrode surface.**



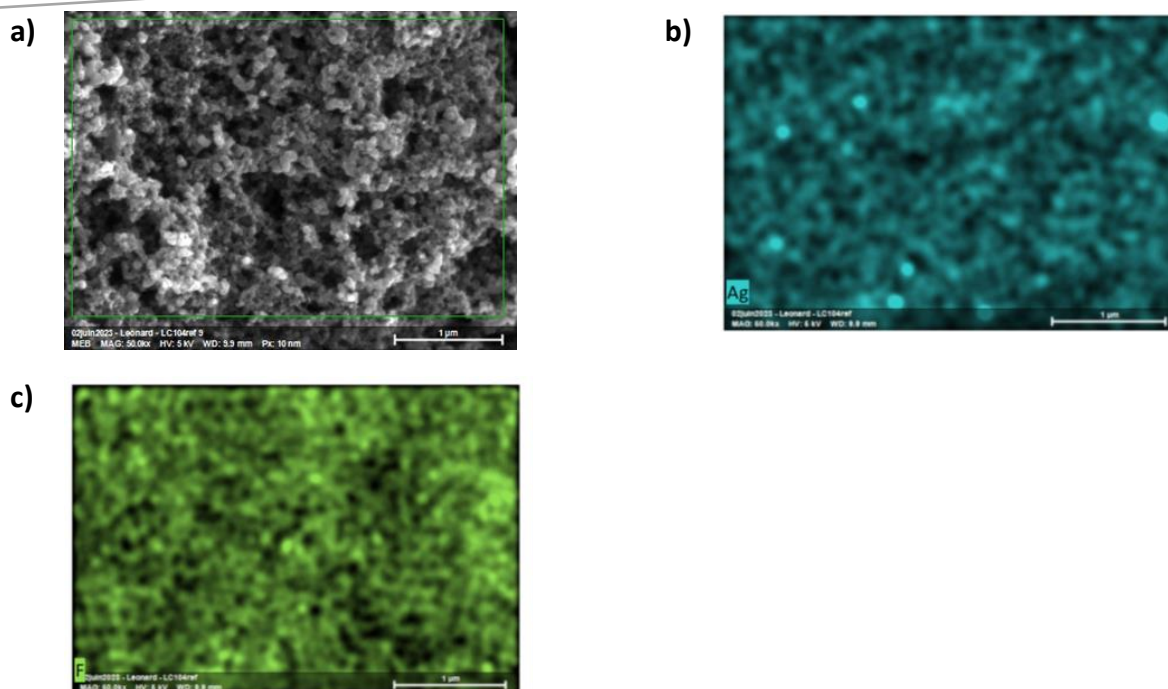


**Figure S3-25:** EDS elemental mapping of AgPh electrodes **a)** SEM image at 50 000 magnification **b)** Silver elemental mapping **c)** Fluorine elemental mapping EDS indicates a homogeneous deposition of AgPh and Nafion on the electrode surface. **The images show a good dispersion of the catalytic Silver material on the surface alongside the Nafion binder.**

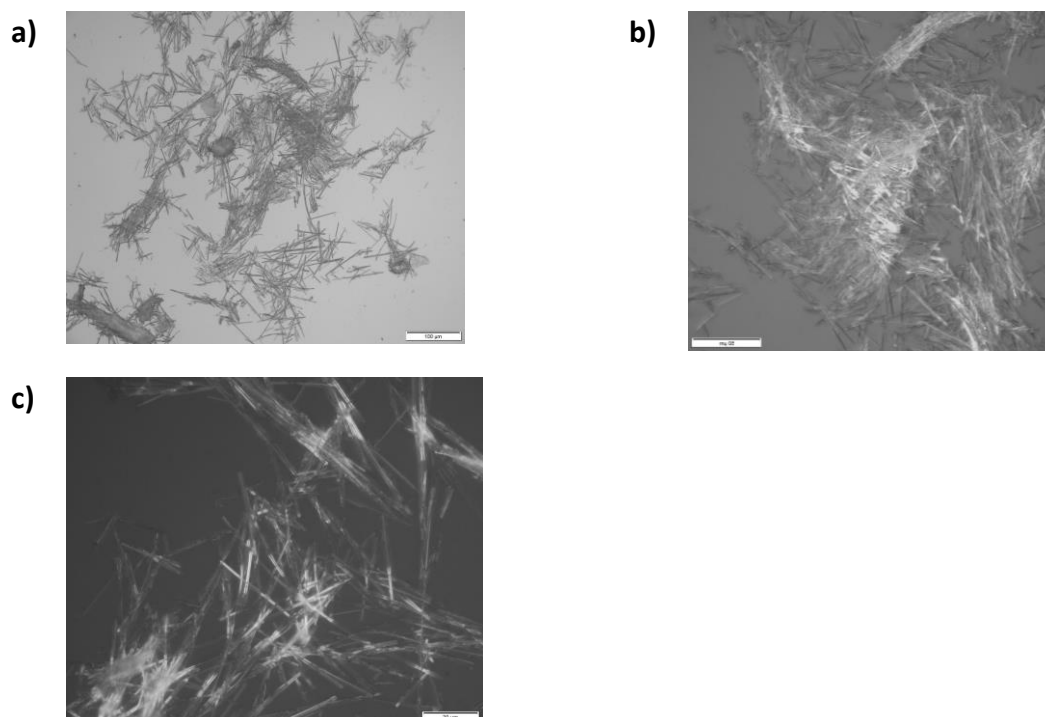
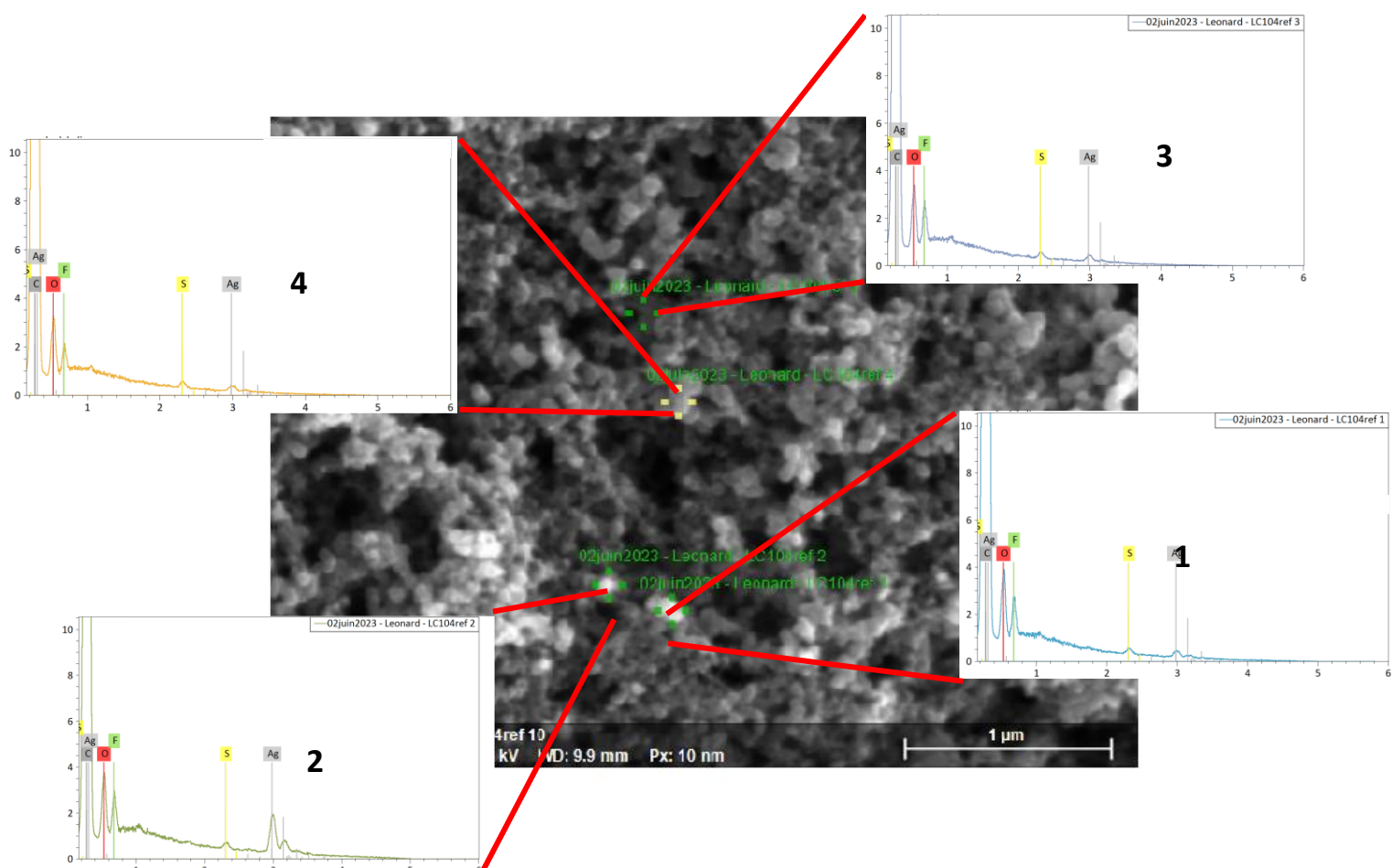


**Figure S3-26:** Microscope images of AgPh **a)** 10x magnification **b)** 20x with polarized light **c)** 50x with polarized light. **Formation of anisotropic structures is directly observed upon reaction, leading to needle-shaped crystals. They were confirmed to be of crystalline nature from polarized light.**



Spectrum	Carbon (%)	Oxygen (%)	Fluorine (%)	Sulfur (%)	Silver (%)
1	96.58	1.70	0.71	0.30	0.71
2	92.23	2.06	0.93	0.38	4.39
3	96.69	1.62	0.76	0.30	0.64
4	97.11	1.55	0.49	0.30	0.55
mean	95.65	1.73	0.72	0.32	1.57
sigma	2.29	0.23	0.18	0.04	1.88
SigmaMean	1.15	0.11	0.09	0.02	0.94

**Figure S3-27** and **Table S3-3**: Quantitative elemental analysis by EDS at different regions of an AgPh electrode before electrolysis. (X axis: Energy keV; Y axis: cps).

While the EDS image shows a homogenous dispersion of the silver on a large scale the results are here pointing out specific sites where the silver concentration is important indicative of the crystals integrity.

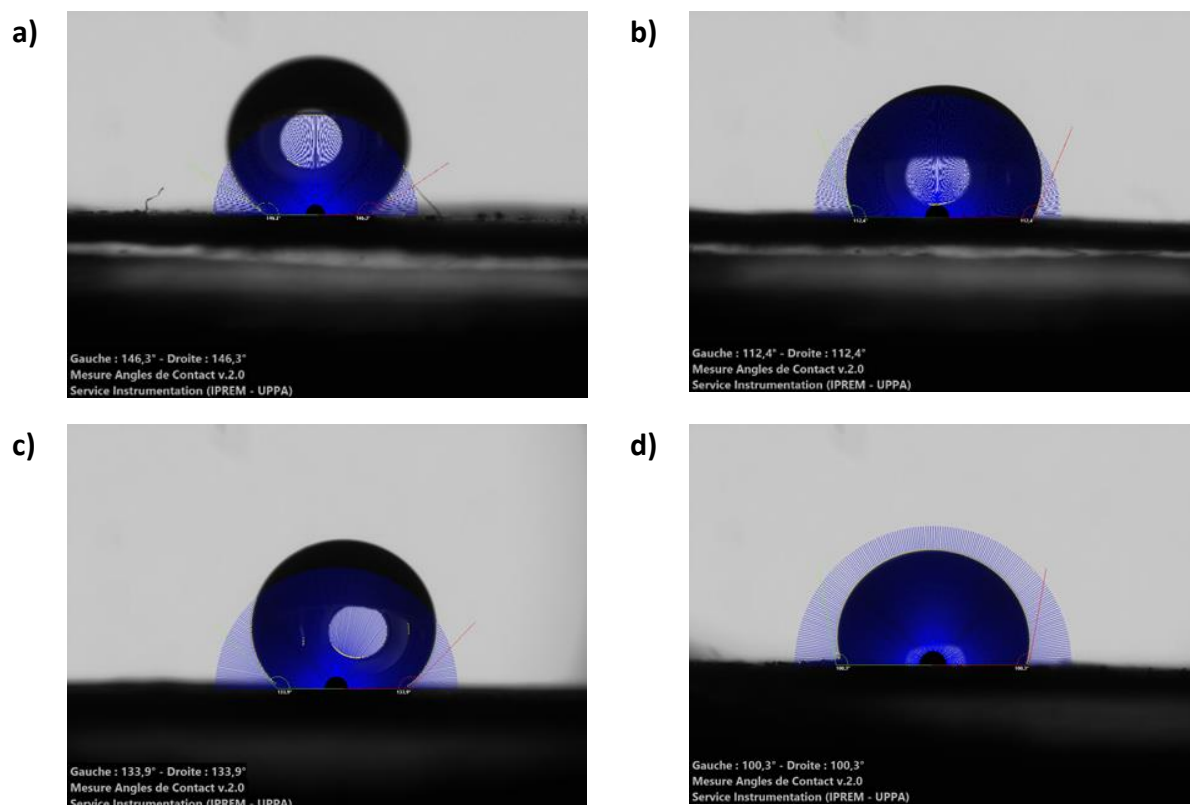


**Figure S3-28:** Contact angle of Freudenberg carbon paper **a)** before and **b)** after a 15 min electrolysis at 10 mA and of the prepared AgPh electrodes **c)** before and **d)** after electrolysis at 200 mA/cm<sup>2</sup>.

**A Hydrophobicity loss was observed both after electrolysis in the flow cell device and on a bare GDL after electrolysis at a relatively low current (10 mA.cm<sup>-2</sup>), a similar result as Sargent et al.**

25

	MP-AES Ag concentration (ppm)	Atomic Ag (mass%)	Theoretical Ag % (1:1 complex)
Ag-Ph	5.07	50.7	51.61

**Table S 3-4:** MP-AES measurement of AgPh (10 ppm solution in 3% HNO<sub>3</sub> prepared from a 1000 ppm solution in TFA: H<sub>2</sub>O (1:3)).

**The results are obtained from a calibration curve of 6 points between 1 and 20 ppm made from a 1000 ppm AgNO<sub>3</sub> solution in 3% HNO<sub>3</sub> (R<sup>2</sup>=0.998). The measured value is in accordance with a 1:1 complex family being the major product**

- (1) Qiao, J.; Liu, Y.; Zhang, J. *Electrochemical Reduction of Carbon Dioxide: Fundamentals and Technologies*. 396.
- (2) Chatterjee, T.; Boutin, E.; Robert, M. Manifesto for the Routine Use of NMR for the Liquid Product Analysis of Aqueous CO<sub>2</sub> Reduction: From Comprehensive Chemical Shift Data to Formaldehyde Quantification in Water. *Dalton Trans.* **2020**, 49 (14), 4257–4265. <https://doi.org/10.1039/C9DT04749B>.
- (3) Frisch, M. J.; Trucks, G. W.; Schlegel, H. B.; Scuseria, G. E.; Robb, M. A.; Cheeseman, J. R.; Scalmani, G.; Barone, V.; Petersson, G. A.; Nakatsuji, H.; Li, X.; Caricato, M.; Marenich, A. V.; Bloino, J.; Janesko, B. G.; Gomperts, R.; Mennucci, B.; Hratchian, H. P.; Ortiz, J. V.; Izmaylov, A. F.; Sonnenberg, J. L.; Williams-Young, D.; Ding, F.; Lipparini, F.; Egidi, F.; Goings, J.; Peng, B.; Petrone, A.; Henderson, T.; Ranasinghe, D.; Zakrzewski, V. G.; Gao, J.; Rega, N.; Zheng, G.; Liang, W.; Hada, M.; Ehara, M.; Toyota, K.; Fukuda, R.; Hasegawa, J.; Ishida, M.; Nakajima, T.; Honda, Y.; Kitao, O.; Nakai, H.; Vreven, T.; Throssell, K.; Montgomery, J. A., Jr.; Peralta, J. E.; Ogliaro, F.; Bearpark, M. J.; Heyd, J. J.; Brothers, E. N.; Kudin, K. N.; Staroverov, V. N.; Keith, T. A.; Kobayashi, R.; Normand, J.; Raghavachari, K.; Rendell, A. P.; Burant, J. C.; Iyengar, S. S.; Tomasi, J.; Cossi, M.; Millam, J. M.; Klene, M.; Adamo, C.; Cammi, R.; Ochterski, J. W.; Martin, R. L.; Morokuma, K.; Farkas, O.; Foresman, J. B.; Fox, D. J. *Gaussian 16 Revision C.01*, 2016.
- (4) Becke, A. D. Density-functional Thermochemistry. III. The Role of Exact Exchange. *J. Chem. Phys.* **1993**, 98 (7), 5648–5652. <https://doi.org/10.1063/1.464913>.
- (5) Vosko, S. H.; Wilk, L.; Nusair, M. Accurate Spin-Dependent Electron Liquid Correlation Energies for Local Spin Density Calculations: A Critical Analysis. *Can. J. Phys.* **1980**, 58 (8), 1200–1211. <https://doi.org/10.1139/p80-159>.
- (6) Lee, C.; Yang, W.; Parr, R. G. Development of the Colle-Salvetti Correlation-Energy Formula into a Functional of the Electron Density. *Phys. Rev. B* **1988**, 37 (2), 785–789. <https://doi.org/10.1103/PhysRevB.37.785>.
- (7) Stephens, P. J.; Devlin, F. J.; Chabalowski, C. F.; Frisch, M. J. Ab Initio Calculation of Vibrational Absorption and Circular Dichroism Spectra Using Density Functional Force Fields. *J. Phys. Chem.* **1994**, 98 (45), 11623–11627. <https://doi.org/10.1021/j100096a001>.
- (8) Grimme, S.; Ehrlich, S.; Goerigk, L. Effect of the Damping Function in Dispersion Corrected Density Functional Theory. *J. Comput. Chem.* **2011**, 32 (7), 1456–1465. <https://doi.org/10.1002/jcc.21759>.
- (9) Feller, D. The Role of Databases in Support of Computational Chemistry Calculations. *J. Comput. Chem.* **1996**, 17 (13), 1571–1586. [https://doi.org/10.1002/\(SICI\)1096-987X\(199610\)17:13<1571::AID-JCC9>3.0.CO;2-P](https://doi.org/10.1002/(SICI)1096-987X(199610)17:13<1571::AID-JCC9>3.0.CO;2-P).
- (10) Schuchardt, K. L.; Didier, B. T.; Elsethagen, T.; Sun, L.; Gurumoorthi, V.; Chase, J.; Li, J.; Windus, T. L. Basis Set Exchange: A Community Database for Computational Sciences. *J. Chem. Inf. Model.* **2007**, 47 (3), 1045–1052. <https://doi.org/10.1021/ci600510j>.
- (11) Pritchard, B. P.; Altarawy, D.; Didier, B.; Gibson, T. D.; Windus, T. L. New Basis Set Exchange: An Open, Up-to-Date Resource for the Molecular Sciences Community. *J. Chem. Inf. Model.* **2019**, 59 (11), 4814–4820. <https://doi.org/10.1021/acs.jcim.9b00725>.
- (12) Ehlers, A. W.; Böhme, M.; Dapprich, S.; Gobbi, A.; Höllwarth, A.; Jonas, V.; Köhler, K. F.; Stegmann, R.; Veldkamp, A.; Frenking, G. A Set of F-Polarization Functions for Pseudo-Potential Basis Sets of the Transition Metals Sc–Cu, Y–Ag and La–Au. *Chem. Phys. Lett.* **1993**, 208 (1), 111–114. [https://doi.org/10.1016/0009-2614\(93\)80086-5](https://doi.org/10.1016/0009-2614(93)80086-5).



- (13) Hay, P. J.; Wadt, W. R. Ab Initio Effective Core Potentials for Molecular Calculations. Potentials for K to Au Including the Outermost Core Orbitals. *J. Chem. Phys.* **1985**, *82* (1), 299–310. <https://doi.org/10.1063/1.448975>.
- (14) Boys, S. F.; Bernardi, F. The Calculation of Small Molecular Interactions by the Differences of Separate Total Energies. Some Procedures with Reduced Errors. *Mol. Phys.* **1970**, *19* (4), 553–566. <https://doi.org/10.1080/00268977000101561>.
- (15) Simon, S.; Duran, M.; Dannenberg, J. J. How Does Basis Set Superposition Error Change the Potential Surfaces for Hydrogen-bonded Dimers? *J. Chem. Phys.* **1996**, *105* (24), 11024–11031. <https://doi.org/10.1063/1.472902>.
- (16) Wang, M.; Torbensen, K.; Salvatore, D.; Ren, S.; Joulié, D.; Dumoulin, F.; Mendoza, D.; Lassalle-Kaiser, B.; Işci, U.; Berlinguette, C. P.; Robert, M. CO<sub>2</sub> Electrochemical Catalytic Reduction with a Highly Active Cobalt Phthalocyanine. *Nat. Commun.* **2019**, *10* (1), 3602. <https://doi.org/10.1038/s41467-019-11542-w>.
- (17) Seah, M. P.; Gilmore, I. S.; Beamson, G. XPS: Binding Energy Calibration of Electron Spectrometers 5—Re-Evaluation of the Reference Energies. *Surf. Interface Anal.* **1998**, *26* (9), 642–649. [https://doi.org/10.1002/\(SICI\)1096-9918\(199808\)26:9<642::AID-SIA408>3.0.CO;2-3](https://doi.org/10.1002/(SICI)1096-9918(199808)26:9<642::AID-SIA408>3.0.CO;2-3).
- (18) Bird, R. J.; Swift, P. Energy Calibration in Electron Spectroscopy and the Re-Determination of Some Reference Electron Binding Energies. *J. Electron Spectrosc. Relat. Phenom.* **1980**, *21* (3), 227–240. [https://doi.org/10.1016/0368-2048\(80\)85050-X](https://doi.org/10.1016/0368-2048(80)85050-X).
- (19) Liu, X.; Yi, Q.; Han, Y.; Liang, Z.; Shen, C.; Zhou, Z.; Sun, J.; Li, Y.; Du, W.; Cao, R. A Robust Microfluidic Device for the Synthesis and Crystal Growth of Organometallic Polymers with Highly Organized Structures. *Angew. Chem. Int. Ed.* **2015**, *54* (6), 1846–1850. <https://doi.org/10.1002/anie.201411008>.
- (20) Song, M.-J.; Hwang, S. W.; Whang, D. Non-Enzymatic Electrochemical CuO Nanoflowers Sensor for Hydrogen Peroxide Detection. *Talanta* **2010**, *80* (5), 1648–1652. <https://doi.org/10.1016/j.talanta.2009.09.061>.
- (21) Krejci, J.; Sajdlova, Z.; Nedela, V.; Flodrova, E.; Sejnohova, R.; Vranova, H.; Plicka, R. Effective Surface Area of Electrochemical Sensors. *J. Electrochem. Soc.* **2014**, *161* (6), B147. <https://doi.org/10.1149/2.091406jes>.
- (22) Ameer, Z. O.; Husein, M. M. Electrochemical Behavior of Potassium Ferricyanide in Aqueous and (w/o) Microemulsion Systems in the Presence of Dispersed Nickel Nanoparticles. *Sep. Sci. Technol.* **2013**, *48* (5), 681–689. <https://doi.org/10.1080/01496395.2012.712594>.
- (23) Morozan, A.; Johnson, H.; Roiron, C.; Genay, G.; Aldakov, D.; Ghedjatti, A.; Nguyen, C. T.; Tran, P. D.; Kinge, S.; Artero, V. Non-Precious Bimetallic Iron-Molybdenum Sulfide Electrocatalysts for Hydrogen Evolution Reaction in Proton-Exchange Membrane Electrolyzers.
- (24) Ma, M.; Trzeźniewski, B. J.; Xie, J.; Smith, W. A. Selective and Efficient Reduction of Carbon Dioxide to Carbon Monoxide on Oxide-Derived Nanostructured Silver Electrocatalysts. *Angew. Chem. Int. Ed.* **2016**, *55* (33), 9748–9752. <https://doi.org/10.1002/anie.201604654>.
- (25) Dinh, C.-T.; Burdyny, T.; Kibria, M. G.; Seifitokaldani, A.; Gabardo, C. M.; García de Arquer, F. P.; Kiani, A.; Edwards, J. P.; De Luna, P.; Bushuyev, O. S.; Zou, C.; Quintero-Bermudez, R.; Pang, Y.; Sinton, D.; Sargent, E. H. CO<sub>2</sub> Electroreduction to Ethylene via Hydroxide-Mediated Copper Catalysis at an Abrupt Interface. *Science* **2018**, *360* (6390), 783–787. <https://doi.org/10.1126/science.aas9100>.

## Chapter 4: Synthesis and characterization of a library of silver acetylides nanoclusters for CO<sub>2</sub> reduction

### Introduction

The electrochemical reduction of CO<sub>2</sub> into feedstocks, such as permanent gases or alcohols, is a promising alternative for offsetting greenhouse gas emissions.<sup>1–4</sup> This transformation is often done through electrochemistry and mediated by a catalytic species, usually a metal<sup>5,6</sup> or an insoluble molecular catalyst.<sup>7</sup> The advances in flow-cell and membrane electrode assembly designs have led to an important increase in performance compared to laboratory-scale electrolysis.<sup>8–12</sup> They use specific types of electrodes called gas diffusion layers (GDLs). Their porous nature allows them to overcome the intrinsically limited solubility of CO<sub>2</sub> in aqueous media. These electrodes, onto which the active species are deposited, enable the formation of a gas/electrolyte/catalyst interface where the local CO<sub>2</sub> concentration rises far above its solubility limit. The metals possessing sufficient reaction rates for industrial purposes have been limited to gold<sup>13</sup> and silver<sup>14–18</sup>, producing CO with high selectivity and copper, the only metal for which consistent C<sub>2+</sub> production has been shown<sup>19–25</sup>. Their deposition onto electrode substrates is particularly tedious<sup>26,27</sup> and issues related to flow reactors upscaling have prevented a fast performance increase, but recent works have shown that, given proper operating conditions and GDL nature, copper could form ethylene selectively<sup>11,22</sup>. While organometallic structures have been crucial for mechanistic characterisation, only a few can maintain catalytic currents above 100 mA.cm<sup>-2</sup>, and degradation of the structures commonly occurs during prolonged electrolysis.<sup>9,28–30</sup>

In this context, ligand-protected clusters have attracted attention in the field of electrocatalysis.<sup>31–37</sup> Among these, alkyne-based gold and silver clusters have recently been shown to possess excellent properties for the reduction of CO<sub>2</sub> towards CO.<sup>32,33,38–41</sup> They form a unique subclass of crystalline materials possessing a wide variety of geometries ranging from molecule-like to tubular infinite clusters. Their perfect crystalline arrangement is particularly attractive as these structures consequently possess well-defined reactive sites, giving access to intrinsic catalytic properties normally limited to molecular catalysts. They have been shown to undergo a specific reduction pattern in **Chapter 3**, leading to the formation of Ag(0) and the concomitant departure of a ligand from the structure both experimentally and from theoretical calculations. This mechanism has been shown to decrease the activation barrier, leading to greatly enhanced catalytic properties. Their particularly constrained and unusual geometries compared to common metallic nanoparticles could furthermore lead to important selectivity shifts, given that proper structures and ligands are found.

Before the novelty of the field, herein we describe the synthesis of an extensive library of silver acetylide clusters and study their characteristics in detail. The library was designed in such a way to provide clusters whose ligands bear antagonist electronic properties such as polyaromatic or alkyl groups with electron withdrawing or donating groups, to study the effect of the electronic structure of the ligand, bulkiness, and crystallinity on the catalytic properties of the compounds. The library was designed from commercially available alkyne precursors, demonstrating the versatility of the synthetic method in providing clusters with

different structural properties. Overall, the nature of the ligand was shown to have a significant impact on both the overpotential and activities but that the selectivity towards CO remained high in most cases.

## Results and discussion

Silver acetylides have long been known by experimental chemists. Indeed, silver salts have been used since the beginning of the 20th century as a test for alkyne group detection in organic molecules. A characteristic white precipitate of silver acetylide was known to form upon the addition of an ammoniacal silver salt solution to an alkyne-containing mixture. The silver (I) atoms readily form an  $\pi$  bond with the alkyne, effectively increasing the terminal proton lability. The latter is readily abstracted in the presence of a base such as ammonia, and a network of  $\sigma$  and  $\pi$  bonds is formed between the Silver (I) and the terminal alkynes. Similarly to other metallic clusters, the favourable formation of metal-metal bonds dictates the formation of large clusters of silver atoms with alkynyl groups positioned on the outer edge. The perfect ordering of the silver atoms is transferred over long distances, therefore leading to highly crystalline powders. Although generally limited to hundredth of nanometers in size, large single crystals of silver acetylides have been isolated,<sup>42</sup> and a plethora of X-Ray crystal structures are available to date. The highly crystalline nature of the clusters, distinguish themselves from classical metallic nanoparticles, in that a very high degree of order is maintained through both the metallic and ligand constituents of the assembly, hence the recent coining of “atomically precise” structures.

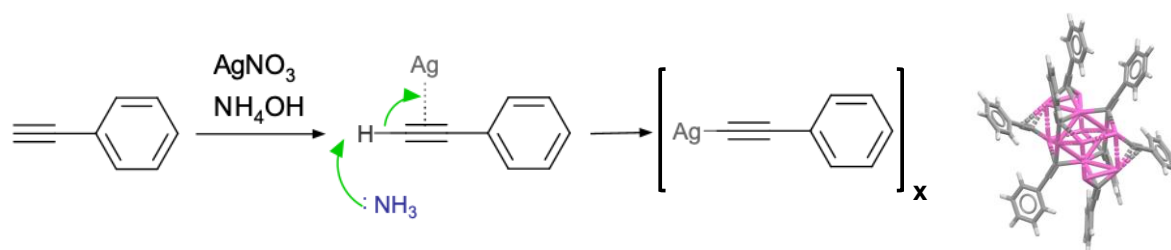


**Figure 4.1** Schematic representation of the mechanistic details of Scheiber's synthetic route to silver acetylides. The inset shows an X-ray crystal structure of phenyl acetylene-based silver acetylide.

Contrary to other metal complexes, however, silver acetylides have no significant nucleophilic character, conferring them high stability at neutral and basic pHs. As a consequence of both above-mentioned features, silver acetylides have found a perfect application in the field of CO<sub>2</sub> reduction. The extremely high level of structural control and extended stability confer silver acetylides remarkable catalytic properties.

Although the synthesis of silver acetylides relies on the underlying mechanistic details expounded above, a variety of different routes have been described. Silver salts such as silver nitrates, triflates or halogenates have been used in combination with different bases such as triethyl amine, ammonia, or hydroxide ions. In our previous report, however, we found that the general synthetic route described in the early 1960s by Schreiber and coworkers,<sup>43</sup> involving the preparation of a silver nitrate ammoniacal solution to which is added a solution of the alkyne derivative in methanol, was very well suited to multigram scale synthesis of silver acetylides clusters (**Figure 4.1**). The formation of a white, foam-like, precipitate ensues instantly, indicative of the formation of the silver acetylide species, isolated as an insoluble solid by simple filtration. The solubility in polar solvents such as DMSO or DMF is however sometimes sufficient to characterise the cluster via <sup>1</sup>H NMR, which shows unusually broad protons peaks reminiscent of polymeric species.

These results prompted us to apply the synthetic methodology to a library of commercial alkynes to confirm the versatility of the procedure and, more importantly, to draw a structure-properties relationship between the nature of the ligand comprising the thus formed acetylide and the catalytic properties towards the CO<sub>2</sub>RR. For that matter, alkyne precursors with a wealth of antagonistic structural properties were selected to form four main categories: alkyl, aromatics, electron acceptors and electron donors.

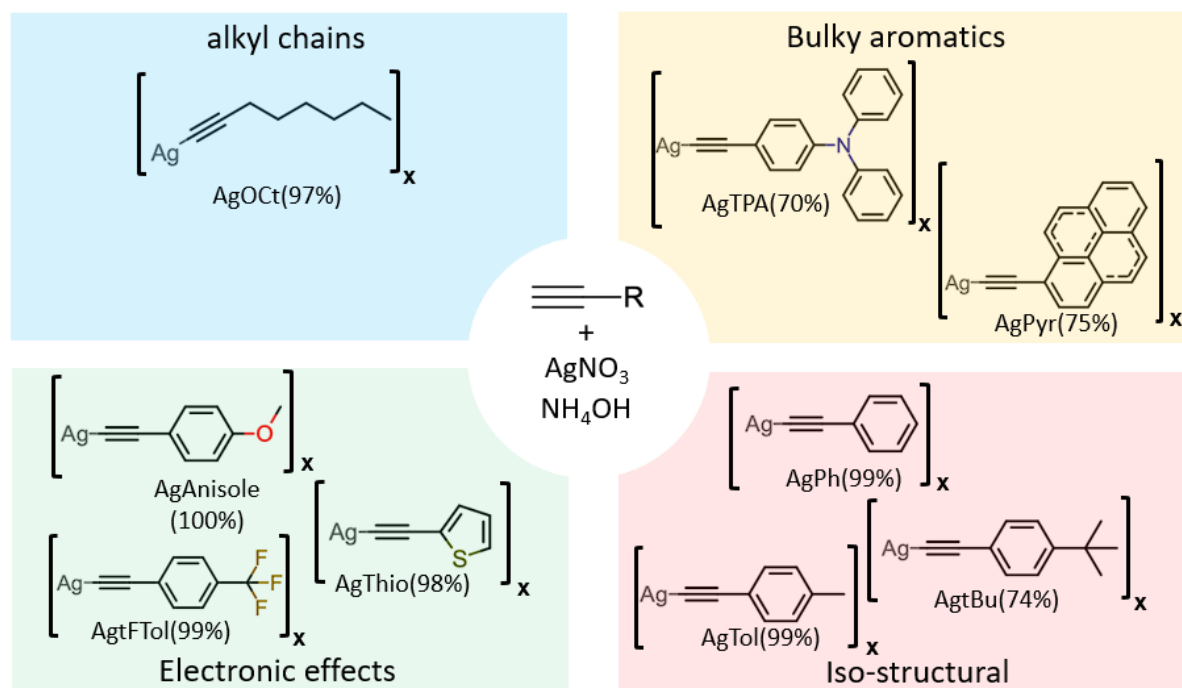


**Figure 4.2.** Schematic overview of the library of silver acetylides synthesised using Scheiber's route. The chemical structures are represented in their simplified form as the silver-carbanion species. However, crystal structures of identical and similar derivatives show that the solid-state structure of the compounds depicted form metallic clusters.

## Synthesis and spectral measurements

The main approach towards the design of the library was to build on the structure of our previously reported phenyl silver acetylide as a reference, swapping the benzyl group with groups possessing iso-structural features, groups inducing different electronic properties and sterically-hindered groups. As such, the anisole, thiophene and trifluorotoluene alkynes were selected to respectively introduce electron donating and electron withdrawing effects on the resulting silver acetylide. The pyrene and triphenylamine acetylides were synthesised to assess the effect of steric hindrance on both the structural and catalytic properties, while the synthesis of the AgOct alkyl analogue was attempted to assess if the order in the silver structure was maintained without the presence of  $\pi$ - $\pi$  interactions on the outer layer. Finally, two alkynes, namely compounds AgTol and Agt-Bu, were synthesized to assess the impact of subtle structural changes with respect to our reference phenylacetylene-based cluster on the crystallinity and on the derived catalytic properties. **Figure 4.2** summarises the chemical structures of the clusters thus synthesized, with their corresponding yields. A glance at the different classes of compounds shows how the reaction conditions are remarkably tolerant to different chemical groups. Second, it shows that very bulky groups, such as triphenylamine and pyrene groups, lead to silver acetylides in slightly lower yields, which we assume are limited by the high concentration reaction conditions favouring intermolecular  $\pi$ - $\pi$  stacking and a

consequent moderate reactive site availability. All acetylides were readily isolated by filtration and washing. All were found to be stable over time given that they are protected from the light.

For alkyl chain-based reagents, upon the reaction of the acetylene with an ammoniacal solution of silver, the formation of a white foamy compound is observed, followed by an almost instantaneous colour change to a darker colour. The synthesis of silver acetylides from shorter alkyl groups, propargyl amine and propargyl alcohol, resulted in a similar behaviour; however, in these cases, the final product corresponded to silver (0) nanoparticles. Interestingly, AgOOct acetylide was sufficiently soluble in organic solvents to record a <sup>1</sup>H NMR in deuterated chloroform, which showed a large shift of the alkyl peaks close to the alkynyl function and a complete disappearance of the acetylene proton indicative of the product formation. Apart from this unusual behaviour, the other clusters all formed fine white or yellow insoluble solid upon the addition of the acetylene in the ammoniacal silver solution. These clusters were insoluble in all common solvents; however, compound AgPh was soluble enough to record an NMR spectrum in DMSO-d<sub>6</sub>, displaying similar features as AgOOct, such as broad peaks and the absence of the acetylene proton peak from the starting alkyne.

We qualitatively confirmed the formation of the acetylide species by ATR-IR (**Figure S4-4**). The absence of the intense C≡C-H stretching band with respect to the starting alkyne and an additional shift of the lower intensity peak corresponding to C≡C stretching is observed in some cases which is characteristic of a silver acetylide species.

### Structural characterisations

From a structural point of view, however, powder X-ray diffraction was employed to assess the crystallinity of the acetylides. The growth of single crystals was concomitantly attempted using two different methods. However, no crystals suitable for single-crystal XRD could be isolated. Nonetheless, powder diffraction provided valuable information on the overall crystallinity as well as on the crystallite size. Partial diffractograms of the acetylides, recorded on a powder diffractometer (Bragg-Brentano configuration), are shown in **Figure 4.3**. Interestingly, all the derivatives showed characteristic features of crystalline powders with varying degrees of crystallinity. AgPh displays a strikingly high degree of order, with well-resolved peaks over a wide range of the diffractogram twoθ angle values. A survey of the literature allowed comparing the diffraction patterns of the derivatives with calculated patterns from existing XRD single crystal structures. Among the several available structures for AgTol, AgtFTol, and Agt-Bu, none was shown to fit with our experimental diffractograms. However, the crystal structure obtained from AgPh (chapter 3) indicates that the reaction conditions likely favour the formation of infinite cluster types. The ligands' structure presumably has an equally important impact on the formation of such types of structures, with π-π stacking possibly providing a direct structuration feature effectively helping the formation of the cluster. Despite the lack of structural information, the crystallite sizes (calculated from the Scherrer equation) are seen to follow four broad trends (**Table 4-1**). AgOOct, despite a diffractogram with a limited number of peaks, the latter fit with rather large crystallite sizes (43 nm), which are smaller than the AgPh crystals (62 nm), though. Then, a category comprising AgTol, AgtFTol, AgThio and Agt-Bu possesses crystals of 25 to 30 nm size. AgAnisole and AgTPA are 17 and 15 nm large, respectively, while AgPyr shows crystallites of around 6nm, with peaks reminiscent of amorphous materials.

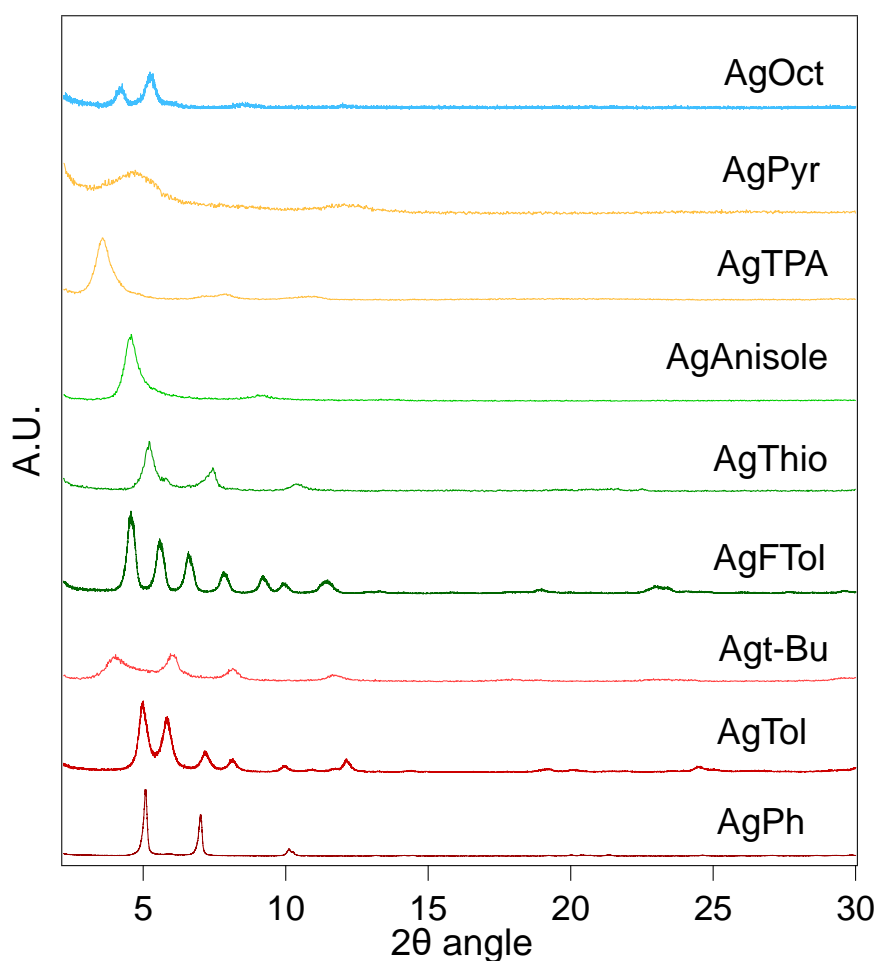


**Figure 4.3** Powder XRD of the derivatives recorded from 2 to 30° of  $2\theta$  values, on a 2D-Phaser benchtop diffractometer (Bragg-Brentano)

Although XRD results provided invaluable information on the degree of crystallinity of the catalysts and the average size of the crystallites, no precise structural information arose from the powder diffractograms. As such, XPS analysis was carried out on all the acetylides to confirm the nature of the cluster and obtain additional information on the silver/ligand stoichiometry (**Figure S4-7**/**Figure S4-8**). Indeed, the semi-quantitative nature of the XPS technique allows for drawing a molar ratio of the elements comprising the sample. The ratio between C and Ag atoms stands out as the most representative for the silver clusters bearing purely carbon-based ligands. Fluorine, sulfur and oxygen were also used as their quantification can strictly be related to specific ligands. As expected from previous studies from our group, all XPS spectra show the presence of unambiguously assigned Ag (I) and Ag-C $\equiv$ C emission peaks. Interestingly, the nature of the ligand largely influences the core electrons binding energies for both the silver and C $\equiv$ C carbons (**Figure 4.4**). Further comparison of peak positions with those recorded from reference compounds (**Figure 3.3**) allowed for a precise assignment and quantitative analysis. The total molar fraction of the elemental constituents of the acetylides (C to Ag ratio) allowed drawing an experimental Ag/ligand ratio, shown to be in the range of 1:1 for all the derivatives. The ratio was confirmed from the quantification of F, S and O atoms in the case of AgtFTol, AgThio and AgAnisole, (**Figure SXX**). A precise ligand to silver ratio was obtained from carrying out the quantification of elemental silver via Microwave plasma atomic emission spectroscopy (MP-AES) from solutions of the acetylides prepared from a precisely weighed number of

samples (**Figure S4-10**). The intrinsic insolubility of the acetylides could be circumvented by hydrolyzing the sample in concentrated TFA, followed by dissolution in aqueous HNO<sub>3</sub> to a final 10ppm (w/w) concentration. Solutions of digested samples were submitted to quantification with respect to an external standard calibration curve. The silver atomic ratios confirm a 1:1 ligand-to-silver ratio for all the compounds except for AgOct, where the silver content is found to be 66% with a ligand-to-silver ratio of 1:2.

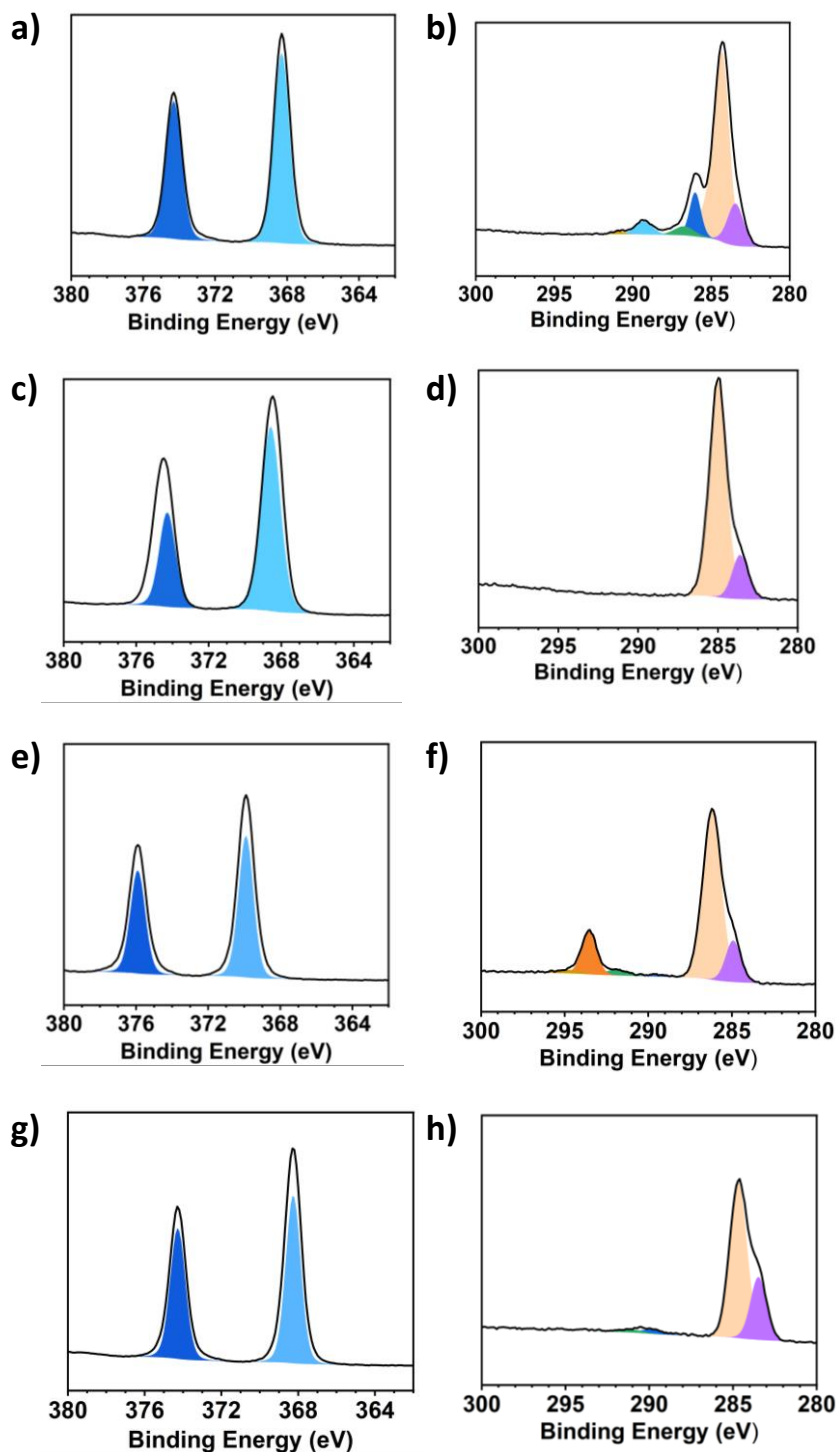


**Figure 4.4** XPS spectra of AgAnisole **a)** Ag3d **b)** C1s ; AgOct **c)** Ag3d **d)** C1s;AgtFtol **e)** Ag3d **f)** C1s;AgThio **g)** Ag3d **h)** C1s

## CO<sub>2</sub>RR Catalytic properties

The preparation of electrodes comprising the individual catalysts was based on a previously developed methodology. Ethanol-based inks of the different derivatives were prepared with carbon black and Nafion® additives, and were then deposited by drop casting on a Sigracet gas diffusion layer (GDL) at 80°C. The electrodes were subsequently dried at 40°C under reduced pressure. The choice of carbon-based GDLs allowed for a high electrical conductivity, high surface area and the suitability of the electrodes for further flow cell applications.

The electrochemical activity of the above GDEs were first tested in a 3-electrode cell (**Figure S4-1**) in a N<sub>2</sub>-saturated 1 M potassium bicarbonate electrolyte (**Figure S4-9**). Cyclic voltammetry (CV) between 0 and -2 V vs Ag/AgCl provides important evidence of the formation of the catalytic species. Indeed, the exclusive Ag(I) nature of the silver cluster was previously shown to undergo the formation of Ag(0) catalytic centres in situ prior to the CO<sub>2</sub> reduction reaction. As seen in **Figure 4.5**, the first cycle of the CV experiment shows a characteristic irreversible reduction for all the compounds. The reaction potential and the charge deriving from the reduction faradic current are intimately linked to the nature of the cluster's ligand type and are seen to vary greatly from one catalyst to the other. AgTol, for example, shows a relatively weak reduction wave (**Figure 4.5a**) while AgAnisole shows a particularly intense reduction wave (**Figure 4.5b**).

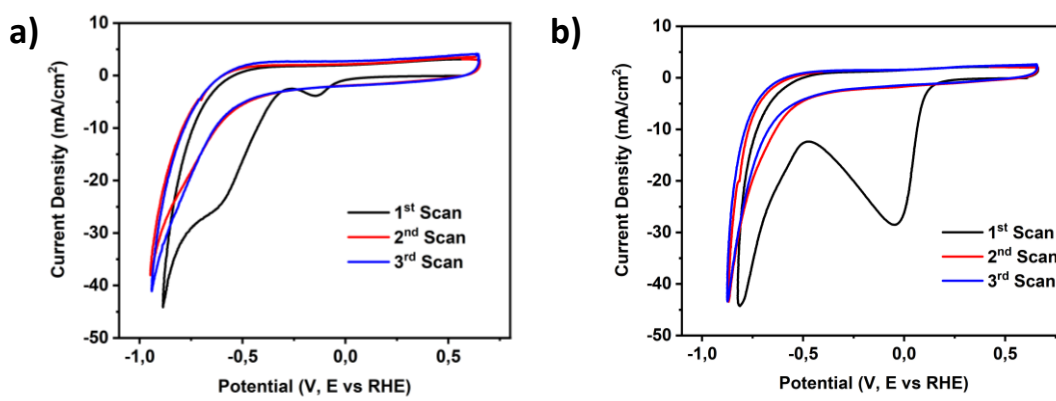


**Figure 4.5** Cyclic voltammetry of **a)** AgTol and **b)** AgAnisole

Considering the potential range and the intensity of the reaction, we assumed that it corresponded to the formation of Ag(0) species with the metal cluster core, which was necessarily followed by the subsequent elimination of a ligand (see **Chapter 3**). The reduction potentials and the corresponding electrical charges obtained from the peaks integration are shown in **Table 4-1** For all the catalysts. The experimental measurement of the electrochemically active surface area of the electrodes (ECSA, **Figure S4-15****Figure S4-16**) coupled with the latter charge value allowed estimating the number of active catalytic sites on the electrode and their relative percentages with respect to the actual amount of deposited material on the GDLs (**Table 4-1**). Interestingly, we observed that the amount of in-situ formed silver catalytic species amounts, in some cases, to a very large portion of the total catalyst quantity. Quite unexpectedly, up to 80% of some catalyst's silver content, for example, for AgPyr, is being reduced during this process. We assume that at this stage, due to the associated loss of ligands, the cluster has presumably lost its structural integrity and that the active species would most probably consist of metallic silver aggregates.



Compound	crystallite size (nm)	$\eta$ CO <sub>2</sub> RR (V vs RHE)	Q (mC)	$\Gamma$ [Ag] (nmol)	active Ag (load%)
AgPh	62	-0,38	9,02	129	7
AgTol	30	-0,35	2,55	36	1,6
AgAnisole	17	-0,47	7,11	90	3,6
AgOct	43	-0,33	5,83	46.2	1,8
AgtFTol	27	-0,40	5,83	34,2	1,4
Agt-Bu	25	-0,35	3,08	37,2	2
AgThio	26	-0,35	31,7	342	17
AgPyr	6	-0,45	98,0	1270	80
AgTPA	15	-0,43	6,93	226	18

**Table 4-1** Summary of the most important characteristics of the silver acetylides.

Prior to any CO<sub>2</sub>RR experiment, we measured the system impedance. The electrochemical impedance spectroscopy results (EIS) are reported in **Figure S4-14** both in the form of Bode and Nyquist plots. The system resistance is extracted from the impedance measurements and is used to correct all the presented potentials in this article. iR corrected Linear sweep voltammetry (LSV) are presented against RHE in **Figure 4.6a**.

The LSV curves display three distinct potential regions with prominent inflexion points for all the acetylides. The lower potential range, defined from the faradic onset to the first inflexion point, corresponds to a potential window where the CO<sub>2</sub> reduction is greatly favoured over the Hydrogen evolution reaction (HER). Above the latter range, the faradic currents are consistently reaching a plateau in all the experiments corresponding to a region where the reaction shifts from being kinetically-dominated to being mass-transport-limited, consistent with previous results from Jaramillo et al. on metallic silver.<sup>14</sup> In the higher potential region, the HER dominates the reaction while the CO<sub>2</sub>RR activity remains relatively constant (see SI for individual LSV curves, **Figure S4-12**). This behaviour is further confirmed by quantification experiments for which the fraction of the CO faradic current density reaches a plateau in a potential range roughly matching that observed in the LSV (**Figure 4.7**). Noteworthy, we showed that this limitation could be overcome in conditions where the mass transport is not limited by the CO<sub>2</sub> solubility in the electrolyte, such as inflow cell electrolyzers (**Chapter 3**). The CO<sub>2</sub>RR overpotentials measured from the LSV experiments are reported in **Table 4-1**. In all the cases the CO<sub>2</sub>RR overpotentials are extremely low and are competing with the state-of-the-art gold-based catalysts.<sup>44</sup> Nonetheless, we can separate the catalysts in 3 different groups. The first ones possess overpotentials lower than -0.35V vs RHE, comprising AgOct (which possess the lowest overpotential -0.33 V vs RHE), AgTol, Agt-Bu and AgThio. The second comprises the AgPh and AgtFTol with  $\eta$  lower than -0.41V vs RHE. A final group with  $\eta$  superior to -0.43 V vs RHE comprises AgTPA, AgPyr and AgAnisole.

Quite interestingly, these overpotentials are partially correlated with the crystallite sizes observed in the PXRD measurements, with the smallest crystallites possessing the highest overpotentials. Insofar as the overpotential is an experimental extrapolation of the reaction kinetic energy barrier, the highly ordered structures seem, consequently, to possess the reaction intermediates with the lowest energy barrier. We assume it to be related to an easier charge transfer from the cluster to the bound \*COOH intermediate and to the more efficient delocalisation of the excess charge through the cluster core.

Following the above preliminary results, a series of chronoamperometry experiments were performed between -0.63 and -1.13 V vs RHE with 0.1V potential increments (**Figure S4-17**). Each measurement was performed in the 3-electrode cell mentioned previously. The gaseous products were sampled and quantified from the cell's headspace after 15 min of constant potential electrolysis. An increase in catalytic activity was observed with each incremental increase in potential, as well as a change in selectivity. The corresponding current is seen to remain constant throughout the experiment time length, which is indicative of a stable catalytic species. A marked selectivity for CO as the major product is observed for all of the acetylides. Faradic efficiencies at -0.63V are reported in **Figure 4.6b**. The selectivity ratio between CO<sub>2</sub>RR and HER varies greatly within the library, however for the FE for H<sub>2</sub> is kept below 20% for most catalysts except for AgFTol, AgAnisole, and AgPyr. As a for the extremes, AgTol reaches a maximum faradic efficiency of 91% for CO whereas AgPyr shows the poorest of all the derivatives with a modest 44% selectivity for CO.

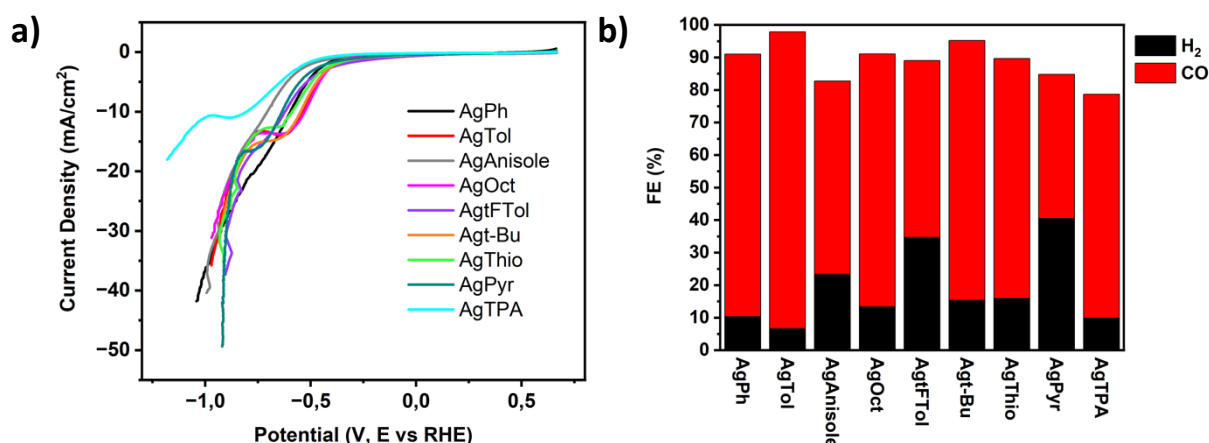


**Figure 4.6.** a) LSV curves of the derivatives recorded from 0 to -2 V vs Ag/AgCl and converted vs RHE; b) Faradic efficiencies of the different derivatives. The data is extracted from 15-minute long chronoamperometry experiments at -0.63 V vs RHE in a CO<sub>2</sub>-saturated 1M KHCO<sub>3</sub> solution.

From these experiments, we extracted partial current densities for CO, which are reported in **Figure 4.7a**. A first trend is observed with the isostructural and alkyl ligand showing superior current densities compared to both electron-donating and electron-withdrawing derivatives with particularly low current densities for the bulky donor groups. With the CO current densities and the number of catalytic silver species being known, we were consequently able to calculate Turnover numbers (TONs) and Turnover Frequencies (TOFs) for CO. The extrapolated TOF (**Figure 4.7b**) are evidence of large variations of activity between each catalytic species, which we related to the organization of the crystals and the relative crystallinity of the samples. We observe that triphenylamine, pyrene and methoxy groups tend to lead to a rather similar type of

crystalline features, with crystallite size in the lower end of the distribution, which we linked to their poorer activity for CO<sub>2</sub>RR.

From another perspective, this activity can also be related to the nature of the groups present in the structure. Indeed, the mesomeric donor ligands all possess relatively low TOFs, which we attribute to their electron-dense nature destabilising the structure upon applied reductive conditions. AgtFTol seems, on the other hand, to lead to better performances with respect to the reference material while possessing a relatively similar overpotential. Most interesting is the fact that the iso-structural compounds are overperforming the reference, which is indicative of the major influence of positive inductive donor effects. The latter effect is also largely influencing the activity of AgOct even though its structure cannot be related to these crystalline derivatives. All in all, the results point to the fact that an optimum ratio between Ag(0) centers/catalyst is necessary to provide high catalytic activity towards CO production, while maintaining the catalysts structure integrity. The latter factor is likely enhanced in catalyst displaying the highest degree of crystallinity while preferentially possessing donating inductive effects.

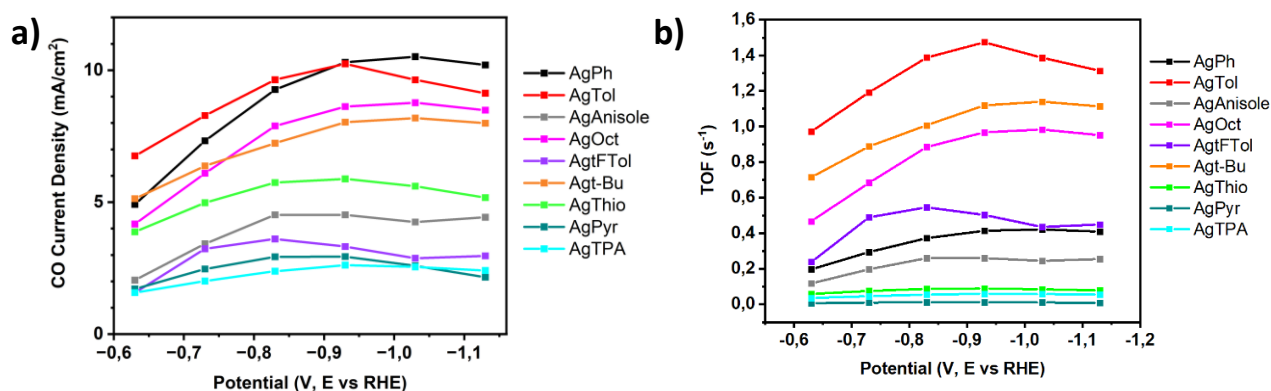


**Figure 4.7 a)** CO<sub>2</sub> to CO current density extracted from the faradic efficiencies measured between -0.63 and -1.13 V vs RHE. **b)** CO<sub>2</sub> to CO Turnover frequencies (TOFs). The data is extracted from the 15 min long chronoamperometry experiments at -0.63 V vs RHE in a CO<sub>2</sub>-saturated 1M KHCO<sub>3</sub> solution correlated with the calculated catalytically active silver species.

Theoretical studies expounded in Chapter 3 have shown that the Gibbs free energy of the \*COOH intermediate formation is highly unfavourable against the H<sub>2</sub> evolution in the case of a fully coordinated silver cluster. The reduction-triggered partial ligand removal observed experimentally has been confirmed through theoretical calculations, demonstrating that ligand elimination is a prerequisite for lowering the CO<sub>2</sub>RR activation barrier. The CO<sub>2</sub>RR is consequently greatly favoured with respect to the H<sub>2</sub> from the exposed undercoordinated silver atoms. The results herein further show from an experimental perspective that the structure of the catalysts and, consequently, the local environment of the Ag(0) formed have a further impact on the activation energy. Overpotential and selectivity are both affected by the above parameters.

## Conclusion

Herein, we have demonstrated that the silver cluster formation reaction we have previously optimised is a robust methodology for the synthesis of large libraries of silver acetylides. The reaction conditions are tolerant to numerous alkyne chemical structures and lead to silver acetylides with very different crystallinity

features. We further carried out a complete powder XRD data and surface characterisation, which allowed us to link the catalytic activity in terms of overpotential, TOF and selectivity to these features.

First, we established that the overpotential follows the trend of crystallinity (crystallite size), showing that the more crystalline the catalyst, the lower the overpotential. The precise underpinnings of the latter observation are not entirely resolved; however, considering an electron transfer from an Ag(0) intermediate centre, it seems sensible to assume that the latter would occur with a lower activation barrier if the \*COOH intermediate species is bound to an ordered catalytic species. Consequently, the kinetics of the CO<sub>2</sub>RR would also be expected to be faster with respect to the competing HER, explaining the correlation between crystallinity, overpotential and selectivity. Indeed, the more amorphous the material, the higher the overpotential and the lower the selectivity for CO. This is particularly the case for AgPyr, whose amorphous nature is likely the reason for its poor catalytic characteristics.

Quite importantly, our study pointed to the importance of determining the number of active species formed prior to the catalysis. In this respect, the acetylides described herein vary greatly in terms of the proportion of Ag(0) sites with respect to the amount of catalyst. It is important, therefore, that the structure of the acetylide at the molecular and crystalline level remain stable upon the activation-triggered ligand loss. It appears that the number of Ag (0) active sites formed under reducing conditions are directly linked to the ligand chemical structure, while the catalytic activity in terms of overpotential and selectivity is rather dictated by the degree of order (crystallinity) of the whole cluster.

Finally, future work is ongoing to further understand the critical factors determining the selectivity of silver acetylides. However, we can generally assume that the overall selectivity is dictated by the metal and therefore limited to CO, and that the crystal structure and the ligand arrangement will have an impact on the extent of the selectivity and overpotential. The ease of synthesis of silver acetylides make them the perfect candidate for high throughput catalyst screening.

## References

- (1) Service, R. Can the World Make the Chemicals It Needs without Oil? *Science* **2019**. <https://doi.org/10.1126/science.aaz5517>.
- (2) Smith, W. A.; Burdyny, T.; Vermaas, D. A.; Geerlings, H. Pathways to Industrial-Scale Fuel Out of Thin Air from CO<sub>2</sub> Electrolysis. *Joule* **2019**, *3* (8), 1822–1834. <https://doi.org/10.1016/j.joule.2019.07.009>.
- (3) Hepburn, C.; Adlen, E.; Beddington, J.; Carter, E. A.; Fuss, S.; Mac Dowell, N.; Minx, J. C.; Smith, P.; Williams, C. K. The Technological and Economic Prospects for CO<sub>2</sub> Utilization and Removal. *Nature* **2019**, *575* (7781), 87–97. <https://doi.org/10.1038/s41586-019-1681-6>.
- (4) Bushuyev, O. S.; De Luna, P.; Dinh, C. T.; Tao, L.; Saur, G.; van de Lagemaat, J.; Kelley, S. O.; Sargent, E. H. What Should We Make with CO<sub>2</sub> and How Can We Make It? *Joule* **2018**, *2* (5), 825–832. <https://doi.org/10.1016/j.joule.2017.09.003>.
- (5) Bagger, A.; Ju, W.; Varela, A. S.; Strasser, P.; Rossmeisl, J. Electrochemical CO<sub>2</sub> Reduction: A Classification Problem. *ChemPhysChem* **2017**, *18* (22), 3266–3273. <https://doi.org/10.1002/cphc.201700736>.

- (6) Hori, Y.; Kikuchi, K.; Suzuki, S. Production of CO and CH<sub>4</sub> in Electrochemical Reduction of CO<sub>2</sub> at Metal Electrodes in Aqueous Hydrogencarbonate Solution. *Chemistry Letters* **1985**, *14*, 1695–1698.
- (7) Franco, F.; Rettenmaier, C.; Jeon, H. S.; Roldan Cuenya, B. Transition Metal-Based Catalysts for the Electrochemical CO<sub>2</sub> Reduction: From Atoms and Molecules to Nanostructured Materials. *Chem. Soc. Rev.* **2020**, *49* (19), 6884–6946. <https://doi.org/10.1039/D0CS00835D>.
- (8) Lees, E. W.; Mowbray, B. A. W.; Salvatore, D. A.; Simpson, G. L.; Dvorak, D. J.; Ren, S.; Chau, J.; Milton, K. L.; Berlinguette, C. P. Linking Gas Diffusion Electrode Composition to CO<sub>2</sub> Reduction in a Flow Cell. *J. Mater. Chem. A* **2020**, *8* (37), 19493–19501. <https://doi.org/10.1039/D0TA03570J>.
- (9) Ren, S.; Joulié, D.; Salvatore, D.; Torbensen, K.; Wang, M.; Robert, M.; Berlinguette, C. P. Molecular Electrocatalysts Can Mediate Fast, Selective CO<sub>2</sub> Reduction in a Flow Cell. *Science* **2019**, *365* (6451), 367–369. <https://doi.org/10.1126/science.aax4608>.
- (10) Weekes, D. M.; Salvatore, D. A.; Reyes, A.; Huang, A.; Berlinguette, C. P. Electrolytic CO<sub>2</sub> Reduction in a Flow Cell. *Acc. Chem. Res.* **2018**, *51* (4), 910–918. <https://doi.org/10.1021/acs.accounts.8b00010>.
- (11) Dinh, C.-T.; Burdyny, T.; Kibria, M. G.; Seifitokaldani, A.; Gabardo, C. M.; García De Arquer, F. P.; Kiani, A.; Edwards, J. P.; De Luna, P.; Bushuyev, O. S.; Zou, C.; Quintero-Bermudez, R.; Pang, Y.; Sinton, D.; Sargent, E. H. CO<sub>2</sub> Electroreduction to Ethylene via Hydroxide-Mediated Copper Catalysis at an Abrupt Interface. *Science* **2018**, *360* (6390), 783–787. <https://doi.org/10.1126/science.aas9100>.
- (12) Perazio, A.; Creissen, C. E.; Rivera De La Cruz, J. G.; Schreiber, M. W.; Fontecave, M. Acidic Electroreduction of CO<sub>2</sub> to Multi-Carbon Products with CO<sub>2</sub> Recovery and Recycling from Carbonate. *ACS Energy Lett.* **2023**, *8* (7), 2979–2985. <https://doi.org/10.1021/acscenergylett.3c00901>.
- (13) Ahangari, H. T.; Marshall, A. T. Preventing the Deactivation of Gold Cathodes During Electrocatalytic CO<sub>2</sub> Reduction While Avoiding Gold Dissolution. *Electrocatalysis* **2020**, *11* (1), 25–34. <https://doi.org/10.1007/s12678-019-00564-z>.
- (14) Hatsukade, T.; Kuhl, K. P.; Cave, E. R.; Abram, D. N.; Jaramillo, T. F. Insights into the Electrocatalytic Reduction of CO<sub>2</sub> on Metallic Silver Surfaces. *Phys. Chem. Chem. Phys.* **2014**, *16* (27), 13814–13819. <https://doi.org/10.1039/C4CP00692E>.
- (15) Kim, C.; Jeon, H. S.; Eom, T.; Jee, M. S.; Kim, H.; Friend, C. M.; Min, B. K.; Hwang, Y. J. Achieving Selective and Efficient Electrocatalytic Activity for CO<sub>2</sub> Reduction Using Immobilized Silver Nanoparticles. *J. Am. Chem. Soc.* **2015**, *137* (43), 13844–13850. <https://doi.org/10.1021/jacs.5b06568>.
- (16) Kostecki, R.; Augustynski, J. Electrochemical Reduction of CO<sub>2</sub> at an Activated Silver Electrode. *Berichte der Bunsengesellschaft für physikalische Chemie* **1994**, *98* (12), 1510–1515. <https://doi.org/10.1002/bbpc.19940981203>.
- (17) Zhu, X.; Huang, J.; Eikerling, M. Electrochemical CO<sub>2</sub> Reduction at Silver from a Local Perspective. *ACS Catal.* **2021**, *11* (23), 14521–14532. <https://doi.org/10.1021/acscatal.1c04791>.
- (18) Farmand, M.; Landers, A. T.; Lin, J. C.; Feaster, J. T.; Beeman, J. W.; Ye, Y.; Clark, E. L.; Higgins, D.; Yano, J.; Davis, R. C.; Mehta, A.; Jaramillo, T. F.; Hahn, C.; Drisdell, W. S. Electrochemical Flow Cell Enabling Operando Probing of Electrocatalyst Surfaces by X-Ray Spectroscopy and

- Diffraction. *Phys. Chem. Chem. Phys.* **2019**, *21* (10), 5402–5408. <https://doi.org/10.1039/C8CP07423B>.
- (19) Dinh, C.-T.; Burdyny, T.; Kibria, M. G.; Seifitokaldani, A.; Gabardo, C. M.; García De Arquer, F. P.; Kiani, A.; Edwards, J. P.; De Luna, P.; Bushuyev, O. S.; Zou, C.; Quintero-Bermudez, R.; Pang, Y.; Sinton, D.; Sargent, E. H. CO<sub>2</sub> Electroreduction to Ethylene via Hydroxide-Mediated Copper Catalysis at an Abrupt Interface. *Science* **2018**, *360* (6390), 783–787. <https://doi.org/10.1126/science.aas9100>.
- (20) Dinh, C.-T.; García De Arquer, F. P.; Sinton, D.; Sargent, E. H. High Rate, Selective, and Stable Electroreduction of CO<sub>2</sub> to CO in Basic and Neutral Media. *ACS Energy Lett.* **2018**, *3* (11), 2835–2840. <https://doi.org/10.1021/acsenergylett.8b01734>.
- (21) Li, F.; Li, Y. C.; Wang, Z.; Li, J.; Nam, D.-H.; Lum, Y.; Luo, M.; Wang, X.; Ozden, A.; Hung, S.-F.; Chen, B.; Wang, Y.; Wicks, J.; Xu, Y.; Li, Y.; Gabardo, C. M.; Dinh, C.-T.; Wang, Y.; Zhuang, T.-T.; Sinton, D.; Sargent, E. H. Cooperative CO<sub>2</sub>-to-Ethanol Conversion via Enriched Intermediates at Molecule–Metal Catalyst Interfaces. *Nat Catal* **2019**, *3* (1), 75–82. <https://doi.org/10.1038/s41929-019-0383-7>.
- (22) Zhong, M.; Tran, K.; Min, Y.; Wang, C.; Wang, Z.; Dinh, C.-T.; De Luna, P.; Yu, Z.; Rasouli, A. S.; Brodersen, P.; Sun, S.; Voznyy, O.; Tan, C.-S.; Askerka, M.; Che, F.; Liu, M.; Seifitokaldani, A.; Pang, Y.; Lo, S.-C.; Ip, A.; Ulissi, Z.; Sargent, E. H. Accelerated Discovery of CO<sub>2</sub> Electrocatalysts Using Active Machine Learning. *Nature* **2020**, *581* (7807), 178–183. <https://doi.org/10.1038/s41586-020-2242-8>.
- (23) Dickinson, H. L. A.; Symes, M. D. Recent Progress in CO<sub>2</sub> Reduction Using Bimetallic Electrodes Containing Copper. *Electrochemistry Communications* **2022**, *135*, 107212. <https://doi.org/10.1016/j.elecom.2022.107212>.
- (24) Huan, T. N.; Simon, P.; Rouse, G.; Génois, I.; Artero, V.; Fontecave, M. Porous Dendritic Copper: An Electrocatalyst for Highly Selective CO<sub>2</sub> Reduction to Formate in Water/Ionic Liquid Electrolyte. *Chem. Sci.* **2017**, *8* (1), 742–747. <https://doi.org/10.1039/C6SC03194C>.
- (25) Karapinar, D.; Creissen, C. E.; Rivera De La Cruz, J. G.; Schreiber, M. W.; Fontecave, M. Electrochemical CO<sub>2</sub> Reduction to Ethanol with Copper-Based Catalysts. *ACS Energy Lett.* **2021**, *6* (2), 694–706. <https://doi.org/10.1021/acsenergylett.0c02610>.
- (26) Zhu, W.; Zhang, Y.-J.; Zhang, H.; Lv, H.; Li, Q.; Michalsky, R.; Peterson, A. A.; Sun, S. Active and Selective Conversion of CO<sub>2</sub> to CO on Ultrathin Au Nanowires. *J. Am. Chem. Soc.* **2014**, *136* (46), 16132–16135. <https://doi.org/10.1021/ja5095099>.
- (27) Liu, W.; Zhai, P.; Li, A.; Wei, B.; Si, K.; Wei, Y.; Wang, X.; Zhu, G.; Chen, Q.; Gu, X.; Zhang, R.; Zhou, W.; Gong, Y. Electrochemical CO<sub>2</sub> Reduction to Ethylene by Ultrathin CuO Nanoplate Arrays. *Nat Commun* **2022**, *13* (1), 1877. <https://doi.org/10.1038/s41467-022-29428-9>.
- (28) Wang, M.; Torbensen, K.; Salvatore, D.; Ren, S.; Joulié, D.; Dumoulin, F.; Mendoza, D.; Lassalle-Kaiser, B.; Işci, U.; Berlinguette, C. P.; Robert, M. CO<sub>2</sub> Electrochemical Catalytic Reduction with a Highly Active Cobalt Phthalocyanine. *Nat Commun* **2019**, *10* (1), 3602. <https://doi.org/10.1038/s41467-019-11542-w>.
- (29) Boutin, E.; Merakeb, L.; Ma, B.; Boudy, B.; Wang, M.; Bonin, J.; Anxolabéhère-Mallart, E.; Robert, M. Molecular Catalysis of CO<sub>2</sub> Reduction: Recent Advances and Perspectives in Electrochemical and Light-Driven Processes with Selected Fe, Ni and Co Aza Macrocyclic and Polypyridine Complexes. *Chem. Soc. Rev.* **2020**, *49* (16), 5772–5809. <https://doi.org/10.1039/D0CS00218F>.

- (30) Boutin, E.; Robert, M. Molecular Electrochemical Reduction of CO<sub>2</sub> beyond Two Electrons. *Trends in Chemistry* **2021**, *3* (5), 359–372. <https://doi.org/10.1016/j.trechm.2021.02.003>.
- (31) Chakraborty, I.; Pradeep, T. Atomically Precise Clusters of Noble Metals: Emerging Link between Atoms and Nanoparticles. *Chem. Rev.* **2017**, *117* (12), 8208–8271. <https://doi.org/10.1021/acs.chemrev.6b00769>.
- (32) Chen, L.; Sun, F.; Shen, Q.; Qin, L.; Liu, Y.; Qiao, L.; Tang, Q.; Wang, L.; Tang, Z. Homoleptic Alkynyl-Protected Ag<sub>32</sub> Nanocluster with Atomic Precision: Probing the Ligand Effect toward CO<sub>2</sub> Electroreduction and 4-Nitrophenol Reduction. *Nano Res.* **2022**, *15* (10), 8908–8913. <https://doi.org/10.1007/s12274-022-4812-6>.
- (33) Deng, G.; Kim, J.; Bootharaju, M. S.; Sun, F.; Lee, K.; Tang, Q.; Hwang, Y. J.; Hyeon, T. Body-Centered-Cubic-Kernelled Ag<sub>15</sub> Cu<sub>6</sub> Nanocluster with Alkynyl Protection: Synthesis, Total Structure, and CO<sub>2</sub> Electroreduction. *J. Am. Chem. Soc.* **2023**, *145* (6), 3401–3407. <https://doi.org/10.1021/jacs.2c10338>.
- (34) Gao, Z.-H.; Wei, K.; Wu, T.; Dong, J.; Jiang, D.; Sun, S.; Wang, L.-S. A Heteroleptic Gold Hydride Nanocluster for Efficient and Selective Electrocatalytic Reduction of CO<sub>2</sub> to CO. *J. Am. Chem. Soc.* **2022**, *144* (12), 5258–5262. <https://doi.org/10.1021/jacs.2c00725>.
- (35) Jin, R.; Zeng, C.; Zhou, M.; Chen, Y. Atomically Precise Colloidal Metal Nanoclusters and Nanoparticles: Fundamentals and Opportunities. *Chem. Rev.* **2016**, *116* (18), 10346–10413. <https://doi.org/10.1021/acs.chemrev.5b00703>.
- (36) Ma, G.; Qin, L.; Liu, Y.; Fan, H.; Qiao, L.; Yu, C.; Tang, Z. A Review of CO<sub>2</sub> Reduction Reaction Catalyzed by Atomical-Level Ag Nanomaterials: Atom-Precise Nanoclusters and Atomically Dispersed Catalysts. *Surfaces and Interfaces* **2023**, *36*, 102555. <https://doi.org/10.1016/j.surfin.2022.102555>.
- (37) Zhang, X.-G.; Liu, Y.; Zhan, C.; Jin, X.; Chi, Q.; Wu, D.-Y.; Zhao, Y.; Tian, Z.-Q. Reaction Selectivity for Plasmon-Driven Carbon Dioxide Reduction on Silver Clusters: A Theoretical Prediction. *J. Phys. Chem. C* **2019**, *123* (17), 11101–11108. <https://doi.org/10.1021/acs.jpcc.9b01448>.
- (38) Maity, P.; Tsunoyama, H.; Yamauchi, M.; Xie, S.; Tsukuda, T. Organogold Clusters Protected by Phenylacetylene. *J. Am. Chem. Soc.* **2011**, *133* (50), 20123–20125. <https://doi.org/10.1021/ja209236n>.
- (39) Maity, P.; Takano, S.; Yamazoe, S.; Wakabayashi, T.; Tsukuda, T. Binding Motif of Terminal Alkynes on Gold Clusters. *J. Am. Chem. Soc.* **2013**, *135* (25), 9450–9457. <https://doi.org/10.1021/ja401798z>.
- (40) Qin, L.; Sun, F.; Ma, X.; Ma, G.; Tang, Y.; Wang, L.; Tang, Q.; Jin, R.; Tang, Z. Homoleptic Alkynyl-Protected Ag<sub>15</sub> Nanocluster with Atomic Precision: Structural Analysis and Electrocatalytic Performance toward CO<sub>2</sub> Reduction. *Angewandte Chemie International Edition* **2021**, *60* (50), 26136–26141. <https://doi.org/10.1002/anie.202110330>.
- (41) Ma, X.; Sun, F.; Qin, L.; Liu, Y.; Kang, X.; Wang, L.; Jiang, D.; Tang, Q.; Tang, Z. Electrochemical CO<sub>2</sub> Reduction Catalyzed by Atomically Precise Alkynyl-Protected Au<sub>7</sub>Ag<sub>8</sub>, Ag<sub>9</sub>Cu<sub>6</sub>, and Au<sub>2</sub>Ag<sub>8</sub>Cu<sub>5</sub> Nanoclusters: Probing the Effect of Multi-Metal Core on Selectivity. *Chem. Sci.* **2022**, *13* (34), 10149–10158. <https://doi.org/10.1039/D2SC02886G>.
- (42) Liu, X.; Yi, Q.; Han, Y.; Liang, Z.; Shen, C.; Zhou, Z.; Sun, J.; Li, Y.; Du, W.; Cao, R. A Robust Microfluidic Device for the Synthesis and Crystal Growth of Organometallic Polymers with Highly Organized Structures. *Angew Chem Int Ed* **2015**, *54* (6), 1846–1850. <https://doi.org/10.1002/anie.201411008>.

- (43) Davis, R. B.; Scheiber, D. H. The Preparation of Acetylenic Ketones Using Soluble Silver Acetylides. *J. Am. Chem. Soc.* **1956**, *78* (8), 1675–1678. <https://doi.org/10.1021/ja01589a050>.
- (44) Zhu, W.; Michalsky, R.; Metin, Ö.; Lv, H.; Guo, S.; Wright, C. J.; Sun, X.; Peterson, A. A.; Sun, S. Monodisperse Au Nanoparticles for Selective Electrocatalytic Reduction of CO<sub>2</sub> to CO. *J. Am. Chem. Soc.* **2013**, *135* (45), 16833–16836. <https://doi.org/10.1021/ja409445p>.

## Experimental Section

### Materials

25% ammonia solution (for analysis EMSURE® ISO, Reag. Ph Eur), silver nitrate (ReagentPlus®, ≥99.0% for titration), absolute ethanol, Nafion® perfluorinated resin (5 wt% solution in a mixture of lower aliphatic alcohols containing 5% water), 4-ethynyltoluene (97%), 1-Octyne (97%), 4-Ethynylanisole (97%), 4-Ethynyl- $\alpha,\alpha,\alpha$ -trifluorotoluene (97%), 4-tert-Butylphenylacetylene (96%), 3-ethynylthiophene (96%), 1-Ethynylpyrene and potassium bicarbonate (ACS reagent, 99.7%, powder, crystals, or granules) were purchased from Sigma-Aldrich. 4-Ethynyl-N,N-diphenylaniline(97%) was purchased from BLDpharm. K<sub>4</sub>(Fe(CN)<sub>6</sub>·3H<sub>2</sub>O (>99%) was purchased from ChemLab. Vulcan XC-72 carbon black, FAB PK AEM membrane (Fumasep) and Sigracet GDL (39BB) were purchased from Fuel Cell Store. Methanol (>99.5%, Ph Eur, BP, NF) was obtained from Scharlab. CDCl<sub>3</sub> (99.8%) and D<sub>2</sub>O were purchased from Innovachem. All electrolytes were prepared using Milli-Q water.

### Materials characterization

#### NMR

The <sup>1</sup>H-NMR analyses were conducted using a Bruker Ultrashield spectrometer with a <sup>1</sup>H frequency of 400 MHz.

#### MP-AES

MP-AES measurements were performed on an Agilent 4210 model using a 1000 ppm Ag standard (prepared from AgNO<sub>3</sub>) and diluted accordingly in a 3% HNO<sub>3</sub> solution to obtain a calibration curve ranging from 1 to 20 ppm (6 points). Quantification was done by preparing precisely a 1000 ppm solution of AgPh in a mixture of trifluoroacetic acid and Milli-Q water. The prepared solution was then diluted in HNO<sub>3</sub> (3%) to obtain a 10 ppm concentration of the compound.

#### XPS

X-ray Photoelectron Spectroscopy (XPS) measurements were conducted using a Thermo K-alpha spectrometer equipped with a 120 mm mean radius Hemispherical Analyzer (HAS) and a microfocused monochromated radiation source (Al K $\alpha$ , 1486.6 eV), with a continuously variable microspot size ranging from 30 to 400  $\mu$ m in diameter. These measurements were performed under ultra-high vacuum (UHV) conditions, with a residual pressure of 1 x 10<sup>-9</sup> mbar. The X-ray power operated at 72 W (12 kV, 6 mA) for a typical 400  $\mu$ m beam diameter. The spectra were recorded in the constant Pass Energy (PE) mode, specifically CAE, which was used for both wide high-sensitivity survey spectra (PE = 200 eV) and high-energy resolution analyses (PE = 20 eV) to achieve quantitatively resolved chemical analyses. To compensate for charge effects, a charge neutralization system employing low-energy electrons was employed.



For data analysis, the spectra were mathematically fitted using Casa XPS software, employing a least-squares algorithm and a non-linear baseline. The fitting of peaks in the experimental curves was achieved through a combination of Gaussian (70%) and Lorentzian (30%) distributions. Only core-level spectra for elements with the highest photoionization cross-section were recorded to ensure the extraction of more reliable information.

## Powder XRD

Powder X-ray Diffraction (PXRD) characterization was performed using a Bruker D2 Phaser powder diffractometer equipped with a Cu K $\alpha$  radiation source with a wavelength of 1.5406 Å. XRD patterns were recorded in the 2 $\theta$  range of 10° to 80° with a step size of 0.021° and a counting time of 0.05 seconds per step. The crystallite sizes were determined using DIFFRAC.EVA software.

## ATR-IR

ATR-IR characterization was performed on a Nicolet iS50 (Thermo Scientific) with 64 scans.

## Gas quantification

Permanent gases were identified and quantified using gas chromatography (GCMS-QP2010-plus, Shimadzu, Japan) equipped with a packed column (ShinCarbon ST, 2m; 0.53 mm, mesh80/100, Restek, USA) for permanent gas separation. Helium (6.0, Alphagaz 2, AirLiquide) was used as carrier gas. A Dielectric-Barrier Discharge Ionisation Detector (BID, Shimadzu, DL < 0.1ppm) was used to quantify all permanent gases (H<sub>2</sub>, CO, Methane, Ethane, ethylene) with a range of calibration curves made from 0.1, 1 and 10% standard mixtures in CO<sub>2</sub> with at least 4 points for each calibration curve (R<sup>2</sup>>0.98). A relative linearity is observed between calibration curves indicating a trustworthy method for results comparison between each calibration curve. Sampling from the electrolysis cell's headspace was carried out via a proprietary automated sampling system operating solenoid valve at timed intervals, transferring a sample of the cell's head space to a GC-sample loop (500  $\mu$ L) followed by the subsequent injection to the GC column.

## 3-Electrodes Cell Electrochemical Characterization

Electrochemical tests were conducted using a custom-made three-electrode, leak-tight cell. The anode, consisting of a platinum wire, was enclosed in a bridge tube. The cell was filled with 40 mL of a 1 M KHCO<sub>3</sub> solution as the electrolyte. The reference electrode employed was an Ag/AgCl electrode immersed in a 3M KCl solution (E<sub>0</sub>=0.210 vs NHE). The working electrode was a Gas Diffusion Electrode (GDE) with a surface area of 2 cm<sup>2</sup>, integrated into a support structure, exposing 1 cm<sup>2</sup> of its surface directly to the electrolyte.

The pH value of the CO<sub>2</sub>-saturated electrolyte was measured to be 6.8 before electrolysis. The potentials were measured against Ag/AgCl (3M). iR compensation losses between the working and reference electrodes were measured using electrochemical impedance spectroscopy (EIS) measurements from 100kHz to 0.1Hz. Electrode potential after iR correction converted to the RHE (Reversible Hydrogen Electrode) scale using



**Figure S4-1:** 3-electrodes Electrochemical Cell

$E (RHE) = E (Ag/AgCl) + 0.059 * pH + E_0(Ag/AgCl)$ . pH value is measured to be 7.8 for the CO<sub>2</sub>-saturated electrolyte and 8.4 when N<sub>2</sub> is saturated. The overpotential ( $\eta$ ) was calculated according to **Equation S4-2**<sup>1</sup>. Faradaic efficiency was calculated from (**Equation S4-3**). The intrinsic activity of the catalyst was calculated from **Equation S4-4** and **Equation S4-5** For Turnover Number and Turnover Frequency respectively.

Before chronoamperometry experiments, the electrolyte underwent a 15 min purge with either N<sub>2</sub> or CO<sub>2</sub> (at a flow rate of 35 mL/min). This purge was done using a Mass Flow Controller (MFC) (Bronkhorst EL-FLOW prestige FG-201CV) and constant stirring to eliminate air from both the solution and the cell headspace. Electrochemical tests were carried out using a potentiostat PGSTAT 204 (Metrohm).

$$E (RHE) = E (Ag/AgCl) + 0.059 * pH + E_0(Ag/AgCl)$$

**Equation S4-1**

With  $E (Ag/AgCl)$  the measured corrected potential,  $E^0(Ag/AgCl)=0.210$  V the standard potential at 3M KCl, pH=7.8 in CO<sub>2</sub> saturated 1M KHCO<sub>3</sub> solution

$$\eta = E - E_{RHE}^0$$

**Equation S4-2**

With  $E_{RHE}^0 = -0.075$  V for the CO<sub>2</sub> to CO reduction at pH = 7.8

Faradaic efficiency was obtained by direct quantification of the gas products:

$$Faradaic\ efficiency\ (\%) = \frac{Q_{exp}}{Q_{theo}} \times 100 = \frac{z \times n \times F}{Q} \times 100$$

**Equation S4-3**

Where  $z$  is the number of electrons involved in the reaction,  $n$  is the number of moles of generated product,  $F$  is the Faraday constant, and  $Q$  is the charge passed during the catalytic experiment.

### Calculation of TON and TOF

Turnover Number (TON) and Turnover frequency (TOF) for CO production were calculated from the following equations:

$$TON = \frac{n_{max\ CO}}{n_{active\ sites}}$$

**Equation S4-4**

$$TOF = \frac{TON}{t_{experiment}}$$

**Equation S4-5**

With  $n_{\max CO}$  corresponding to the CO production at a given potential or current and  $n_{active\ sites}$  corresponding to the number of active catalytic species on the electrode and  $t_{experiment}$  the experiment time in seconds.

Following a common methodology<sup>2-5</sup>, the Electrochemically active surface area (ECSA) of the electrode was estimated by probing the redox reaction of the ferricyanide/ferrocyanide couple. Cyclic voltammetry (CV) were recorded at various scan rates (5, 10, 15 and 20 mV/s) with a 25 mM concentration of K<sub>3</sub>[Fe(CN)<sub>6</sub>] in a 0.1 M KCl supporting electrolyte solution. The solution was initially degassed with N<sub>2</sub>. Then the potential of the working electrode was swept between 700 mV and -200 mV vs. Ag/AgCl (3 M KCl) at variable scan rates (mV s<sup>-1</sup>). Between each CV, the solution was bubbled with N<sub>2</sub> and stirred to quickly reach back to the initial conditions.

Electrochemically active surface areas (ECSA) were estimated from the Randles-Sevcik equation, as follows:

$$I_p = (2.69 \times 10^5) n^{3/2} A D^{1/2} \nu^{1/2} C$$

**Equation S4-6**

with  $I_p$ : reduction peak current,  $n$ : number of moles of electrons per mole of electroactive species,  $A$ : area of electrode (cm<sup>2</sup>),  $D$ : diffusion coefficient (cm<sup>2</sup> s<sup>-1</sup>),  $\nu$ : scan rate (V s<sup>-1</sup>),  $C$ : concentration (mol cm<sup>-3</sup>). The diffusion coefficient of ferricyanide is  $3.85 \times 10^{-6}$  cm<sup>2</sup> s<sup>-1</sup> and its concentration  $25 \times 10^{-6}$  mol cm<sup>-3</sup>. The ECSA ( $A$ ) is estimated from the slope of the plot of  $I_p$  versus  $\nu^{1/2}$ .

The surface loading ( $\Gamma[Ag]$  as mol cm<sup>-2</sup>) of the catalyst was calculated through the integration of the reduction wave at -0.218V vs RHE attributed to  $Ag^+ \rightarrow Ag$  on the CV scans (**Figure S4-15**) using the equation:

$$\Gamma[Ag] = q/nFA$$

**Equation S4-7**

where  $q$  is the charge (C) obtained from integration of the reduction peak divided by the scan rate,  $n$  the number of electrons involved the redox process per Ag center ( $n = 1$ ),  $F$  is the Faraday constant (96485 C mol<sup>-1</sup>), and  $A$  is the electrode surface area (0.724 cm<sup>2</sup>).

The obtained value was then correlated with the amount of Ag deposited on the electrode (1.85 μmol) which corresponds to 6.96% of active silver catalyst on the electrode.

### Computational details

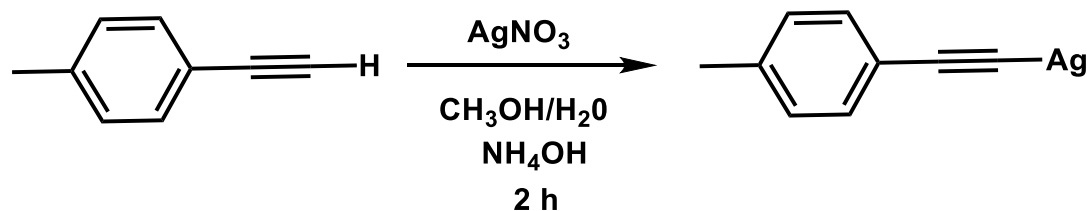
All density functional theory (DFT) calculations were performed using the Gaussian 16 software<sup>6</sup> under the B3LYP functional<sup>6-10</sup> Van der Waals interactions were considered by introducing D3(BJ) empirical dispersion correction proposed by Grimme<sup>11</sup> The 6-31+G(d) basis set was chosen for describing C, H and O atoms, while the LANL2TZ(f) one was used for Ag atoms<sup>12-16</sup>. All simulations were performed within the gas phase. Geometry optimizations were carried out with the opt=tight Gaussian's option. Vibrational frequency

calculations were done to verify the stability of all obtained stationary point and estimate Gibb's free energies. Interaction energies were computed with the 6-311++G(d,p) basis set on top of relaxed structures and by removing the BSSE contribution estimated with the Counterpoise correction<sup>17,18</sup>.

### CV and LSV electrodes preparation

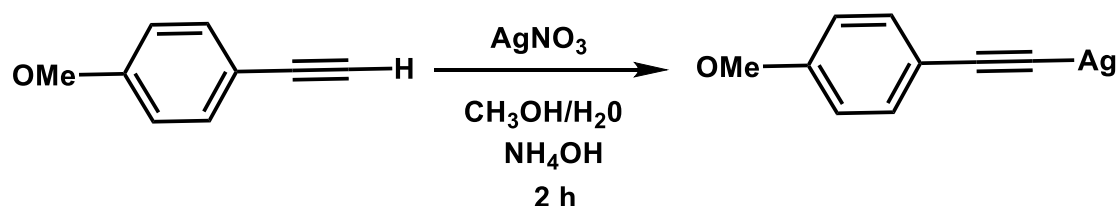
The Electrodes were prepared following a modified procedure from M. Robert et al<sup>19</sup>. Vulcan XC-72 Carbon Black (3 mg) was sonicated in Absolute ethanol (2mL) for 30min. To the slurry was added Nafion® perfluorinated resin (10 µL of a 5 wt% solution in a mixture of lower aliphatic alcohols containing 5% water) and the mixture was sonicated for 30min. To this mixture was added a suspension of the acetylide (0.8 mg) in absolute ethanol (1mL) and the mixture was sonicated for 30min. The suspension was then deposited by dropcasting on a gas diffusion layer (Sigracet 39BB; 2 cm<sup>2</sup>) at 80°C. The electrodes were then dried under reduced pressure at 40°C overnight.

## Material Synthesis



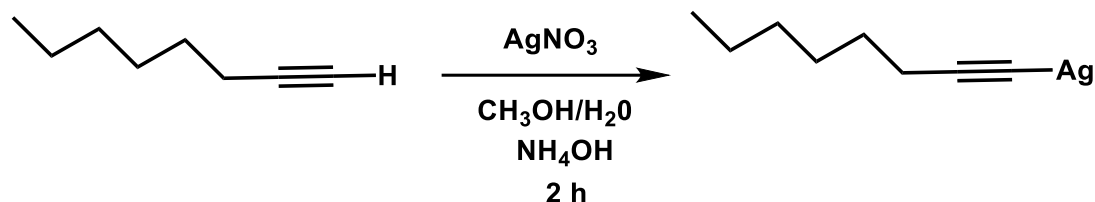
AgNO<sub>3</sub> (293 mg; 1.72 mmol) was solubilized in a mixture of MeOH (12 mL) and water (4 mL). To this solution was added NH<sub>4</sub>OH until the brown colour completely disappeared. A solution of 4-ethynyltoluene (100 mg; 86 μmol) in MeOH (10mL) was added slowly to the mixture. A white precipitate formed directly and the solution was stirred at RT for 2h. The solution was filtered, and the resulting white solid was washed with water, then MeOH and dried under a reduced atmosphere at 45°C for 48H. The product was obtained as an insoluble hydrophobic white powder (189mg; 99% yield for a 1:1 complex) sensitive to light but stable under atmospheric conditions (>6 months).

MP-AES: Ag (%mass) 46.3



AgNO<sub>3</sub> (257 mg; 1.51 mmol) was solubilized in a mixture of MeOH (12 mL) and water (4 mL). To this solution was added NH<sub>4</sub>OH until the brown colour completely disappeared. A solution of 4-ethynylanisole (100 mg; 757 μmol) in MeOH (10mL) was added slowly to the mixture. A precipitate formed directly and the solution was stirred at RT for 2h. The solution was filtered, and the resulting white solid was washed with water, then MeOH and dried under a reduced atmosphere at 45°C for 48H. The product was obtained as an orange insoluble hydrophobic powder (180mg;99%), which is stable under atmospheric conditions (> 6 months).

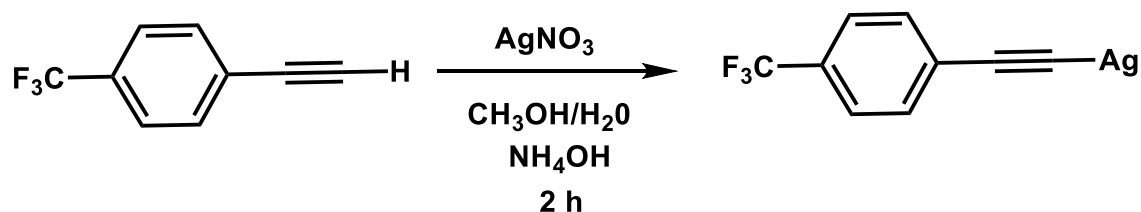
MP-AES : Ag (%mass) 52.6



AgNO<sub>3</sub> (154 mg 907 μmol) was solubilized in a mixture of MeOH (12mL) and water (4mL). To this solution was added NH<sub>4</sub>OH until the brown color completely disappeared. A solution of 1-octyne (50mg; 454 μmol) in MeOH (10mL) was added slowly to the mixture. A white precipitate formed directly and the solution was stirred at RT for 2h. The solution was filtered and the resulting white solid was washed with water then MeOH and dried under reduced atmosphere at 45°C for 48H. the product was sensitive to light and formed a dark powder soluble in chloroform (96 mg ; 97% ).

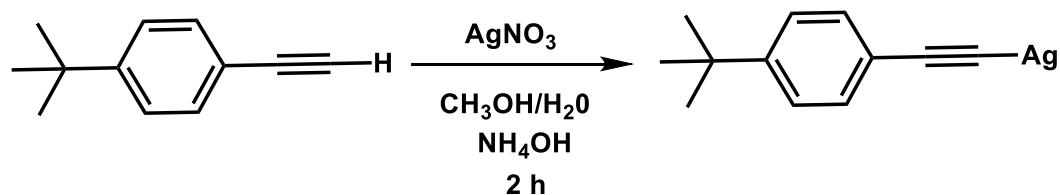
MP-AES : Ag(%mass) 66.4

<sup>1</sup>H NMR (400 MHz) CDCl<sub>3</sub>: 0.92 (t, 3H, J=6.7Hz) ; 1.31(m, 2H) ; 1.45(m, 2H) ; 1.66 (q, 2H, J=7.4Hz) ; 2.48 (t, 2H, J=7.4Hz)



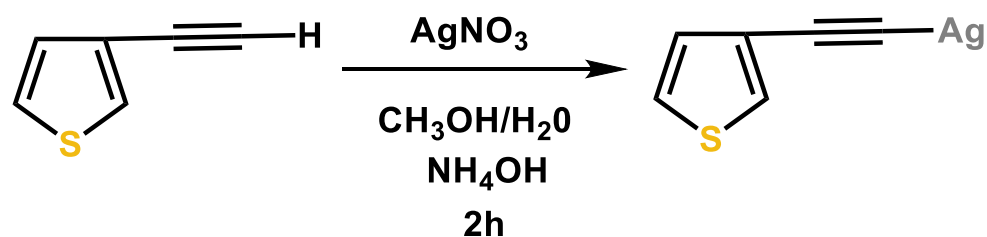
AgNO<sub>3</sub> (400 mg; 2.35 mmol) was solubilized in a mixture of MeOH (12mL) and water (4mL). To this solution was added NH<sub>4</sub>OH until the brown color completely disappeared. A solution of 4-Ethynyl-α,α,α-trifluorotoluene (200 mg; 1.17 mmol) in MeOH (10mL) was added slowly to the mixture. A white precipitate formed directly and the solution was stirred at RT for 2h. The solution was filtered and the resulting white solid was washed with water then MeOH and dried under reduced atmosphere at 45°C for 48H. The product was obtained as a insoluble hydrophobic white powder (321mg; 99%) sensitive to light but stable under atmospheric conditions (>6 months).

MP-AES : Ag(%mass) 47.3



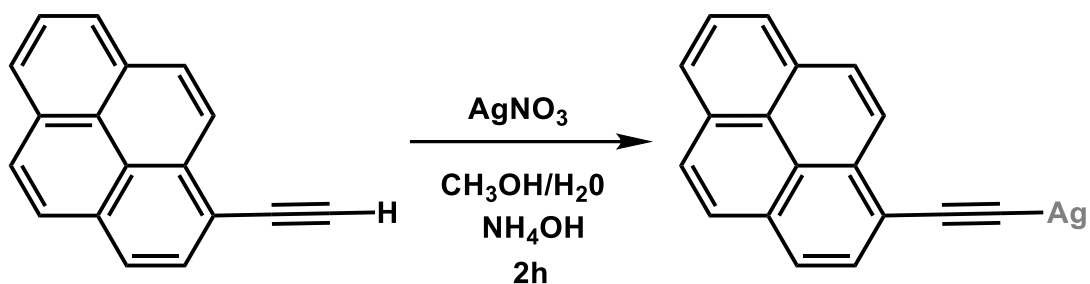
AgNO<sub>3</sub> (215 mg ; 1.26 mmol) was solubilized in a mixture of MeOH (12mL) and water (4mL). To this solution was added NH<sub>4</sub>OH until the brown color completely disappeared. A solution of 4-tert-Butylphenylacetylene (100 mg ; 632μmol) in MeOH (10mL) was added slowly to the mixture. A white precipitate formed directly and the solution was stirred at RT for 2h. The solution was filtered and the resulting insoluble hydrophobic white solid was washed with water then MeOH and dried under reduced atmosphere at 45°C for 48h. (124mg; 74%)

MP-AES : Ag(%mass) 49.5



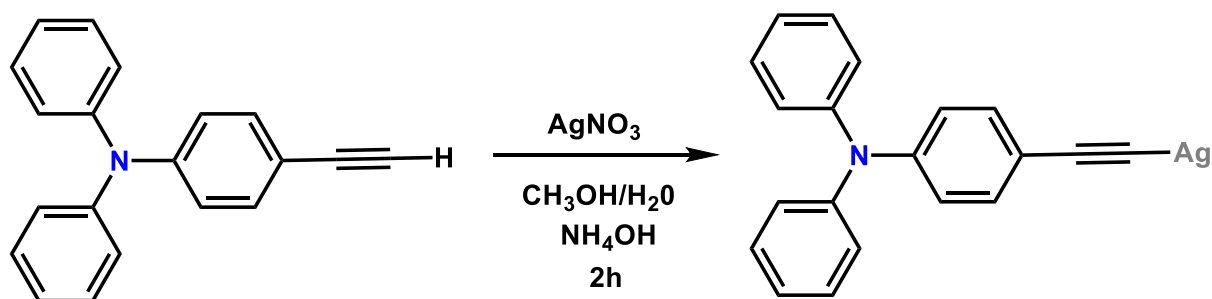
AgNO<sub>3</sub> (470 mg; 2.77 mmol) was solubilized in a mixture of MeOH (12mL) and water (4mL). To this solution was added NH<sub>4</sub>OH until the brown color completely disappeared. A solution of 3-ethynylthiophene (150 mg; 1.39 mmol) in MeOH (10mL) was added slowly to the mixture. A white precipitate formed directly and the solution was stirred at RT for 2h. The solution was filtered and the resulting pale yellow insoluble solid was washed with water then MeOH and dried under reduced atmosphere at 45°C for 48h (292 mg; 98%)

MP-AES : Ag(%mass) 54



AgNO<sub>3</sub> (75 mg ; 442 μmol) was solubilized in a mixture of MeOH (12mL) and water (4mL). To this solution was added NH<sub>4</sub>OH until the brown color completely disappeared. A solution of 1-ethynylpyrene (50mg; 221 μmol) in MeOH:DCM (1:1) (10mL) was added slowly to the mixture. A white precipitate formed directly and the solution was stirred at RT for 2h. The solution was filtered and the resulting red insoluble hydrophobic solid was washed with water then MeOH and dried under reduced atmosphere at 45°C for 48h. (55mg; 75 %)

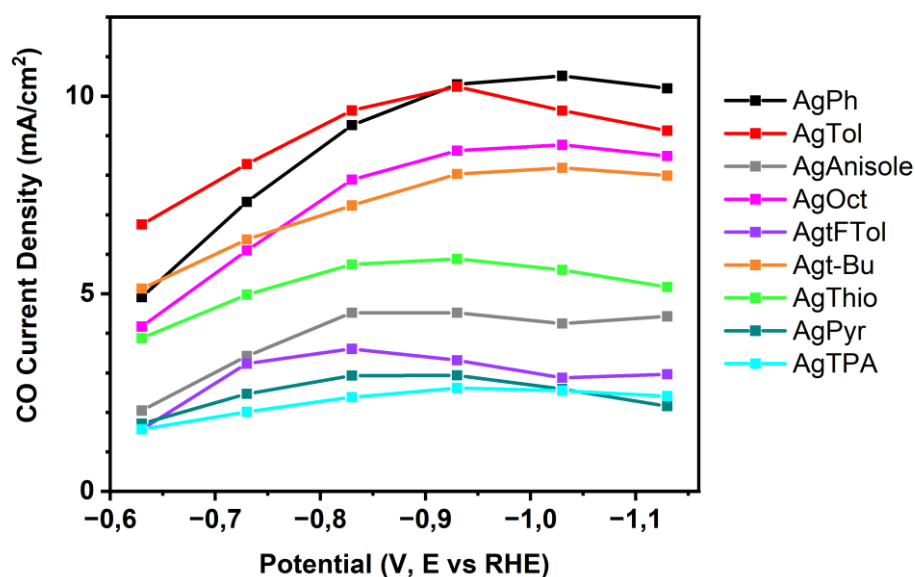
MP-AES : Ag(%mass) 42.9



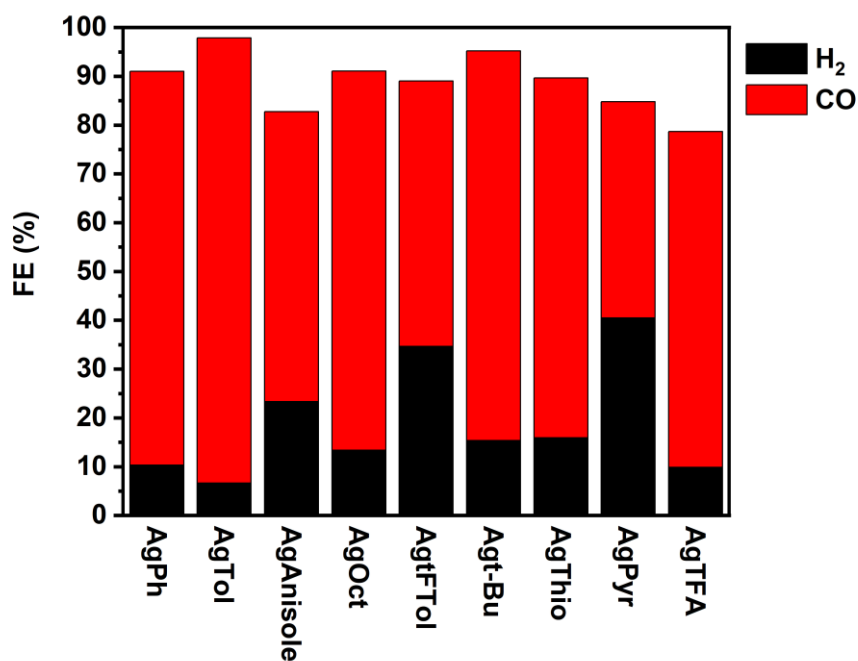
AgNO<sub>3</sub> (126 mg; 742 μmol) was solubilized in a mixture of MeOH (12mL) and water (4mL). To this solution was added NH<sub>4</sub>OH until the brown color completely disappeared. A solution of 4-Ethynyl-N,N-diphenylaniline (100mg; 371 μmol) in MeOH:DCM (1:1) (10mL) was added slowly to the mixture. A white precipitate formed directly and the solution was stirred at RT for 2h. The solution was filtered and the resulting yellow insoluble hydrophobic solid was washed with water then MeOH and dried under reduced atmosphere at 45°C for 48h. (98mg; 70%)

MP-AES : Ag(%mass) 33.9

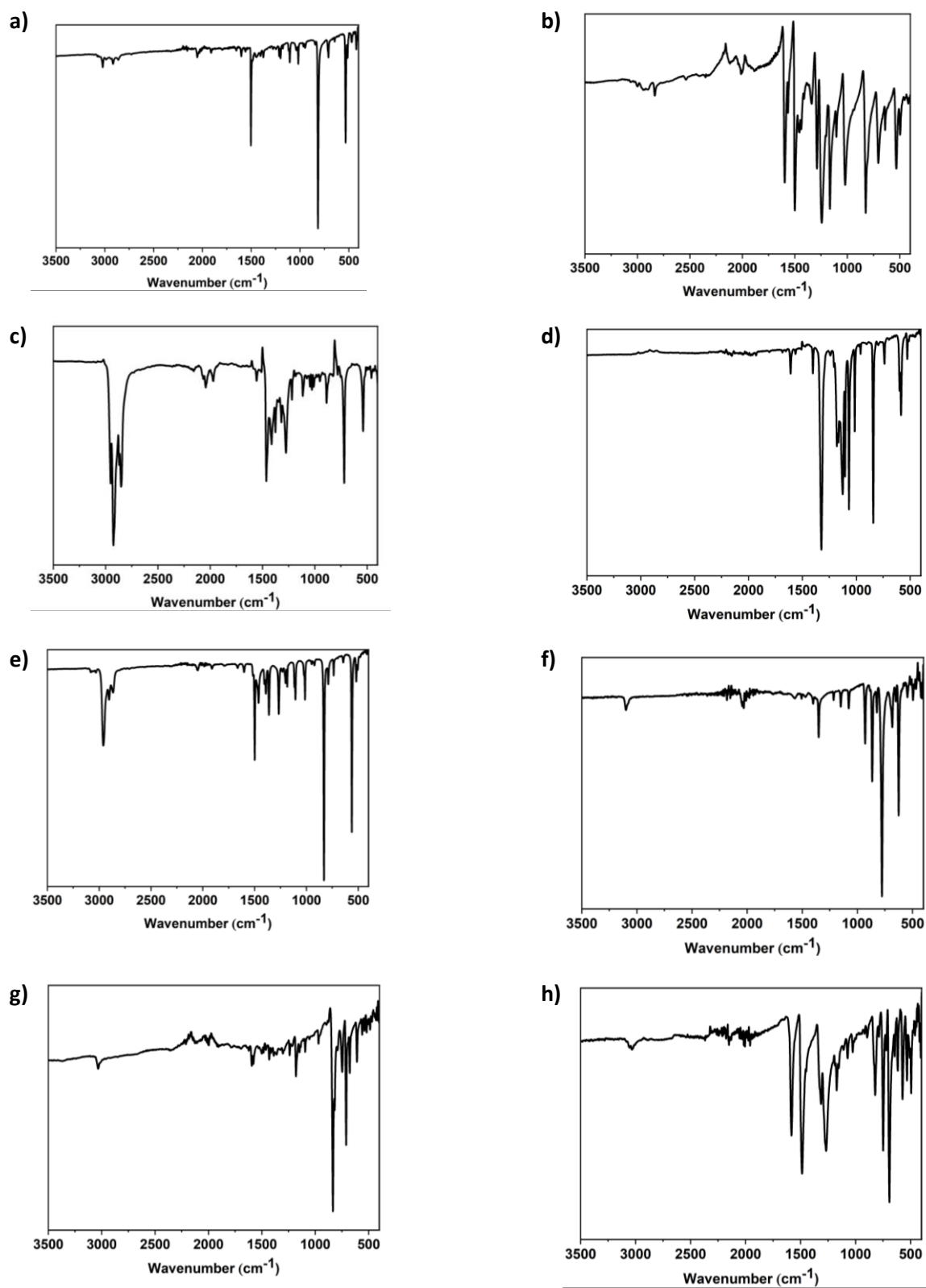




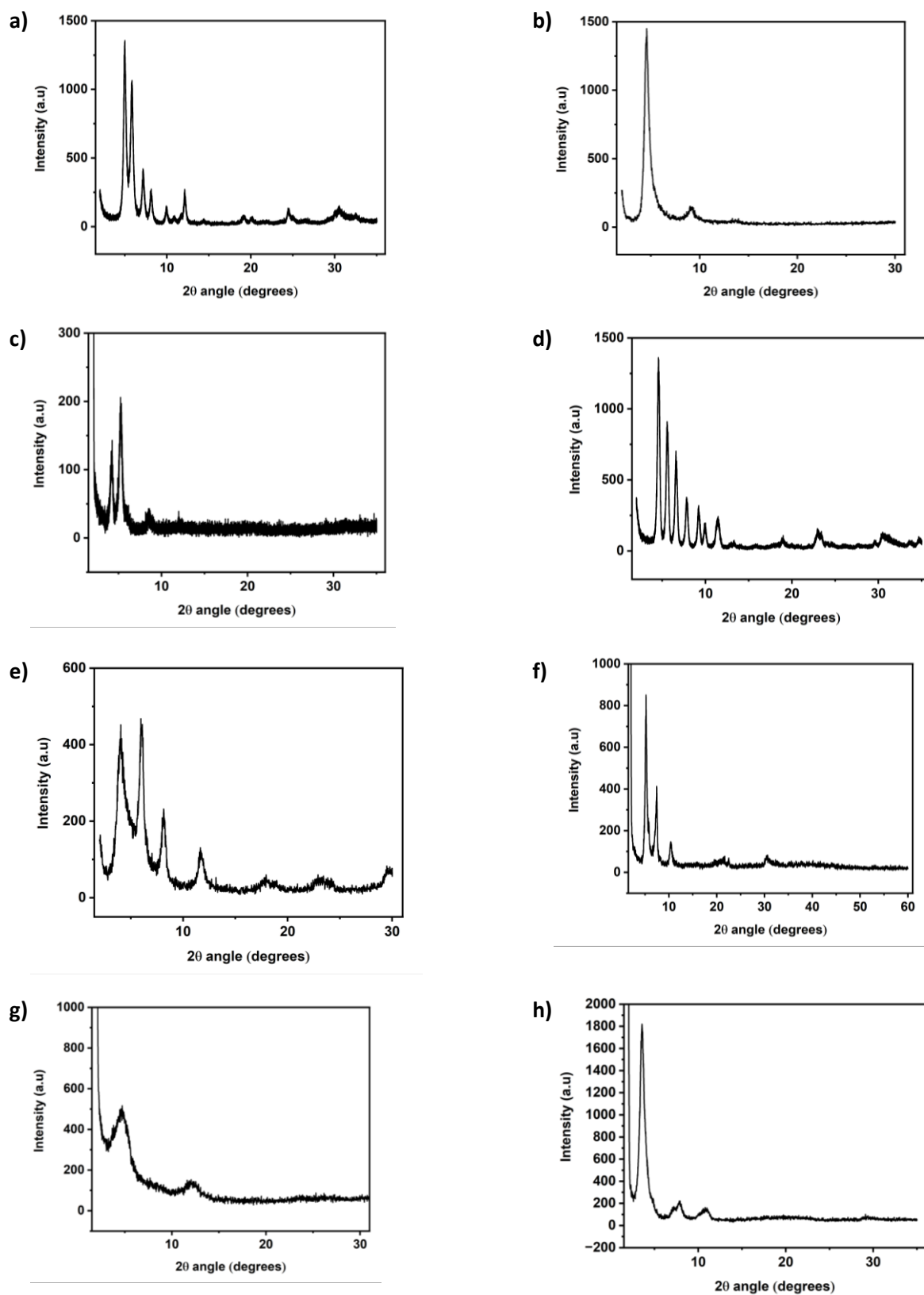
**Figure S4-2:** CO current density evolution with potential of the deposited Ag species on GDE substrates in CO<sub>2</sub> saturated 1 M KHCO<sub>3</sub> solution. **Fully carbonated groups are increasing CO current density compared with heteronuclear ligands. Bulky and  $\pi$ -extended structures seem to disfavor reactivity**



**Figure S4-3** Faradaic efficiency comparison at -0.63V vs RHE from Chronoamperometry (CA)(15min) of the deposited Acetylides on GDE substrates in a CO<sub>2</sub> saturated 1 M KHCO<sub>3</sub>.



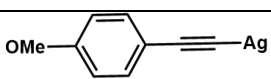
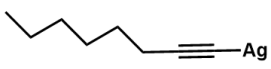
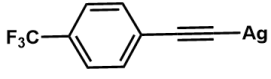
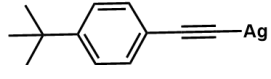
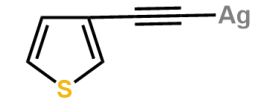
**Figure S4-4:** IR-ATR of **a)** AgTol **b)** AgAnisole **c)** AgOct **d)** AgtFTol **e)** Agt-Bu **f)** AgThio **g)** AgPyr **h)** AgTPA. The disappearance of the strong C≡C-H band is assumed to be due to the formation of the C≡C-Ag bond.



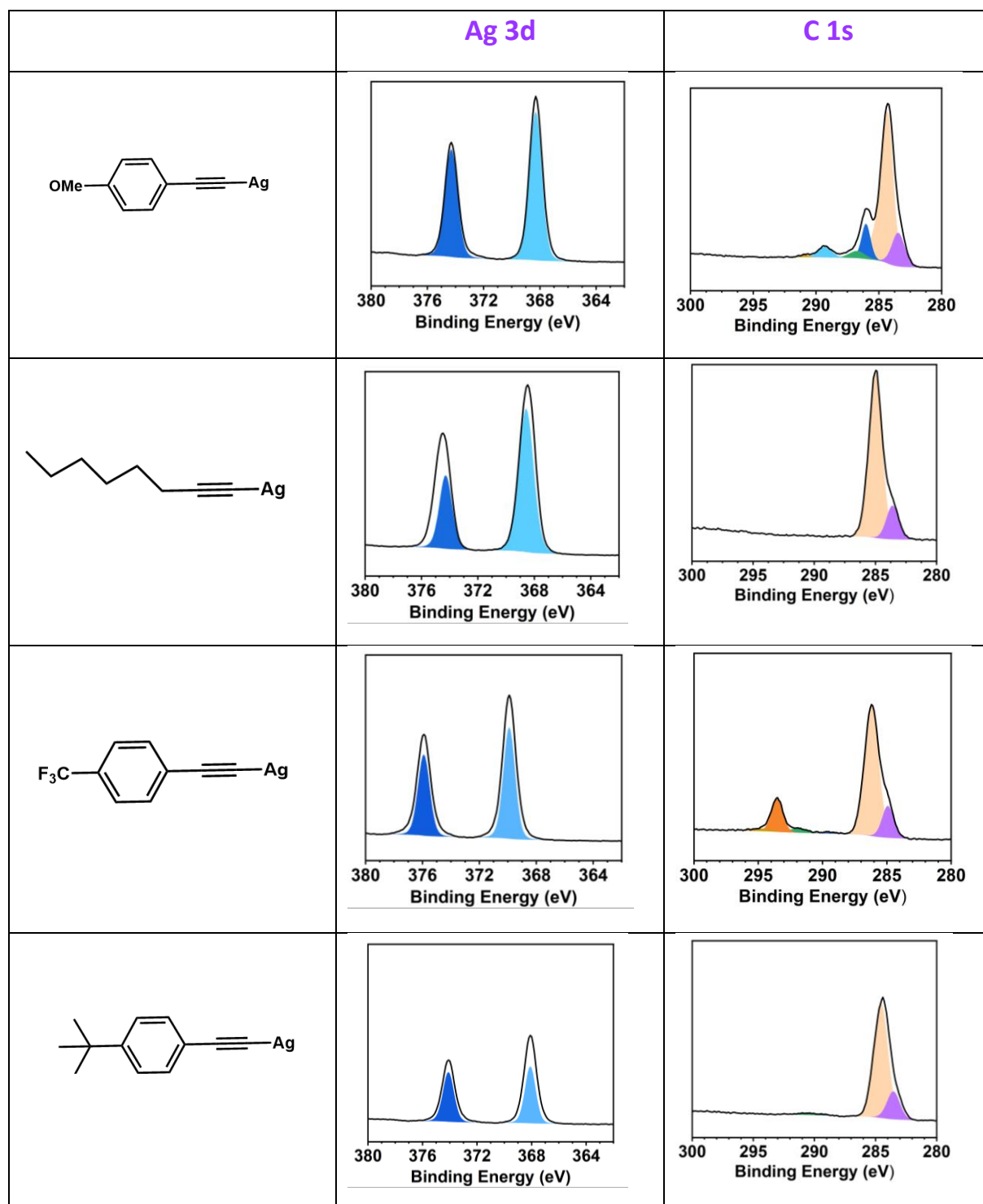
**Figure S4-5:** Powder X-Ray diffraction (PXRD) of **a) AgTol b) AgAnisole c) AgOct d) AgtFTol e) Agt-Bu f) AgThio g) AgPyr h) AgTPA.**

Compound	Crystallinity (%)	crystallite size (Å)
<b>AgTol</b>	85	305
<b>AgAnisole</b>	83	173
<b>AgOct</b>	76	427
<b>AgtFTol</b>	88	270
<b>Agt-Bu</b>	83	250
<b>AgThio</b>	88	260
<b>AgPyr</b>	72	64
<b>AgTPA</b>	81	154

**Figure S4-6:** Sample crystallinity and crystallite size calculated by Scherrer equation.

Compound	C	O	Ag	S	F	Si	C/Ag
	72.4	12.2	9.4	0.9	4.5	1.6	7.7
	81.4	2.4	15.6	0.9			5.2
	62.9	0.6	9.6		26.9		6.6
	87.9	1.9	10.3				8.5
	65.6	1.7	16.9	15	0.9	0.9	3.9

**Figure S4-7:** XPS Elemental quantification. **AgAnisole C/O ratio is 5.9; AgtFTol C/F is 2.33 and AgThio C/S is 4.37.**



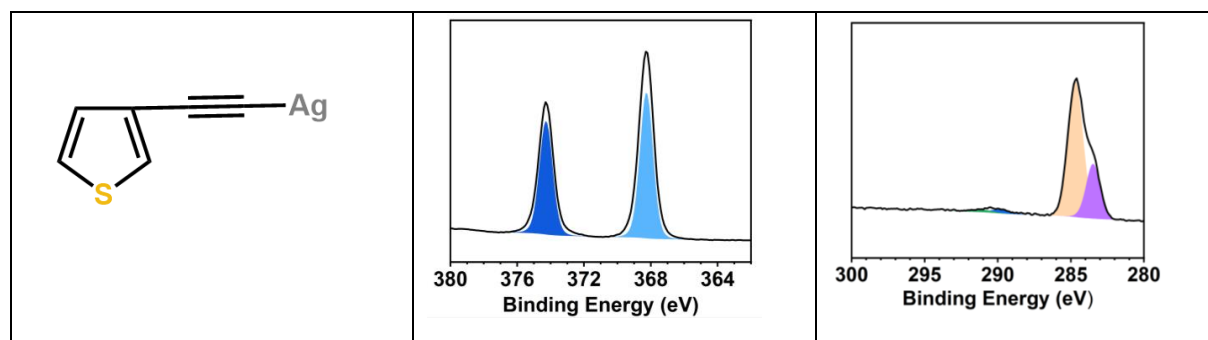


**Figure S4-8** XPS spectra (Ag 3d and C 1s regions). **The species are Ag(I) complexes and the carbon spectra are showing a band corresponding to an Ag-C≡C**

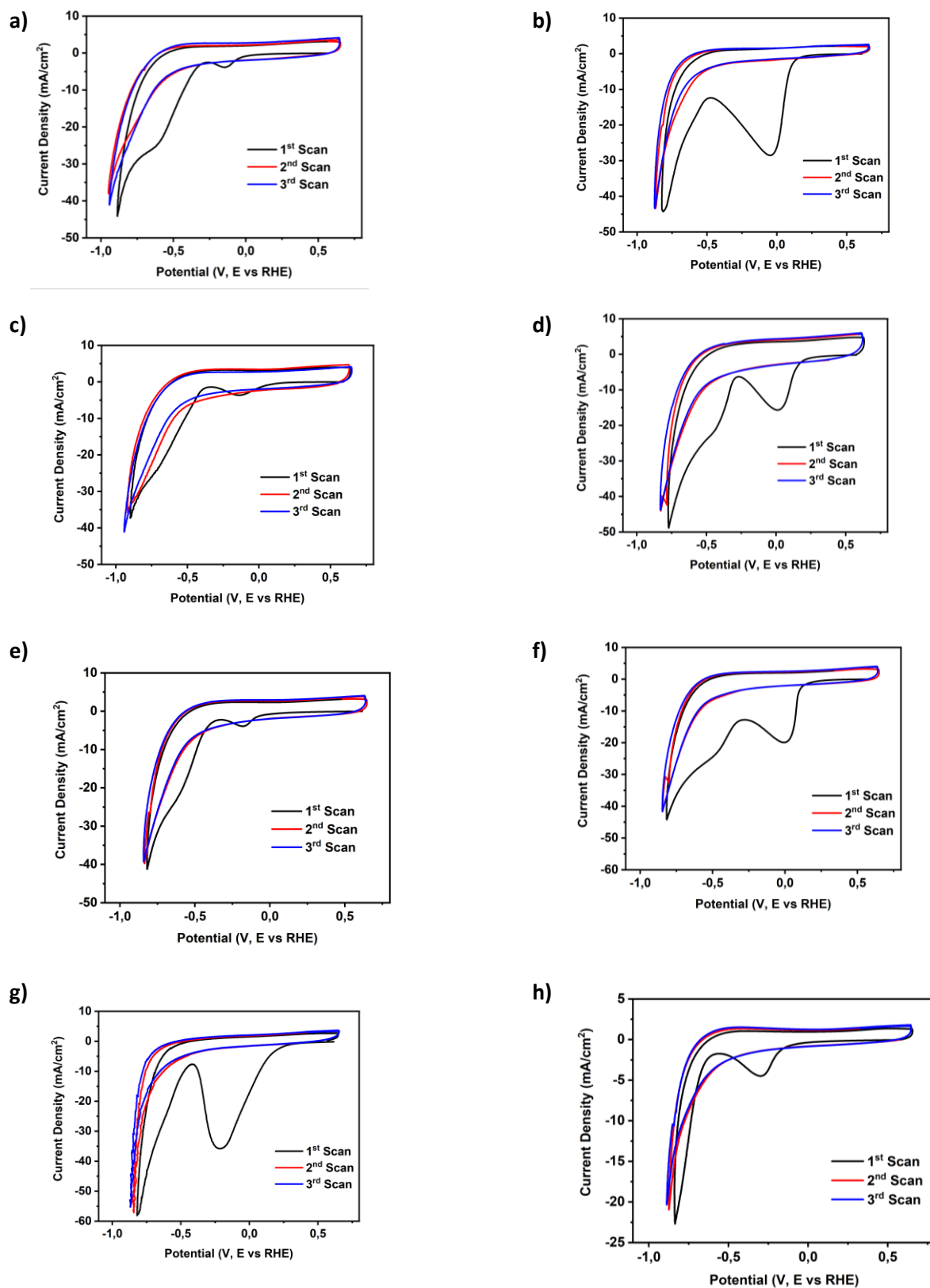


**Figure S4-9:** CV measurement at 100 mV/s (3 scans) on the GDE substrate in a N<sub>2</sub> saturated 1 M KHCO<sub>3</sub> solution. **a)** AgTol **b)** AgAnisole **c)** AgOct **d)** AgtFTol **e)** Agt-Bu **f)** AgThio **g)** AgPyr **h)** AgTPA

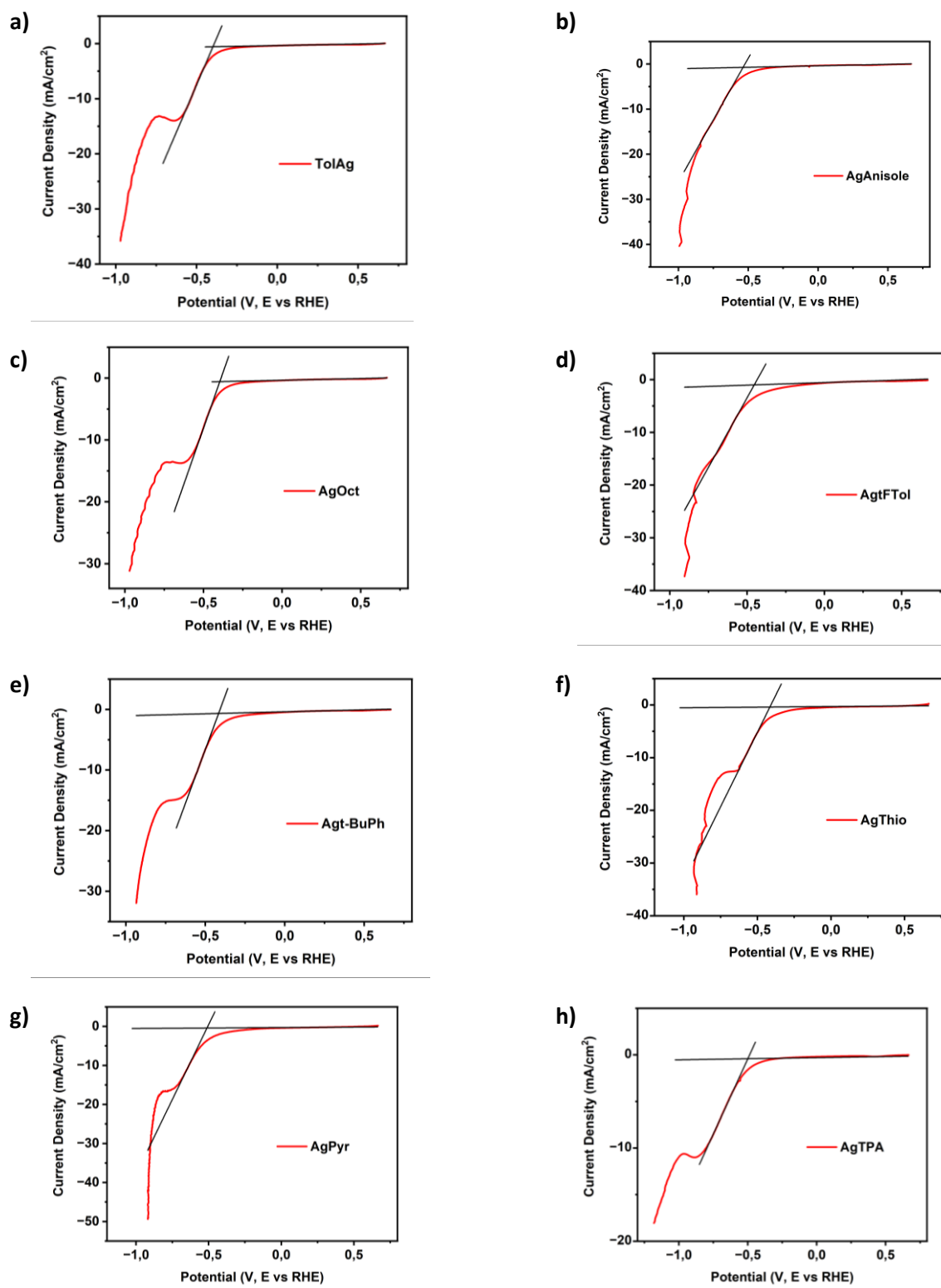
Compound	Ag content (mass%)
<b>AgPh*</b>	50.7
<b>AgTol</b>	46.3
<b>AgAnisole</b>	52.6
<b>AgOct</b>	66.4
<b>AgtFTol</b>	47.3
<b>Agt-Bu</b>	49.5
<b>AgThio</b>	54.0
<b>AgPyr</b>	42.9
<b>AgTPA</b>	33.9

**Figure S4-10:** MP-AES quantification (10 ppm solution in 3% HNO<sub>3</sub> prepared from a 1000 ppm solution in TFA: H<sub>2</sub>O (1:3)) The results are obtained from a calibration curve of 6 points between 1 and 20 ppm made from a 1000 ppm AgNO<sub>3</sub> solution in 3% HNO<sub>3</sub> (R<sup>2</sup>=0.998). The measured value is in accordance with 1:1 complex being the major product

Compound	Potential (V vs RHE)	Q (mC)	Γ[Ag] (nmol)	active Ag (load%)
<b>AgPh</b>	-0.208	9.02	129	7
<b>AgTol</b>	-0.184	2.55	36.4	1.6
<b>AgAnisole</b>	-0.046	7.11	90	3.6
<b>AgOct</b>	-0.179	5.83	342	1.8
<b>AgtFTol</b>	0.024	5.83	34.2	1.4
<b>Agt-Bu</b>	-0.233	3.08	37.2	2
<b>AgThio</b>	-0.014	31.7	342	17
<b>AgPyr</b>	-0.215	98	1270	80
<b>AgTPA</b>	-0.270	6.93	226	18

**Figure S4-11:** reduction peak potential integration, electroactive species and active silver loading calculations.

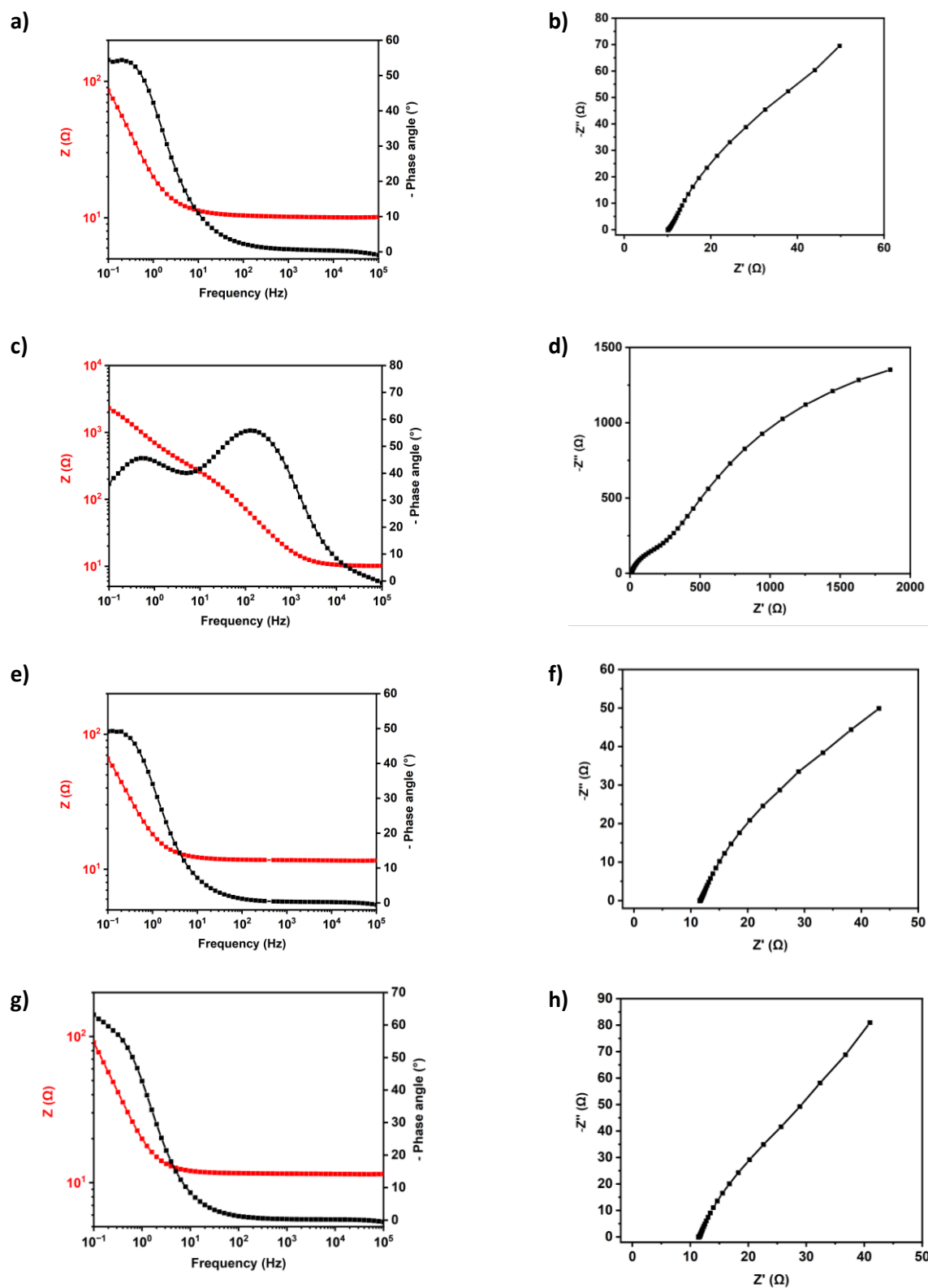


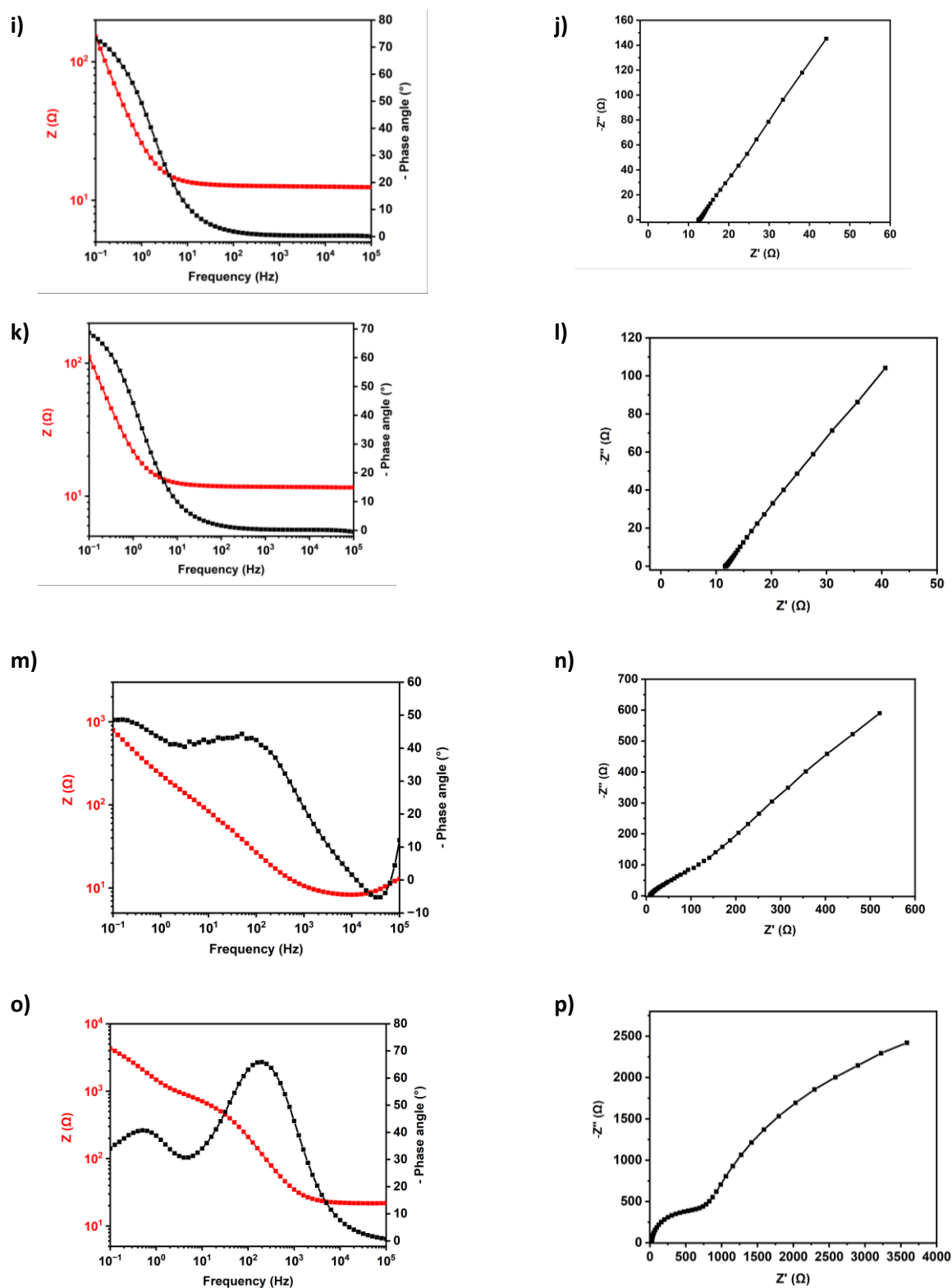


**Figure S4-12:** LSV measurement at 10 mV/s (2<sup>nd</sup> scan) of the deposited materials on GDE substrates in CO<sub>2</sub> saturated 1 M KHCO<sub>3</sub> solution **a)** AgTol **b)** AgAnisole **c)** AgOct **d)** AgtFTol **e)** Agt-Bu **f)** AgThio **g)** AgPyr **h)** AgTPA

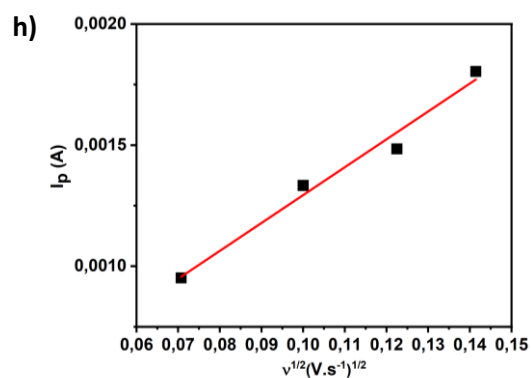
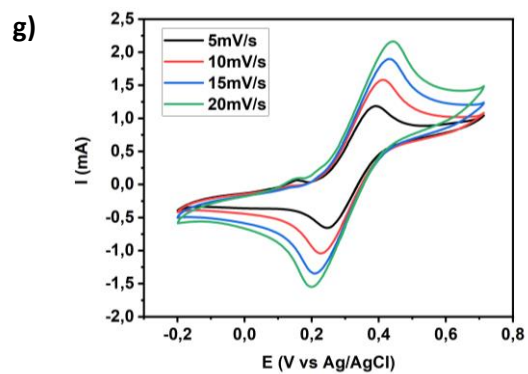
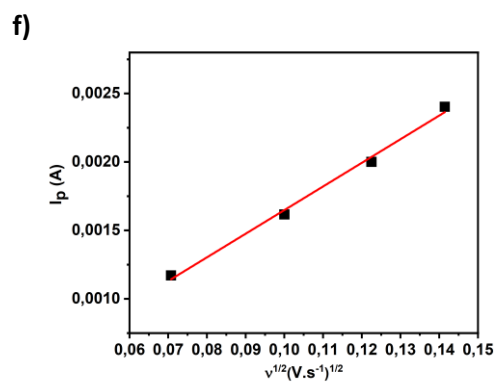
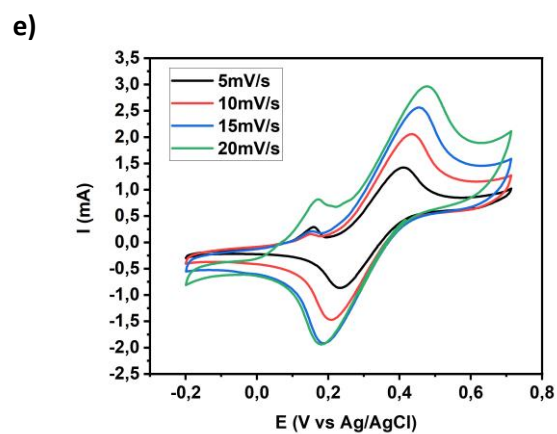
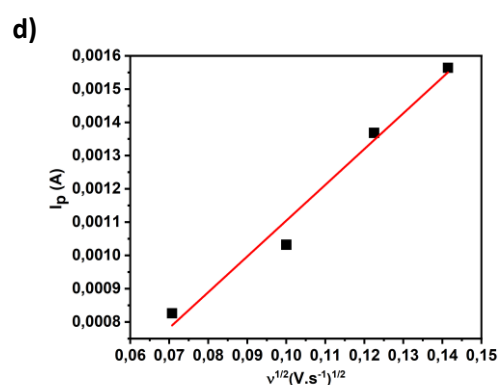
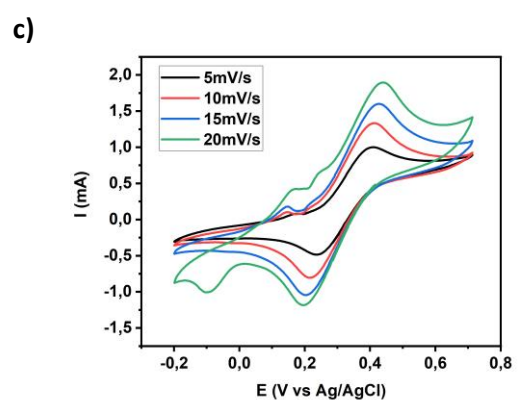
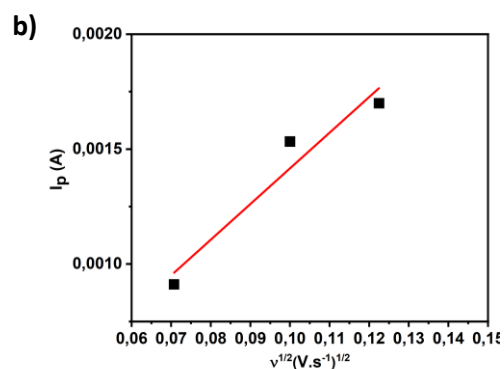
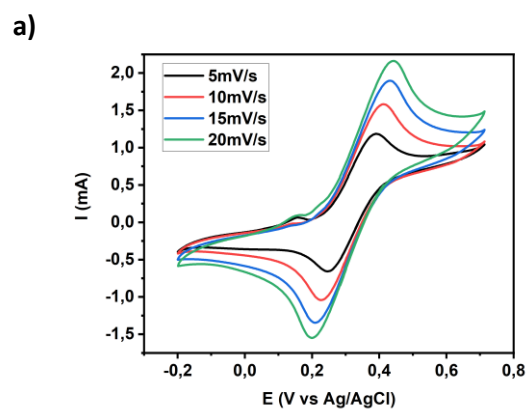
Compound	Onset potential (V vsRHE)	CO <sub>2</sub> RR Overpotential (V vsRHE)
<b>AgPh*</b>	-0,452	-0,383
<b>AgTol</b>	-0,415	-0,346
<b>AgAnisole</b>	-0,53747	-0,46847
<b>AgOct</b>	-0,39673	-0,32773
<b>AgtFTol</b>	-0,47353	-0,40453
<b>AgT-Bu</b>	-0,41678	-0,34778
<b>AgThio</b>	-0,41584	-0,34684
<b>AgPyr</b>	-0,516	-0,447
<b>AgTPA</b>	-0,4998	-0,4308

**Figure S4-13:** Onset potential and CO<sub>2</sub>RR overpotentials. CO<sub>2</sub>RR overpotentials were calculated from the thermodynamic -0.53 V vs SHE for CO<sub>2</sub> to CO conversion (converted as -0.069 V vs RHE).





**Figure S4-14** Electrochemical Impedance Spectroscopy (EIS) AgTol **a)** Bode plot **b)** Nyquist plot; AgAnisole **c)** Bode plot **d)** Nyquist plot ; AgOct **e)** Bode plot **f)** Nyquist plot ; AgtFTol **g)** Bode plot **h)** Nyquist plot ; Agt-Bu **i)** Bode plot **j)** Nyquist plot ; AgThio **k)** Bode plot **l)** Nyquist plot AgPyr ; **m)** Bode plot **n)** Nyquist plot ; AgTPA **o)** Bode plot **p)** Nyquist plot.



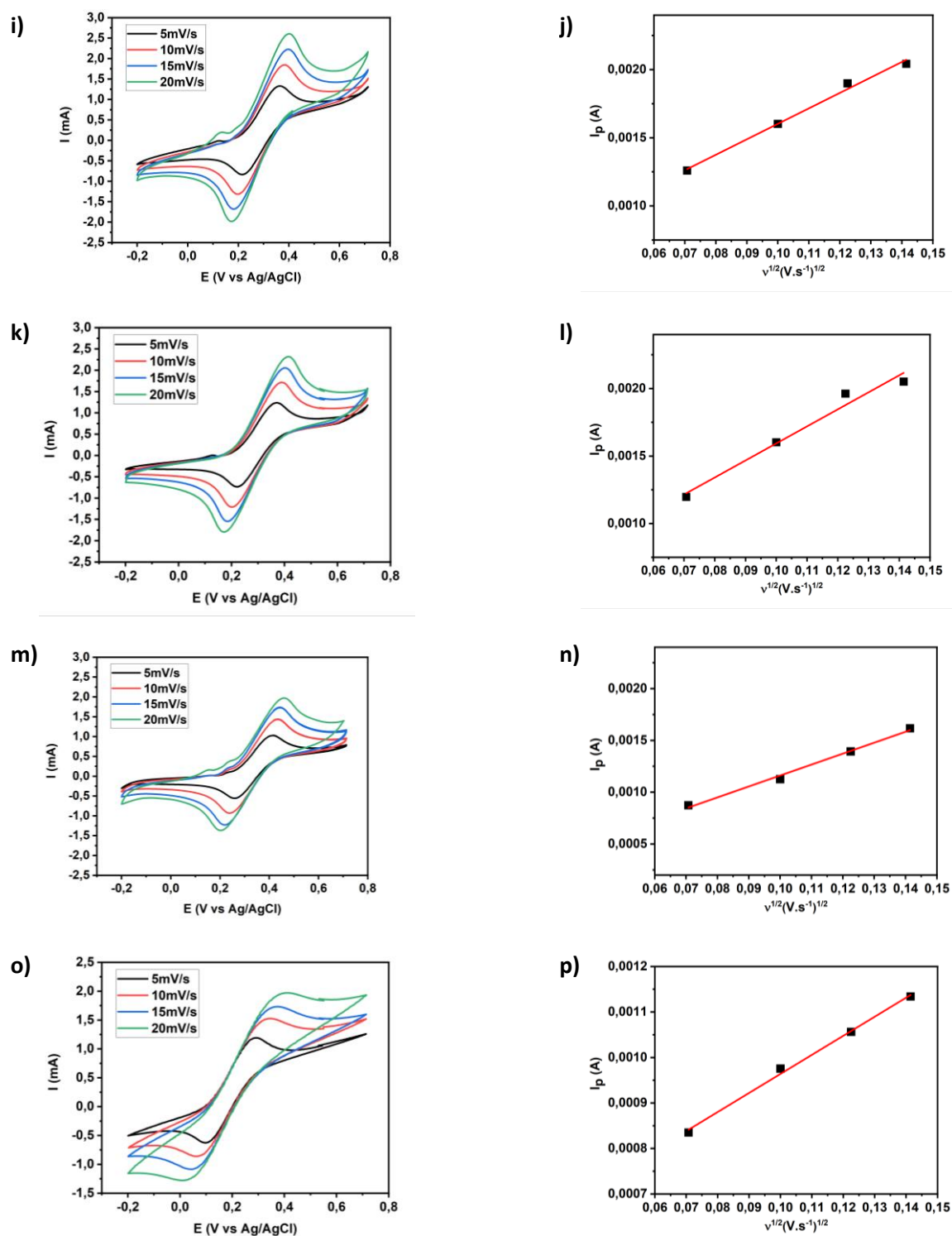


**Figure S4-15** Cyclic voltammograms (CV) of a 25 mM potassium ferrocyanide in a 0.1M KCl solution using an AgAnisole electrode at various scan rates (5, 10, 15 and 20mV/s) and peak current as a function of the square root of the scan rate variation. AgTol **a)** CV scans **b)** fitted curve; AgAnisole **c)** CV scans **d)** fitted curve; AgOct **e)** CV scans **f)** fitted curve Agt-Bu **g)** CV scans **h)** fitted curve Agt-Bu **i)** CV scans **j)** fitted curve AgThio **k)** CV scans **l)** fitted curve AgPyr **m)** CV scans **n)** fitted curve AgTPA **o)** CV scans **p)** fitted curve.

Compound	ECSA (cm <sup>2</sup> )
<b>AgPh*</b>	0.72
<b>AgTol</b>	1.17
<b>AgAnisole</b>	0.81
<b>AgOct</b>	1.31
<b>AgtFTol</b>	0.87
<b>Agt-Bu</b>	0.86
<b>AgThio</b>	0.96
<b>AgPyr</b>	0.80
<b>AgTPA</b>	0.301

**Figure S4-16** The ECSA is calculated from the slope of the plot using the Randles-Sevcik equation.

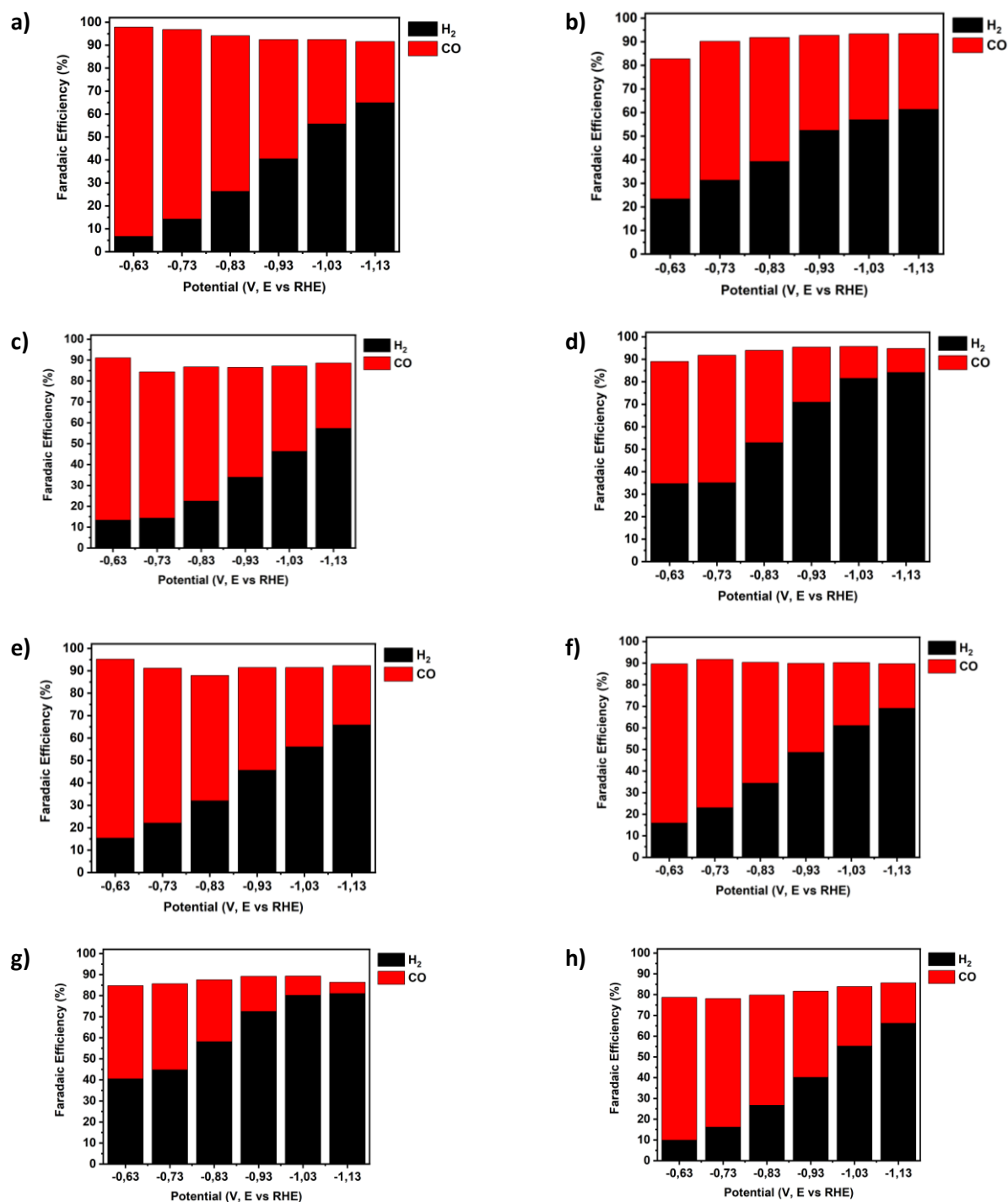


**Figure S4-17** Faradic efficiencies (FE) from direct GC quantification of 15 min long Chronoamperometry (CA) of the deposited materials on the GDE substrate in a CO<sub>2</sub> saturated 1 M KHCO<sub>3</sub> between -0.63 and -1.13 applied potentials (V, E vs RHE) with a step of 0.1 V. **a)** AgTol **b)** AgAnisole **c)** AgOct **d)** AgtFTol **e)** Agt-Bu **f)** AgThio **g)** AgPyr **h)** AgTPA



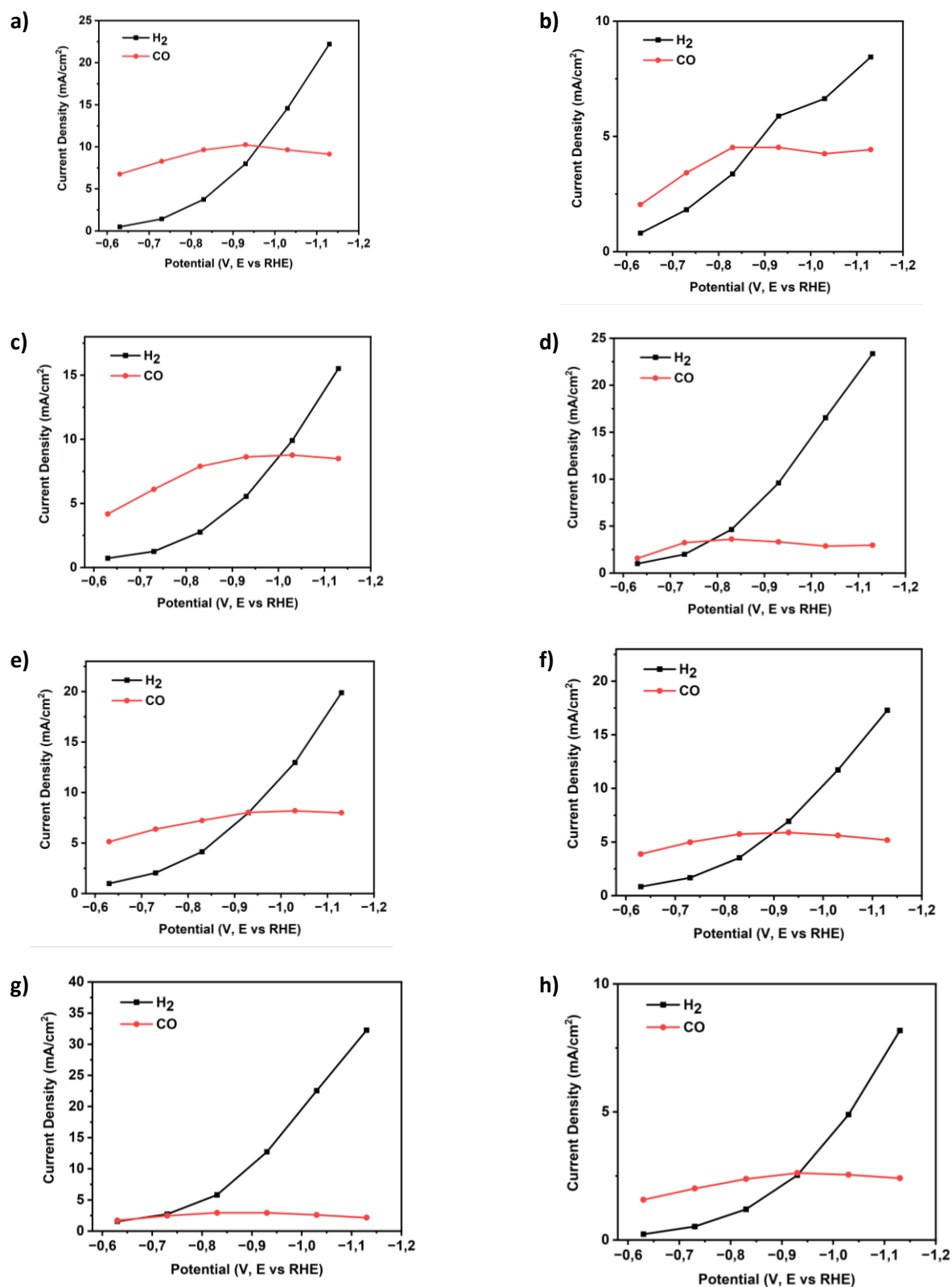


**Figure S4-18** CO and H<sub>2</sub> partial Current densities between -0.63 and -1.13 applied potentials (V, E vs RHE) with a step of 0.1 V (15min chronoamperometry) in the 1M KHCO<sub>3</sub> aqueous solution a) AgTol b) AgAnisole c) AgOct d) AgtFTol e) Agt-Bu f) AgThio g) AgPyr h) AgTPA

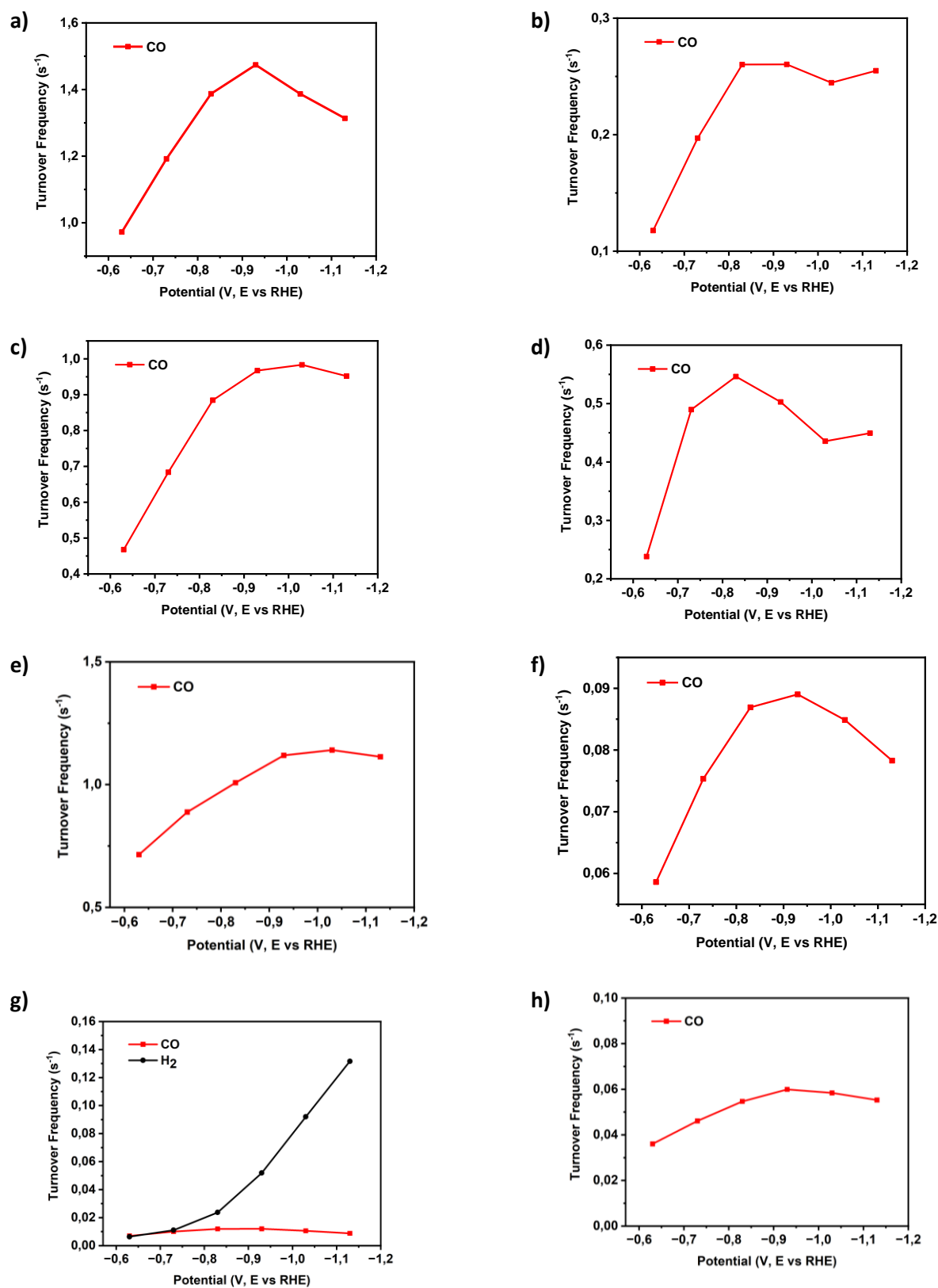


**Figure S4-19** Calculated TOF variation for CO<sub>2</sub>RR a) AgTol b) AgAnisole c) AgOct d) AgtFTol e) Agt-Bu f) AgThio g) AgPyr h) AgTPA

- (1) Qiao, J.; Liu, Y.; Zhang, J. Electrochemical Reduction of Carbon Dioxide: Fundamentals and Technologies. 396.
- (2) Song, M.-J.; Hwang, S. W.; Whang, D. Non-Enzymatic Electrochemical CuO Nanoflowers Sensor for Hydrogen Peroxide Detection. *Talanta* **2010**, *80* (5), 1648–1652. <https://doi.org/10.1016/j.talanta.2009.09.061>.
- (3) Krejci, J.; Sajdlova, Z.; Nedela, V.; Flodrova, E.; Sejnohova, R.; Vranova, H.; Plicka, R. Effective Surface Area of Electrochemical Sensors. *J. Electrochem. Soc.* **2014**, *161* (6), B147. <https://doi.org/10.1149/2.091406jes>.
- (4) Ameer, Z. O.; Husein, M. M. Electrochemical Behavior of Potassium Ferricyanide in Aqueous and (w/o) Microemulsion Systems in the Presence of Dispersed Nickel Nanoparticles. *Sep. Sci. Technol.* **2013**, *48* (5), 681–689. <https://doi.org/10.1080/01496395.2012.712594>.
- (5) Morozan, A.; Johnson, H.; Roiron, C.; Genay, G.; Aldakov, D.; Ghedjatti, A.; Nguyen, C. T.; Tran, P. D.; Kinge, S.; Artero, V. Non-Precious Bimetallic Iron-Molybdenum Sulfide Electrocatalysts for Hydrogen Evolution Reaction in Proton-Exchange Membrane Electrolyzers.
- (6) Frisch, M. J.; Trucks, G. W.; Schlegel, H. B.; Scuseria, G. E.; Robb, M. A.; Cheeseman, J. R.; Scalmani, G.; Barone, V.; Petersson, G. A.; Nakatsuji, H.; Li, X.; Caricato, M.; Marenich, A. V.; Bloino, J.; Janesko, B. G.; Gomperts, R.; Mennucci, B.; Hratchian, H. P.; Ortiz, J. V.; Izmaylov, A. F.; Sonnenberg, J. L.; Williams-Young, D.; Ding, F.; Lipparini, F.; Egidi, F.; Goings, J.; Peng, B.; Petrone, A.; Henderson, T.; Ranasinghe, D.; Zakrzewski, V. G.; Gao, J.; Rega, N.; Zheng, G.; Liang, W.; Hada, M.; Ehara, M.; Toyota, K.; Fukuda, R.; Hasegawa, J.; Ishida, M.; Nakajima, T.; Honda, Y.; Kitao, O.; Nakai, H.; Vreven, T.; Throssell, K.; Montgomery, J. A., Jr.; Peralta, J. E.; Ogliaro, F.; Bearpark, M. J.; Heyd, J. J.; Brothers, E. N.; Kudin, K. N.; Staroverov, V. N.; Keith, T. A.; Kobayashi, R.; Normand, J.; Raghavachari, K.; Rendell, A. P.; Burant, J. C.; Iyengar, S. S.; Tomasi, J.; Cossi, M.; Millam, J. M.; Klene, M.; Adamo, C.; Cammi, R.; Ochterski, J. W.; Martin, R. L.; Morokuma, K.; Farkas, O.; Foresman, J. B.; Fox, D. J. Gaussian 16 Revision C.01, 2016.
- (7) Becke, A. D. Density-functional Thermochemistry. III. The Role of Exact Exchange. *J. Chem. Phys.* **1993**, *98* (7), 5648–5652. <https://doi.org/10.1063/1.464913>.
- (8) Vosko, S. H.; Wilk, L.; Nusair, M. Accurate Spin-Dependent Electron Liquid Correlation Energies for Local Spin Density Calculations: A Critical Analysis. *Can. J. Phys.* **1980**, *58* (8), 1200–1211. <https://doi.org/10.1139/p80-159>.
- (9) Lee, C.; Yang, W.; Parr, R. G. Development of the Colle-Salvetti Correlation-Energy Formula into a Functional of the Electron Density. *Phys. Rev. B* **1988**, *37* (2), 785–789. <https://doi.org/10.1103/PhysRevB.37.785>.
- (10) Stephens, P. J.; Devlin, F. J.; Chabalowski, C. F.; Frisch, M. J. Ab Initio Calculation of Vibrational Absorption and Circular Dichroism Spectra Using Density Functional Force Fields. *J. Phys. Chem.* **1994**, *98* (45), 11623–11627. <https://doi.org/10.1021/j100096a001>.
- (11) Grimme, S.; Ehrlich, S.; Goerigk, L. Effect of the Damping Function in Dispersion Corrected Density Functional Theory. *J. Comput. Chem.* **2011**, *32* (7), 1456–1465. <https://doi.org/10.1002/jcc.21759>.
- (12) Feller, D. The Role of Databases in Support of Computational Chemistry Calculations. *J. Comput. Chem.* **1996**, *17* (13), 1571–1586. [https://doi.org/10.1002/\(SICI\)1096-987X\(199610\)17:13<1571::AID-JCC9>3.0.CO;2-P](https://doi.org/10.1002/(SICI)1096-987X(199610)17:13<1571::AID-JCC9>3.0.CO;2-P).
- (13) Schuchardt, K. L.; Didier, B. T.; Elsethagen, T.; Sun, L.; Gurumoorthi, V.; Chase, J.; Li, J.; Windus, T. L. Basis Set Exchange: A Community Database for Computational Sciences. *J. Chem. Inf. Model.* **2007**, *47* (3), 1045–1052. <https://doi.org/10.1021/ci600510j>.

- (14) Pritchard, B. P.; Altarawy, D.; Didier, B.; Gibson, T. D.; Windus, T. L. New Basis Set Exchange: An Open, Up-to-Date Resource for the Molecular Sciences Community. *J. Chem. Inf. Model.* **2019**, *59* (11), 4814–4820. <https://doi.org/10.1021/acs.jcim.9b00725>.
- (15) Ehlers, A. W.; Böhme, M.; Dapprich, S.; Gobbi, A.; Höllwarth, A.; Jonas, V.; Köhler, K. F.; Stegmann, R.; Veldkamp, A.; Frenking, G. A Set of F-Polarization Functions for Pseudo-Potential Basis Sets of the Transition Metals Sc–Cu, Y–Ag and La–Au. *Chem. Phys. Lett.* **1993**, *208* (1), 111–114. [https://doi.org/10.1016/0009-2614\(93\)80086-5](https://doi.org/10.1016/0009-2614(93)80086-5).
- (16) Hay, P. J.; Wadt, W. R. Ab Initio Effective Core Potentials for Molecular Calculations. Potentials for K to Au Including the Outermost Core Orbitals. *J. Chem. Phys.* **1985**, *82* (1), 299–310. <https://doi.org/10.1063/1.448975>.
- (17) Boys, S. F.; Bernardi, F. The Calculation of Small Molecular Interactions by the Differences of Separate Total Energies. Some Procedures with Reduced Errors. *Mol. Phys.* **1970**, *19* (4), 553–566. <https://doi.org/10.1080/00268977000101561>.
- (18) Simon, S.; Duran, M.; Dannenberg, J. J. How Does Basis Set Superposition Error Change the Potential Surfaces for Hydrogen-bonded Dimers? *J. Chem. Phys.* **1996**, *105* (24), 11024–11031. <https://doi.org/10.1063/1.472902>.
- (19) Wang, M.; Torbensen, K.; Salvatore, D.; Ren, S.; Joulié, D.; Dumoulin, F.; Mendoza, D.; Lassalle-Kaiser, B.; Işci, U.; Berlinguette, C. P.; Robert, M. CO<sub>2</sub> Electrochemical Catalytic Reduction with a Highly Active Cobalt Phthalocyanine. *Nat. Commun.* **2019**, *10* (1), 3602. <https://doi.org/10.1038/s41467-019-11542-w>.

## Chapter 5 : Porphyrin-silver acetylide cluster catalysts with dual active sites for the electrochemical reduction of CO<sub>2</sub>

### Introduction

The electrochemical reduction of CO<sub>2</sub> into feedstocks, such as permanent gases or alcohols, is a promising alternative for offsetting greenhouse gas emissions.<sup>1-3</sup> The transformation is generally mediated by a catalyst of metallic nature under electrochemical conditions. Since the pioneering work of Hori on CO<sub>2</sub> electroreduction, the properties of copper, gold or silver have been well studied.<sup>4,5</sup> However, catalysts with high selectivity for C<sub>2+</sub> products are still scarce.

Molecular catalysts have seen a surge of interest in recent years. Indeed, high faradic efficiencies for CO or methane have been described under high electrolysis currents. They benefit from a high structural versatility with respect to elemental metals and can generally be deposited from a liquid slurry or colloidal suspension directly onto carbon or PTFE-based gas diffusion layers (GDLs). However, molecular catalysts suffer from a main drawback: their catalytic selectivity is, to date, limited to C<sub>1</sub> products. Their chemical structure, typically a metal bound by coordinating ligands, holds the former catalytic centres further apart, impeding the formation of the necessary dimerised intermediate leading to C<sub>2+</sub> adducts. As such, CO has remained the primary CO<sub>2</sub> reduction adduct from molecular catalysts in the CO<sub>2</sub>RR. However, hybrid systems have recently emerged in which a molecular catalyst is coupled to a metallic catalyst with complementary selectivity. For example, CO-selective catalysts such as Cobalt-phthalocyanine or porphyrin have been adsorbed on the surface of copper nanoparticles<sup>6,7</sup> or sputtered copper layers,<sup>8</sup> boosting the overall selectivity for ethylene and ethanol. Although very elegant, this strategy lacks the versatility attributes of molecular catalysts since their deposition on the copper surfaces remains somewhat challenging.

To remedy this setback, herein we propose an approach in which both the molecular and metallic counterparts are synthesised in one step from wet chemical methods. This is achieved through the controlled synthesis of metallic clusters, whose organic part is composed of catalytically active porphyrins, and the cluster's core is made from a CO<sub>2</sub>RR-active metal (**Figure 5.1**). The material is generally isolated as an organo-metallic discrete molecule, which can be further deposited on an electrode or GDL. Clusters have recently been proven catalytically active for the CO<sub>2</sub>RR, with impressive selectivity and unique crystalline properties.<sup>9-11</sup> Silver acetylide clusters have particularly shown outstanding selectivity for CO and ease of synthesis. Copper acetylides are equally attractive in that C<sub>2+</sub> selectivity could be expected since the metal cluster would allow the formation of dimeric intermediates.<sup>12</sup> A synergetic effect would be expected by combining the molecular and metallic species in a single entity. Therefore, this study is intended as a proof of concept for the further development of molecular catalyst hybrid structures with complementary catalytic properties. Silver acetylides are formed upon adding an alkyne-containing mixture to a solution of silver salts. The extremely high selectivity to alkyne groups results from the favourable formation of a  $\pi$ -bond between the silver (I) atoms and the triple bond. Thus, the activation provided renders the alkynyl proton labile, which is readily abstracted by any base, however weak, leading to the formation of a silver-acetylene bond (**Figure 5.2**). The favourable formation of metal-metal bonds dictates the formation of large clusters of silver atoms with alkynyl groups at the outer edge. Consequently, the near-perfect ordering of the silver atoms is most often transferred over long distances, leading to highly crystalline materials with

discrete molecular packing. Although generally limited to hundreds of nanometers in size, large single crystals of silver acetylides have been isolated, and a plethora of X-ray crystal structures are available to date.<sup>13</sup> The clusters distinguish themselves from classical metallic nanoparticles in that a very high degree of order is maintained through both the metallic and ligand constituents of the assembly, hence the recent coining of “atomically precise” materials.<sup>9</sup>

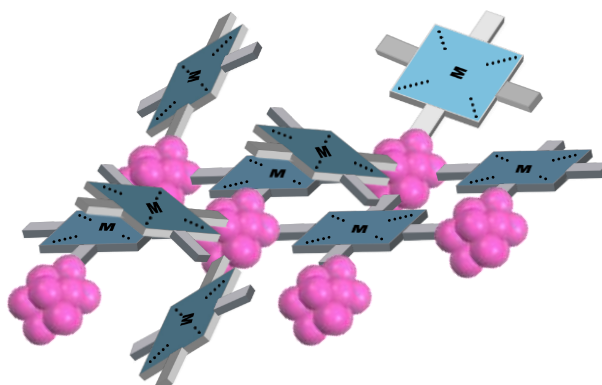


**Figure 5.1.** Schematic representation of a metal-porphyrin silver acetylide cluster 2D network synthesised from an alkyne-tetra functionalised porphyrin. This is a hypothetical structure based on reported X-Ray diffraction crystal structures of silver acetylides.

Contrary to other metal-carbon bonds, however, silver acetylides have no significant nucleophilic character, conferring them high stability at neutral and basic pH. As a consequence of both above-mentioned features, silver acetylides have been found to have a perfect application in the field of CO<sub>2</sub> reduction.<sup>14–17</sup> The extremely high level of structural control and extended stability confer silver acetylides remarkable catalytic properties. We, therefore, used the silver acetylide reaction to design two different types of catalyst structures with hypothetical complementary activity by forming silver acetylides from mono and tetra-functionalised porphyrins. The aim was to demonstrate the compatibility of a previously described silver acetylide synthesis method to the synthesis of complex architectures. Cobalt and iron porphyrin were chosen as the organic ligands for their known catalytic efficiency towards the CO<sub>2</sub>RR.

## Results and discussion

For that matter, alkyne mono- and tetra-functionalised porphyrins were synthesised using reported procedures. In brief, a typical Lindsey synthetic route from 4-((trimethylsilyl)ethynyl) benzaldehyde and freshly distilled pyrrole yielded a mixture of poly-substituted porphyrins (see ESI for details).<sup>18</sup> The mono and tetra substituted derivatives were readily purified using flash chromatography followed by preparative size exclusion chromatography. The respective adducts were metallated using 10 molar equivalents of a cobalt precursor and H<sub>2</sub>TPP derivatives in DMF at room temperature for 48 hours, yielding the metallated porphyrins in high yields. The iron metalation proved challenging, and long reaction times in refluxing DMF with lutidine were required to obtain the Iron-metallated porphyrins in high yields (83%).<sup>19,20</sup> Their corresponding acetylides were synthesised using an adapted version of Sheiber’s original route to silver acetylides.<sup>21</sup>

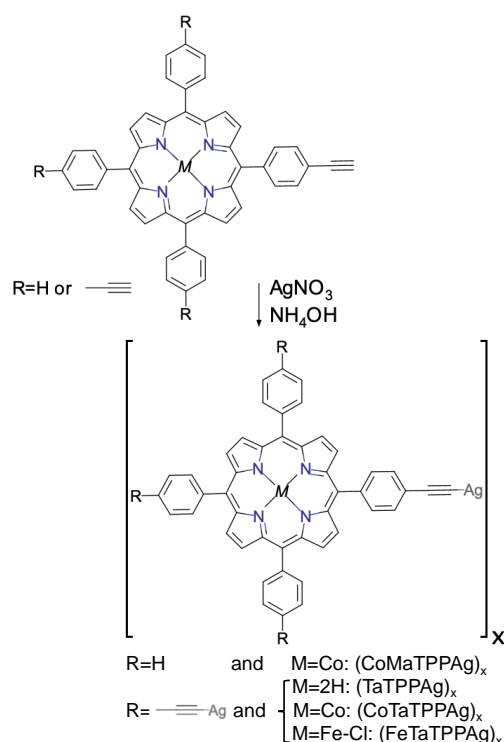


**Figure 5.2.** Depiction of the synthetic route to mono- and tetrasubstituted silver acetylides clusters.

The procedure involved, first, forming an aqueous silver ammoniacal complex by adding concentrated ammonia to a solution of silver nitrate in a mixture of water and methanol. A solution of the alkyne-functionalised porphyrin dissolved in a mixture of DMF, methanol and dichloromethane was subsequently added to the latter silver precursor. The reaction was first carried out on the monoalkylated Co-metallated porphyrin to optimise reaction conditions. Although the rate was slower than with simpler substrates, a dark precipitate corresponding to the silver acetylide formed upon stirring overnight. Simple filtration followed by washing with copious amounts of dichloromethane, methanol and water afforded the final product in relatively low yields. The very sluggish reaction kinetics, together with the limited weight of material recovered, prompted us to focus our attention on the reaction with alkyne tetrasubstituted porphyrins substrates. Using identical conditions to those described above, the precipitation of the expected ‘polymeric’ cluster occurred readily in quantitative yields. The insoluble nature of the latter confirmed the poly-substitution, forming a presumable pseudo-2D material. An acetylide of an unmetallated porphyrin was synthesised as a control compound, [TaTPPAg]<sub>x</sub>, to assess the extent to which further catalytic activity could be attributed to one or the other metallic species of the cluster. Despite the insolubility of the isolated solids, solid-state ATR FT-IR spectroscopy first confirmed the formation of the silver-carbon bond. Both the disappearance of the characteristic C≡C-H stretching band and the appearance of a characteristic C≡C stretching band confirm the formation of the desired adduct from a qualitative perspective (**Figure S5-15**, **Figure S5-22**, **Figure S5-29**).

Encouraged by the above features, we recorded powder XRD diffractograms on the tetrasubstituted porphyrins samples. **Figure 5.3** shows that, in agreement with our expectations, the diffractogram of all four acetylides shows unresolved peaks archetypical of polymeric 2D materials. The large values of full-width-at-half maximum (FWHM) advocate for very short-range order corresponding to diffraction planes with d-spacing in the order of 1 nm and 0.5 nm.

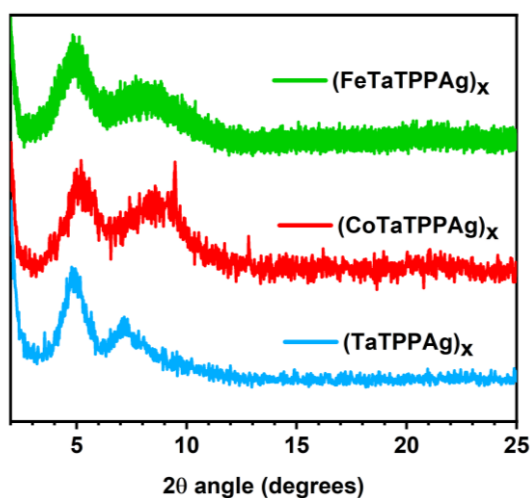


**Figure 5.3.** Powder diffractogram of all four silver acetylides, recorded on a Bruker D2-Phaser X-Ray diffractogram (Bragg-Brentano geometry).

Additionally, XPS data allowed for further structure elucidation. The presence of emission peaks arising from chlorine, iron, nitrogen and silver atoms provided qualitative information. Further comparison of peak positions with those recorded from reference compounds (**Figure S5-13**) allowed for a precise assignment and quantitative analysis (**Figure S5-14** and **Table S5-1**). Consequently, the position of the silver peak (Ag3d<sub>3/2</sub>=368,0eV), together with the presence of the carbon peak at 284.0 eV, confirms the nature of the Ag-C acetylide bonds (**Figure 5.4a** and **c**). Further details on the stoichiometry of the elemental constituents of the acetylides (Fe to Ag ratio and N to Ag ratio) allowed drawing an experimental Ag/porphyrin ratio, shown to be in the range of 1:1 (**Table S5-1**). A Comparison of the N1s emission spectrum (**Figure 5.4b**) with that of a reference non-metallated porphyrin pointed to a singular environment around the nitrogen atoms. This confirms the nearly exclusive presence of C-N-Fe bonds and attests to the porphyrinic origin of the Fe atoms. Finally, a weak peak with a characteristic binding energy corresponding to a Fe-O bond observed on the O1s spectrum (530 eV) initially raised our suspicion about the potential presence of residual iron oxide (**Figure 5.4d**). However, a close inspection of the sample's powder revealed the presence of minute amounts of monocrystalline fragments, morphologically distinct from the bulk of the sample.

A single crystal XRD structure was obtained from isolated crystals and revealed that the subproduct corresponded to a porphyrin dimer, in which two porphyrin units are linked by a bridging oxygen atom (**Figure S 5-37**), hence the Fe-O peak observed in the XPS spectrum. The formation was readily rationalised by the fact that the labile chlorine atom bore by the iron centre is readily pulled out of solution by the halophilic silver reagent, thus favouring the formation of the dimer. This is, fortunately, only limited to a small fraction of the sample. Overall, the combination of all the characterisation techniques expounded above points to a metal cluster with bridging porphyrin units. Above all, the synthesis conditions showed to be mild enough to leave the porphyrin's metals largely unaffected.

To assess the catalytic activity of our catalysts, electrochemical CO<sub>2</sub>RR experiments were carried out. The silver clusters were deposited on carbon-based gas diffusion layers typically used for CO<sub>2</sub> reduction. Hydrophobised (Sigracet 39BB) GDLs incorporating a top microporous carbon nanoparticle-based layer were utilised. The catalyst was immobilised on the GDL using a procedure reported by Robert and co-workers.<sup>22</sup> The GDL was coated with a carbon nanoparticles-Nafion-catalyst slurry by successive sonication-deposition-evaporation sequences until the appropriate weight-amount of catalyst was deposited. Field



emission SEM images of the resulting electrode and electron diffraction (EDX) (**Figure S5-25**, **Figure S5-18**, **Figure S5-25**) show segregation between the catalyst and the former two compounds. This was to be expected due to the insoluble nature of the catalysts, however, this was not expected to have a significant impact on the catalyst selectivity. The catalyst loading was further optimised by varying the weight-amount of catalyst with respect to the carbon nanoparticles and Nafion to maximise the catalytic characteristics, particularly the faradic efficiency towards the major adduct. Results showed that the catalyst loading could be decreased to a great extent without significant impact on the selectivity, however, for values below 0.05 mg/cm<sup>2</sup>, the HER became the dominating process.

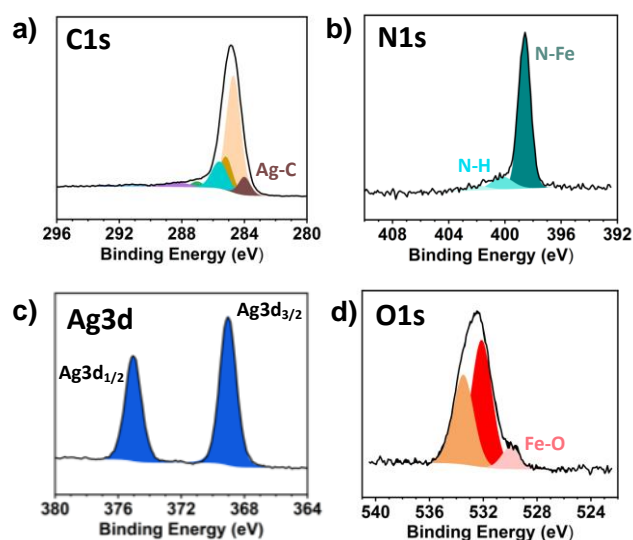


**Figure 5.4.** Zoomed in fragments of the XPS spectrum of [FeTaTTPAg]<sub>x</sub> a) C1s electrons emission b) N1s electrons emission c) Ag3d electrons emission d) O1s electrons emission.

The catalytic activity of the above GDEs was tested with a homemade 3-electrode cell (**Figure S5-1**) in a CO<sub>2</sub>-saturated 0.5 M potassium bicarbonate electrolyte. First, Linear sweep voltammetry (LSV) experiments carried out in identical conditions showed a clear catalytic wave with varying catalytic thresholds corresponding to overpotentials in the range of -0.40 to -0.6 V vs RHE. Interestingly, a very significant drop of overpotential is seen in the metalated porphyrin versions of the clusters with respect to the un-metalated control compound, the effect of which is attributed to the lower CO<sub>2</sub>RR overpotential of metalated porphyrins.

The selectivity of our catalyst was assessed in a series of CO<sub>2</sub>RR carried out with 0.1V increments from -0.55 to -1.15 V applied potentials (vs RHE) in chronoamperometry (CA) experiments, and the produced gaseous adducts were sampled and quantified from the cell's headspace after a 15min (see SI for details). Interestingly, all samples showed a rather high faradic efficiency towards CO at somewhat low overpotentials, with FE over 70 % at electrolysis potentials as low as 0.65 Volts (vs RHE) for [CoTaTPPAg]<sub>x</sub> (**Figure 5.5**). Apart from the latter catalyst, most acetylides show a modest total FE under applied potentials below 0.55V. The rationale lies in that a significant portion of the electric charge is consumed in a pre-activation step, forming a reduced metallic species, both from the Ag and Fe or Co centres. The selectivity of the CO<sub>2</sub>RR remains reasonably high over a wide range of voltages, reaching electrolysis currents in the range of 5 mA/cm<sup>2</sup> for laboratory-scale electrolysis cells (**Figure S5-11**). Both [FeTaTPPAg]<sub>x</sub> and [CoTaTPPAg]<sub>x</sub> show an elevated propensity to suppress the competing hydrogen evolution reaction (HER),

however, HER tends to dominate at high potentials. Surprisingly, the unmetalated porphyrin showed somewhat good selectivity for CO, being only slightly lower than its metalated counterparts. This advocates for a predominant role of the silver on the catalytic properties of the acetylides, however, the slightly higher selectivity of the latter two catalysts toward CO is evidence of a co-activity between the silver and iron or cobalt centres.

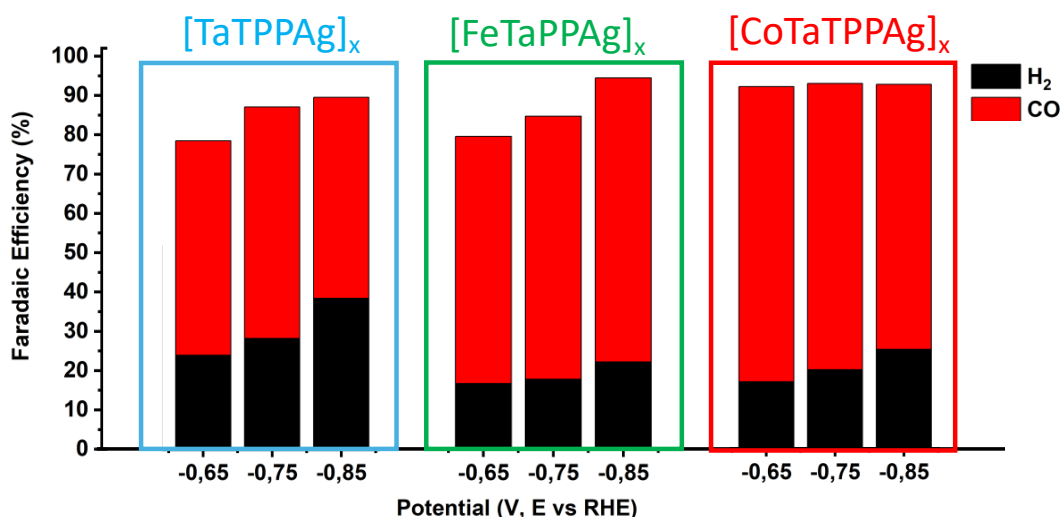


**Figure 5.5** Faradaic efficiency of all four porphyrin-silver acetylide clusters studied herein calculated from chronoamperometry experiments carried out at fixed potential in 3-electrode cell-type. The potentials are reported against RHE.

## Conclusion

To conclude, to the best of our knowledge, this study is the first example of a one-pot synthesis of catalysts composed of an inorganic core involving metal-metal bonds and a molecular macrocyclic catalyst. The methodology relies on a mild synthetic procedure compatible with organometallic complexes and yields products with high added value without requiring a purification step. Most importantly, the high catalytic properties obtained from silver acetylides synthesised from tetrasubstituted porphyrins indicate that a prior low-yielding porphyrin-de-symmetrisation step is not required. The disordered nature of the tetrasubstituted acetylides was not shown to be linked with any significant decrease in catalytic activity. Additionally, the highly insoluble nature of the materials synthesised from the alkyne-tetrasubstituted porphyrins constitutes a further positive point for the immobilisation of such catalysts. The methodology described herein demonstrates that such materials can be synthesised in large quantities from less synthetically demanding precursors. Although only intended as a proof of concept, some compounds show a subtle catalytic additivity feature, which augurs positively for future porphyrin-functionalised copper acetylide, currently being investigated in our laboratory.

## References

- (1) Smith, W. A.; Burdyny, T.; Vermaas, D. A.; Geerlings, H. Pathways to Industrial-Scale Fuel Out of Thin Air from CO<sub>2</sub> Electrolysis. *Joule* **2019**, *3* (8), 1822–1834. <https://doi.org/10.1016/j.joule.2019.07.009>.
- (2) Hepburn, C.; Adlen, E.; Beddington, J.; Carter, E. A.; Fuss, S.; Mac Dowell, N.; Minx, J. C.; Smith, P.; Williams, C. K. The Technological and Economic Prospects for CO<sub>2</sub> Utilization and Removal. *Nature* **2019**, *575* (7781), 87–97. <https://doi.org/10.1038/s41586-019-1681-6>.
- (3) Bushuyev, O. S.; De Luna, P.; Dinh, C. T.; Tao, L.; Saur, G.; van de Lagemaat, J.; Kelley, S. O.; Sargent, E. H. What Should We Make with CO<sub>2</sub> and How Can We Make It? *Joule* **2018**, *2* (5), 825–832. <https://doi.org/10.1016/j.joule.2017.09.003>.
- (4) Hori, Y.; Murata, A.; Takahashi, R.; Suzuki, S. Enhanced Formation of Ethylene and Alcohols at Ambient Temperature and Pressure in Electrochemical Reduction of Carbon Dioxide at a Copper Electrode. *J. Chem. Soc., Chem. Commun.* **1988**, No. 1, 17. <https://doi.org/10.1039/c39880000017>.
- (5) Hori, Y.; Murata, A.; Takahashi, R. Formation of Hydrocarbons in the Electrochemical Reduction of Carbon Dioxide at a Copper Electrode in Aqueous Solution. *J. Chem. Soc., Faraday Trans. 1* **1989**, *85* (8), 2309. <https://doi.org/10.1039/f19898502309>.
- (6) Hori, Y.; Murata, A.; Kikuchi, K.; Suzuki, S. Electrochemical Reduction of Carbon Dioxide to Carbon Monoxide at a Gold Electrode in Aqueous Potassium Hydrogen Carbonate.
- (7) Wang, M.; Nikolaou, V.; Loiudice, A.; Sharp, I. D.; Llobet, A.; Buonsanti, R. Tandem Electrocatalytic CO<sub>2</sub> Reduction with Fe-Porphyrins and Cu Nanocubes Enhances Ethylene Production. *Chem. Sci.* **2022**, *13* (43), 12673–12680. <https://doi.org/10.1039/D2SC04794B>.
- (8) Wang, M.; Loiudice, A.; Okatenko, V.; Sharp, I. D.; Buonsanti, R. The Spatial Distribution of Cobalt Phthalocyanine and Copper Nanocubes Controls the Selectivity towards C<sub>2</sub> Products in Tandem Electrocatalytic CO<sub>2</sub> Reduction. *Chem. Sci.* **2023**, *14* (5), 1097–1104. <https://doi.org/10.1039/D2SC06359J>.
- (9) Li, F.; Li, Y. C.; Wang, Z.; Li, J.; Nam, D.-H.; Lum, Y.; Luo, M.; Wang, X.; Ozden, A.; Hung, S.-F.; Chen, B.; Wang, Y.; Wicks, J.; Xu, Y.; Li, Y.; Gabardo, C. M.; Dinh, C.-T.; Wang, Y.; Zhuang, T.-T.; Sinton, D.; Sargent, E. H. Cooperative CO<sub>2</sub>-to-Ethanol Conversion via Enriched Intermediates at Molecule–Metal Catalyst Interfaces. *Nat Catal* **2019**, *3* (1), 75–82. <https://doi.org/10.1038/s41929-019-0383-7>.
- (10) Ma, G.; Qin, L.; Liu, Y.; Fan, H.; Qiao, L.; Yu, C.; Tang, Z. A Review of CO<sub>2</sub> Reduction Reaction Catalyzed by Atomical-Level Ag Nanomaterials: Atom-Precise Nanoclusters and Atomically Dispersed Catalysts. *Surfaces and Interfaces* **2023**, *36*, 102555. <https://doi.org/10.1016/j.surfin.2022.102555>.
- (11) Zhao, S.; Jin, R.; Jin, R. Opportunities and Challenges in CO<sub>2</sub> Reduction by Gold- and Silver-Based Electrocatalysts: From Bulk Metals to Nanoparticles and Atomically Precise Nanoclusters. *ACS Energy Lett.* **2018**, *3* (2), 452–462. <https://doi.org/10.1021/acseenergylett.7b01104>.

- (12) Chen, L.; Wang, L.; Shen, Q.; Liu, Y.; Tang, Z. All-Alkynyl-Protected Coinage Metal Nanoclusters: From Synthesis to Electrocatalytic CO<sub>2</sub> Reduction Applications. *Mater. Chem. Front.* **2023**. <https://doi.org/10.1039/D2QM01282K>.
- (13) Zhang, W.; Bai, Y.; Tian, M.; Liu, Y.; Hou, J.; Li, C.; Jiang, H.; Tang, J. Improvement of the Photoelectrochemical Stability of Cu<sub>2</sub>O Photocathode by Ph<sub>3</sub>C≡C≡Cu Grafting. *Adv Materials Inter* **2023**, *10* (3), 2201380. <https://doi.org/10.1002/admi.202201380>.
- (14) Lei, Z.; Wan, X.-K.; Yuan, S.-F.; Guan, Z.-J.; Wang, Q.-M. Alkynyl Approach toward the Protection of Metal Nanoclusters. *Acc. Chem. Res.* **2018**, *51* (10), 2465–2474. <https://doi.org/10.1021/acs.accounts.8b00359>.
- (15) Wang, J.; Xu, F.; Wang, Z.; Zang, S.; Mak, T. C. W. Ligand-Shell Engineering of a Au<sub>28</sub> Nanocluster Boosts Electrocatalytic CO<sub>2</sub> Reduction. *Angew Chem Int Ed* **2022**, *61* (32). <https://doi.org/10.1002/anie.202207492>.
- (16) Deng, G.; Kim, J.; Bootharaju, M. S.; Sun, F.; Lee, K.; Tang, Q.; Hwang, Y. J.; Hyeon, T. Body-Centered-Cubic-Kernelled Ag<sub>15</sub>Cu<sub>6</sub> Nanocluster with Alkynyl Protection: Synthesis, Total Structure, and CO<sub>2</sub> Electroreduction. *J. Am. Chem. Soc.* **2023**, *145* (6), 3401–3407. <https://doi.org/10.1021/jacs.2c10338>.
- (17) Liu, X.; Ma, J.; Niu, Z.; Yang, G.; Cheng, P. An Efficient Nanoscale Heterogeneous Catalyst for the Capture and Conversion of Carbon Dioxide at Ambient Pressure. *Angewandte Chemie* **2015**, *127* (3), 1002–1005. <https://doi.org/10.1002/ange.201409103>.
- (18) Qin, L.; Sun, F.; Ma, X.; Ma, G.; Tang, Y.; Wang, L.; Tang, Q.; Jin, R.; Tang, Z. Homoleptic Alkynyl-Protected Ag<sub>15</sub> Nanocluster with Atomic Precision: Structural Analysis and Electrocatalytic Performance toward CO<sub>2</sub> Reduction. *Angewandte Chemie International Edition* **2021**, *60* (50), 26136–26141. <https://doi.org/10.1002/anie.202110330>.
- (19) Drouet, S.; Merhi, A.; Yao, D.; Cifuentes, M. P.; Humphrey, M. G.; Wielgus, M.; Olesiak Banska, J.; Matczyszyn, K.; Samoc, M.; Paul, F.; Paul-Roth, C. O. Cubic Nonlinear Optical Properties of New Zinc Tetraphenyl Porphyrins Peripherally Functionalized with Electron-Rich Ru(II) Alkynyl Substituents. *Tetrahedron* **2012**, *68* (50), 10351–10359. <https://doi.org/10.1016/j.tet.2012.09.108>.
- (20) Costentin, C.; Drouet, S.; Robert, M.; Savéant, J.-M. A Local Proton Source Enhances CO<sub>2</sub> Electroreduction to CO by a Molecular Fe Catalyst. *Science* **2012**, *338* (6103), 90–94. <https://doi.org/10.1126/science.1224581>.
- (21) Sun, Z.-C.; She, Y.-B.; Zhou, Y.; Song, X.-F.; Li, K. Synthesis, Characterization and Spectral Properties of Substituted Tetraphenylporphyrin Iron Chloride Complexes. *Molecules* **2011**, *16* (4), 2960–2970. <https://doi.org/10.3390/molecules16042960>.
- (22) Davis, R. B.; Scheiber, D. H. The Preparation of Acetylenic Ketones Using Soluble Silver Acetylides. *J. Am. Chem. Soc.* **1956**, *78* (8), 1675–1678. <https://doi.org/10.1021/ja01589a050>.
- (23) Wang, M.; Torbensen, K.; Salvatore, D.; Ren, S.; Joulié, D.; Dumoulin, F.; Mendoza, D.; Lassalle-Kaiser, B.; Işci, U.; Berlinguette, C. P.; Robert, M. CO<sub>2</sub> Electrochemical Catalytic Reduction with a Highly Active Cobalt Phthalocyanine. *Nat Commun* **2019**, *10* (1), 3602. <https://doi.org/10.1038/s41467-019-11542-w>.

## Experimental section

### Materials

25% ammonia solution (for analysis EMSURE® ISO, Reag. Ph Eur), silver nitrate (ReagentPlus®, ≥99.0% for titration), FeBr<sub>2</sub> (98%), Cobalt(II) acetate tetrahydrate (ACS reagent, ≥98.0%), Benzaldehyde (ReagentPlus®, ≥99%), Pyrrole (for synthesis), Boron trifluoride diethyl etherate (for synthesis), DDQ (98%), TBAF solution (1.0 M in THF), DIPEA (ReagentPlus®, ≥99%), 2,6-lutidine (ReagentPlus®, ≥98%), absolute ethanol, Nafion® perfluorinated resin (5 wt% solution in a mixture of lower aliphatic alcohols containing 5% water), DMF (anhydrous, 99.8%) and potassium bicarbonate (ACS reagent, 99.7%, powder, crystals, or granules) were purchased from Sigma-Aldrich. 4-(Trimethylsilyl)ethynylbenzaldehyde (95%) was purchased from Manchester organics. Graphite powder (microcrystal grade, APS 2-15 micron, 99.9995%) was obtained from Alfa Aesar. Sigracet GDL (39BB) was purchased from Fuel Cell Store. CDCl<sub>3</sub> (99.8%) was purchased from Innovachem. Biobeads S-X3 support was purchased from Bio-Rad Laboratories. All electrolytes were prepared using Milli-Q water. All solvents were of HPLC grade or higher. Dry DCM was purified on a SPS.

### Materials characterization

#### NMR

The <sup>1</sup>H-NMR analyses were conducted using a Bruker Ultrashield spectrometer with a <sup>1</sup>H frequency of 400 MHz.

#### SEM-EDS

Scanning electron microscopy (SEM) was performed on an APREO 2 SEM (Thermo-Fisher Scientific) with an EDX XFlash 6-100 (Bruker) for qualitative and quantitative elemental measurements. Measurements were done using a 2.00 kV accelerating Voltage and 25pA for the beam current.

#### XPS

X-ray Photoelectron Spectroscopy (XPS) measurements were carried out with a THERMO Escalab 250Xi spectrometer, using focused monochromatic Al K $\alpha$  radiation ( $h\nu = 1486.6$  eV) with an Xray spot size of 650 $\mu$ m for longer axis ellipse. The high-energy resolution spectra were recorded with constant pass energy of 20 eV. The charge neutralization was used for all the acquisitions. The pressure in the analysis chamber was around  $2 \times 10^{-7}$  mbar during analyses. Short acquisition time spectra were recorded before each experiment to check that the samples were not subject to degradation during the X-ray irradiation. The binding energy scale was calibrated using the C 1s peak at 285.0 eV from the hydrocarbon contamination always present at the samples surface. For data analysis, the spectra were mathematically fitted using Casa XPS software, employing a least-squares algorithm and a non-linear baseline. The fitting of peaks in the experimental curves was achieved through a combination of Gaussian (70%) and Lorentzian (30%) distributions.

## Powder XRD

Powder X-ray Diffraction (PXRD) characterization was performed using a Bruker D2 Phaser powder diffractometer equipped with a Cu K $\alpha$  radiation source with a wavelength of 1.5406 Å. XRD patterns were recorded in the 2 $\theta$  range of 10° to 80° with a step size of 0.021° and a counting time of 0.05 seconds per step. The crystallite sizes were determined using DIFFRAC.EVA software.

## ATR-IR

ATR-IR characterization was performed on a Nicolet iS50 (Thermo Scientific) with 64 scans.

## 3-Electrodes Cell Electrochemical Characterization

Electrochemical tests were conducted using a custom-made three-electrode, leak-tight cell. The anode, consisting of a platinum wire, was enclosed in a bridge tube. The cell was filled with 40 mL of a 1 M KHCO<sub>3</sub> solution as the electrolyte. The reference electrode employed was an Ag/AgCl electrode immersed in a 3M KCl solution ( $E^0=0.210$  vs NHE). The working electrode was a Gas Diffusion Electrode (GDE) with a surface area of 2 cm<sup>2</sup>, integrated into a support structure, exposing 1 cm<sup>2</sup> of its surface directly to the electrolyte.



**Figure S5-1:** 3 electrodes Electrochemical Cell

The pH value of the CO<sub>2</sub>-saturated electrolyte was measured to be 6.8 before electrolysis. The potentials were measured against Ag/AgCl (3M). iR compensation losses between the working and reference electrodes were measured using electrochemical impedance spectroscopy (EIS). Electrode potential after iR correction converted to the RHE (Reversible Hydrogen Electrode) scale using

$E(RHE) = E(Ag/AgCl) + 0.059 * pH + E_0(Ag/AgCl)$ . pH value is measured to be 7.8 for the CO<sub>2</sub> saturated electrolyte and 8.4 when N<sub>2</sub> saturated. The overpotential ( $\eta$ ) was calculated according to Equation S5-2<sup>1</sup>.

Before chronoamperometry experiments, the electrolyte underwent a 15 min purge with either N<sub>2</sub> or CO<sub>2</sub> (at a flow rate of 35 mL/min). This purge was done using a Mass Flow Controller (MFC) (Bronkhorst EL-FLOW prestige FG-201CV) and constant stirring to eliminate air from both the solution and the cell headspace. Electrochemical tests were carried out using a potentiostat PGSTAT 204 (Metrohm).

$$E(RHE) = E(Ag/AgCl) + 0.059 * pH + E_0(Ag/AgCl)$$

**Equation S 5-1**

With  $E(Ag/AgCl)$  the measured corrected potential,  $E^0(Ag/AgCl)=0.210$  V the standard potential at 3M KCl, pH=7.8 in CO<sub>2</sub> saturated 1M KHCO<sub>3</sub> solution

$$\eta = E - E_{RHE}^0$$

**Equation S5-2**

With  $E_{RHE}^0 = -0.075$  V for the CO<sub>2</sub> to CO reduction at pH = 7.8

Faradaic efficiency was obtained by direct quantification of the gas products:

$$\text{Faradaic efficiency (\%)} = \frac{Q_{exp}}{Q_{theo}} \times 100 = \frac{z \times n \times F}{Q} \times 100$$

**Equation S5-3**

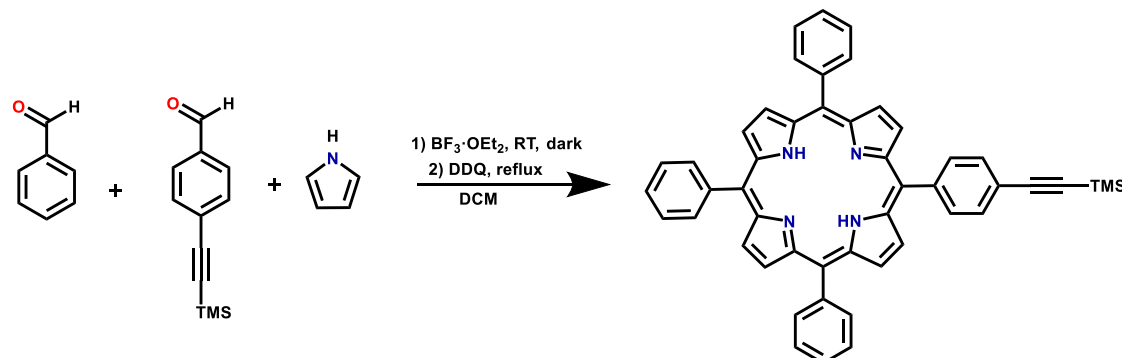
Where z is the number of electrons involved in the reaction, n the number of moles of generated product, F the faraday constant and Q the charge passed during the catalytic experiment.

### Electrodes preparation

The Electrodes were prepared following a modified procedure from M. Robert et al <sup>16</sup>. Vulcan XC-72 Carbon Black (3 mg) was sonicated in Absolute ethanol (2mL) for 30min. To the slurry was added Nafion® perfluorinated resin (10 µL of a 5 wt% solution in a mixture of lower aliphatic alcohols containing 5% water) and the mixture was sonicated for 30min. To this mixture was added a suspension of the acetylide (0.8 mg) in absolute ethanol (1mL) and the mixture was sonicated for 30min. The suspension was then deposited by dropcasting on a gas diffusion layer (Sigracet 39BB; 2 cm<sup>2</sup>) at 80°C. The electrodes were then dried under reduced pressure at 40°C overnight.

## Synthesis protocol

### C1 5,10,15-triphenyl-20- ((4-(trimethylsilyl)ethynyl)phenyl) -21H,23H-porphyrin



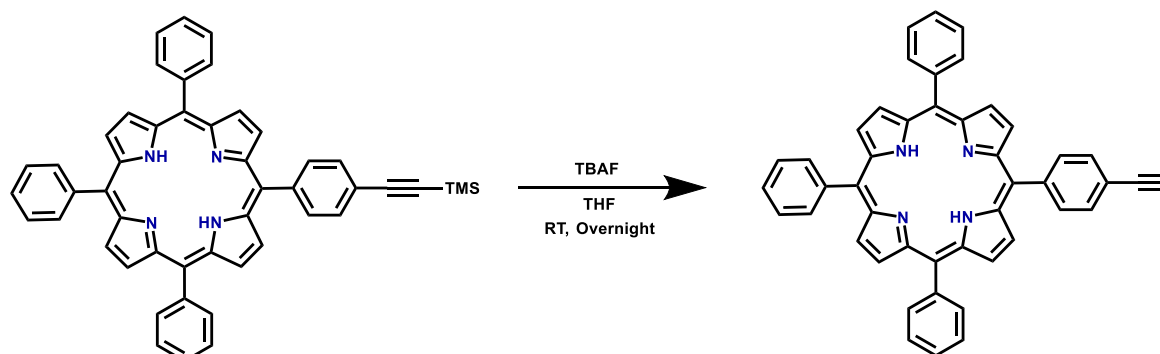
A solution of 4-((trimethylsilyl)ethynyl)benzaldehyde (1.032 g ; 5.10 mmol), benzaldehyde (1.624 g ; 15.30 mmol) and pyrrole (1.41 mL ; 20 mmol) in dry dichloromethane (1,5L) was degassed for 30 min in a vacuum dried round flask (3 cycles). The flask was covered with aluminum foil as the reaction is light sensitive at this stage and BF<sub>3</sub>·OEt<sub>2</sub> (1.03 mL; 8.3 mmol) was added by piercing a septum with a syringe. The reaction was stirred at room temperature for 3 hours (280 rpm). Then p-chloranil was added (3.78 g; 15.4 mmol) and the reaction was refluxed for 1 hour. The solution was then cooled to room temperature and two pipettes of triethylamine were added to neutralize the excess acid. The solvent was evaporated under reduced pressure and the residue was separated on a column chromatography (silica gel; hexane/DCM 50:50) to obtain a purple powder containing a mixture of the 5 derivatives. The solid was further purified on a Preparative size exclusion chromatography column in THF (**Figure S5-2**), Dried under reduced pressure and precipitated in hexane to remove the excess BHT to obtain **C2** (242mg; 340μmol; 6.67% yield) as the main product and the 4 other resulting derivatives as dark purple powders.



**Figure S5-2** SEC column at different stages of the separation. Each spot corresponds to a porphyrin derivative.

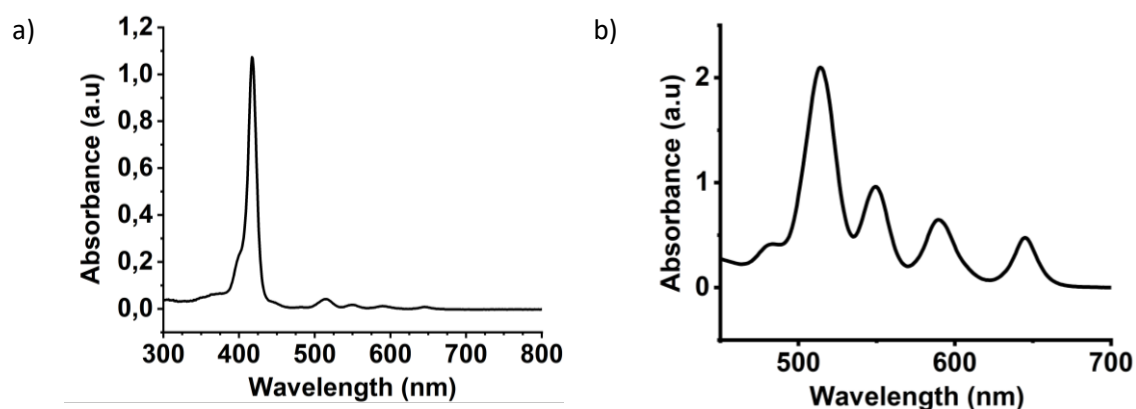
<sup>1</sup>H NMR (400 MHz) CDCl<sub>3</sub>: 8.85 (s, 4H) ; 8.84 (dd,4H,J=4.8) ; 8.20-8.24 (m, 6H) ; 8.17 and 7.88 (d,2x2H,J=8.2) ; 7.72-7.82 (m, 9H) ; 0.39 (s,9H) ; -2.77 (s, 2H)



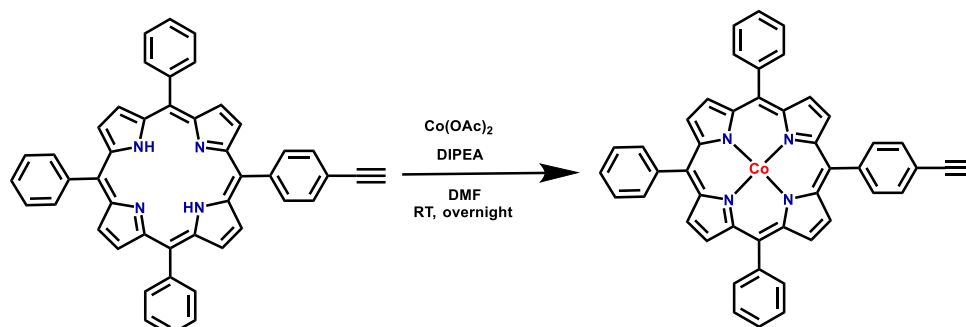
**C2 5,10,15-triphenyl-20-(4-ethynylphenyl)-21H,23H-porphyrin**

**C1** (150 mg; 210  $\mu\text{mol}$ ) was solubilized in THF (50 mL) and the solution was cooled to 0°C. TBAF (1.0M in THF) (0.25 ml; 250  $\mu\text{mol}$ ) was added dropwise and the solution was stirred at RT overnight. The reaction mixture was passed through a silica gel plug with DCM as eluent and the solution was dried under reduced pressure. The product was further purified by preparative SEC (THF) and dried under reduced pressure. The solid was then recrystallized in hexane, filtered and washed with cold hexane to obtain LC048 as a purple powder (125 mg; 195  $\mu\text{mol}$ ; 93%)

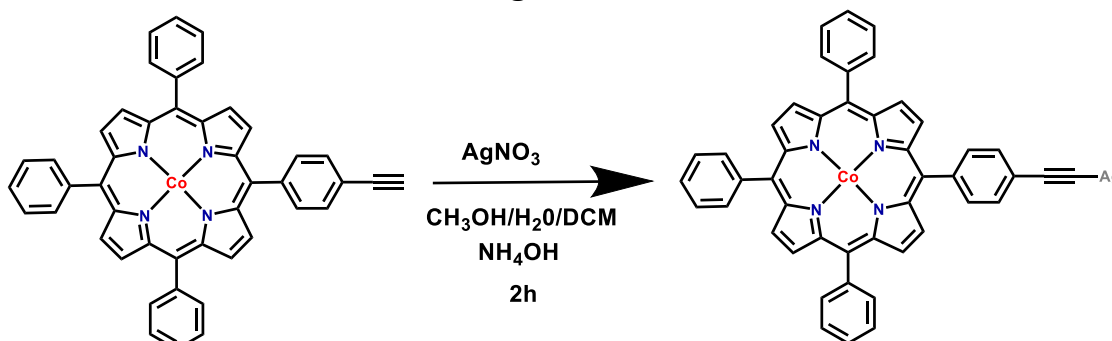
<sup>1</sup>H NMR (400 MHz) CDCl<sub>3</sub>: 8.87 (s, 4H) ; 8.86 (dd,4H, J=4.8) ; 8.22-8.26 (m, 6H) ; 8.21 (d,2H,J=8.2) and 7.91 (d,2H,J=8.2) ; 7.72-7.82 (m, 9H) ; 3.33 (s,1H) ; -2.69 (s, 2H)



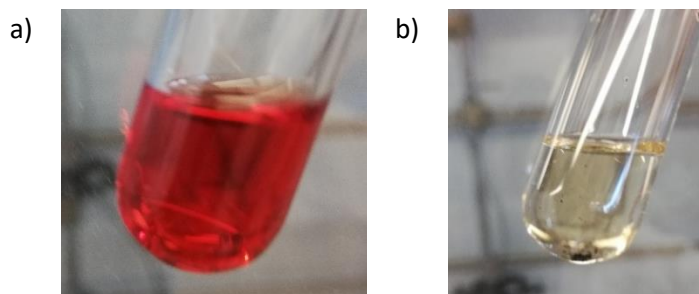
**Figure S5-3 a)** UV spectrum of a 10<sup>-6</sup> M solution of C2 in DCM **b)** UV spectrum of a 10<sup>-4</sup> M solution of C2 in DCM. Soret: 417 q bands: 514,549,590,645

**C3 Cobalt (II) 5,10,15-triphenyl-20-(4-ethynylphenyl)-21H,23H-porphyrin**

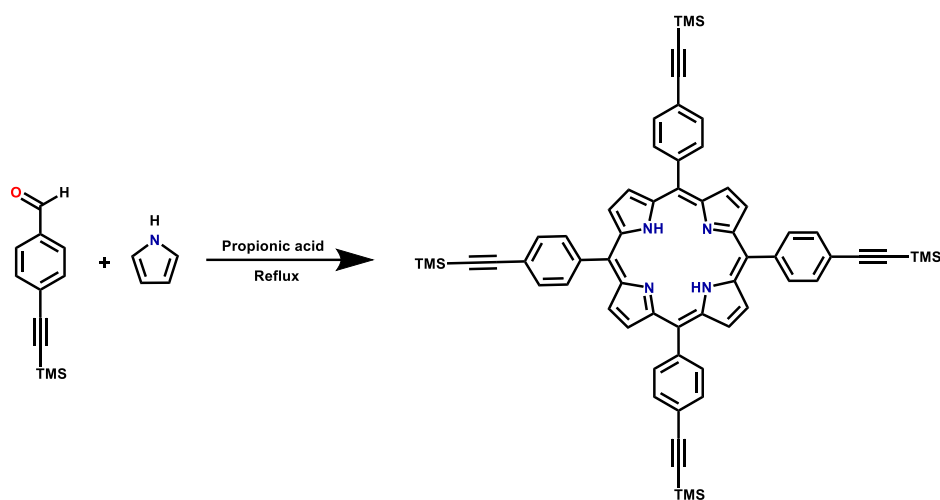
Co(OAc)<sub>2</sub>·4H<sub>2</sub>O (78,6 mg, 316 μmol; 5eq) was added to a solution of **C2** (40mg ; 78 μmol; 1eq) in DMF (10 mL). DIPEA was added (20 μL; 114 μmol; 1,5eq) and the mixture was stirred at RT overnight. Water was then added and the precipitate was washed with water solubilised in DCM and purified by column chromatography using a DCM as eluent. The solvents were evaporated the obtained **C8** dark purple powder was dried under vacuum (41,8mg; 60 μmol; 96%).

**C4 Ag-CoMaTPP**

AgNO<sub>3</sub> (25,1 mg; 148 μmol; 5eq) was solubilized in a mixture of MeOH (12mL) and water (4mL). To this solution was added NH<sub>4</sub>OH until the brown color completely disappeared. A solution of CoMaTPP (20 mg; 28.8 μmol; 1eq) and in DMF: DCM 1:1 (10mL) was added slowly to the mixture. After being stirred at RT overnight a dark precipitate had formed. The solution was filtered and the resulting purple dark solid was washed with water, MeOH and DCM (which removed a large amount of unreacted product) and dried under reduced atmosphere to obtain 10,4 mg of **C4**.

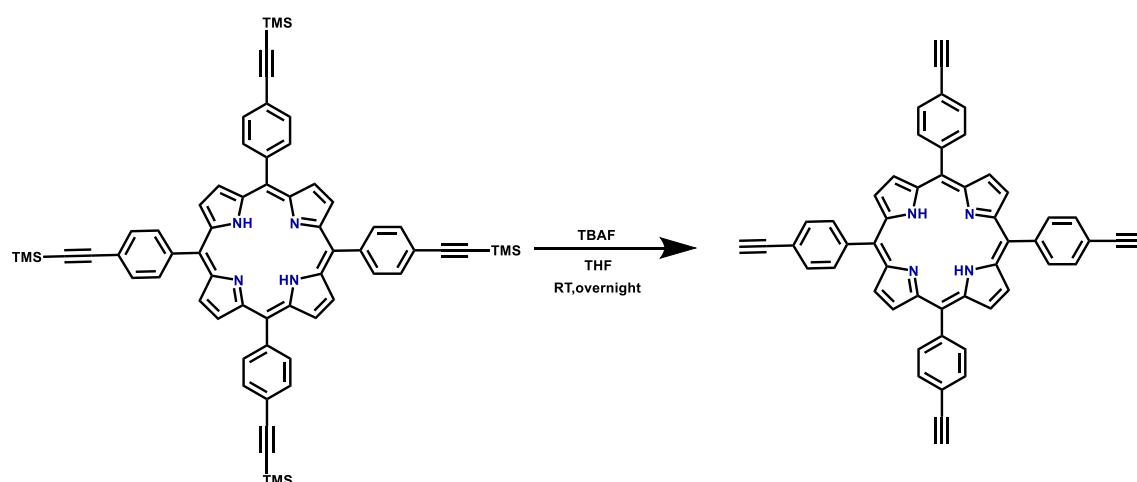


**Figure S5-4 a)** C3 solubilised in DCM **b)** C4 solubilised in DCM. A loss of solubility is observed upon silver addition indicative of the complex formation.

**C5 5,10,15,20-tetrakis((4-(trimethylsilyl)ethynyl)phenyl)-21H,23H-porphyrin**

In a 250 mL round flask, 4-((trimethylsilyl)ethynyl)benzaldehyde (4.0443g, 20mmol) in propionic acid (150 mL) was heated at 100°C for 1H. Freshly distilled pyrrole (1.38 mL, 20 mmol) was added dropwise and the solution was refluxed for 3H in the dark. The solvent was evaporated and the residue was purified by crystallization in MeOH. The obtained solid was separated on a column chromatography (silica gel; hexane/DCM 50:50). A second column chromatography (silica gel; hexane/DCM 60:40) was used to obtain the purified product as a purple powder (555 mg; 11% yield; 555 μmol).

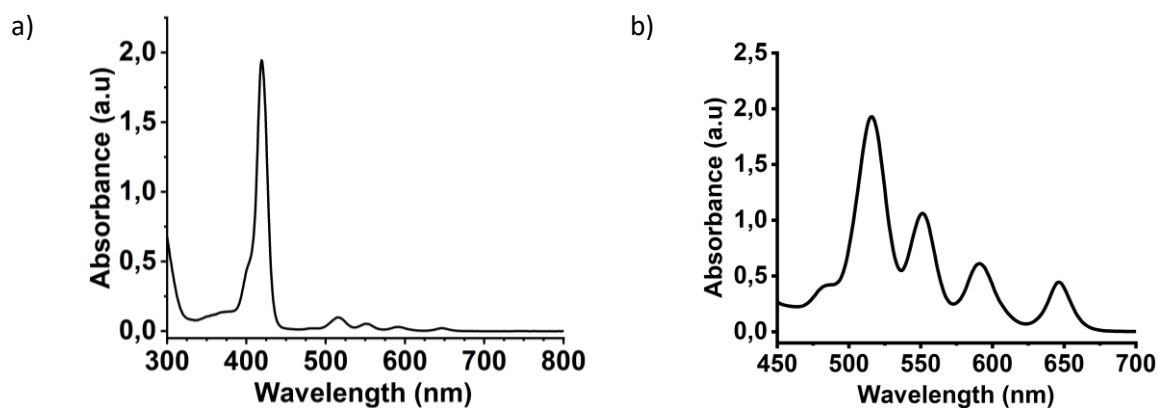
<sup>1</sup>H NMR (400 MHz) CDCl<sub>3</sub>: 8.81 (s, 8H) ; 8.14 and 7.87 (dd, 16H, J=8.2) ; 0.38 (s, 36H) ; -2.84 (s, 2H)

**C6 5,10,15,20-tetrakis((4-ethynyl)phenyl)-21H,23H-porphyrin**

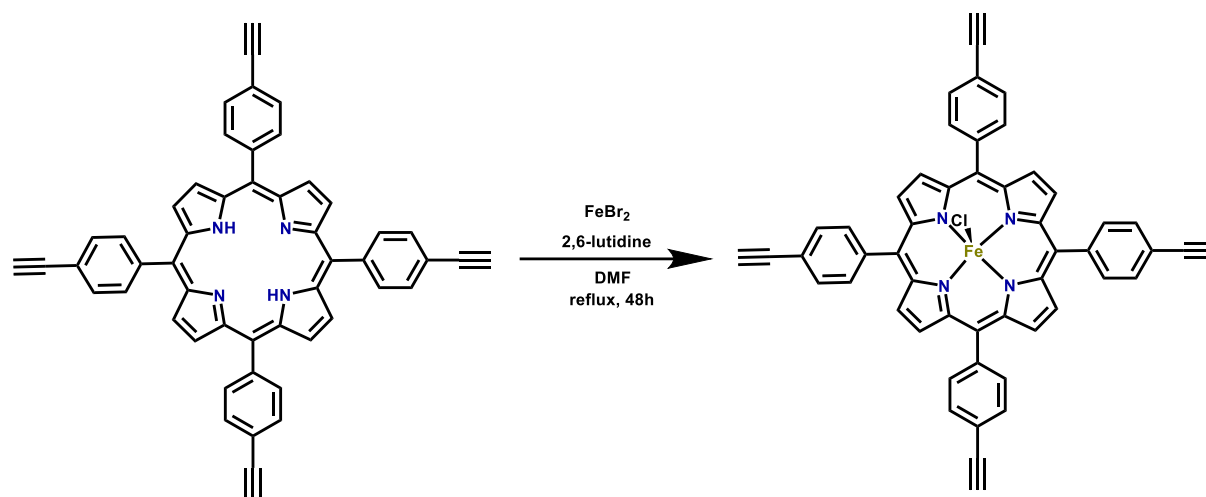
To a solution of LC020 (152.4mg; 152.5 $\mu$ mol) in THF (60 mL) at 0°C was added TBAF (0.8mL; 0.8mmol; 6eq). The mixture was stirred at RT overnight. The solvent was evaporated and the crude material was purified by silica gel chromatography. The solvent was evaporated and the product **C6** was recovered as a purple solid (105.4mg ;148  $\mu$ mol; 97% yield).

Solubility: DCM, Chloroform, THF, DMF

<sup>1</sup>H NMR (400 MHz) CDCl<sub>3</sub>: 8.83 (s, 8H) ; 8.17 and 7.88 (dd,16H, J=8.0) ; 3.32 (s, 4H) ; -2.83 (s, 2H)

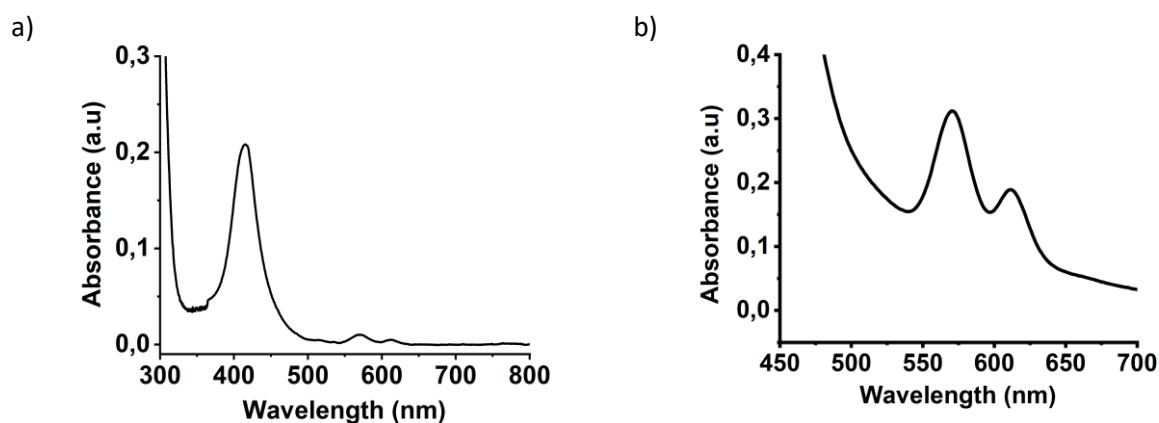


**Figure S5-5 a)** UV spectrum of a 10<sup>-6</sup> M solution of C6 in DCM **b)** UV spectrum of a 10<sup>-4</sup> M solution of C6 in DCM. Soret: 419 q bands: 516, 551, 591, 646

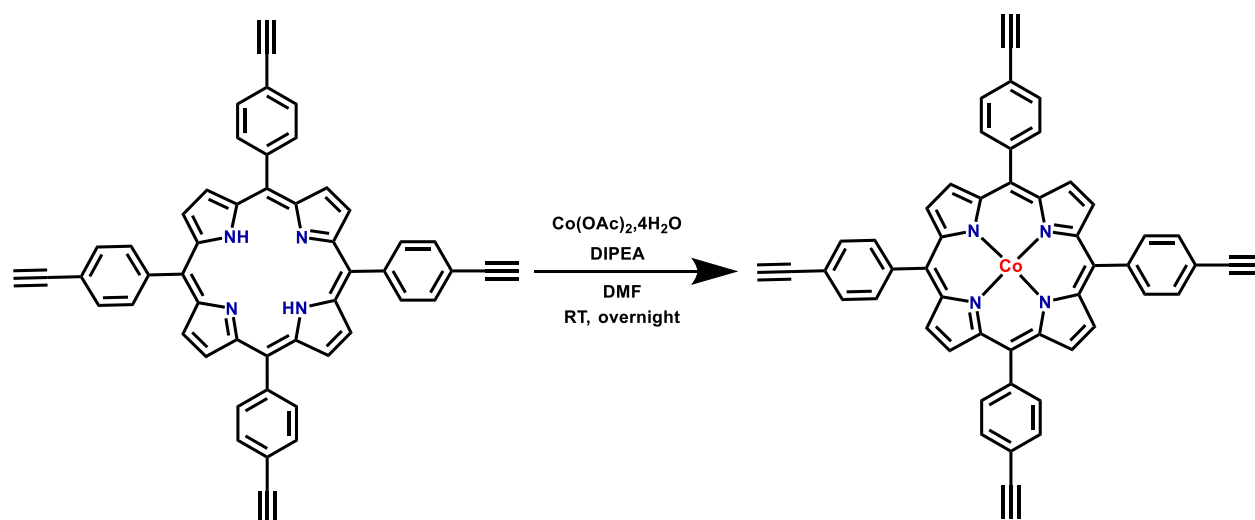
**C7 Iron (III) 5,10,15,20-tetrakis((4-ethynyl)phenyl)-21H,23H-porphyrin chloride**

A solution of **C6** (100 mg ; 141 μmol ; 1eq), FeBr<sub>2</sub> (303 mg ; 1.41 mmol ; 10eq) and 2,6-lutidine (33 μL; 281 μmol ; 2eq) in DMF (20 mL) was refluxed for 24 h under N<sub>2</sub>. The material was precipitated by adding an acidic (HCl 1M) solution (50 mL) and washed with distilled water until neutral pH. The obtained solid was purified by column chromatography (silica gel, DCM:MeOH 0 to 20%) and preparative SEC to obtain **C7** (93.2 mg; 116 μmol; 83% yield)

Solubility: DCM, Chloroform, THF, DMF



**Figure S5-6 a)** UV spectrum of a 10<sup>-6</sup> M solution of C7 in DCM **b)** UV spectrum of a 10<sup>-4</sup> M solution of C7 in DCM. Soret: 416; q bands: 571, 612

**C8 Cobalt (II) 5,10,15,20-tetrakis((4-ethynyl)phenyl)-21H,23H-porphyrin**

$\text{Co}(\text{OAc})_2 \cdot 4\text{H}_2\text{O}$  (74,5mg, 500 $\mu\text{mol}$ ; 4eq) was added to a solution of C6 (50mg ; 70,4  $\mu\text{g}$ ; 1eq) in DMF (10 mL). DIPEA was added (20 $\mu\text{L}$ ; 114 $\mu\text{mol}$ ; 1,5eq) and the mixture was stirred at RT overnight. Water was then added and the precipitate was washed with water solubilised in DCM: hexane (1:1) and purified by column chromatography using a DCM: hexane (1:1) mixture. The solvents were evaporated the obtained C8 dark purple powder was dried under vacuum (52mg; 68  $\mu\text{mol}$ ; 96%).

Solubility: DCM, Chloroform, THF, DMF

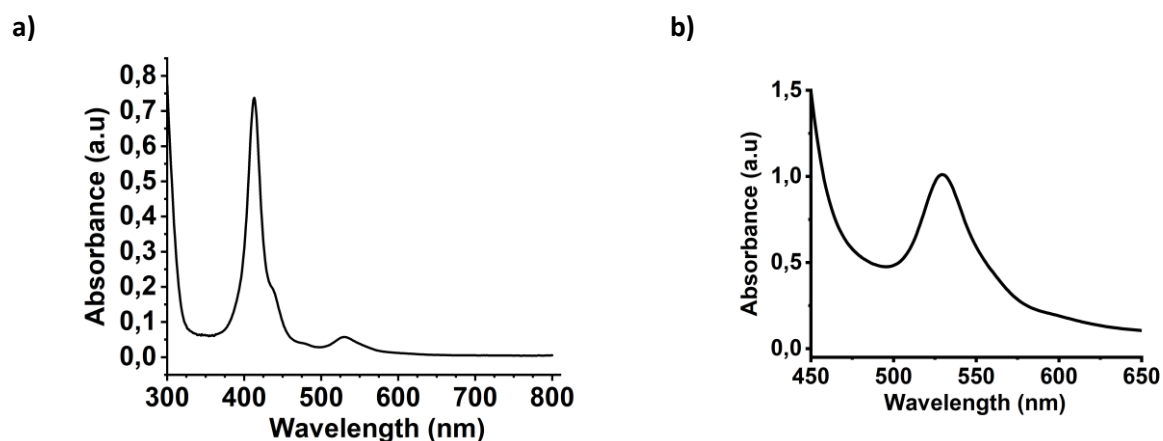
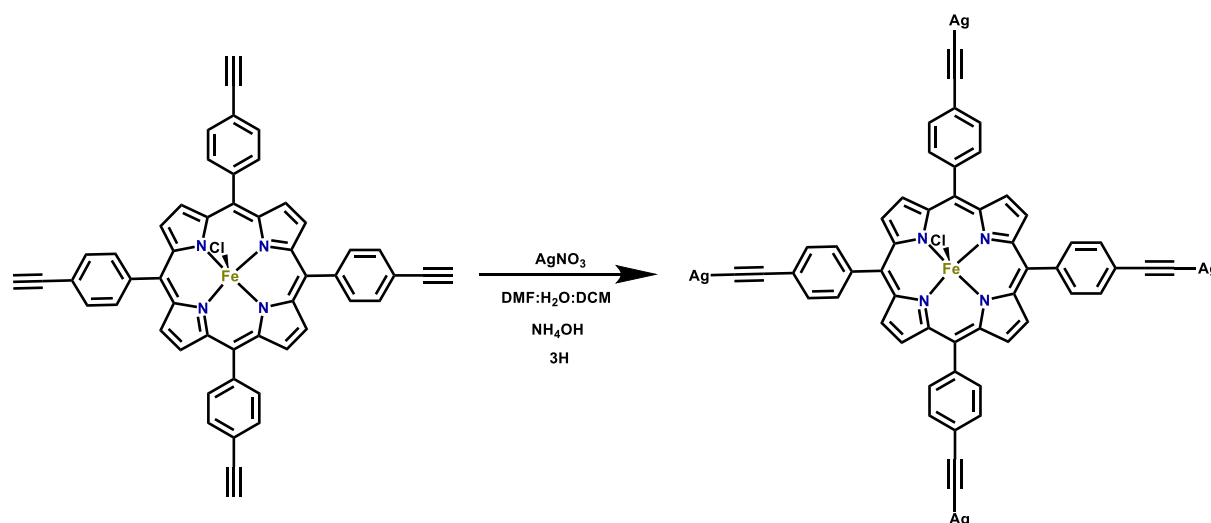


**Figure S5-7** a) UV spectrum of a  $10^{-6}$  M solution of C8 in DCM b) UV spectrum of a  $10^{-4}$  M solution of C8 in DCM. Soret: 413 q bands: 531

## C9 Ag-FeTaTPP



AgNO<sub>3</sub> (203.3 mg; 1.20 mmol; 10 eq) was solubilized in a mixture of MeOH (10 mL) and water (5 mL). To this solution was added NH<sub>4</sub>OH until the brown color completely disappeared. FeTaTPP (100mg; 120 μmol; 1eq) was dissolved in a mixture of DMF (10mL) and DCM (15mL) and added slowly to the mixture. A precipitate started to form after 10 min and the reaction mixture was stirred at RT for 3H. The solution was filtered and the obtained solid was washed with DMF, water, THF, MeOH and DCM. The resulting dark green solid was obtained quantitatively and dried under high vacuum with phosphorus pentoxide overnight.

a)



b)

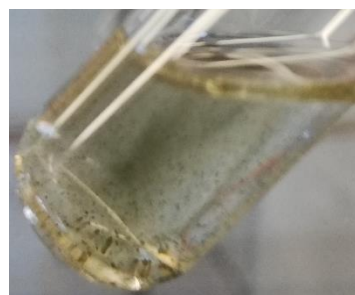
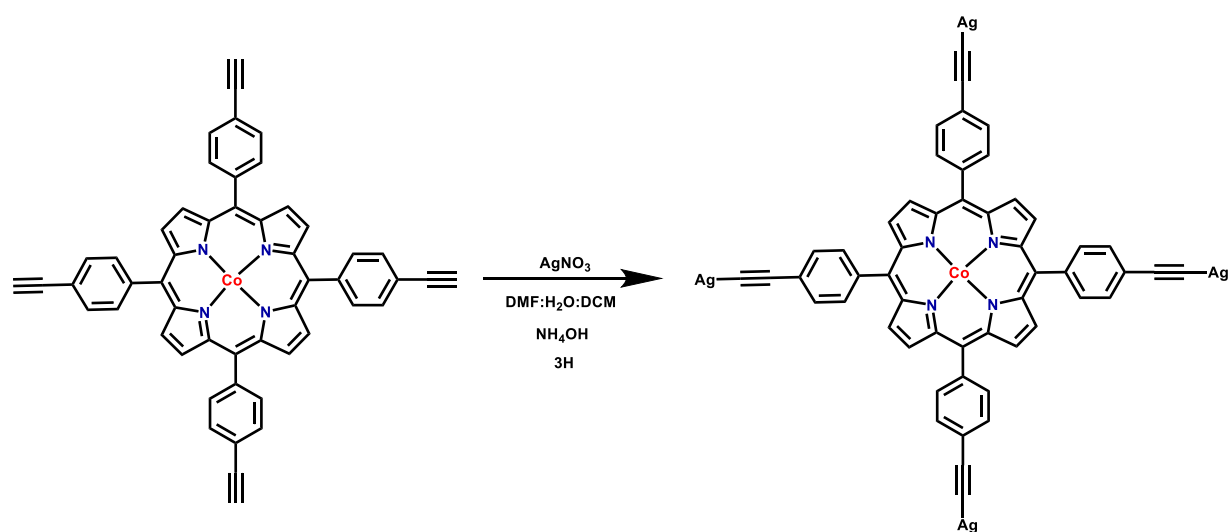


**Figure S5-8 a)** C7 solubilised in DCM **b)** C9 solubilised in DCM. A loss of solubility is observed upon silver addition indicative of the complex formation.

## C10 Ag-CoTaTPP



AgNO<sub>3</sub> (110.6 mg; 651 μmol; 10 eq) was solubilized in a mixture of MeOH (10 mL) and water (5 mL). To this solution was added NH<sub>4</sub>OH until the brown color completely disappeared. CoTaTPP (50mg; 65μmol; 1 eq) was dissolved in a mixture of DMF (10mL) and DCM (15mL) and added slowly to the mixture. A precipitate started to form after 10 min and the reaction mixture was stirred at RT for 3H. The solution was filtered and the obtained solid was washed with DMF, water, THF, MeOH and DCM. The resulting dark insoluble solid was obtained quantitatively and dried under vacuum with phosphorus pentoxide overnight.

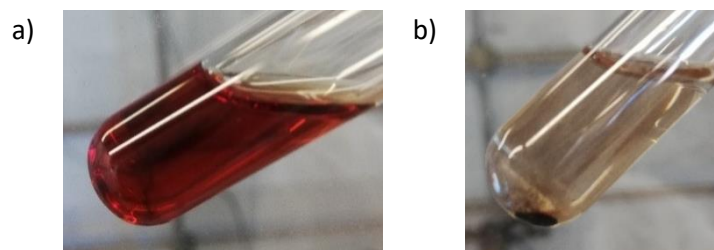
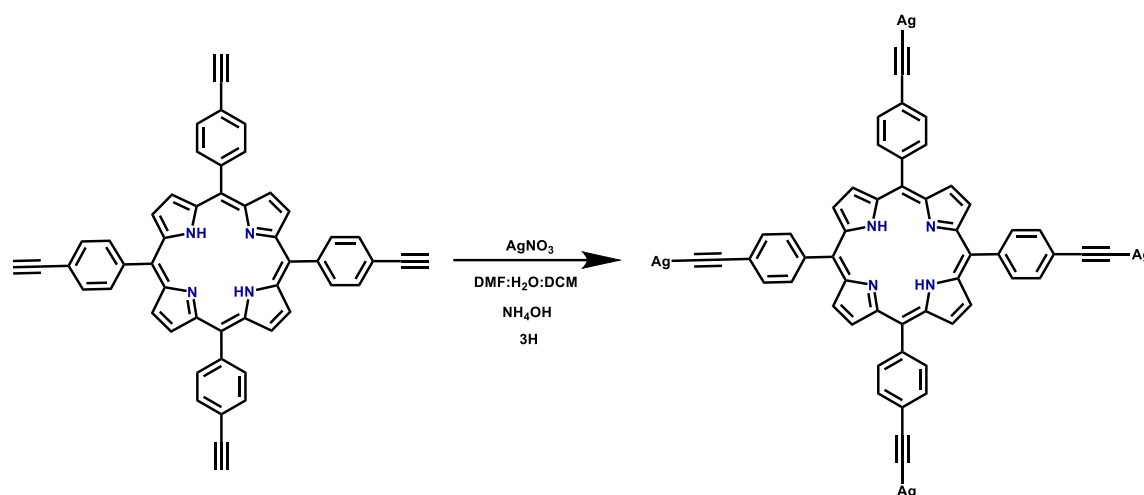


**Figure S5-9 a)** C8 solubilised in DCM **b)** C10 in DCM. A loss of solubility is observed upon silver addition indicative of the complex formation.



## C11 Ag-TaTPP



AgNO<sub>3</sub> (120.1 mg; 700 μmol) was solubilized in a mixture of MeOH (10 mL) and water (5 mL). To this solution was added NH<sub>4</sub>OH until the brown color completely disappeared. TATPP (50mg; 70 μmol; 1 eq) was dissolved in a mixture of DMF (10mL) and DCM (15mL) and added slowly to the mixture. A precipitate started to form after 10 min and the reaction mixture was stirred at RT for 3H. The solution was filtered and the obtained solid was washed with DMF, water, THF, MeOH and DCM. The resulting dark insoluble solid was obtained quantitatively and dried under high vacuum with phosphorus pentoxide overnight.

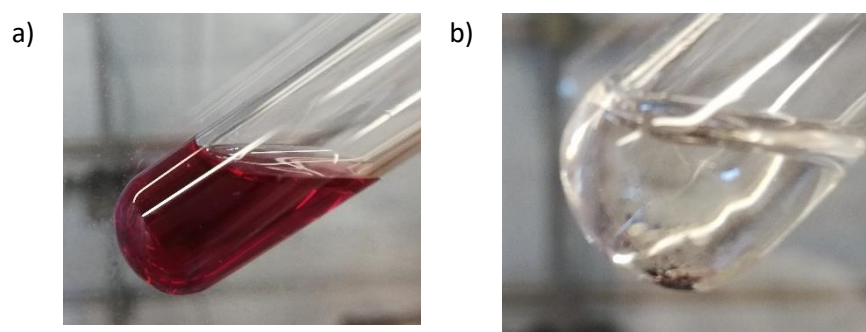


**Figure S5-10** a) C6 solubilised in DCM b) C10 in DCM. A loss of solubility is observed upon silver addition indicative of the complex formation.

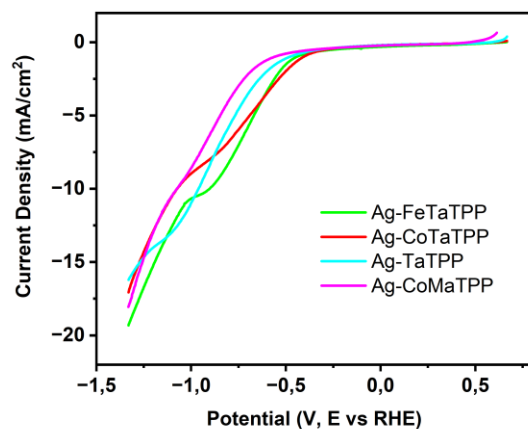


**Figure S5-11:** LSV comparison at 10 mV/s of the deposited materials in a 0.5 M KHCO<sub>3</sub> solution. Potential is uncorrected.

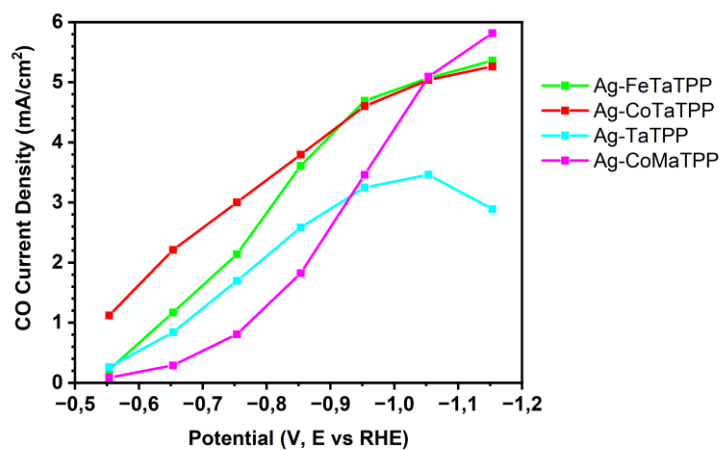
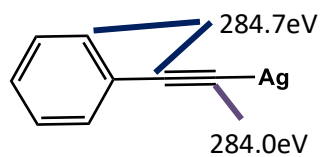


**Figure S5-12:** Current density comparison at varying potential of the deposited materials in a 0.5 M KHCO<sub>3</sub> solution. Potential is uncorrected. **Ag-TaTPP activity for CO reaches a plateau (corresponding to H<sub>2</sub> evolution increase) while the presence of metalated porphyrins are delaying this effect.**

AgPh



(TaTPPAg)<sub>n</sub>

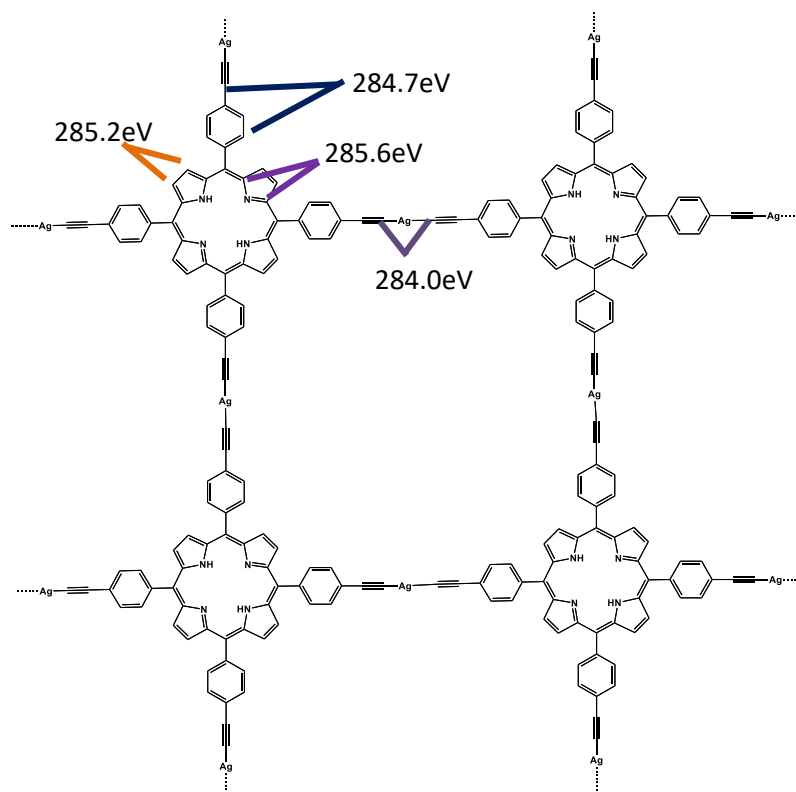


**Figure S5-13:** XPS identification and attribution of the carbon chemical environments in the chemical structure.

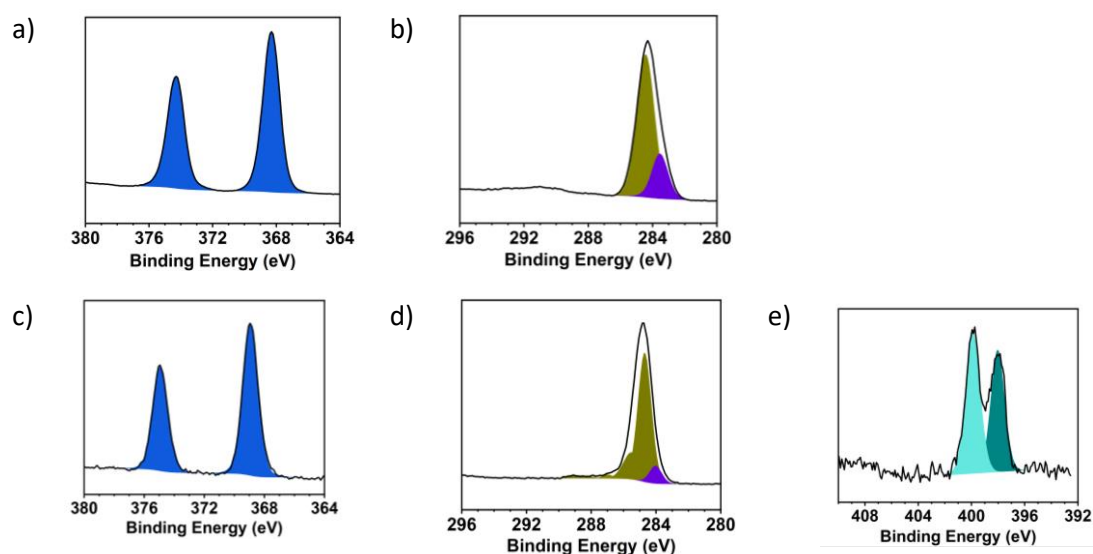


**Figure S5-14:** XPS measurements for a reference compound AgPh (a-b) and Ag-TaTPP (c-e). **a)** Ag3d spectrum of the reference compound **b) c)** Ag3d spectrum shows an Ag(I) species (Ag3d 1/2 (375 eV) Ag3d 3/2 (369 eV). **d)** C1s deconvolution shows a maintained porphyrin structure (Pyrrole band (285.2 and 285.6 eV) and Phenyl band (284.7 eV) with a component at 284 eV attributed to the Ag-C≡C bond. **e)** N1s shows 2 bands corresponding to the N-H (399.9eV) and N (398 eV) of the free base porphyrin.

	C	O	N	Fe	Cl	Ag	Ag/acetylene
AgPh	84	1.5				15	
(TaTPPAg) <sub>n</sub>	67	15	2,2			2,7	1.23
(FeTaTPPAg) <sub>n</sub>	80	7,1	4,8	1,3	0,8	5,2	1.08

**Table S5-1** Elemental values obtained from the XPS measurement. The value Ag/acetylene corresponds to the division of total silver integration by the N content (assumed to be only present on the porphyrin core)

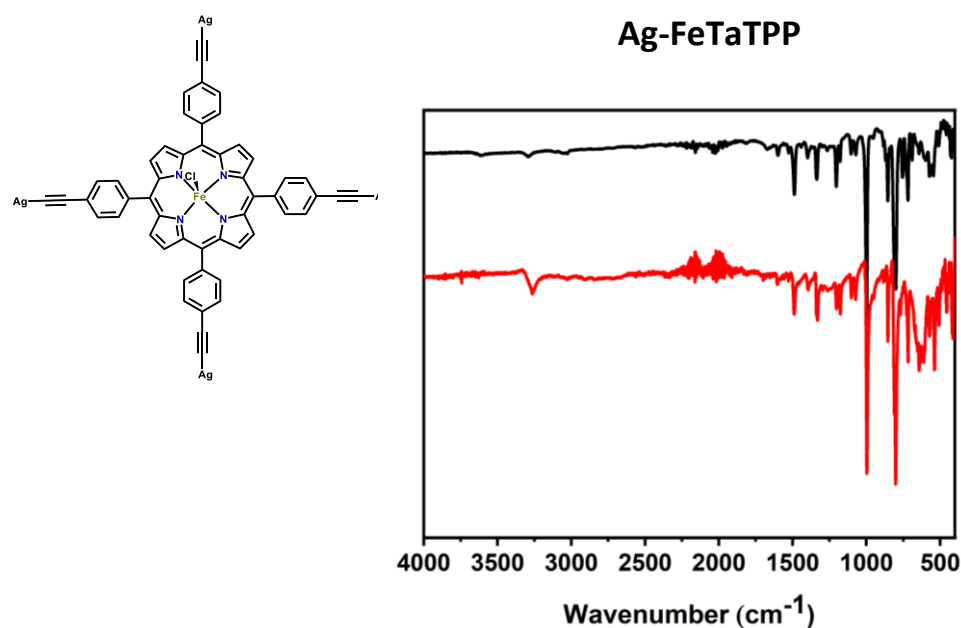


**Figure S5-15** IR spectrum of compound C9 (Black) and its starting material C7 (red). The intensity of the C≡C-H band (3265 cm<sup>-1</sup>) is decreased significantly from C7 to C9 upon addition of silver indicative of the C≡C-Ag bond formation.

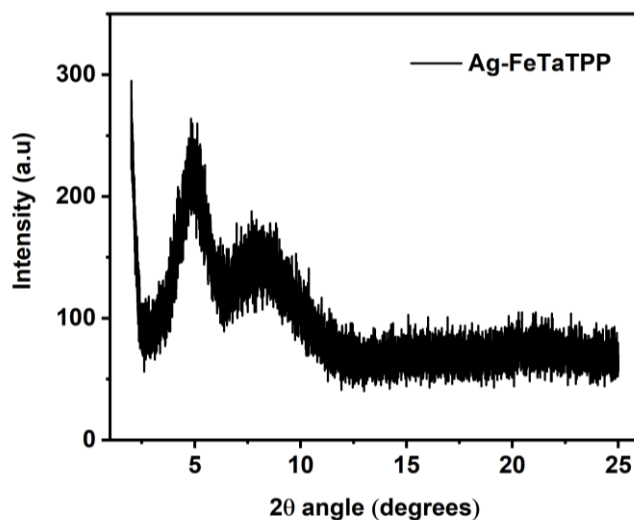
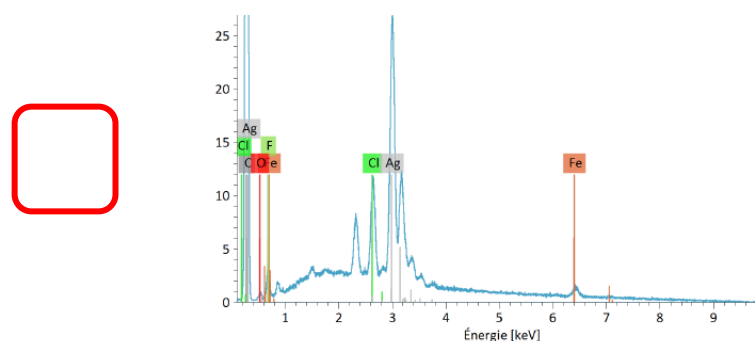
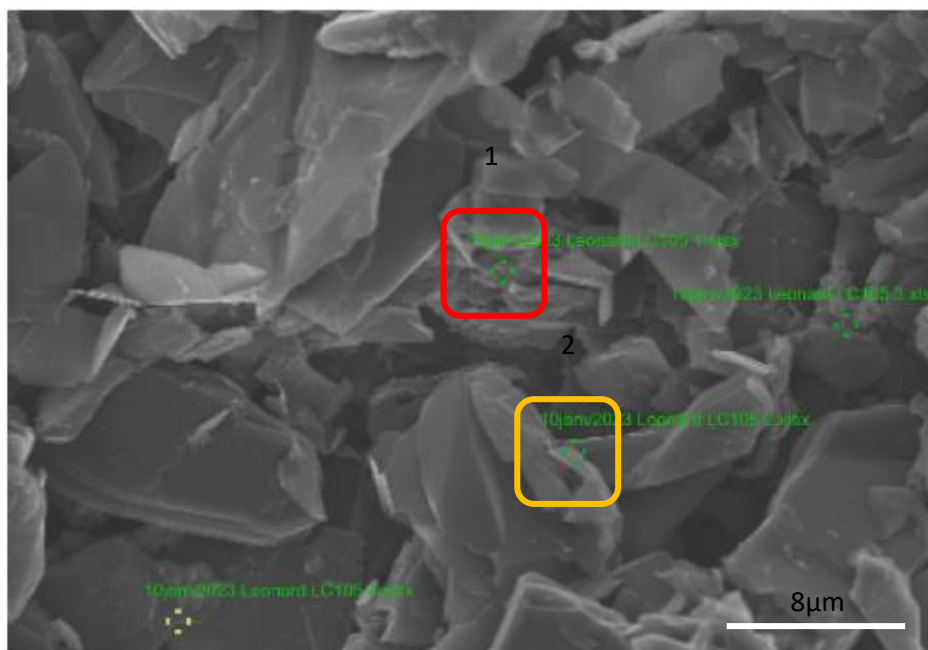
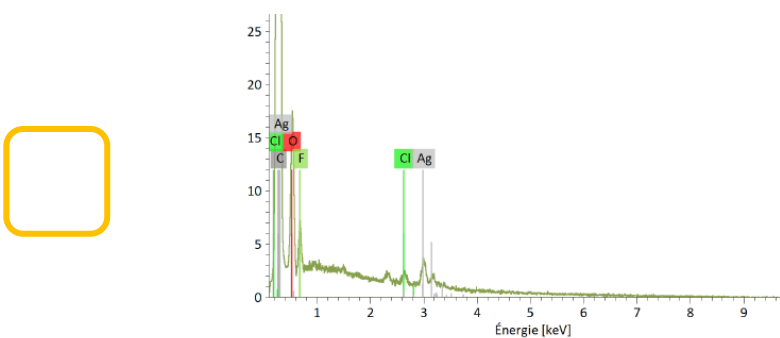


**Figure S5-16:** Powder XRD pattern of Ag-FeTaTPP between 2 and 25°. The starting material is not crystalline. The observed peaks are of low intensity hinting for a poorly crystalline final structure with a COF-like arrangement. Crystallinity is measured to be 66% (obtained by comparing the integrated intensity of the background with the peaks). Crystal size is calculated to be 83 Å by Scherrer equation.



Élément	A	Raies	Net	Mass. [%]	Mass. norm. [%]	Atom. [%]
carbone	6	K	291991	26.73	41.75	81.68
oxygène	8	K	718	0.14	0.21	0.31
fluor	9	K	7400	0.93	1.45	1.80
chlore	17	K	33052	2.89	4.51	2.99
fer	26	K	5656	5.92	9.24	3.89
argent	47	L	173619	27.42	42.83	9.33
			<b>Total</b>	<b>64.02</b>	<b>100.00</b>	<b>100.00</b>



Élément	A	Raies	Net	Mass. [%]	Mass. norm. [%]	Atom. [%]
carbone	6	K	875158	---	90.41	94.24
oxygène	8	K	20687	---	5.84	4.57
fluor	9	K	7604	---	1.29	0.85
chlore	17	K	1821	---	0.26	0.09
argent	47	L	8515	---	2.21	0.26
			<b>Total</b>		<b>100.00</b>	<b>100.00</b>

**Figure S5-17:** SEM Picture of a prepared Ag-FeTaTPP Electrode. 1 and 2 show quantitative elemental measurements by EDS of Ag-FeTaTPP containing spot and without catalyst respectively. **Material concentration seems to be highly localized (consequently poorly dispersed) and corresponds to the charging parts of the electrode.**

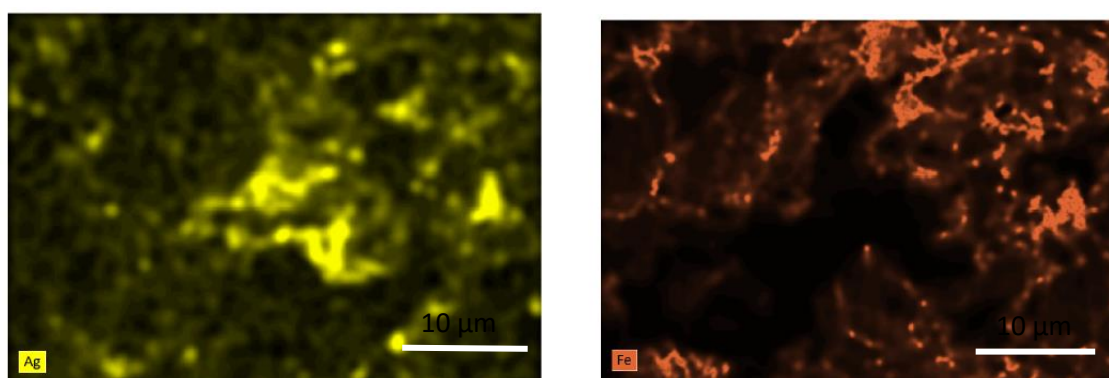


**Figure S5-18:** SEM-EDS Pictures of Iron and Silver of a prepared Ag-FeTaTPP Electrode at 5000x magnification. Fe and Ag signals intensity correspond to charging amorphous particles which we assume to be the chemical of interest confirming the poor catalyst distribution on the electrode.

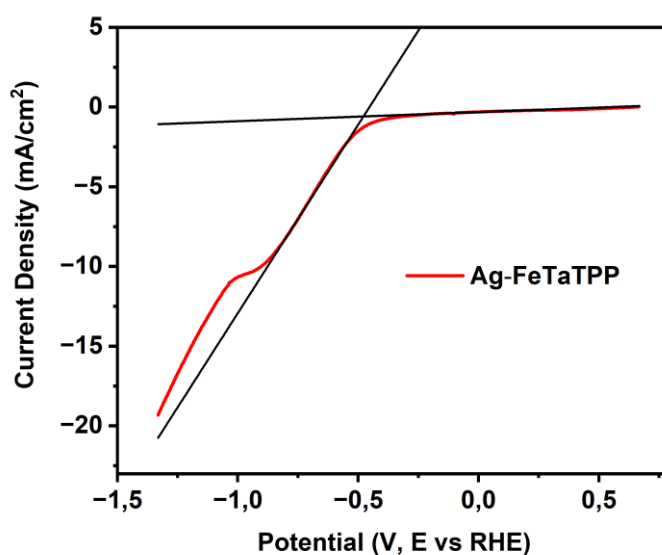


**Figure S5-19:** LSV measurement at 10 mV/s (2<sup>nd</sup> scan) of the deposited Ag-FeTaTPP in a 0.5 M KHCO<sub>3</sub> solution. Potential is uncorrected. The overpotential is measured as -0.478 V vs RHE as the cross point of the coulombic and faradic currents.

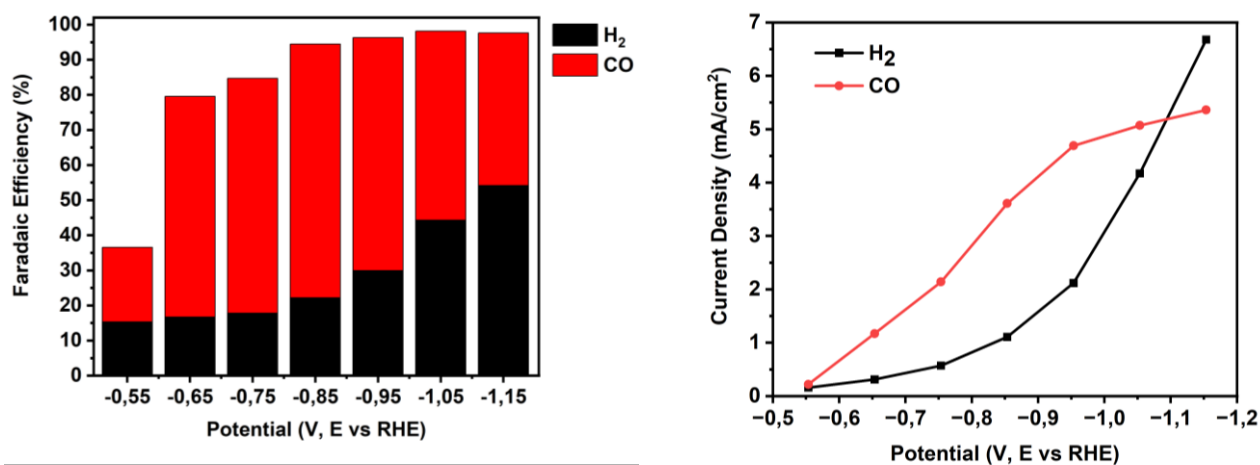


**Figure S5-20: a)** Ag-FeTaTPP measured faradaic efficiency (FE) from direct GC quantification at potential varied between -0.55 and -1.15 V vs RHE in a 0.5 M KHCO<sub>3</sub> solution. Potential is uncorrected **b)** Measured current densities for CO and H<sub>2</sub> with varying potential.

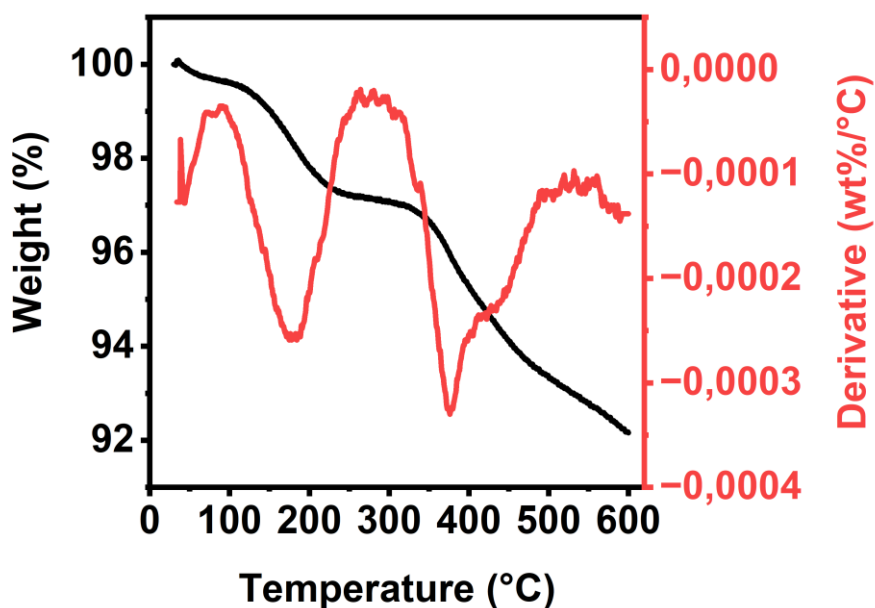


**Figure S5-21:** TGA measurement of (FeTaTPPAg)<sub>n</sub>. The derivative shows two main weight loss steps at 174°C and 376°C.



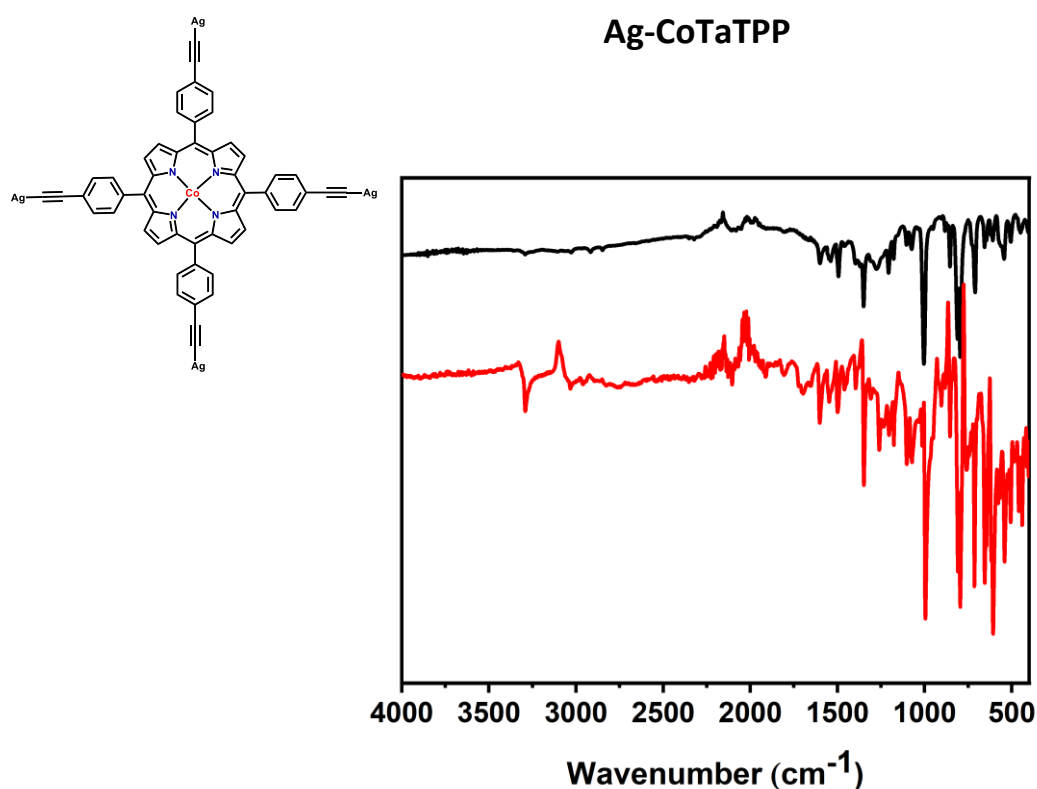


**Figure S5-22** IR spectrum of compound C10 (Black) and its starting C8 (red). The intensity of the C≡C-H band (3291 cm<sup>-1</sup>) is decreased significantly from C8 to C10 due to the addition of the silver.

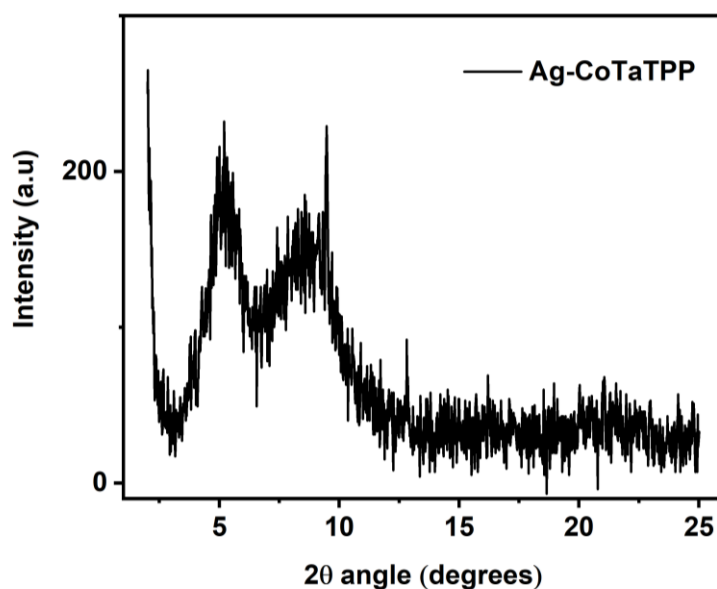
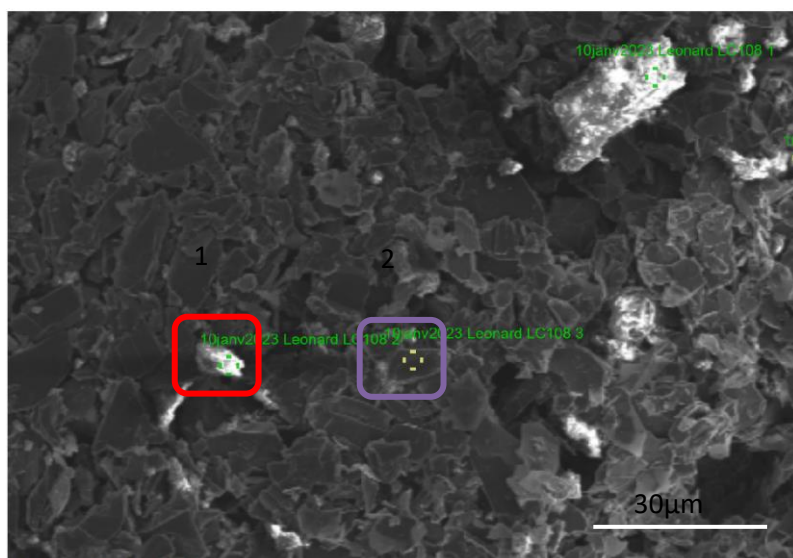
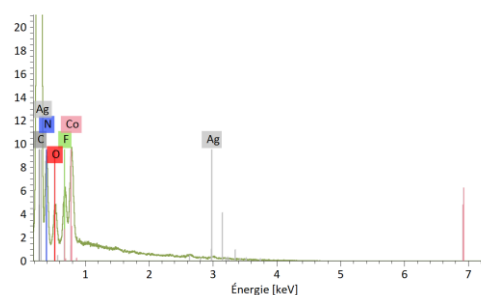


**Figure S5-23:** Powder XRD pattern of Ag-CoTaTPP between 2 and 25°. The starting material is crystalline. The observed peaks are of low intensity hinting for a poorly crystalline final structure with a COF-like arrangement. Crystallinity is measured to be 61% (obtained by comparing the integrated intensity of the background with the peaks). Crystal size is calculated to be 95 Å by Scherrer equation.

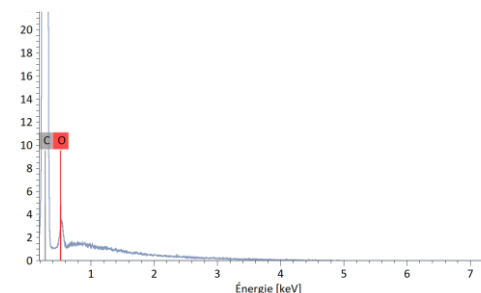


1



Élément	A	Raies	Net	Mass. [%]	Mass. norm. [%]	Atom. [%]
carbone	6	K	803865	---	81.00	87.98
azote	7	K	26858	---	8.89	8.28
oxygène	8	K	9554	---	1.75	1.43
fluor	9	K	9596	---	1.41	0.97
cobalt	27	L	36079	---	5.03	1.11
argent	47	L	1034	---	1.93	0.23
<b>Total</b>					<b>100.00</b>	<b>100.00</b>

2



Élément	A	Raies	Net	Mass. [%]	Mass. norm. [%]	Atom. [%]
carbone	6	K	986959	---	98.95	99.21
oxygène	8	K	5440	---	1.05	0.79
<b>Total</b>					<b>100.00</b>	<b>100.00</b>

**Figure S5-24:** SEM Picture of a prepared Ag-CoTaTPP Electrode. 1 and 2 show quantitative elemental measurements by EDS of Ag-CoTaTPP containing spot and without catalyst respectively. **Material concentration seems to be highly localized (consequently poorly dispersed) and corresponds to the charging parts of the electrode.**

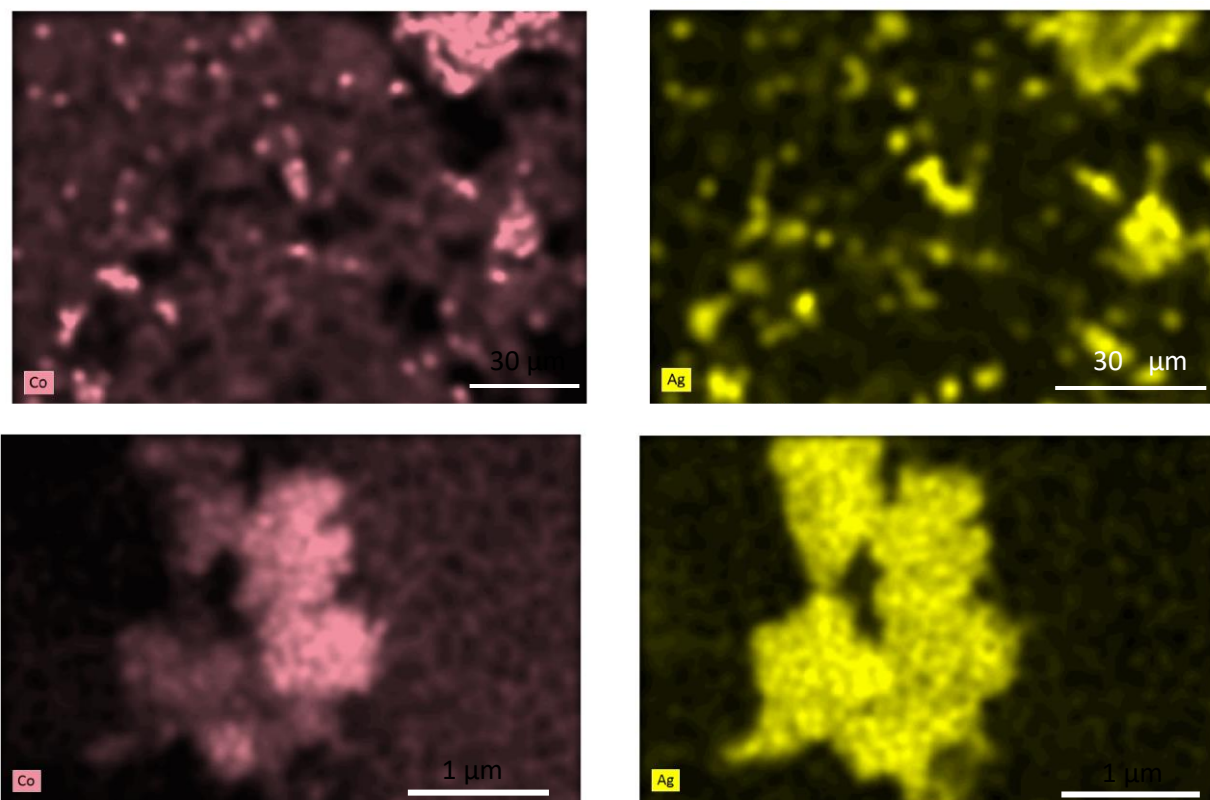


**Figure S5-25:** SEM-EDS Pictures of Cobalt and Silver of a prepared Ag-CoTaTPP Electrode at 1500x and 50 000x magnification. Co and Ag signals intensity correspond to charging amorphous particles which we assume to be the chemical of interest confirming the poor catalyst distribution on the electrode.

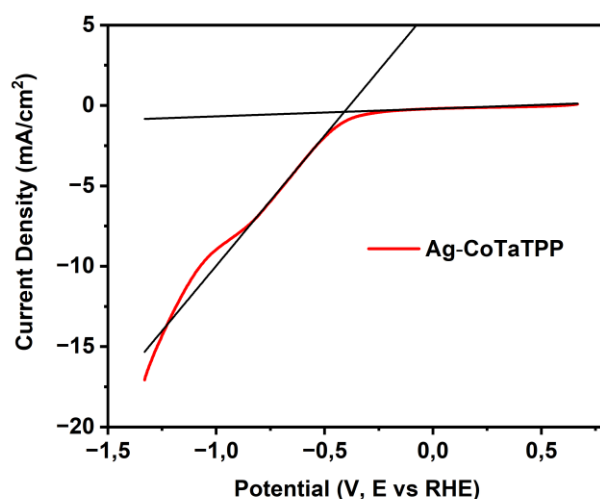


**Figure S5-26:** LSV measurement at 10 mV/s (2<sup>nd</sup> scan) of the deposited Ag-CoTaTPP in a 0.5 M KHCO<sub>3</sub> solution. Potential is uncorrected. The overpotential is measured as -0.409V vs RHE as the cross point of the coulombic and faradic currents.

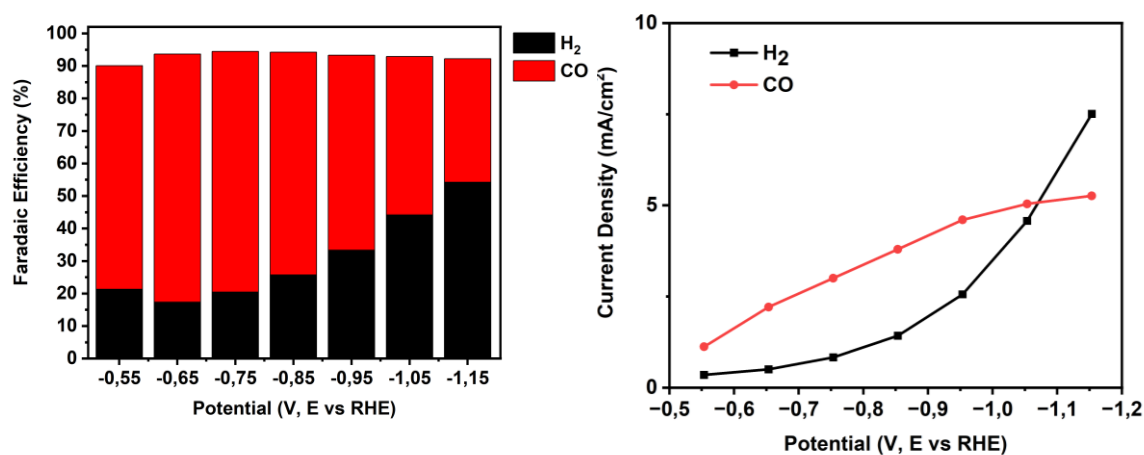


**Figure S5-27: a)** Ag-CoTaTPP measured faradaic efficiency (FE) from direct GC quantification at potential varied between -0.55 and -1.15 V vs RHE in a 0.5 M KHCO<sub>3</sub> solution. Potential is uncorrected **b)** Measured current densities for CO and H<sub>2</sub> with varying potential.

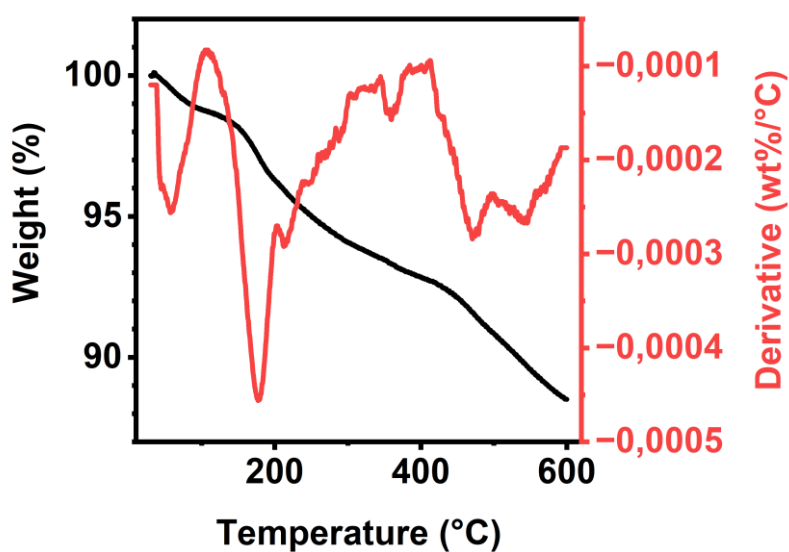


**Figure S5-28:** TGA measurement of (CoTaTPPAg)<sub>n</sub>. A first step at low temperature is assumed to be a solvent evaporation. The derivative shows two main weight loss steps at 179°C and 475-542°C.

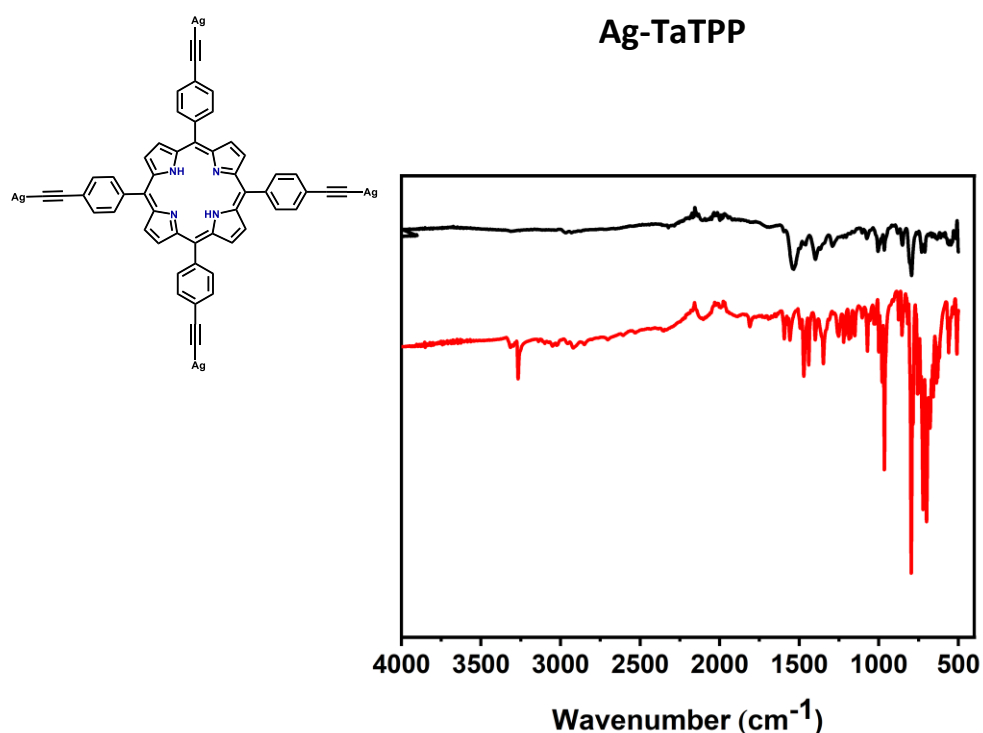


**Figure S5-29** IR spectrum of compound C11 (Black) and its starting C6 (red). The intensity of the C≡C-H band (3267 cm<sup>-1</sup>) is decreased significantly from C6 to C11 due to the addition of the silver.

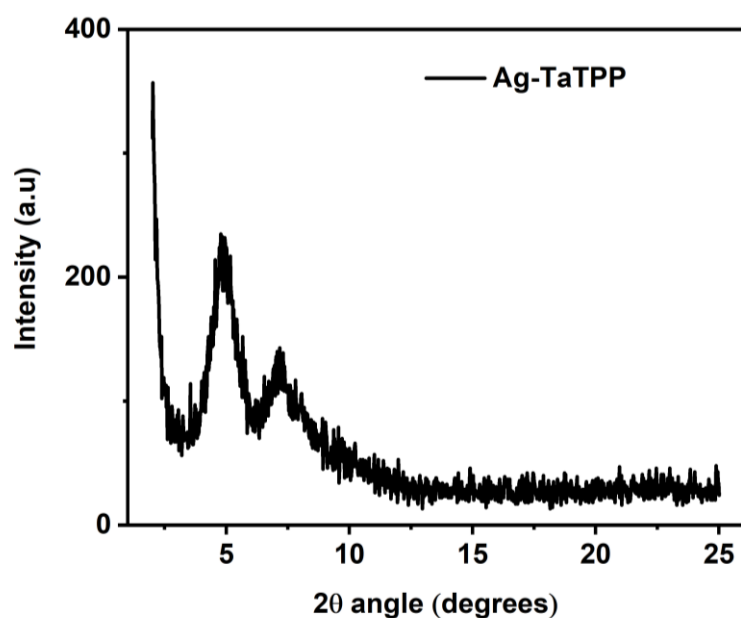


**Figure S5-30:** Powder XRD pattern of Ag-TaTPP between 2 and 25°. The starting material is amorphous. The observed peaks are of low intensity hinting for a poorly crystalline final structure with a COF-like arrangement. Crystallinity is measured to be 68% (obtained by comparing the integrated intensity of the background with the peaks). Crystal size is calculated to be 115 Å by Scherrer equation.

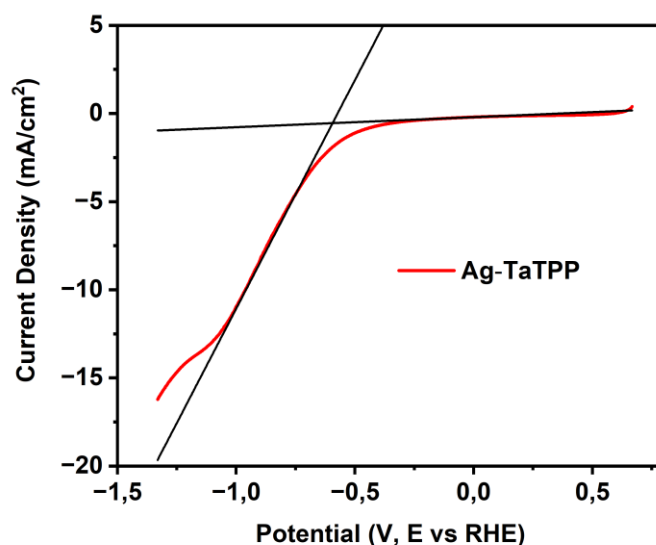


**Figure S5-31:** LSV measurement at 10 mV/s (2<sup>nd</sup> scan) of the deposited Ag-TaTPP in a 0.5 M KHCO<sub>3</sub> solution. Potential is uncorrected. The overpotential is measured as -0.59427 V vs RHE as the cross point of the coulombic and faradic currents

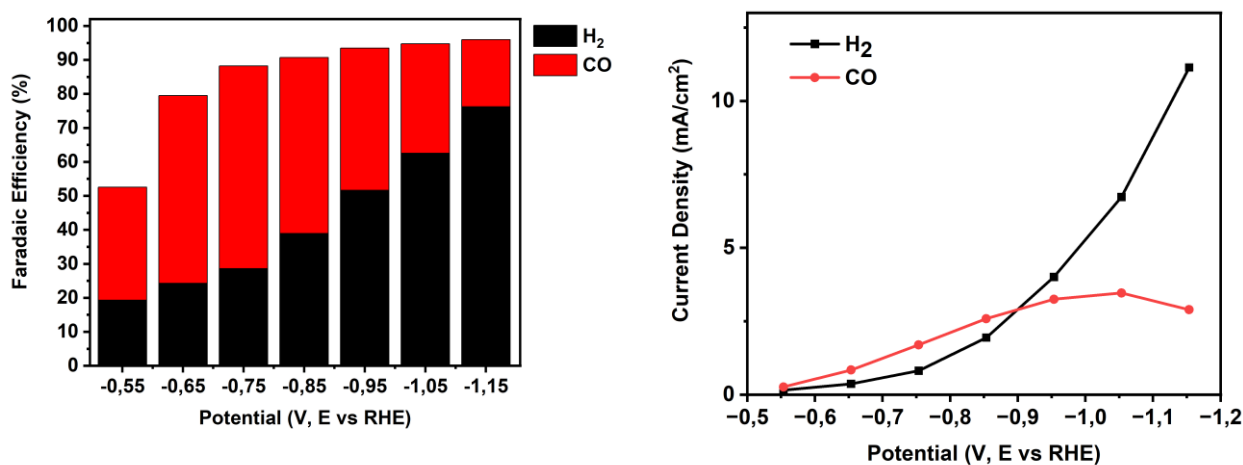


**Figure S5-32: a)** Ag-TaTPP measured faradaic efficiency (FE) from direct GC quantification at potential varied between -0.55 and -1.15 V vs RHE in a 0.5 M KHCO<sub>3</sub> solution. Potential is uncorrected **b)** Measured current densities for CO and H<sub>2</sub> with varying potential.

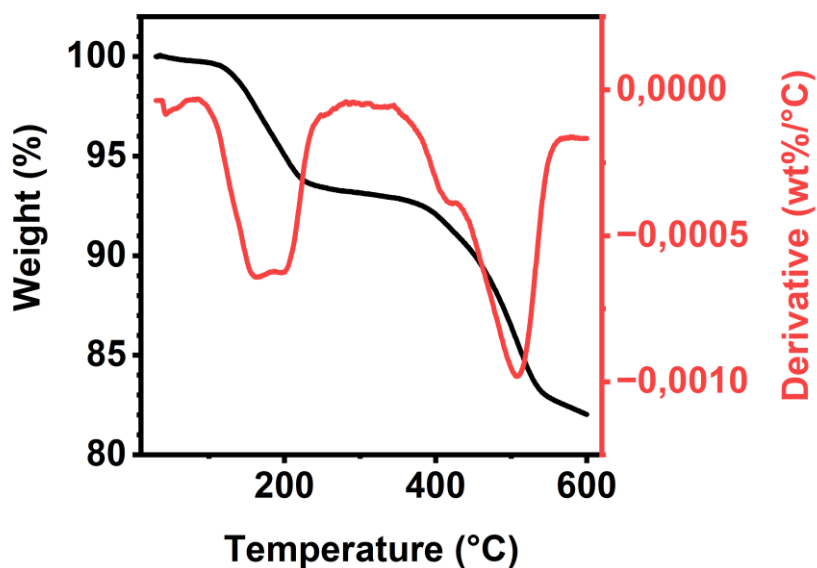


Figure S5-33: TGA measurement of (TaTPPAg)<sub>n</sub>. The derivative shows 3 main weight loss steps at 161°C, 198°C and 507°C

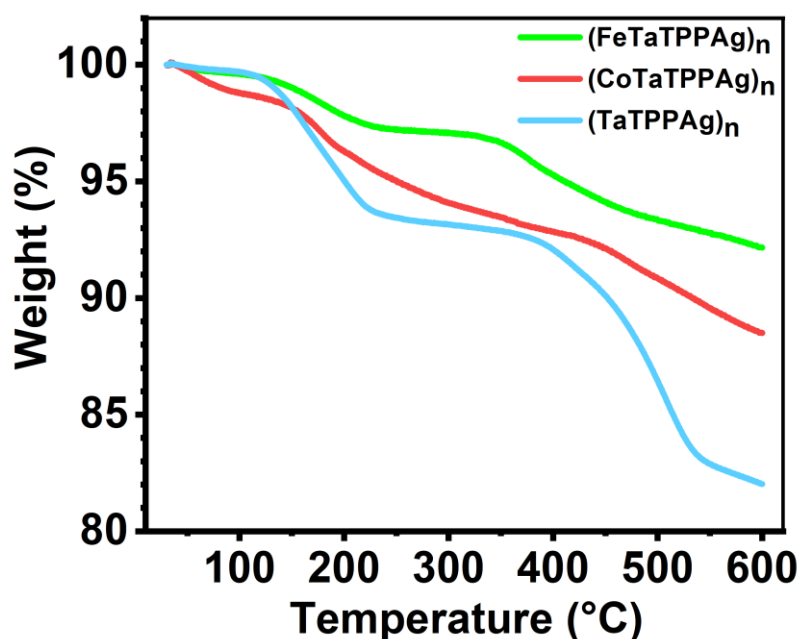
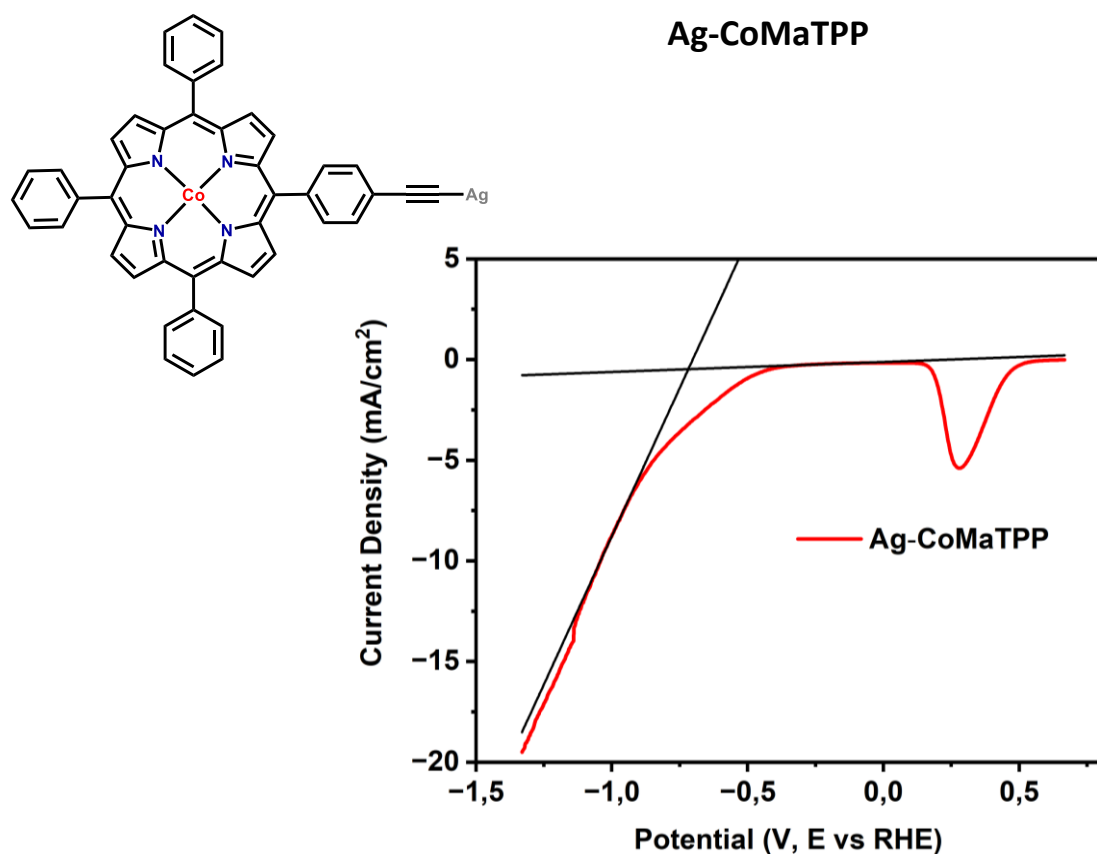
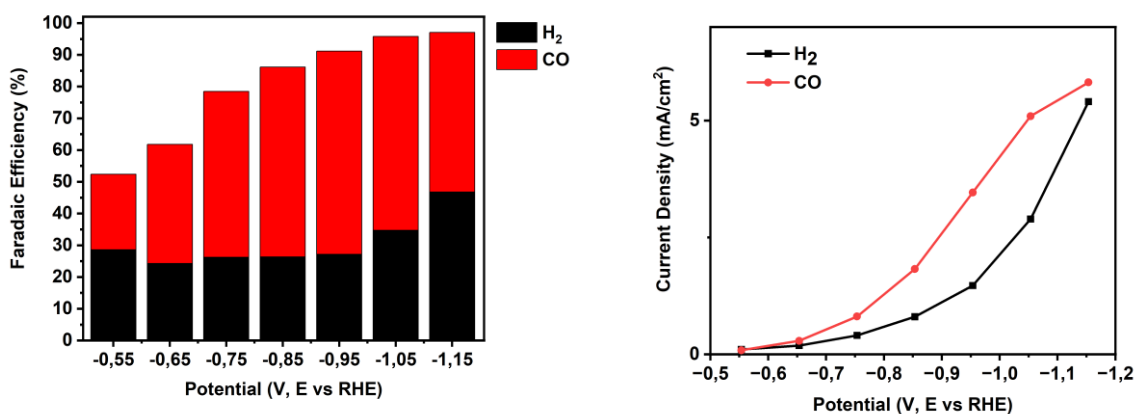


Figure S5-34: TGA measurement comparison for the derivatives. The mass loss is more important for the unmetalloporphyrin but a similar decomposition pattern is observed in every case with a first mass loss between 160 and 200°C followed by a second step.



**Figure S5-35:** LSV measurement at 10 mV/s (2<sup>nd</sup> scan) of the deposited Ag-CoMaTPP in a 0.5 M KHCO<sub>3</sub> solution. Potential is uncorrected. The overpotential is measured as -0.718 V vs RHE as the cross point of the coulombic and faradic currents.



**Figure S5-36: a)** Ag-TaTPP measured faradaic efficiency (FE) from direct GC quantification at potential varied between -0.55 and -1.15 V vs RHE in a 0.5 M KHCO<sub>3</sub> solution. Potential is uncorrected **b)** Measured current densities for CO and H<sub>2</sub> with varying potential.



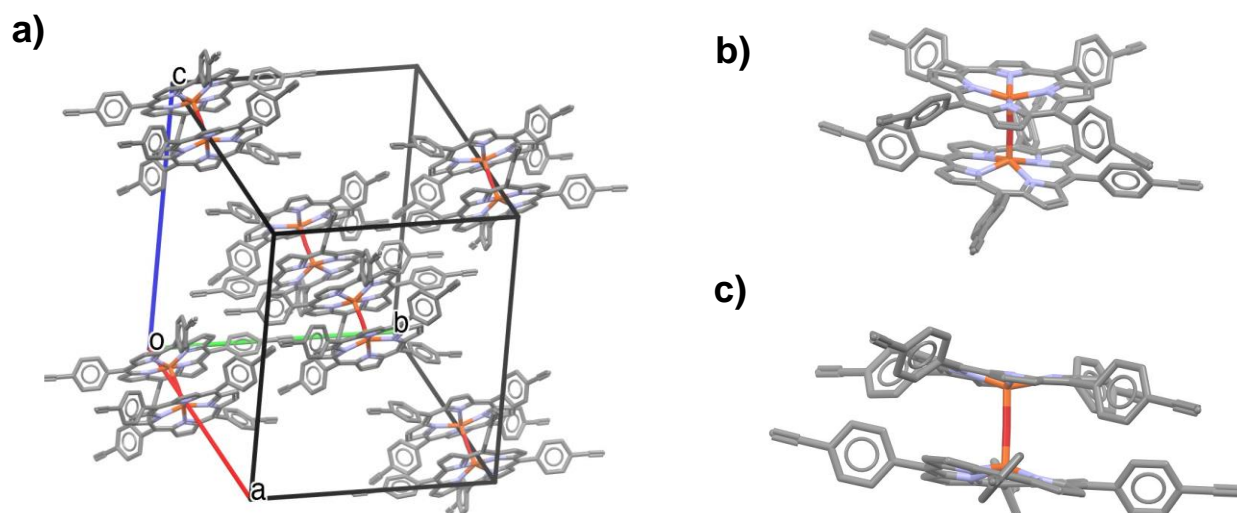


**Figure S 5-37:** X-Ray diffraction single crystal structure of the Oxygen-bridged porphyrin dimer; **a)** unit cell view of the dimers' packing arrangement; **b)** view of the dimer; **c)** side view of the dimer.

## Conclusion and perspectives

### THESIS CONCLUSIONS

The work presented in this thesis was a part of the *Intermat* international chair awarded to Prof. Emilio Palomares by the E2S funding scheme to develop a research line on the photo and electroreduction of CO<sub>2</sub> for which no previous expertise was present at the IPREM. As such, it is worth pointing out that a laboratory dedicated to the characterization of our catalysts was created, a lengthy process in which I took an active part. During my PhD, the laboratory evolved gradually from primitive facilities to a highly advanced characterization environment with a fully automated characterization setup for both CO<sub>2</sub>RR and HER either for photo or electrochemical applications. Numerous results ensued as a result of the setup's constant evolution, and only a portion of them were hereby presented for consistency.

This thesis was centred on the electroreduction of CO<sub>2</sub>, and my first year primarily focused on the synthesis and evaluation of the catalytic properties of porphyrin-based catalysts, of which only a handful have been mentioned. While these types of catalysts are particularly efficient, they intrinsically possess limitations. Their overall cost and relatively poor stability under prolonged electrolysis led us to shift our interest towards the use of rather different, unusual catalysts. Amongst these, we unexpectedly found that silver acetylide clusters were a particularly interesting family of organometallic structures for which, at the time, very few results related to catalysis in the context of CO<sub>2</sub> reduction had been published. We, therefore, started by characterizing and testing the properties of a silver phenylacetylide cluster, which showed impressive properties compared to state-of-the-art metallic silver electrodes. We revisited their synthesis methodology and found that a slightly modified version of Scheiber's original method was very well suited to their large-scale synthesis in quantitative yields and high purity. The methodology was later applied to the synthesis of an extensive library of silver acetylide clusters with a wide variety of organic ligands, of which some of the porphyrins synthesized early on in my PhD were included. All the clusters synthesized were shown to possess a clear ability to reduce CO<sub>2</sub> to CO and showed a relatively high degree of crystallinity overall. Differences in catalytic activity were observed and related to the nature of the ligand forming the cluster structure. For the most active structures, we observe activities and overpotentials similar to the ones observed for gold nanoparticles, a benchmark in the field. We put particular emphasis on understanding the properties of silver acetylides from a fundamental perspective, seeking a link between the solid-state structure of the clusters and their catalytic properties. As such, we have been collaborating with the ICIQ (Tarragona) and their crystallography unit, which resolved a crystal structure of one of our silver clusters from the catalyst powders *via* electron diffraction. We have been collaborating actively with the theoretical chemistry department of IPREM which has obtained conclusive calculation results related to CO<sub>2</sub>RR and our structure organisation. These results will be included in the final manuscripts of the chapters.

The silver acetylide clusters were shown to shine as catalysts for bulk electrolysis, a field I embraced early on in my PhD due to its capital importance for potential applications. We have put great effort into designing a homemade flow-cell electrolyzer from the ground up that allowed demonstrating for the first time that these silver acetylides are particularly effective for CO<sub>2</sub>RR to CO applications (>95% FE) at industrially relevant rates with currents reaching 300 mA/cm<sup>2</sup>.

Aside from the development of catalysts for the electroreduction of CO<sub>2</sub>, I dedicated part of my time to studying fundamental aspects of CO<sub>2</sub> interactions with organic molecules, such as macrocyclic guests. A standardized NMR titration procedure for the measurement of the association constant between CO<sub>2</sub> and a solubilized species was developed. To the best of our knowledge, this procedure is the first occurrence of the direct measurement of an association constant between a gas and a solubilized species.

### PERSPECTIVES

Although the synthesis of silver acetylide clusters has led to very positive results, we faced important issues regarding the supporting electrodes under bulk electrolysis conditions. A clear decrease in hydrophobicity was observed, generally after a few hours of constant current electrolysis in flow cells, leading to consistent flooding and loss of activity. We have consequently been unable to precisely assess the catalyst stability over prolonged periods in these conditions. In this context, XAS measurements would provide a powerful tool to understand these species' evolution during catalysis. Applications for synchrotron can, therefore, be anticipated. To circumvent this issue, we have shifted our interest to the use of Teflon-based membranes instead of the carbon GDLs. Teflon GDLs have become an intense field of research, enabling the de-coupling of the electrically conductive properties of the GDLs with the catalytic activity, effectively preventing electrode flooding. Preliminary results have been obtained from flow-cell experiments; however, these early experiments point to the need for further optimization of the electrode preparation. An important increase in selectivity and long-term stability is foreseen; therefore, this field will be given great emphasis in the near future, together with the adaptation of silver acetylide catalysts to MEA electrolyzers.

The synthetic success of silver acetylides and their exclusive selectivity for CO naturally steered our focus on the development of a synthetic method for the formation of copper acetylide analogues. Their expected cluster structure and the presence of copper instead of silver would theoretically allow the formation of C<sub>2</sub> products. The above methodology was modified, and a small library of copper acetylides was synthesized. We observed similar crystalline features as their silver analogues; the products are air-stable and display additional luminescence properties. Only one of these derivatives has been tested on carbon GDLs so far, with hydrogen being the major product. Future work will focus on the in-depth study of copper acetylides and their implementation in a high throughput synthesis of CO<sub>2</sub>RR catalysts.

Finally, the NMR titration methodology expounded above will be applied to the quantification of host-gas interaction of gases other than CO<sub>2</sub>. The end goal would be, among others, a better understanding of the main parameters favouring host/gas interactions and, consequently, designing hosts with a significant affinity for CO. Such hosts would find interesting applications as catalyst additives, possibly shifting the catalyst's selectivity by maintaining the CO intermediate close to the catalyst surface.

The projects expounded in this thesis have been accompanied by numerous side projects, with focus closely related to the work described herein. I have, so far, co-authored two papers that are currently under review in *Chemical Communication* and *ACS Applied Materials & Interfaces*. Three additional papers will be submitted very shortly, and two more are currently in preparation.

CONTACT

[curetleonard@gmail.com](mailto:curetleonard@gmail.com)